

MECHANICAL INSTABILITY OF THE INTERFACES
IN SOLID-STATE BATTERIES

by

Chunhao Yuan

A dissertation submitted to the faculty of
The University of North Carolina at Charlotte
in partial fulfillment of the requirements
for the degree of Doctor of Philosophy in
Mechanical Engineering

Charlotte

2022

Approved by:

Dr. Jun Xu

Dr. Ronald E. Smelser

Dr. Qiuming Wei

Dr. Haitao Zhang

Dr. Tiefu Zhao

Dr. Tao Hong

ABSTRACT

CHUNHAO YUAN. Mechanical Instability of the Interfaces in Solid-State Batteries
(Under the direction of DR. JUN XU)

All-solid-state batteries (ASSBs) are considered promising candidates for next-generation batteries due to their excellent safety performance guaranteed by inorganic solid electrolytes (SEs) with the non-flammability nature, as well as the greatly increased energy density enabled by the adoption of lithium metal anode. Unlike conventional lithium-ion batteries (LIBs) using liquid electrolytes, all the components within the ASSBs system, including the composite cathode, lithium anode, and solid electrolyte, are solid-state. Solid-solid interfacial contacts within ASSBs, such as the dendrite-electrolyte interface and electrode-electrolyte interface, are the origin of interfacial instability issues. The interfacial instability problems mainly exhibit in the form of lithium dendrite growth-induced short circuits and interfacial debonding failure inside composite cathode, which are the major hurdles on the road towards the large-scale commercialization of ASSBs. Experimental characterizations are limited by the coupling of the solid nature of SE (vision overlap), and ultrasmall length scale. Therefore, versatile and physics-based models to describe the electrochemical behaviors of the ASSBs are in pressing need.

Herein, considering the highly multiphysics nature of ASSB behaviors, fully coupled electrochemo-mechanics models at different scales are developed to investigate the underlying mechanism of dendrite growth and interfacial failure. From the energy conservation perspective, the electrochemical-mechanical phase-field model at the

electrolyte scale is firstly established to explore the dendrite growth behavior in polycrystalline SE. The newly formed crack and the grain boundary are found to be the preferential dendrite growth paths, and stacking pressure affects the driving force for both dendrite growth and crack propagation. Next, the cell-scale multiphysics modeling framework integrating the battery model, mechanical model, phase-field model, and short-circuit model is developed to study the entire process from battery charging to dendrite growth and to the final short circuit. The governing effects from various dominant factors are comprehensively discussed. Further on, inspired by the “brick-and-mortar” structure, the strategy of inserting heterogeneous blocks into SEs is proposed to mitigate dendrite penetration-induced short circuit risk, and the overall dendrite mitigation mechanism map is given. Finally, the three-dimensional fully coupled electrochemical-mechanical model is developed to investigate the interfacial failure phenomena, taking into account the electrochemical reaction kinetics, Li diffusion within the particle, mechanical deformation, and interfacial debonding. The randomly distributed $\text{LiNi}_{1/3}\text{Co}_{1/3}\text{Mn}_{1/3}\text{O}_2$ primary particles result in the anisotropic Li diffusion and volume variation inside the secondary particle, leading to significant nonuniformity of the Li concentration, strain, and stress distributions. This also serves as a root cause for the internal cracks or particle pulverization. The particle volume shrinkage under the constraint of the surrounding SE triggers the interfacial debonding with increased interfacial impedance to degrade cell capacity. This study explores the dendritic issue and mechanical instability inside ASSBs from the multiphysics

perspective at different scales, obtaining an in-depth understanding of the electrochemical-mechanical coupling nature as well as providing insightful mechanistic design guidance maps for robust and safe ASSB cells.

ACKNOWLEDGMENTS

I would like to express my sincerest gratitude to my advisor Dr. Jun Xu. Without his support and thoughtful guidance from the beginning of my undergraduate to the ending of my Ph.D., it would be impossible for me to become what I am today. His broad vision of life and research, keen insight into scientific problems, rigorous logical thinking, and perseverance in problem-solving, have gradually shaped my character both as a person and a researcher.

I am so honored to have Dr. Ronald E. Smelser, Dr. Qiuming Wei, Dr. Haitao Zhang, Dr. Tiefu Zhao, and Dr. Tao Hong as my committee members. I greatly appreciate their constructive comments and insightful suggestions that have helped me strengthen my research base and improve my topic.

I am very grateful to all the previous and current group members of VESL. Thanks to Dr. Binghe Liu and Dr. Lubing Wang for helping me a lot at the beginning of my research. Thanks to Dr. Xiang Gao and Dr. Yikai Jia for their great help in conducting experiment, solving the problems in numerical modeling, and working on the projects. Thanks to Dr. Wen Zhang, Ms. Jiani Li, Mr. Xudong Duan and other group members for their support and help.

I want to thank my father, Mr. Guangqiang Yuan, and my mother, Mrs. Xuelan Liu, for their unconditional support and understanding wherever I am and whatever I do. I would like to thank my brother, Mr. Xiaoxu Yuan, and his family (Mrs. Li Hua, Mr. Yihang

Yuan) for their support for me and care for my parents. Lastly, I want to thank my girlfriend, Ms. Mengmeng Zhang for her spiritual support over the years and accompanying me through ups and downs.

TABLE OF CONTENTS

| | |
|--|------|
| LIST OF TABLES | xii |
| LIST OF FIGURES | xiii |
| NOMENCLATURE | xx |
| CHAPTER 1 INTRODUCTION | 1 |
| 1.1 Background..... | 1 |
| 1.2 Literature review..... | 2 |
| 1.2.1 Solid electrolyte..... | 2 |
| 1.2.2 Dendrite initiation and growth..... | 4 |
| 1.2.3 Mechanical property of lithium..... | 8 |
| 1.2.4 Composite electrode particle expansion | 10 |
| 1.2.5 Optimization methodology | 12 |
| 1.3 Challenges and motivation..... | 13 |
| 1.4 Chapter arrangement..... | 14 |
| CHAPTER 2 COUPLED DENDRITE GROWTH AND CRACK | |
| PROPAGATION AT ELECTROLYTE SCALE | 15 |
| 2.1 Methodology..... | 15 |
| 2.2 Representative computational results..... | 24 |
| 2.3 Discussion..... | 28 |
| 2.3.1 Geometric information of the initial defect..... | 28 |

| | | |
|---|----|----|
| 2.3.1.1 Length effect..... | 28 | |
| 2.3.1.2 Angle effect..... | 31 | |
| 2.3.1.3 Shape effect..... | 33 | |
| 2.3.2 Stacking pressure effect..... | 35 | |
| 2.3.3 Fracture threshold strain effect..... | 40 | |
| 2.4 Conclusions..... | 43 | |
| CHAPTER 3 COUPLED DENDRITE GROWTH AND CRACK | | |
| PROPAGATION AT CELL SCALE..... | | 46 |
| 3.1 Methods..... | 46 | |
| 3.1.1 Coupling strategy..... | 46 | |
| 3.1.2 Modeling methodology..... | 50 | |
| 3.2 Results and discussion..... | 58 | |
| 3.2.1 Representative results..... | 58 | |
| 3.2.2 Governing effect from overpotential-driven stress..... | 61 | |
| 3.2.3 Governing effect from the charging rate..... | 65 | |
| 3.2.4 Governing effect from the electrolyte conductivity..... | 68 | |
| 3.2.5 Governing effect from Young's modulus..... | 72 | |
| 3.2.6 Governing effect from fracture toughness..... | 75 | |
| 3.2.7 Implication on engineering application..... | 78 | |
| 3.3 Conclusions..... | 80 | |

| | |
|--|-----|
| CHAPTER 4 MITIGATION STRATEGY OF DENDRITE GROWTH | 83 |
| 4.1 Methodology..... | 83 |
| 4.2 Results and discussion | 85 |
| 4.2.1 Dendrite propagation..... | 85 |
| 4.2.2 Dendrite mitigation effect with single HB..... | 92 |
| 4.2.3 Dendrite mitigation effect with multiple HBs in small e | 97 |
| 4.2.4 Dendrite mitigation effect with multiple HBs in medium e | 100 |
| 4.2.5 Multilayer electrolyte design to mitigate dendrite | 103 |
| 4.4 Conclusions..... | 109 |
| CHAPTER 5 ELECTROCHEMICAL-MECHANICAL COUPLING | |
| FAILURE MECHANISM OF COMPOSITE CATHODE | 111 |
| 5.1 Methodology..... | 111 |
| 5.2 Results..... | 120 |
| 5.3 Discussion..... | 126 |
| 5.3.1 Charging rate effect..... | 126 |
| 5.3.2 Heterogeneity effect..... | 131 |
| 5.3.3 Interfacial strength effect | 135 |
| 5.3.4 Particle position effect | 138 |
| 5.4 Conclusion | 141 |
| CHAPTER 6 CONCLUDING REMARKS | 143 |

| | |
|---|-----|
| REFERENCES | 146 |
| APPENDIX A: Validation of the Established Modeling Framework..... | 155 |
| APPENDIX B: List of Governing Equations | 157 |
| APPENDIX C: Clarification of the Phase-field Modeling Approach..... | 158 |
| APPENDIX D: PERMISSION LETTERS | 160 |

LIST OF TABLES

| | |
|---|-----|
| Table 1 Summary of material properties and simulation parameters..... | 22 |
| Table 2 Summary of material properties and simulation parameters..... | 57 |
| Table 3 Summary of material properties and simulation parameters..... | 119 |
| Table 4 Main governing equations in the modeling framework | 157 |

LIST OF FIGURES

| | |
|---|----|
| Figure 1 Summary of the interfacial issues in all-solid-state batteries ⁹ | 2 |
| Figure 2 Dendrite initiation behavior in ASSBs: (a) schematic illustration of dendrite initiation; (b) dendrite initiation at the Li-electrolyte interface ⁵⁴⁻⁵⁸ ; (c) dendrite formation inside electrolytes ^{52, 53} | 5 |
| Figure 3 Dendrite growth behavior in ASSBs: (a) intergranular dendrite penetration ^{54, 63} ; (b) dendrite growth along interconnected micropores inside electrolyte ⁶¹ ; (c) dendrite growth coupled with crack propagation ^{50, 65, 66} | 7 |
| Figure 4 Mechanical strength of lithium at different length scale ⁷⁷ | 10 |
| Figure 5 Particle volume variation issues in composite electrode: (a) experimental characterization ⁸³ ; (b) numerical simulation ²⁵ | 12 |
| Figure 6 Optimization methodology for interfacial instability: (a) interphase material ⁸⁷ ; (b) electrolyte improvement ⁵⁵ ; (c) electrode structure design ⁸⁶ ; (d) mechanical stack pressure ⁹⁷ | 13 |
| Figure 7 Schematics of the established model. The anode and cathode are on the left and right sides, respectively. A preset defect is embedded within one grain near the Li/SE interface. Uniformly distributed pressure is applied on the anode side to mimic the stacking pressure, while a fixed boundary is set on the cathode side. | 16 |
| Figure 8 Typical simulation results with rectangular pre-defect with $\theta=30^\circ$ under 50 MPa pressure: (a) Li dendrite growth ξ , (b) dimensionless Li-ion concentration evolution \tilde{c}_+ , (c) potential field evolution φ , and (d) crack area propagation ϕ_{cr} when pre-defect is located at the center of grain edge; (e) crack area propagation ϕ_{cr} when pre-defect is close to grain boundary; (f) crack area propagation ϕ_{cr} when crack propagation is considered in two grains and grain boundary region..... | 27 |
| Figure 9 Effect of initial defect size on dendrite growth and crack propagation behavior: (a) Li dendrite growth of different pre-defect lengths at 200 s, i.e., 10, 20, 30 and 40 μm ; (b) newly grown Li dendrite area in whole domain (WD) and grain boundary (GB); (c) evolution of normalized crack area S ; (d) average value E_{ave} and maximum value E_{max} of strain energy density in the crack area; (e) average strain energy density in pre-defect area E_{ave_pd} ; and (f) average strain energy density in crack propagation area E_{ave_pr} | 31 |
| Figure 10 Effect of initial defect angle on dendrite growth and crack propagation behavior: (a) evolution of normalized crack area S ; (b) maximum von Mises stress σ_{max} in the crack propagation area under different pre-defect angle; (c) Li dendrite ξ growth of different pre-defect angle at 200 s, i.e., 0° , 15° , 30° , 45° , 60° , 75° , and 90° ; (d) von Mises stress σ contour plots for selected pre-defect angles, i.e., 0° , 30° , and 75° | 33 |

- Figure 11 Effect of initial defect shape on dendrite growth and crack propagation behavior: (a) newly grown Li dendrite area in whole domain and in grain boundary; (b) evolution of normalized crack area S ; (c) maximum Mises stress σ_{\max} of different pre-defect shape; (d) Average strain energy density E_{ave} of different pre-defect shape..... 35
- Figure 12 Effect of stacking pressure on dendrite behavior: (a) farthest Li dendrite growth distance X in grain boundary; (b) newly grown dendrite area S_{GB} in grain boundary; (c) mechanical contribution term F_{M} to the dendrite growth; (d) electrochemical contribution term F_{EC} to the dendrite growth; (e) dendrite growth for 60 MPa pressure; and (f) mechanical contribution term contour plots for 60 MPa pressure..... 38
- Figure 13 Effect of stacking pressure on crack propagation behavior: (a) normalized crack area S ; (b) contour plots of the crack parameter at 200 s under different pressures; (c) average value σ_{ave} and maximum value σ_{\max} of Mises stress in crack propagation area; and (d) average value E_{ave} and maximum value E_{\max} of strain energy density in crack propagation area for different stacking pressure..... 40
- Figure 14 Effect of fracture threshold strain on crack propagation and dendrite growth behavior: (a) evolution of normalized crack area S ; (b) normalized crack area increasing rate dS/dt ; (c) contour plots of the crack parameter at 200 s under different fracture threshold strains; (d) newly grown dendrite area in whole domain and in grain boundary region; and (e) contour plots of dendrite parameter at 200 s under different fracture threshold strains..... 43
- Figure 15 Multiphysics coupling strategy for battery model, mechanical model, phase-field model, and short-circuit model..... 47
- Figure 16 Schematics of the established model including geometry, boundary condition, and defect area. 49
- Figure 17 Crack propagation behavior with pre-existing defect of different dimensions. (a) for the large defect, the length $L=100 \mu\text{m}$, width $W=50 \mu\text{m}$; for the small defect, the length $L=40 \mu\text{m}$, width $W=15 \mu\text{m}$; (b) the voltage response for the model without interfacial defect, i.e. the defect size is 0..... 49
- Figure 18 Representative computational results at 1C charging rate. (a) voltage response and detected phase-field variable ξ at the LCO/LLZO interface at 1C charging rate; (b) dendrite growth ξ evolution ($\xi = -1$ for dendrite/crack, $\xi = 1$ for intact solid electrolyte); (c) von Mises stress evolution σ_{Mises} ; (d) electrolyte potential distribution and current density vector (the thicker and longer arrow indicates larger current density) at the beginning and ending time..... 60
- Figure 19 Representative results: electrolyte potential ϕ_l distribution and current density vector (the arrows indicate only the current direction and distribution, not the magnitude)..... 61
- Figure 20 Effect of electrochemically induced stress at 1C charging rate. (a)

schematics of the crack propagation/dendrite growth driven by the overpotential-induced stress; (b) voltage vs. time curves for models without and with the stress effect; (c) effective electrolyte conductivity σ_{SE} and current density vector (the thicker and longer arrow indicates larger current density); (d) stress tensor components σ_{xx} , σ_{yy} , σ_{zz} and von Mises stress σ_{Mises} at $t=200$ s..... 64

Figure 21 Effect of electrochemically induced stress. (a) dendrite ξ evolution considering the stress effect; (b) von Mises stress evolution σ_{Mises} considering the stress effect; (c) strain energy density considering the stress effect; (d) maximum stress components σ_{xx} and σ_{yy} within the solid electrolyte domain... 65

Figure 22 Effect of charging rate. (a) schematics of the charging-rate effect on dendrite growth; (b) voltage vs. time curves; (c) contour plots of phase-field parameter ξ ; (d) electrolyte potential ϕ_l distribution at $t=200$ s; (e) safety guidance map based on overpotential η_- /short-circuit time t_{short} 67

Figure 23 Effect of charging rate. (a) stress tensor components σ_{xx} , σ_{yy} , σ_{zz} , and von Mises stress σ_{Mises} for different C-rates at $t=200$ s; (b) overpotential vs. time curves during 0~200 s..... 68

Figure 24 Effect of electrolyte conductivity. (a) voltage vs. time curves; (b) contour plots of crack parameter ξ at short-circuit point; coupled effect of charging rate and electrolyte conductivity σ_{LLZO} on the (c) overpotential η_- and (d) short-circuit time t_{short} 71

Figure 25 Effect of electrolyte conductivity. (a) overpotential η_- vs. time curves during 0~360 s; (b) maximum von Mises stress σ_{Mises_max} and average von Mises stress σ_{Mises_ave} 72

Figure 26 Effect of Young's modulus. (a) voltage vs. time curves for different E_{LLZO} ; (b) short-circuit time for different E_{LLZO} ; (c) farthest dendrite growth x in the transverse direction; (d) fracture energy G and average energy density E_{ave} at $t=250$ s as a function of E_{LLZO} 74

Figure 27 Effect of Young's modulus. (a) maximum von Mises stress σ_{Mises_max} and average von Mises stress σ_{Mises_ave} ; (b) maximum strain energy density E_{max} and average strain energy density E_{ave} ; (c) von Mises stress σ_{Mises} , and (d) strain energy density E at short-circuit time..... 75

Figure 28 Effect of fracture toughness: (a) voltage vs. time curves; (b) short-circuit time t_{short} as a function of fracture toughness K_{LLZO} ; (c) design map based on the coupled effect of normalized Young's modulus and normalized fracture toughness. 77

| | |
|--|-----|
| Figure 29 Dendrite ξ evolution at the practical current density $2100 \mu\text{A}/\text{cm}^2$ (i.e., 1.5 C in this study) considering different electrolyte fracture toughness. | 80 |
| Figure 30 Illustration of the strategy of adding heterogenous blocks into ASSBs: (a) schematic of 3-D battery structure, (b) simplified 2-D battery model..... | 85 |
| Figure 31 Effect of initial defect length on dendrite mitigation behavior: (a) initial defect length $4 \mu\text{m}$; (b) initial defect length $6 \mu\text{m}$ | 85 |
| Figure 32 Baseline model: dendrite growth in solid electrolyte without HBs. (a) Voltage response, (b) dendrite growth behavior, (c) electrolyte potential evolution, and (d) von Mises stress distribution. | 86 |
| Figure 33 Effects of HBs' properties on dendrite mitigation: (a) Young's modulus effect, (b) ionic conductivity effect, (c) fracture toughness effect. | 88 |
| Figure 34 Contour plots of strain energy density and stress tensor components when using high fracture toughness for a heterogeneous block. | 91 |
| Figure 35 Dendrite mitigation with HBs of different length: (a) HBs with different Young's modulus, ionic conductivity and fracture toughness from main body of LLZO electrolyte; (b) HBs with only different fracture toughness from main body of LLZO electrolyte. | 92 |
| Figure 36 Dendrite growth behavior with a single heterogeneous block: (a) the electrolyte potential ϕ_i distribution without and with adding HB to the electrolyte (Note: the red arrows represent the gradient of the electrolyte potential); dendrite growth under different ratios $e = L_{\text{HB}} / L_{\text{Cell}}$ and cell length L_{Cell} : (b) $L_{\text{Cell}} = 50 \mu\text{m}$, (c) $L_{\text{Cell}} = 100 \mu\text{m}$; (d) Stress tensor component σ_{ij} ($i, j = x, y$) distribution when the dendrite bypasses the block, with cell length $L_{\text{Cell}} = 100 \mu\text{m}$ | 96 |
| Figure 37 Short-circuit risk and dendrite mitigation effect with a single heterogeneous block under various length ratios $e = L_{\text{HB}}/L_{\text{cell}}$ | 97 |
| Figure 38 Dendrite mitigation with multiple heterogeneous blocks in small length ratio e : (a) illustration of two representative arrangement methods, (b) the dendrite growth behavior and mitigation effect in the two arrangement methods, (c) dendrite growth behavior at various applied current density. | 99 |
| Figure 39 Electrolyte potential distribution with multiple HBs in small e : baseline without any HB, A1 and A2 with multiple HBs ($L_{\text{HB}} = G = D = 4 \mu\text{m}$). | 100 |
| Figure 40 Dendrite mitigation with multiple heterogeneous blocks in medium length ratio e : (a) illustration of two representative arrangement methods, (b) the short-circuit risk as a function of distance ratio D/L , gap ratio G/L , length ratio e | 102 |
| Figure 41 Dendrite mitigation with multiple HBs in medium e | 103 |
| Figure 42 Dendrite mitigation effect with multilayer solid electrolyte design: (a) effect of Young's modulus E_{EL} of the embedded layer, dendrite mitigation behavior of (b) embedded layer with width $W = 10 \mu\text{m}$, (c) two embedded layers with both | |

| | |
|--|-----|
| width $W/2=5\ \mu\text{m}$, gap $5\ \mu\text{m}$, and (d) embedded layer with width $W/2=5\ \mu\text{m}$ | 106 |
| Figure 43 Dendrite mitigation effect by adding the embedded layer (varying Young's modulus E_{EL} , constant fracture resistance G_c): stress tensor component σ_{yy} at 73 s, and dendrite growth at 112 s..... | 107 |
| Figure 44 Dendrite mitigation effect with multilayer solid electrolyte design considering different thicknesses of embedded layer: (a) $T=10\ \mu\text{m}$, (b) $T=5\ \mu\text{m}$, (c) baseline $T=0\ \mu\text{m}$ | 107 |
| Figure 45 Overview of the ISC risk as a function of length ratio e , quantity and arrangement of HB, and quantity and Young's modulus of the embedded layer.... | 108 |
| Figure 46 Illustration of the established 3D model consisting of composite cathode (NCM111 secondary particle, electrolyte-carbon black domain (ECBD)), LLZO solid electrolyte domain (ED), and lithium anode..... | 112 |
| Figure 47 Intercalation-induced volumetric strain β_{c0} of NCM111 particle as a function of normalized concentration c_n . ⁷ | 116 |
| Figure 48 Comparison of the charge/discharge voltage vs specific capacity curves between experiment and simulation..... | 118 |
| Figure 49 Electrochemical-mechanical coupled behavior of the composite cathode. (a) Cell charging/discharging voltage curve. (b) The average and maximum debonding gap at the particle-electrolyte interface, D_{G_ave} and D_{G_max} . (c) The maximum von Mises stress σ_{Mises_max} and maximum volumetric strain ε_{V_max} (negative value due to volume shrinkage) of the particle during charging/discharging. (d) The von Mises stress σ_{Mises} of the 3D cell and its cross sections at X-Y, Z-Y, Z-X planes. The contour plots of various variables at different times, including $t=0\ \text{s}$ (charging beginning), 1550 s (charging midpoint), 3103 s (charging end), 4650 s (discharging midpoint), and 6111 s (discharging end): (e) Li concentration in the particle c , (f) volumetric strain ε_V , and (g) von Mises stress σ_{Mises} | 122 |
| Figure 50 (a) The total volume change of the NCM111 secondary particle during the charging/discharging at 1C. (b) The average interfacial resistance R_{int} calculated from the average debonding gap..... | 125 |
| Figure 51 Effect of charging rate on the electrochemical-mechanical behavior of composite cathode in ASSBs. (a) Cell charging/discharging voltage curves of different charging rates, i.e., C-rate=0.1C, 0.5C, 1C, and 2C. (b) Li amount M_{Li} in the secondary NMC-111 particle. (c) Maximum volumetric strain of the particle ε_{V_max} . (d) Maximum von Mises stress for the particle σ_{Mises_max} . (e) Maximum interfacial debonding gap D_{G_max} . (f) Average interfacial debonding gap D_{G_ave} . Note that the time t is normalized by the nominal charging time τ ($\tau=36000\text{s}$, 7200s, 3600s, and 1800s for 0.1C, 0.5C, 1C and 2C, respectively)..... | 129 |
| Figure 52 The total volume change of the particle during the charging/discharging at various C-rates..... | 130 |

- Figure 53 Effect of charging rate on the electrochemical-mechanical behavior of composite cathode in ASSBs with constant-voltage (CV) charging stage taken into account. (a) Cell charging/discharging voltage curves of different charging rates, i.e., C-rate=0.1C, 0.5C, 1C. (b) Li amount M_{Li} in the secondary NMC-111 particle. (c) Maximum von Mises stress for the particle σ_{Mises_max} . (d) Average interfacial debonding gap D_{G_ave} 130
- Figure 54 Effect of heterogeneity from diffusivity and expansion coefficient on the electrochemical-mechanical behavior of composite cathode in ASSBs. (a) Cell charging/discharging voltage curves at different diffusion and expansion cases. (b) Li amount M_{Li} in the NCM111 secondary particle. (c) Average interfacial debonding gap D_{G_ave} . (d) Maximum von Mises stress for the particle σ_{Mises_max} . (e) Li concentration c profiles of the Z-Y plane in the NCM111 secondary particle, at charging end and discharging end. (f) von Mises stress σ_{Mises} profiles of the Z-Y plane at charging end..... 134
- Figure 55 Effect of heterogeneity from diffusivity and expansion coefficient on the electrochemical-mechanical behavior of composite cathode in ASSBs. (a) Maximum volumetric strain of the particle ε_{V_max} . (b) Total volume change of the particle during the charging/discharging. (c) The average value of the voltage drop caused by the interfacial resistance induced by interface debonding gap. (d) The Z-Y plane contour plots of volumetric strain at charging end. 135
- Figure 56 Effect of interfacial debonding strength on the electrochemical-mechanical behavior of composite cathode in ASSBs. (a) Cell charging/discharging voltage curves at different interface debonding strength, i.e., 50 MPa, 100 MPa, 200MPa, and 500MPa. (b) Average interfacial debonding gap D_{G_ave} . (c) Maximum volumetric strain of the particle ε_{V_max} . (d) Maximum von Mises stress for the particle σ_{Mises_max} . (e) Von Mises stress σ_{Mises} profiles of the particle at charging end. (f) Von Mises stress σ_{Mises} profiles of the Z-Y plane at charging end..... 137
- Figure 57 Effect of interfacial debonding strength on the electrochemical-mechanical behavior of composite cathode in ASSBs. (a) Li amount M_{Li} in the NCM secondary particle at different interfacial strength, i.e., 50 MPa, 100 MPa, 200MPa, and 500MPa. (b) Maximum debonding gap at the electrolyte-particle interface D_{G_max} . (c) The average value of the voltage drop caused by the interfacial resistance induced by interface debonding gap. 138
- Figure 58 Effect of particle position on the electrochemical-mechanical behavior of composite cathode in ASSBs. (a) Von Mises stress σ_{Mises} profiles of the cell at charging end. (b) Maximum interfacial debonding gap D_{G_max} . (c) Maximum volumetric strain of the particle ε_{V_max} . (d) Maximum von Mises stress for the particle σ_{Mises_max} 140
- Figure 59 Li amount in the NCM secondary particles (P1 and P2), with zoomed-in views at charging beginning and discharging end. 141
- Figure 60 Model validation: comparison of charge/discharge curves between experiment and simulation..... 155

Figure 61 (a) Comparison of the dendrite growth between two cases with different exchange current density, electrolyte ionic conductivity, and applied current density. The results show that, these cases have similar dendrite growth pattern.

(b) The crack length and width vs. time..... 159

NOMENCLATURE

| Nomenclature | | | |
|----------------------|--|------------------------|---------------------------------------|
| c_s | Site density of Li metal | Ω_{Li} | Partial molar volume of Li metal |
| n | Number of electrons involved in electrode reaction for Li | E_{Li} | Young's modulus of Li metal |
| σ_{Li} | Conductivity in Li | ν_{Li} | Poisson's ratio of Li metal |
| L_{σ}^{ξ} | Interface mobility of Li | ρ_{Li} | Density of Li metal |
| L_{η}^{ξ} | Reaction constant of Li | c_0 | electrolyte bulk Li-ion concentration |
| W_{Li} | Barrier height of Li | σ_{SE} | Conductivity in solid electrolyte |
| κ_{ξ} | Gradient coefficient of Li | L_{σ}^{ϕ} | Interface mobility of LLZO |
| D_{Li} | Li-ion diffusivity in Li | W_{ϕ} | Barrier height of LLZO |
| κ_{ϕ} | Gradient coefficient of solid electrolyte | δ | Anisotropy strength |
| D_{SE} | Li-ion diffusivity in solid electrolyte | λ | Crystallographic symmetry mode |
| Ω_{SE} | Partial molar volume of solid electrolyte | α | Symmetric factor |
| E_{SE} | Young's modulus of LLZO grain | F | Faraday's constant |
| ν_{SE} | Poisson's ratio of grain | R | Gas constant |
| ρ_{SE} | Density of solid electrolyte | T | Temperature |
| E_{GB} | Young's modulus of grain boundary | W_{cr} | Barrier height for crack |
| L_{σ}^{cr} | Interface mobility for crack | κ_{cr} | Gradient coefficient for crack |
| W_c | Fracture threshold energy density of the solid-state electrolyte | σ_{LLZO} | Conductivity of LLZO |
| F_t | Total free energy | f_{local} | Local energy density |

| | | | |
|--------------------|---|------------------|--|
| f_{grad} | Gradient energy density | f_{elec} | Electrostatic energy density |
| f_{mech} | Mechanical strain energy density | ξ | Phase-field order parameter for Li dendrite |
| ϕ_g | Phase-field order parameter for g-th grain | ϕ_{cr} | Phase-field order parameter for crack |
| $W_{elastic}$ | Elastic strain energy density | C_{ijkl} | Stiffness of the materials |
| F_L | Deformation gradient | S | Piola-Kirchhoff stress tensor |
| α_a | Anodic charge transfer coefficients | α_c | Cathodic charge transfer coefficients |
| σ_s | Conductivity of LCO cathode | ρ_{LLZO} | Density of LLZO |
| D_{s-c} | Li-ion intercalation diffusivity of cathode | E_{LLZO} | Young's modulus of LLZO |
| ν | Poisson's ratio of LLZO | K_{LLZO} | Fracture toughness of LLZO |
| ε_{pf} | Parameter controlling interface thickness | χ | Mobility tuning parameter |
| S_{SE} | Cross-section area of the electrolyte | σ_{Y_Li} | Yield stress of Li metal |
| R_{short} | Short-circuit resistance | $j_{0-, ref}$ | Reference exchange current density |
| j_{0-} | Exchange current density at the anode/electrolyte interface | $\phi_{s, ext}$ | External electric potential for the Li anode |
| j_{0+} | Exchange current density at the cathode/electrolyte interface | I | Identity matrix |
| E_σ | Surface energy | G | Fracture energy |
| ε_l | Electrolyte volume fraction in ECBD | σ_c | Interfacial strength |
| κ_l | Solid electrolyte conductivity | G_c | Fracture toughness |
| κ_s^{eff} | Electrical conductivity in ECBD | E_{SE} | Young's modulus of solid electrolyte |
| κ_l^{eff} | Effective electrolyte conductivity | i_{app} | Applied current density |
| D_s | Li diffusivity in particle | E_{NCM} | Young's modulus of NCM particle |
| a | Mode mixity exponent | $D_{G\ ave}$ | Average debonding gap |

| | | | |
|-------------------------------|---|------------------------------|---|
| $R_{\text{int}}^{\text{ref}}$ | Reference interfacial resistance | D_{G_max} | Maximum debonding gap |
| R_{int} | Interfacial resistance | λ_{ref} | Reference gap |
| ε_V | Volumetric strain | ε_{V_max} | Maximum volumetric strain |
| σ_{Mises} | von Mises stress | $\sigma_{\text{Mises_max}}$ | Maximum von Mises stress |
| M_{Li} | Li amount in the secondary NCM111 particle | ΔM_{Li} | Residual Li amount in the secondary NCM111 particle |
| τ | Nominal charging time | $I_{\text{BV}+}$ | Local charge transfer current density |
| I_{0+} | Exchange current density | η_+ | Overpotential |
| ϕ_s | Electrical potential in the solid phase | ϕ_l | Electrical potential in electrolyte phase |
| E_{eq} | Equilibrium potential | σ_h | Hydrostatic stress |
| $\Delta\eta_{\text{int}}$ | Overpotential drop | i_s | Current density in the remaining electrically conductive domain |
| i_l | Current density in the electrolyte domain | J_s | Li flux |
| c | Bulk Li concentration in the particle | ε | Total strain |
| c_n | Normalized Li concentration | ε_{Li} | Lithiation/delithiation-induced strain |
| c_{max} | Maximum Li concentration at the fully lithiated state | ε_{el} | Elastic strain |
| \mathbf{n}_c | Unit outward normal vector of the cathode surface | f_V | Body force per unit volume |
| \mathbf{n}_l | Unit normal vector from the electrolyte to the particle surface | β_c | Lithiation expansion coefficient |
| \mathbf{u} | Displacement field | θ_β | Coefficient matrix |
| u_m | Mixed-mode relative displacement | G_{Ic} | Critical tensile energy release rates |
| u_I | Displacement in normal direction | G_{IIc} | Critical shear energy release rates |
| u_{II} | Displacement in tangential direction | | |

CHAPTER 1 INTRODUCTION

1.1 Background

With the merits of relatively high energy density and good cyclability performance, lithium-ion batteries (LIBs) are widely used in portable electronic devices, smartphones, and electric vehicles (EVs) ^{1,2}. Under the rapid development of the EVs' market and the huge demand for electronic products, new requirements have been put forward for current LIBs, including improvement of the energy density to increase the EVs' mileage and a guarantee of battery safety to avoid the mechanical/electrical/thermal abuse-caused fire or explosive accidents ³⁻⁶. In this context, all-solid-state batteries (ASSBs) are proposed as promising next-generation batteries to address the thorny energy density and safety issues of current LIBs ⁷⁻⁹. On the one hand, the use of Li metal with low mass density and high specific capacity (3860 mAh/g, ten times higher than that of conventional graphite anode 372 mAh/g) as the anode can greatly improve the battery energy density ¹⁰⁻¹³; on the other hand, the solid electrolytes (SEs) have the nature of non-flammability and a wide stable electrochemical window which can solve the safety issues from the root ¹⁴⁻¹⁸. Nevertheless, different from the liquid electrolyte-based LIBs, all components of ASSBs are solid-state, including the lithium anode, SE, and the composite cathode, and the interfacial instability between adjacent components (i.e., Li-SE, dendrite-SE, cathode particle-SE in Fig. 1 ⁹) causes the poor cyclability and performance degradation of ASSBs ¹⁹⁻²², which needs urgent investigation from both experiment and modeling. Due to the solid nature of all

components, state-of-the-art experimental characterization is insufficient to provide direct *in-situ* observation of buried interfacial evolution. To complement this, numerical simulation is a powerful tool that enables a more in-depth understanding of the underlying mechanism²³⁻²⁵. Moreover, further understanding of the interfacial instability mechanism directs the improvement and safety design of ASSBs.

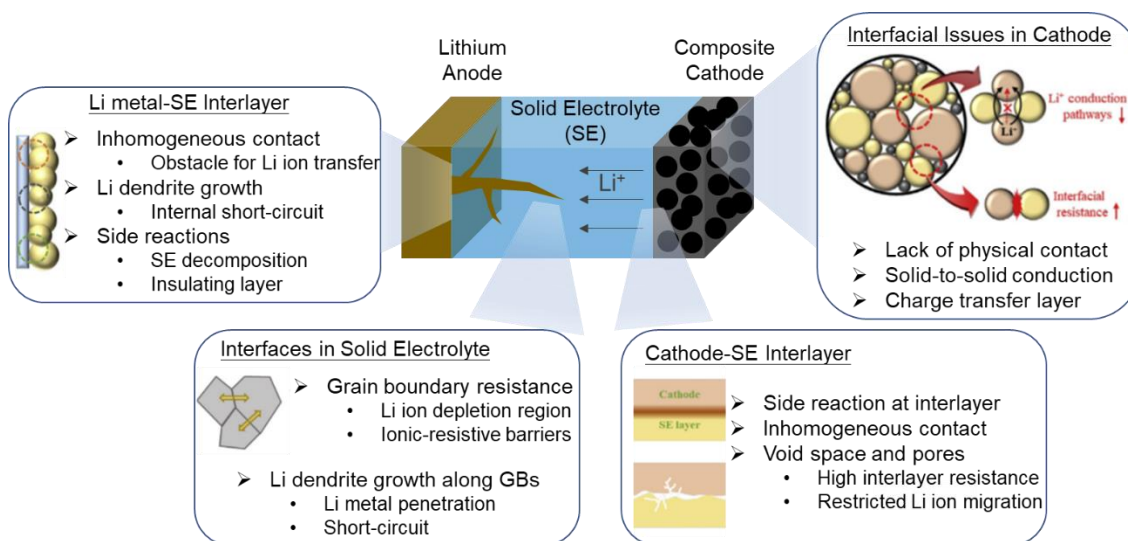


Figure 1 Summary of the interfacial issues in all-solid-state batteries⁹.

1.2 Literature review

1.2.1 Solid electrolyte

Solid electrolytes are considered to resolve the safety issues of ASSBs due to the intrinsic nature of non-flammability and high-temperature stability. There are mainly two types of SEs, i.e., inorganic ceramic electrolytes (ICEs), and solid polymer electrolytes (SPEs)^{12, 26-28}. ICEs are ceramic materials that can transport Li-ions during charging and discharging, including oxides, sulfides, and nitrides, which usually have high Young's modulus and better ionic conductivity. SPEs are mixtures of polymers and Li salts with

good flexibility but low Young's modulus and poor ionic conductivity. In addition to the ICEs and SPEs, another candidate is the mixture of the two (i.e., composite electrolytes) to combine the advantages of ICEs and SPEs²⁸⁻³¹. With research effort in the past decades, the ionic conductivity of ICE-type solid electrolytes has now reached or even surpassed the level compared to their liquid-based counterpart¹⁰. Thus, it is no longer the limiting factor of SEs. As such, ICEs are considered promising solid electrolytes.

Among the ICEs, $\text{L}_7\text{La}_3\text{Zr}_2\text{O}_{12}$ (LLZO) electrolyte with a high Young's modulus, a practical ionic conductivity, and a wide electrochemical stability window is considered one of the most promising applicable SEs. The higher relative density of LLZO results in a lower fracture toughness and larger ionic conductivity³². This finding allows modulating the SE property by controlling fabrication pressure to modify the relative density or by combining SEs with different properties. Since a solid electrolyte is a single-ion conductor, there is no Li-ion concentration gradient within the electrolyte, which is the main reason for the dendrite growth in the liquid LIBs^{10,33}. In addition, previous theoretical work has shown that a solid electrolyte with a shear modulus two times higher than that of the polymer-based separator enables dendrite suppression³⁴. With the aid of advanced characterization techniques (e.g., scanning electron microscope (SEM), transmission electron microscopy (TEM) and synchrotron X-ray computed tomography (CT)), it is found that the dendrite still grows within the SE with an ultra-high modulus (e.g., ~150 GPa for LLZO). This evidence clearly demonstrates that there should be other governing factors

for dendrite growth besides the modulus. Further investigation and improvement for SEs are needed to pave the path of commercialized ASSBs^{26-29, 35-37}.

1.2.2 Dendrite initiation and growth

During the Li plating process, Li ions from the solid electrolytes are reduced at the interface between the lithium anode and electrolyte to deposit as Li atoms at the anode side. The deposited lithium is uniform without any disturbance, and the Li anode surface is smooth. Due to some specific inhomogeneities, the dendritic shape of lithium may occur, i.e., the dendrite nucleation/initiation (Fig. 2(a)). Efforts from both theoretical analysis and experimental characterization have been endeavored to explore the mechanism³⁸⁻⁴⁵.

There are two possible mechanisms to explain the dendrite initiation position in ASSBs: 1) initiation at the Li-SE interface⁴⁶⁻⁵¹ (Fig. 2(b)); 2) initiation inside the SE^{44, 48, 52, 53} (Fig. 2(c)). Firstly, there are inevitable nonuniform contact and interfacial defects at the Li-SE solid-to-solid interface, such as grain boundary, voids, cracks, impurities and pores^{10, 14, 49, 54-57}. Due to the existence of these defects, the local current density will vary with the interface geometry⁵⁸, which will eventually result in localized current density-induced inhomogeneous Li plating. The protruding plated lithium will enhance the surrounding electric potential and further accelerates the dendrite nucleation¹⁰. Most crystalline ICEs exist in polycrystalline form composed of grains and grain boundaries⁴⁹. The low ionic conductivity of the grain boundary is supposed to be the reason for preferential dendrite initiation and growth along grain boundary⁵⁹. Secondly, inside the

SEs, there are also some defects, such as voids and pores ¹⁰, and grain boundaries, especially for polycrystalline SEs. According to DFT calculation, the trapped excess surface electrons inside the grain boundary of SEs can directly reduce Li-ions to lithium dendrite ⁵³. The dendrite formation inside SEs is also reported to be caused by reduced local electric bandgap ⁵². According to the dendrite initiation position, there are also two routes for dendrite to penetrate the cell and trigger the short circuit: 1) dendrite initiates at the Li-SE interfacial defect, then grows and penetrates the SEs, finally reaches the other electrode to trigger short circuit; and 2) dendrite formation occurs at different positions inside the SEs, then the isolated dendrites are interconnected to serve as the electron transport path to short circuit the battery.

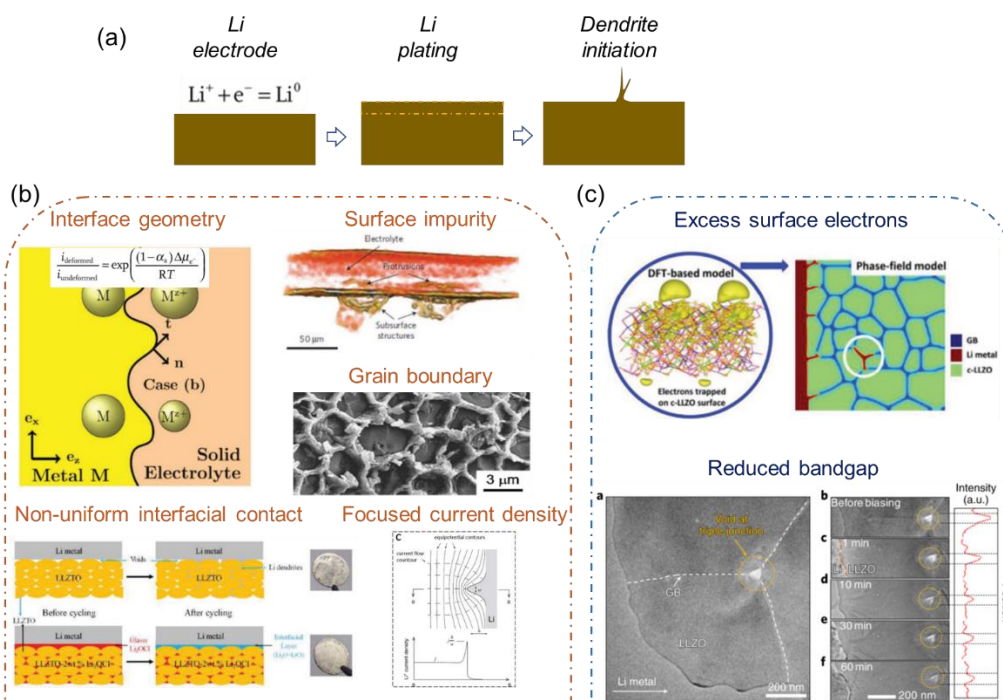


Figure 2 Dendrite initiation behavior in ASSBs: (a) schematic illustration of dendrite initiation; (b) dendrite initiation at the Li-electrolyte interface ⁵⁴⁻⁵⁸; (c) dendrite formation inside electrolytes ^{52,53}.

Plenty of research discovered that, for one specific electrolyte, dendrite penetration-caused short circuit always occurs above a certain current density (i.e., the critical current density (CCD)). Most reported CCD is lower than 1 mA/cm^2 ^{12, 60}, while the practical current density for batteries is above 2 mA/cm^2 ¹⁴. To fully understand the dendrite growth behavior within ASSBs is extremely urgent to develop a resilient solid electrolyte system, and finally to address the short-circuit problem. There are mainly three reported dendrite growth tracks in SEs: 1) along grain boundary⁵⁴, 2) along pore network^{61, 62}, and 3) coupled behavior with crack propagation⁵⁰. As mentioned above, the grain boundary provides the position for dendrite initiation, and dendrite also preferably grows along the grain boundary in the polycrystalline electrolyte (Fig. 3(a)). Possible reasons are the high ionic resistivity, different composition, and low shear modulus compared to the grains, among which the large resistivity mainly affects the electrochemical overpotential/current density. Small modulus demonstrates the soft nature of grain boundary from the perspective of mechanics^{58, 63, 64}. The sintering temperature during fabrication was found to determine the porosity and ionic conductivity of LLZO electrolyte⁶¹. Though high temperature can reduce the porosity and improve the conductivity, the size of grains and pores also increases. Even worse, the interconnected micropore network inside the electrolyte observed by synchrotron X-ray tomography becomes the path for dendrite growth, as shown in Fig. 3(b)⁶¹. In addition to the preferable dendrite growth path of grain boundary and micropores, the dendrite growth itself can generate mechanical stress to drive the crack propagation within

SEs⁶⁵. By applying the *in-situ* X-ray CT^{50,66,67}, the dendrite growth-induced crack was observed with the cycling of ASSBs, as shown in Fig. 3(c). Since the electrolyte is brittle with relatively small fracture toughness, the dendrite-caused stress can drive the crack to propagate. Moreover, the newly formed crack provides further preferable space for dendrite to grow. The battery's internal resistance also increases due to crack formation, and electrochemical performance degrades.

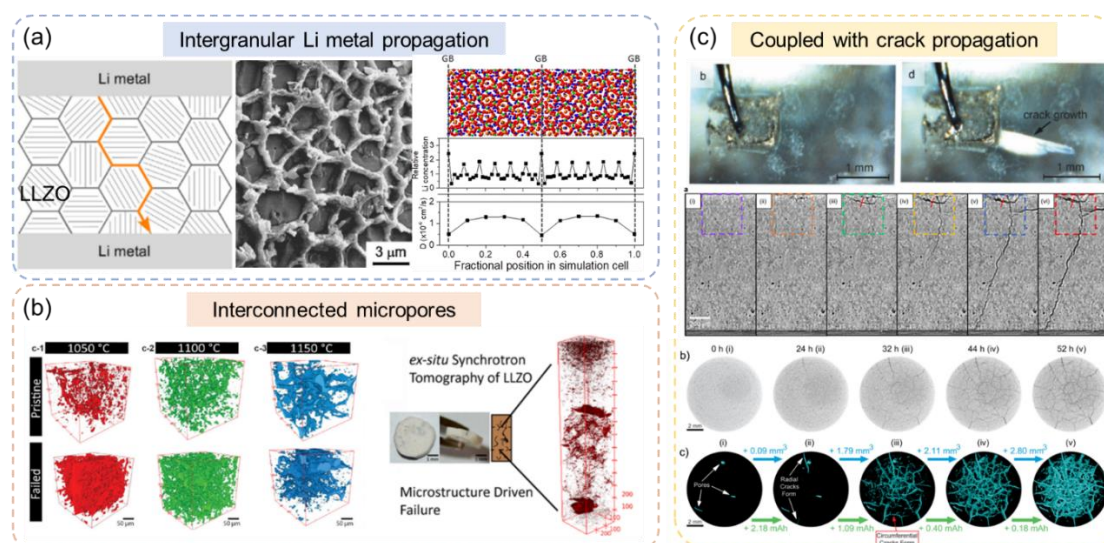


Figure 3 Dendrite growth behavior in ASSBs: (a) intergranular dendrite penetration^{54,63}; (b) dendrite growth along interconnected micropores inside electrolyte⁶¹; (c) dendrite growth coupled with crack propagation^{50,65,66}.

The above state-of-the-art experimental results directly demonstrate the phenomena of Li dendrite initiation and growth within SEs, and thus provide an initial understanding of the coupling behaviors. However, a more theoretical understanding of the mechanisms requires rigorous physics-based modeling work^{13,23}. Dendrite initiation and growth rate in ceramic SEs were theoretically explored by bridging the dendrite growth with the electrochemical potential^{68,69}. The electrochemical-mechanical model studied the effect

of bending of SE on cell potential and lithiation capacity⁷⁰. The concurrent Li dendrite growth and SEI growth modeled by the moving mesh method showed the effect of current density and SEI properties on dendrite growth in lithium metal batteries⁷¹. The two-step computational model studied the fracture and mechanical stress-induced current in grain boundaries⁷². The coupled phase-field model showed that excess surface electrons significantly affect the initiation positions of Li dendrites within the grain boundaries of polycrystalline LLZO SE^{48, 53}. By direct numerical simulation of restructured SE microstructure, the effective SE properties were obtained, and the effects of operating conditions (temperature and external pressure), were parametrically studied⁴⁷. The stack pressure and SE electrochemical properties could influence the interfacial deposition and mechanical stability⁷³. By adopting large-scale molecular dynamics simulations, the Li metal plating and stripping mechanisms are investigated from an atomistic perspective, and the defect effect is also included^{46, 74}. The interaction mechanism of crack propagation and dendrite growth under stacking pressures and the interfacial defect was further explored by the one-way coupled electrochemical-mechanical phase-field model⁴⁹. These numerical models provide an in-depth understanding of the dendritic and interfacial issues, mainly at the grain level. However, currently available modeling work is not built in a fully electrochemical-mechanical coupled fashion.

1.2.3 Mechanical property of lithium

In the past decades, most of the focus on lithium has been on its electrochemical

property, while dendrite initiation and growth in ASSBs is highly mechanics-electrochemistry coupled behavior where the lithium mechanical property may greatly affect. The mechanical property of lithium is significantly determined by its length scale, reported by recent research ⁷⁵⁻⁸⁰. Herein three length scales are distinguished, i.e. bulk lithium ($>10\ \mu\text{m}$), microscale lithium ($1-10\ \mu\text{m}$), and nanoscale lithium ($<1\ \mu\text{m}$). Firstly, for bulk lithium, Young's modulus E_{Li} and yield strength are about 7.8 GPa and 0.8 MPa, respectively ⁷⁷. By adopting tensile testing in inert gas environments with the digital image correlation, the effects of strain rate and temperature on the mechanical response of lithium metal were thoroughly investigated. The strain hardening phenomenon only occurred at a high strain rate and low temperature ⁶⁷. The room-temperature tensile and compression experiment results demonstrated the completely different mechanical behavior of lithium ⁸¹, which may greatly influence the lithium mechanical response in ASSBs where the creep effect is more important during long-time cycling. Secondly, the microscale lithium pillars of diameters from 1 to 10 μm under nanomechanical experiment showed different stiffness and yield strength ($>10\ \text{MPa}$), and stronger mechanical response with larger modulus and higher strength was observed for smaller pillars ⁷⁹. The crystallographic orientation also influences mechanical property of lithium, and $E_{\text{Li}} = 21\ \text{GPa}$ along $\langle 111 \rangle$ direction ⁷⁹. Thirdly, the nanoscale growing/grown lithium whiskers showed higher yield strength (15 to 250 MPa), investigated by the atomic force microscopy (AFM)-environment TEM equipment ⁸⁰. The mechanical property of lithium is greatly size-dependent, which should

be further coupled in the multiphysics model to understand its effect on dendrite initiation and growth behavior.

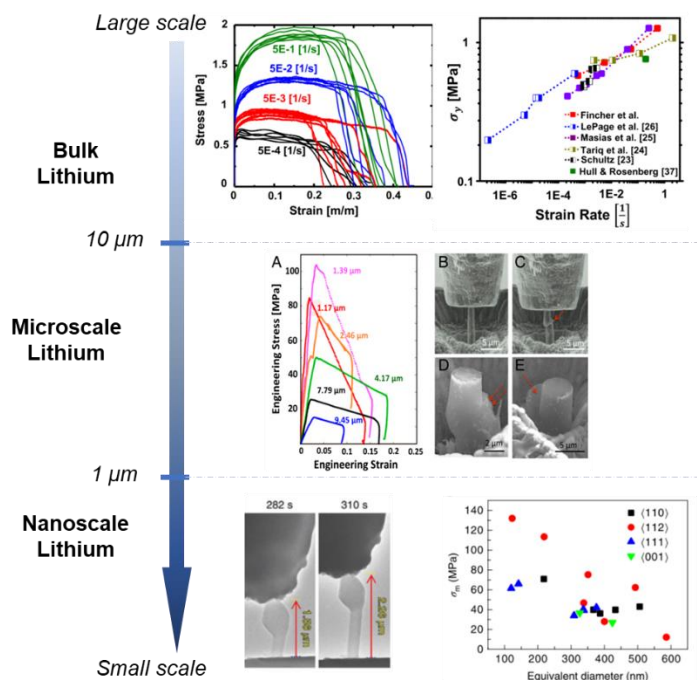


Figure 4 Mechanical strength of lithium at different length scale ⁷⁷.

1.2.4 Composite electrode particle expansion

The composite electrode of ASSBs is composed of active particles (APs) and solid electrolytes where APs are embedded into SEs ⁸². During the battery charging and discharging, the insertion/extraction of Li-ions in APs causes particle volume expansion/shrinkage. As mentioned above, Young's modulus of SEs is usually above 10 GPa, or even 150 GPa for LLZO electrolyte, which serves as a strong constraint of particle volume variation. On the one hand, under the constraint of SE, particle expansion will cause large stress for both particle and SE, possibly inducing the particle pulverization and SE crack. On the other hand, the particle shrinkage may cause the debonding of particles

and SE, increasing the interfacial resistance. As such, particle expansion and shrinkage have the risk of increasing internal resistance, resulting in performance degradation⁸³.

Both experimental characterization and numerical simulation have been conducted to investigate the particle volume variation-induced problems in the composite electrode. By assembling a composite cathode consisting of NCM-811 and β -Li₃PS₄ into ASSBs and performing the charging-discharging experiment, the interfacial debonding and interphase layer formation between APs and SEs were found to cause the interfacial resistance increase, finally leading to the irreversible capacity loss⁸³ (Fig. 5(a)). After cycling, the contact loss between NCM APs and SEs was observed. The interfacial resistance greatly increased, causing the battery discharge capacity to fade²². The mechanical damage initiation and evolution of the composite electrode in ASSBs induced by intercalation expansion was studied by a coupled electro-chemo-mechanical model using the cohesive zone method. Results show that fracture was prevented when the active particle's expansion was below 7.5%²⁵ (Fig. 5(b)). The mesoscale simulation of interconnected particles in SEs demonstrated the inside stress distribution, revealing that smaller particles could improve rate performance and avoid interfacial failure. However, the effect of interfacial failure on battery degradation is not reflected in those numerical models, and further investigation of the coupling behavior of particle-SE interfacial instability and battery degradation should be considered.

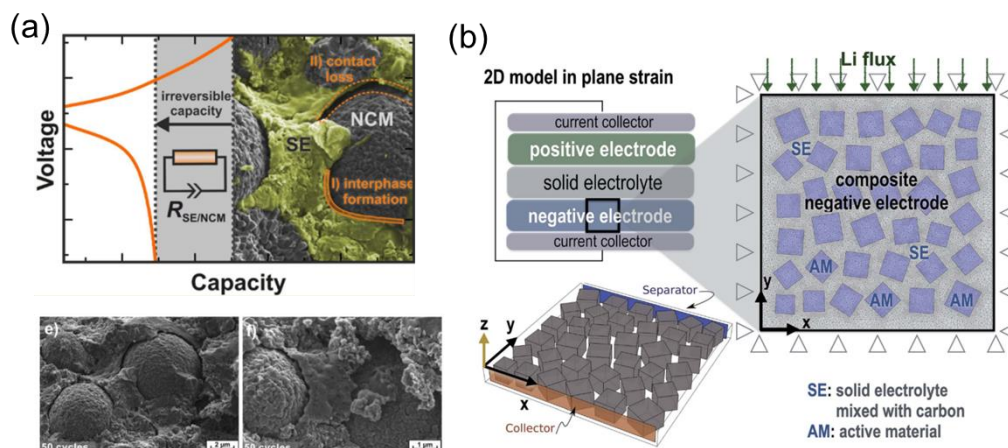


Figure 5 Particle volume variation issues in composite electrode: (a) experimental characterization⁸³; (b) numerical simulation²⁵.

1.2.5 Optimization methodology

Plenty of pioneering efforts from the perspective of material science have addressed the dendritic and interfacial issues, mainly concerning three aspects (Fig. 6(a-c)), i.e., 1) advanced structure design of the electrode or current collector to accommodate the newly grown Li dendrite and release the stress^{45, 84-86}; 2) interfacial modification to improve the solid-solid contact property between the electrode and SE^{31, 87-90}; and 3) improvement of SE electrochemical/mechanical properties to suppress dendrite growth and improve battery performance^{30, 91-96}. From the mechanical perspective, stacking pressure is found to influence dendrite growth significantly, crack propagation, and interface stability^{49, 73, 97-100} (Fig. 6(d)) such that the concept of applying residual compressive stress in SEs is introduced to prevent dendrite penetration¹⁰¹. Although the performance of ASSBs has been dramatically enhanced, inevitable dendrite growth still occurs during charging/discharging⁴¹, and the critical current density and cyclability performance need

to be improved as well ^{31, 60}. Novel designs to mitigate dendrite growth and improve interfacial stability are urgently needed.

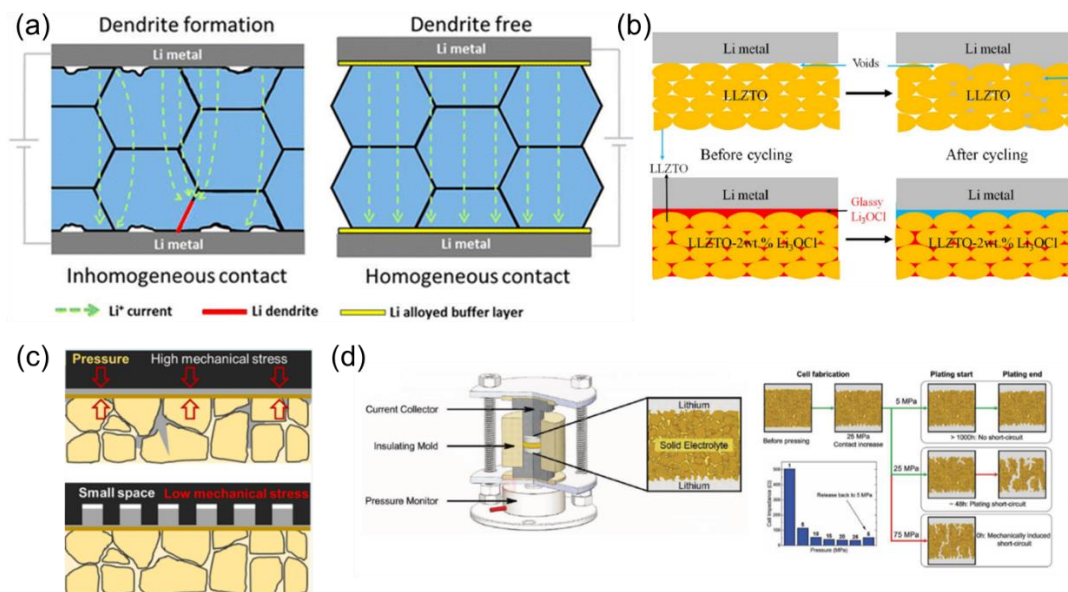


Figure 6 Optimization methodology for interfacial instability: (a) interphase material ⁸⁷; (b) electrolyte improvement ⁵⁵; (c) electrode structure design ⁸⁶; (d) mechanical stack pressure ⁹⁷.

1.3 Challenges and motivation

The dendrite growth and interfacial instability issues inside ASSBs have been extensively investigated by various *in-situ* and *ex-situ* experimental characterizations, and there are also reported models only considering either Li dendrite growth or crack propagation at a time, not built in a fully electrochemical-mechanical coupled fashion. However, the absence of understanding of the electrochemical-mechanical coupling mechanism for the fatal dendritic issue and interfacial instability problem poses challenges to accurately describing the performance degradation of ASSBs. Due to the highly multiphysics-coupled nature, the Li dendrite growth and crack propagation are strongly

coupled, and the mechanical interfacial debonding is originally caused by the electrochemical reaction. Therefore, I developed the fully coupled electrochemical-mechanical modeling framework at both electrolyte scale and cell scale to investigate the dendrite growth behavior and its influence on cell performance. The mechanical instability issue inside the composite is caused by the particle volume variation. Furthermore, the dendrite mitigation strategy is also proposed to reduce lithium penetration-induced short circuit risk.

1.4 Chapter arrangement

Chapter 2 presents the electrochemical-mechanical phase-field model at the electrolyte scale, describing the coupled dendrite growth and crack propagation behaviors. Chapter 3 develops the cell-scale fully coupled electrochemical-mechanical modeling framework to comprehensively study the governing effects of various factors on dendrite penetration-induced short circuits. Chapter 4 proposes the dendrite mitigation strategy by inserting heterogeneous blocks into the electrolyte and evaluates the dendrite-caused short circuit risk under different scenarios. Chapter 5 focuses on the interfacial instability and mechanical damage occurring inside the composite cathode of ASSBs, based on the established three-dimensional fully coupled multiphysics model. Chapter 6 summarizes the conclusions of this dissertation.

CHAPTER 2 COUPLED DENDRITE GROWTH AND CRACK PROPAGATION AT ELECTROLYTE SCALE

In this chapter, the electrochemical-mechanical phase-field model at electrolyte scale is developed to investigate the underlying mechanism of the coupled behaviors of the Li dendrite growth and crack propagation. Due to the high conductivity, high elastic modulus, and stability against Li metal, the promising polycrystalline $\text{L}_7\text{La}_3\text{Zr}_2\text{O}_{12}$ (LLZO) is targeted as the solid electrolyte in the study. The effects of pre-defect patterns, including defect length, angle, and shape, as well as stacking pressure on the crack propagation and dendrite growth behaviors, are comprehensively investigated to give out insightful understanding of the dendritic issue in ASSBs.

2.1 Methodology

We randomly generate with multi grain boundaries in the area of $500\ \mu\text{m} \times 500\ \mu\text{m}$ including lithium anode and polycrystalline solid-state electrolyte as our simulation sample to demonstrate the generality of the coupled model (Fig. 7)⁴⁹. There should be inevitable defects, such as voids, cracks, and impurities at the Li/SE interface, which lead to the initiation and growth of dendrite. As such, we fabricate a defect at the anode/SE interface in the model to investigate the defect effect on the crack propagation and dendrite growth behaviors. The angle θ between the horizontal line and the defect axis is used to describe the position (Fig. 7).

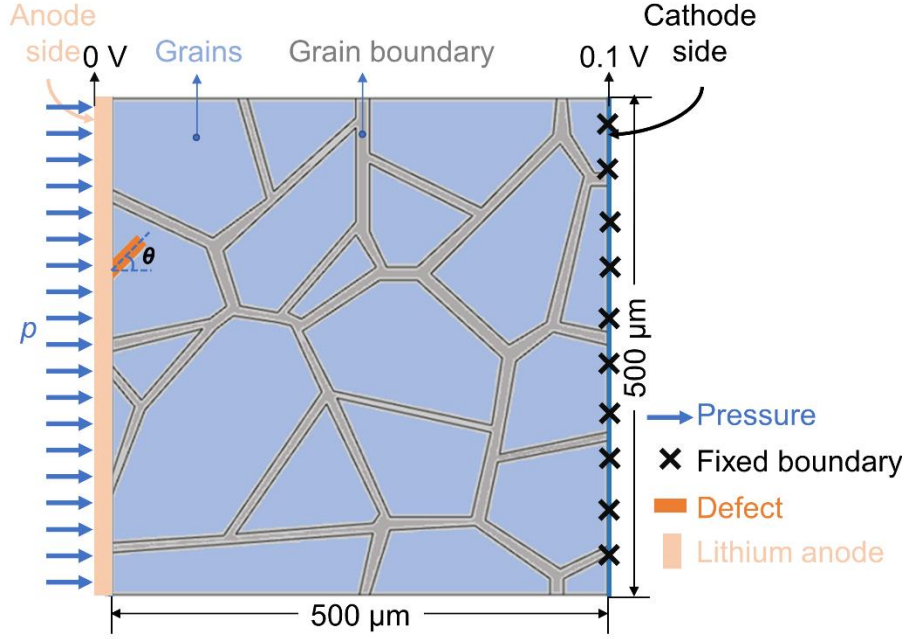


Figure 7 Schematics of the established model. The anode and cathode are on the left and right sides, respectively. A preset defect is embedded within one grain near the Li/SE interface. Uniformly distributed pressure is applied on the anode side to mimic the stacking pressure, while a fixed boundary is set on the cathode side.

The total free energy F of the system in this study is expressed as follows^{53, 102, 103}:

$$F = \int \left[f_{local}(\xi, \phi_g, \phi_{cr}, \tilde{c}_i) + f_{grad}(\nabla \xi, \nabla \phi_g, \nabla \phi_{cr}) + f_{elec}(c_i, \varphi) + f_{mech}(\xi, \phi_g, \phi_{cr}) \right] dV \quad (1)$$

where $f_{local}(\xi, \phi_g, \phi_{cr}, \tilde{c}_i)$ is local energy density, $f_{grad}(\nabla \xi, \nabla \phi_g, \nabla \phi_{cr})$ is gradient energy density, $f_{elec}(c_i, \varphi)$ is electrostatic energy density, $f_{mech}(\xi, \phi_g, \phi_{cr})$ is mechanical strain energy density, ξ is the phase-field order parameter for Li dendrite where $\xi = 0$ and $\xi = 1$ represent no dendrite and pure dendrite regions respectively, ϕ_g is the phase-field order parameter for g -th grain ($g=1, 2, \dots, N$), ϕ_{cr} is the phase-field order parameter for a crack where $\phi_{cr} = 0$ is for the fully broken region and $\phi_{cr} = 1$ is for the intact region, \tilde{c}_i is the set of normalized Li-ion concentration, represented by $\tilde{c}_i = \{\tilde{c} = c / c_s, \tilde{c}_+ = c_+ / c_0, \tilde{c}_e = c_e / c_0\}$ (c_s is the site density of Li metal, c_0 is the bulk concentration in the solid electrolyte) (note that here Li-ion is the only cation that transfers

within the solid electrolyte), ϕ is the electrical potential. As for local energy density, it is represented by the following equation^{53, 102}:

$$f_{local}(\xi, \phi_g, \phi_{cr}, \tilde{c}_i) = f_0(\xi, \phi_g) + c_0 RT \sum_i \tilde{c}_i \ln \tilde{c}_i + \sum_i \tilde{c}_i \mu_i^\ominus + f_{\phi_{cr}} \quad (2)$$

where $f_0 = A\xi^2(1-\xi) + \sum_{g=1}^N B\phi_g^2(1-\phi_g)^2 + \sum_{p=1}^N \sum_{q \neq p}^N \frac{C}{2} \phi_p^2 \phi_q^2 + \sum_{g=1}^N \frac{D}{2} \xi^2 \phi_g^2$, the values of the coefficients are $A = B = 1$, $C = D = 3$, and $f_{\phi_{cr}} = W_{cr} f(\phi_{cr}) = W_{cr} \phi_{cr}^2 (1 - \phi_{cr})^2$ is the free energy density of crack order parameter. The gradient energy is expressed as follows:

$$f_{grad} = \frac{1}{2} \kappa_\xi (\nabla \xi)^2 + \sum_{g=1}^N \frac{1}{2} \kappa_\phi (\nabla \phi_g)^2 - \kappa_{GB} \sum_{p=1}^N \sum_{q \neq p}^N \frac{C}{2} \nabla \phi_p \nabla \phi_q + \frac{1}{2} \kappa_{cr} (\nabla \phi_{cr})^2 \quad (3)$$

where $\kappa_\xi = \kappa_0(1 + \delta \cos \lambda \alpha)$, κ_ϕ , κ_{GB} and κ_{cr} are the gradient coefficients for dendrite, grain, grain boundary and crack, respectively. The anisotropy is considered for the dendrite gradient coefficient by introducing the anisotropy strength δ , crystallographic symmetry mode λ , and the angle α between normal vectors.

In this study, we only consider the crack propagation behavior within one grain where the defect is located to obtain more efficient computational results while maintaining the universality of the study. The mechanical energy density is calculated differently for crack propagation region (i.e., the only grain with pre-defect) and no crack region, since the coupling of the elastic field and crack order parameter should be considered, shown in the following equation¹⁰²:

$$f_{mech}(\xi, \phi_g, \phi_{cr}) = \begin{cases} W_{elastic} & \text{for non-crack region} \\ g(\phi_{cr})(W_{elastic} - W_c) + W_c & \text{for crack region} \end{cases} \quad (4)$$

where $W_{elastic} = \frac{1}{2} \sigma_{ij} \varepsilon_{ij} = \frac{1}{2} C_{ijkl}(\xi, \phi_g, \phi_{cr}) \varepsilon_{ij} \varepsilon_{kl}$ is the elastic strain energy density,

$C_{ijkl}(\xi, \phi_g, \phi_{cr})$ is the stiffness of materials, ε_{ij} and ε_{kl} are the strains, W_c is the

threshold value for strain energy density, the function $g(\phi_{cr}) = \phi_{cr}^3(4 - 3\phi_{cr})$ is related to crack propagation. The crack tends to propagate when W_{elastic} is greater than W_c ; otherwise, the intact status is favored. Here the crack region represents the only grain with defect, and the non-crack region is the rest area.

The material properties in the diffusion interphase region, including electrochemical and mechanical properties, such as conductivity, diffusivity, and stiffness, vary with the evolution of the phases. Thus the interphase properties are a function of the order parameter. As for $C_{ijkl}(\xi, \phi_g, \phi_{cr})$, it varies with dendrite evolution and follows the expression below for different regions:

$$C_{ijkl}(\xi, \phi_g, \phi_{cr}) = \begin{cases} h(\xi)C_{ijkl}^{\text{Li}} + \sum_{n=1}^N h(\phi_n)C_{ijkl}^{\text{Grain}} & \text{for Li/grain} \\ h(\xi)C_{ijkl}^{\text{Li}} + \sum_{n=1}^N h(\phi_n)C_{ijkl}^{\text{Grain}} + (1-h(\xi))C_{ijkl}^{\text{GB}} & \text{for grain boundary} \\ h(\phi_{cr})C_{ijkl}^{\text{Grain}} + (1-h(\phi_{cr}))C_{ijkl}^{\text{Li}} & \text{for crack region} \end{cases} \quad (5)$$

where C_{ijkl}^{Li} , C_{ijkl}^{Grain} and C_{ijkl}^{GB} are the stiffnesses of lithium dendrite, grain, and grain boundary, respectively. The crack region means the only grain with the preset defect. Here all the materials are assumed to be isotropic; thus, Young's modulus is used for the stiffness value. The function $h(\xi) = \xi^3(10 - 15\xi + 6\xi^2)$ is used for the interpolation of the stiffness of the interphase between two phases.

Then the governing equation for the phase evolution is derived from the total energy through the variational method, which follows the form of Cahn-Hilliard equation or Ginzburg-Landau equation based on whether the order parameter is locally conserved or non-conserved¹⁰⁴. Here in this model, $N+2$ non-conserved order parameters are considered,

including ξ for dendrite, ϕ_g for N grains ($g = 1, 2, \dots, N$), and ϕ_{cr} for crack. The following equation considering both mechanical and electrochemical driving forces, is used to describe the dynamic evolution of lithium dendrite⁵³:

$$\begin{aligned} \frac{\partial \xi}{\partial t} = & -L_{\sigma}^{\xi} \left(\frac{\partial f_0}{\partial \xi} + \frac{\partial f_{\text{mech}}}{\partial \xi} - \kappa_{\xi} \nabla^2 \xi \right) \\ & - L_{\eta}^{\xi} h'(\xi) \left\{ \exp \left[\frac{(1-\alpha)nF\eta}{RT} \right] - \tilde{c}_+ \tilde{c}_e \exp \left[\frac{(-\alpha)nF\eta}{RT} \right] \right\} \end{aligned} \quad (6)$$

where the last term is in the form of Butler-Volmer equation accounting for electrochemical reactions, L_{σ}^{ξ} is interface mobility coefficient of lithium, L_{η}^{ξ} is the reaction of constant, α is a symmetric factor, n is the number of electrons involved in electrode reaction for Li, F is Faraday constant, R is gas constant, T is temperature, $\eta = -0.1 - \Omega_{Li}\sigma_h / F$ is activation overpotential where -0.1V is commonly applied overpotential referring to previous literature^{53,105} and $-\Omega_{Li}\sigma_h / F$ considers the effect of back stress from LLZO on overpotential. As for the order parameter in the N grains, the driving force is from the mechanical part, and the governing equation is derived from the variation of energy:

$$\frac{\partial \phi_g}{\partial t} = -L_{\sigma}^{\phi} \frac{\delta F}{\delta \phi_g} \quad (g = 1, 2, \dots, N) \quad (7)$$

where L_{σ}^{ϕ} is the interface mobility coefficient. The governing equation for crack propagation is also derived from the form of the Ginzburg-Landau equation driven by mechanical force, as shown in the following:

$$\begin{aligned} \frac{1}{L_{\sigma}^{cr}} \frac{\partial \phi_{cr}}{\partial t} = & \frac{\delta F}{\delta \phi_{cr}} \\ = & \kappa_{cr} \nabla^2 \phi_{cr} - 2W_{cr} \phi_{cr} (1 - \phi_{cr}) (1 - 2\phi_{cr}) - 12\phi_{cr}^2 (1 - \phi_{cr}) (W_{elastic} - W_c) \end{aligned} \quad (8)$$

where L_σ^{cr} is the interface mobility. It should be noted that the governing equation for crack is only applied within the grain with defect, as mentioned above.

Since the stacking pressure effect is considered in this study, the solid mechanics model is also introduced in the framework to describe the mechanical behavior of the solid-state battery under pressure, the geometry of which includes all the domains shown in Fig. 8 (i.e., anode and solid electrolyte). The governing equation of the mechanical model follows Newton's second law:

$$\rho \frac{\partial^2 \mathbf{u}}{\partial t^2} = \nabla_{\mathbf{x}} (F_L S) + F_V \quad (9)$$

where \mathbf{u} is displacement field, ρ is the material density, F_L is deformation gradient, S is the Piola-Kirchhoff stress tensor, \mathbf{X} is material coordinate, and F_V is body force. The mechanical model calculates the stress, strain, and displacement fields, then outputs the elastic strain energy density to Eqs. (6)-(8).

As for material transportation in the solid electrolyte, Li-ion is considered the only diffusion species in the solid electrolyte. The diffusion process is mainly described by Fick's second law while considering other influencing factors:

$$\frac{\partial \tilde{c}_+}{\partial t} = \nabla \cdot \left[D^{eff} \nabla \tilde{c}_+ + \frac{D^{eff} \tilde{c}_+}{RT} nF \nabla \varphi - \frac{D^{eff} \Omega_e}{RT} \tilde{c}_+ \nabla \sigma_e \right] - \frac{c_s}{c_0} \frac{\partial \xi}{\partial t} \quad (10)$$

where the first two terms are in the form of classic Nernst-Plank equation, the third term describes the effect from mechanical stress, and the last term is for electrochemical reaction induced consumption of Li-ion at the interface, D^{eff} and Ω_e are effective diffusivity

coefficient and partial molar volume, respectively, both of which also depend on the evolution of phases:

$$D^{eff} = \begin{cases} D_{Li}h(\xi) + D_{SE}(1-h(\xi)) & \text{for non-crack region} \\ D_{Li}(1-h(\phi_{cr})) + D_{SE}h(\phi_{cr}) & \text{for crack region} \end{cases} \quad (11)$$

$$\Omega_e = h(\xi)\Omega_{Li} + (1-h(\xi))\Omega_{SE} \quad (12)$$

where D_{Li} and D_{SE} are the diffusivity for Li metal and solid electrolyte, respectively, Ω_{Li} and Ω_{SE} are the partial molar volume for Li metal and solid electrolyte, respectively.

The Poisson equation is used to describe the electrostatic potential distribution:

$$\nabla \cdot [\sigma^{eff} \nabla \varphi] = nFc_s \frac{\partial \xi}{\partial t} \quad (13)$$

where the term on the right is the charge source induced by the electrochemical reaction,

σ^{eff} is the effective conductivity as a function of phase evolution:

$$\sigma^{eff} = \begin{cases} \sigma_{Li}h(\xi) + \sigma_{SE}(1-h(\xi)) & \text{for non-crack region} \\ \sigma_{Li}(1-h(\phi_{cr})) + \sigma_{SE}h(\phi_{cr}) & \text{for crack region} \end{cases} \quad (14)$$

where σ_{Li} and σ_{SE} are the conductivities for Li metal and solid electrolyte, respectively.

As for the boundary conditions, the left side is anode where the stacking pressure is applied, and the right side is cathode which is neglected in this model and fixed. Dirichlet boundaries $\xi = 1$, $\tilde{c}_+ = 0$ and $\varphi = 0 \text{ V}$ are used for the left boundary, and $\tilde{c}_+ = 1$ and $\varphi = 0.1 \text{ V}$ are used for the right boundary. As for the initial conditions, different variables have different initial values in different regions: $\{\xi, \phi_1, \dots, \phi_g, \dots, \phi_N\} = \{1, 0, \dots, 0, \dots, 0\}$ for lithium anode region, $\{\xi, \phi_1, \dots, \phi_g, \dots, \phi_N\} = \{0, 0, \dots, 1, \dots, 0\}$ for the g -th grain region, $\{\xi, \phi_1, \dots, \phi_g, \dots, \phi_N\} = \{0, 0, \dots, 0, \dots, 0\}$ for all the grain boundary region,

$\{\xi, \phi_1, \dots, \phi_g, \dots, \phi_N, \phi_{cr}\} = \{1, 0, \dots, 0, \dots, 0, 0\}$ for the pre-defected region which is fulfilled by lithium, $\{\xi, \phi_1, \dots, \phi_g, \dots, \phi_N, \phi_{cr}\} = \{0, 1, \dots, 0, \dots, 0, 1\}$ for the only grain where the crack propagation governing equation is applied.

All the parameters used in the model are summarized in Table 1. The modeling framework elaborated above is implemented in the COMSOL Multiphysics platform using the workstation with 128 GB memory and 32 CPUs at 3.50 GHz.

The above-proposed modeling framework for LLZO (solid ceramic electrolyte, SCE) can also be used for solid polymer electrolytes (SPEs) after modifying some parts of the model. Firstly, there is no grain or grain boundary in SPEs; then the electrolyte geometry can be modeled as one homogenized domain. Secondly, the energy terms (Eqs. (1-3)), the stiffness expression (Eq. (5)), governing equation (Eq. (7)) related to grains are not required any more, which will be much more computationally efficient compared with polycrystalline SCEs. Besides, SCEs are single-ion conductors in which only Li ions move to transport ions, while there are Li-ions and other anions migrating in SPEs. Thus the iteration number for Li is reduced significantly when modeling SPEs.

Table 1 Summary of material properties and simulation parameters

| Parameter | Symbol | Value | References |
|---|---------------|----------------------------|------------|
| Site density of Li metal | c_s | 7.64e4 mol/m ³ | 53, 103 |
| Number of electrons involved in electrode reaction for Li | n | 1 | 53, 103 |
| Conductivity in Li | σ_{Li} | 1.1e7 S/m | 72, 106 |
| Interface mobility of Li | L_σ^z | 2.5e-6 m ³ /J/s | 53, 103 |

| | | | |
|-----------------------------------|---------------------|----------------------------|-----------|
| Reaction constant of Li | L_{η}^{ξ} | 0.2 s ⁻¹ | estimated |
| Barrier height of Li | W_{Li} | 1.18e6 J/m ³ | 53 |
| Gradient coefficient of Li | κ_{ξ} | 3.68e-6 J/m | 53 |
| Li-ion diffusivity in Li | D_{Li} | 7.5e-13 m ² /s | 103 |
| Partial molar volume of Li metal | Ω_{Li} | 1.3e-5 m ³ /mol | 7, 72 |
| Young's modulus of Li metal | E_{Li} | 4.9 GPa | 53 |
| Poisson's ratio of Li metal | ν_{Li} | 0.362 | 53 |
| Density of Li metal | ρ_{Li} | 534 kg/m ³ | 73 |
| LLZO bulk Li-ion concentration | c_0 | 4.22e4 mol/m ³ | 53 |
| Conductivity in LLZO | σ_{SE} | 4.43e-2 S/m | 92 |
| Interface mobility of LLZO | L_{σ}^{ϕ} | 1.5e-8 m ³ /J/s | 53 |
| Barrier height of LLZO | W_{ϕ} | 2.05e6 J/m ³ | 53 |
| Gradient coefficient of LLZO | κ_{ϕ} | 6.38e-6 J/m | 53 |
| Li-ion diffusivity in LLZO | D_{SE} | 1e-12 m ² /s | 53 |
| Partial molar volume of LLZO | Ω_{SE} | 0 m ³ /mol | 72 |
| Young's modulus of LLZO grain | E_{SE} | 150 GPa | 7, 53, 73 |
| Poisson's ratio of grain | ν_{SE} | 0.257 | 53 |
| Density of LLZO | ρ_{SE} | 4606 kg/m ³ | 107 |
| Young's modulus of grain boundary | E_{GB} | 7.5 GPa | 72 |
| Anisotropy strength | δ | 0.03 | 53 |

| | | | |
|--|-------------------|----------------------------|-----------|
| Crystallographic symmetry mode | λ | 4 | 53, 106 |
| Symmetric factor | α | 0.5 | 53, 103 |
| Faraday's constant | F | 96485 C/mol | ---- |
| Gas constant | R | 8.314 J/mol/K | ---- |
| Temperature | T | 298 K | ---- |
| Barrier height for crack | W_{cr} | 2.05e6 J/m ³ | From LLZO |
| Gradient coefficient for crack | κ_{cr} | 6.38e-6 J/m | From LLZO |
| Interface mobility for crack | L_{σ}^{cr} | 1.5e-6 m ³ /J/s | From LLZO |
| Fracture threshold energy density of the solid-state electrolyte | W_c | 6.66 J/m ² | 72 |

2.2 Representative computational results

A representative case with a rectangular preset crack in the angle $\theta=30^\circ$ and with the applied stacking pressure 50 MPa serves will be illustrated here. The length and width of the pre-defined crack are $L=60 \mu\text{m}$ and $W=10 \mu\text{m}$, respectively.

The pre-defect region is assumed to be fully filled with lithium at $t=0$ s (Fig. 8a). Lithium dendrite grows within the grain boundary region and cracked region driven by both electrochemical and mechanical factors in Eq. (6). The mechanical driving force comes from the strain energy density induced by the applied stacking pressure, and the electrochemical driving force arises from the negative overpotential for the electrochemical reaction. In the meantime, the Li-ion concentration and electrostatic potential both evolve with lithium dendrite growth. From the comparison of Figs. 8a and 8b at each time point,

we can observe that Li-ion concentration decreases in the region where dendrite grows because Li-ion is continuously consumed during the formation of lithium, expressed in the last term of Eq. (10). The blue region ($\tilde{c}_+=0$) and red region ($\tilde{c}_+=1$) in Fig. 8b represent the dendrite and solid electrolyte, respectively. The interfaces between the two regions is the transition area ($0 < \tilde{c}_+ < 1$). There are two aspects to be clarified for the Li-ion concentration gradient within the transition area. On one hand, the concentration evolution in this study is governed by the phase-field method, which describes the microstructure evolution by using phase-field variables that are continuous across the interfacial region¹⁰⁴. Due to the inherent calculation principle, the gradient of the variable inevitably exists at the interfacial region. Thus there is a Li-ion concentration gradient between the pure dendrite and electrolyte. On the other hand, the concentration gradient region lies only within/near the area where the electrolyte is affected by the crack and dendrite, and the unaffected electrolyte area keeps a constant concentration (i.e. $\tilde{c}_+=1$). Please note that the dimension of the area with a relatively large concentration gradient is only about 30 μm (=0.03 mm), much smaller compared with the commonly used LLZO electrolyte pellet thickness ~ 1 mm and diameter ~ 10 mm⁶⁹. As such, from the macroscale view of the overall electrolyte sample, the concentration gradient area is tiny and trivial. Since the effective conductivity σ^{eff} is always changing with the dendrite evolution, σ^{eff} switches to σ_{Li} from σ_{SE} when there is full of the dendrite (Eq. (14)). The value of σ_{Li} is much greater than σ_{SE} , and the anode potential is set as 0 V, then the potential of the newly grown

dendrite region becomes close to the anode potential (Fig. 8c).

To investigate the influence of pre-defect position, we change the pre-defect position closer to the grain boundary (Fig. 8e), and the results show that the crack initiated from the grain boundary region propagates to the grain region. It demonstrates that the pre-defect region significantly affects the initiation point of crack. If the pre-defect is prone to occur within the vicinity of the grain boundary region, then the crack will initiate from the grain boundary and propagate to grains. One step further, we consider the crack propagation in adjacent grains and grain boundary region as well (Fig. 8f). The crack propagates from the pre-defect area within the original grain where the pre-defect is located (Fig. 8f, $t=0\sim 100s$), to the grain boundary and adjacent grain ($t=150\sim 200s$). Before the crack propagates outside of the original grain, the crack propagation behavior is the same in Figs. 8d and 8f, which indicates the interaction of adjacent grains affects little. Once the crack propagates into the grain boundary and other grains, the crack propagation speed in the original grain will be lower, as the crack finds other paths (paths require lower energy) to grow. However, the difference of crack propagation within the original grain in Figs. 8d and 8f is small, demonstrating that the crack propagation behavior in the grain in Fig. 8d is representative. Therefore, to obtain more efficient computational results while maintain the generality of the study, the crack propagation is considered only in one grain in this study.

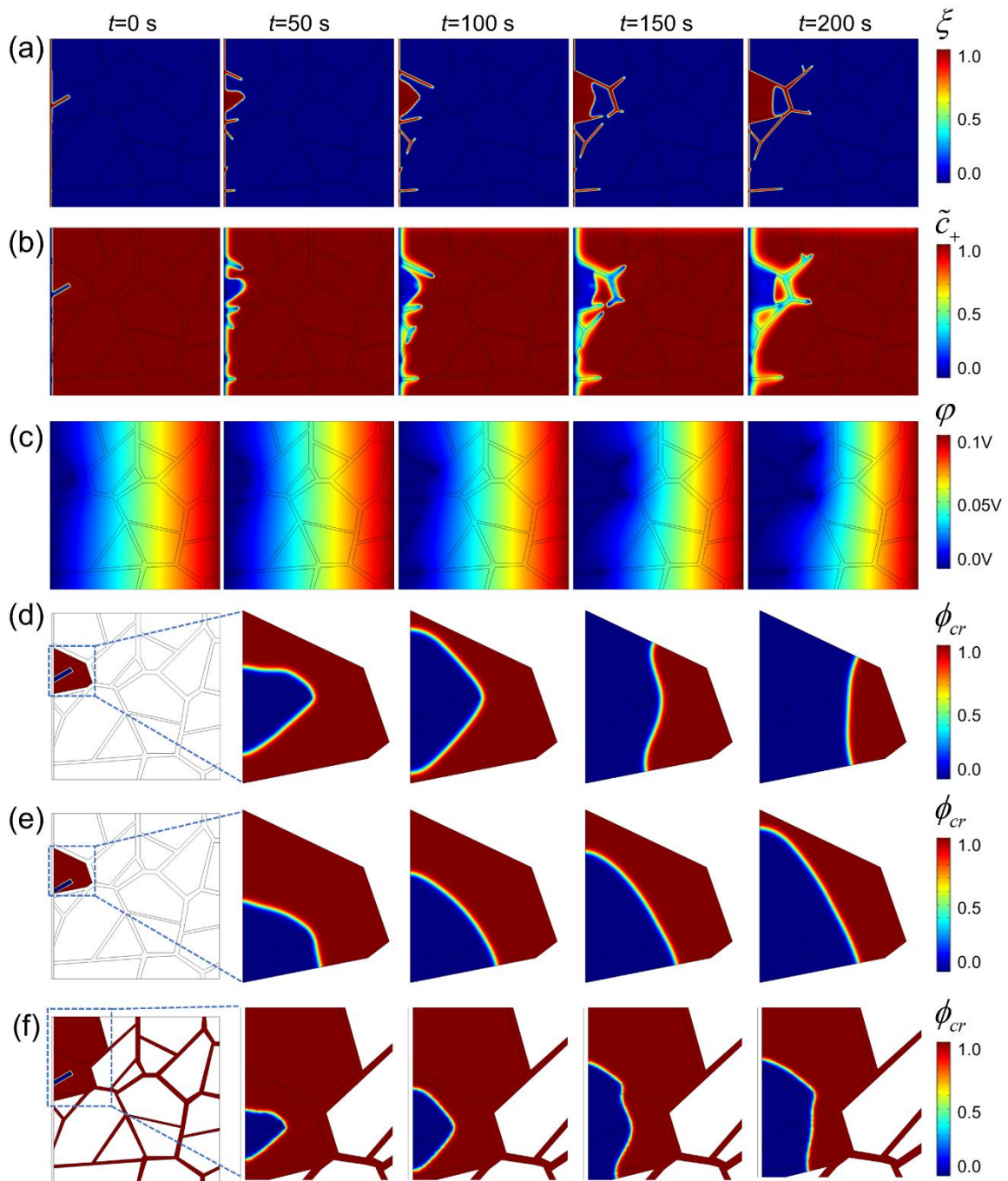


Figure 8 Typical simulation results with rectangular pre-defect with $\theta=30^\circ$ under 50 MPa pressure: (a) Li dendrite growth ξ , (b) dimensionless Li-ion concentration evolution \tilde{c}_+ , (c) potential field evolution ϕ , and (d) crack area propagation ϕ_{cr} when pre-defect is located at the center of grain edge; (e) crack area propagation ϕ_{cr} when pre-defect is close to grain boundary; (f) crack area propagation ϕ_{cr} when crack propagation is considered in two grains and grain boundary region.

The stacking pressure 50 MPa is applied at the left boundary, which causes mechanical damage to the solid electrolyte. The crack gradually propagates from the initial rectangular defect ($t=0$ s) to nearly the full grain region ($t=200$ s) (Fig. 8d). Compared with the primitive solid electrolyte, the cracked region is much easier for dendrite to grow due to the changed properties, including the reduced Young's modulus and increased conductivity (Eqs. (5) and (14)). The major reasons are: (a) the cracked area is much softer, so it is much less resistant to dendrite growth than SE, and (b) area with increased electronic conductivity is easier for electron transportation, thus speeds up the formation of lithium dendrite. Lithium dendrite grows and fulfills the cracked region, demonstrating that lithium growth speed is large enough to grow into the newly cracked region (Figs. 8a and 8d). The newly grown dendrite is mainly within the cracked area (Fig. 8a), while the dendrite in the grain boundary is much farther, thus increasing the risk of a short circuit.

2.3 Discussion

In the following sessions, length L , angle θ , and shape of the defect, and different stacking pressures P are parametrically studied.

2.3.1 Geometric information of the initial defect

2.3.1.1 Length effect

The rectangular shape is selected, and the width and angle of the initial defect are fixed as $W=10$ μm and $\theta=30^\circ$, respectively. $L=10, 20, 30,$ and 40 μm , are chosen here. Note that the same stacking pressure 50 MPa is applied for all the cases in this session. We obviously

observe that longer initial defects lead to more cracks and Li dendrite, especially within the grain (Fig. 9a). Note that in polycrystal materials, Li dendrite grows along the grain boundary and cracked surfaces. We quantitatively compute the newly developed dendrite area for the whole domain (WD) and the grain boundary (GB) region, respectively. The dendrite area in the GB region remains almost the same, i.e., about $6.04 \times 10^{-9} \mu\text{m}^2$ at 200 s with various L values (Fig. 9b). It clearly indicates that the fundamental driving force for dendrite growth in GB is not affected by the initial defect length in the grain. The dendrite area in WD increases from $6.25 \times 10^{-9} \mu\text{m}^2$ to $10.0 \times 10^{-9} \mu\text{m}^2$ with L increases from 10 μm to 40 μm at $t=200$ s (Fig. 9b). The increase of dendrite area with the initial defect is mainly attributed to the increased area in the cracked region such that more void/weak interface is available for the dendrite to grow (Fig. 9c). Furthermore, the normalized crack area S is calculated by $S = S_{\text{Total}} / S_{\text{Initial}}$, where S_{Initial} is the initial defected area and S_{Total} is the total cracked area. S values at $t=200$ s for $L=10, 20, 30$ and $40 \mu\text{m}$ are 2.27, 3.15, 6.16 and 11.47 respectively. It is clearly envisioned that the dendrite area increases with the normalized crack area indicating a fact that dendrite growth is facilitated by the increasing crack area (Figs. 9a and 9c). Mitigating the cracks within the grains can be regarded as a positive and effective way to hinder the growth of dendrite.

In general, E_{max} becomes larger with L , especially when $L > 20 \mu\text{m}$. There are fluctuations for the E_{max} curves due to the fact that the surrounding continuum structure is changing during crack propagation (Fig. 9d). E_{ave} shows a more smooth increasing trend

with L . With larger L , the average energy density in the pre-defected region E_{ave_pd} is smaller at the initial stage. Because there is more room in the longer defect away from the left side where the stacking pressure is applied (Fig. 9e). Since the crack propagates faster with larger L , i.e., more severe change of the structure and more Li dendrite, gradually all pre-defected area fully bears the pressure, resulting in larger time-gradient of E_{ave_pd} . On the contrary, there is less crack propagation with small L values (i.e., 10 and 20 μm), and the structure changes little, causing a flat E_{ave_pd} profile. The average energy density in the crack propagation region E_{ave_pr} increases with L (Fig. 9f), providing stronger force to drive cracks.

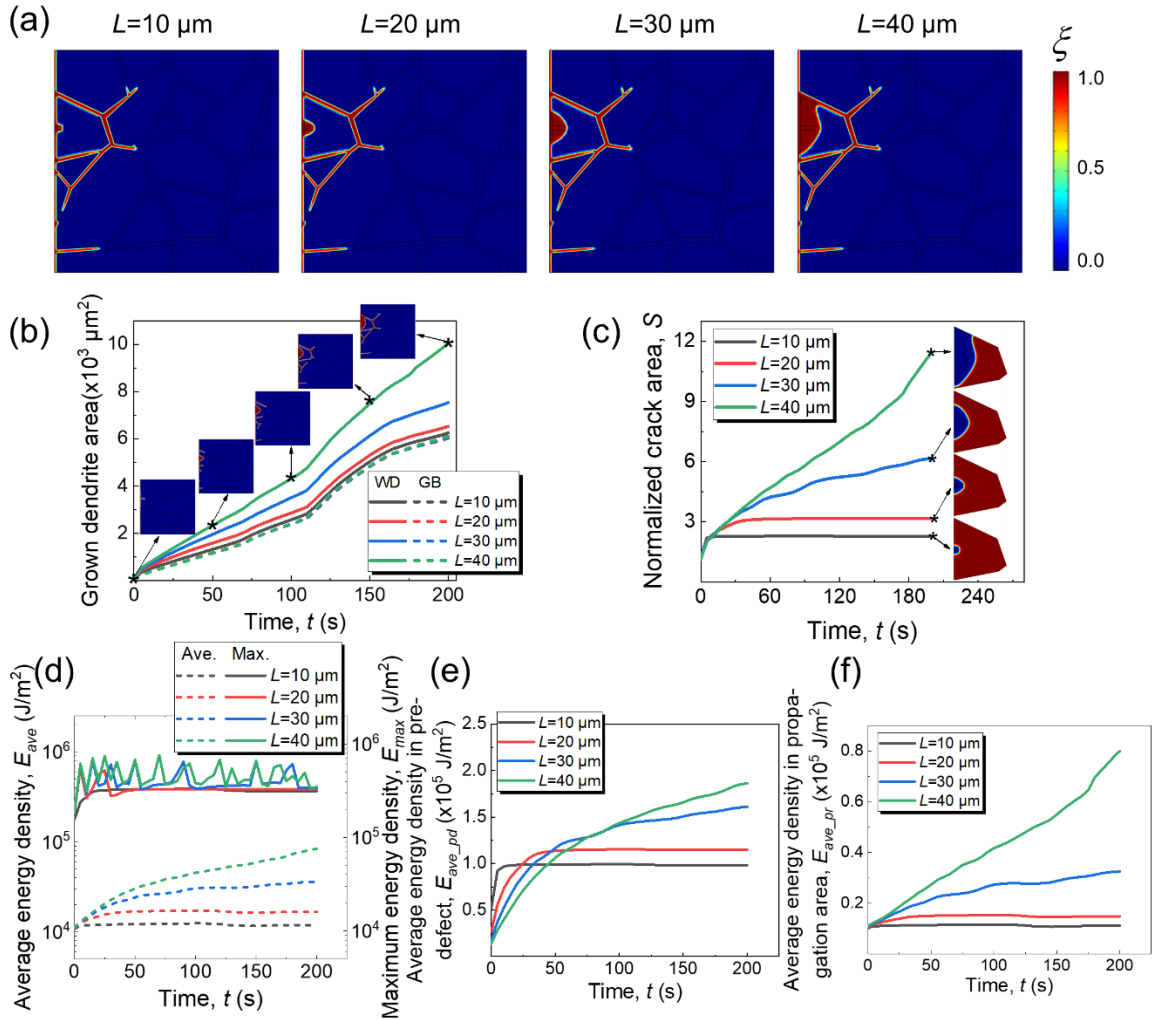


Figure 9 Effect of initial defect size on dendrite growth and crack propagation behavior: (a) Li dendrite growth of different pre-defect lengths at 200 s, i.e., 10, 20, 30 and 40 μm ; (b) newly grown Li dendrite area in whole domain (WD) and grain boundary (GB); (c) evolution of normalized crack area S ; (d) average value E_{ave} and maximum value E_{max} of strain energy density in the crack area; (e) average strain energy density in pre-defect area $E_{\text{ave_pd}}$; and (f) average strain energy density in crack propagation area $E_{\text{ave_pr}}$.

2.3.1.2 Angle effect

Since the initial defects have random orientations θ , and it influences the crack propagation and thus leads to different dendrite growth scenarios. In this session, we parametrically examine cases with $\theta=0^\circ, 15^\circ, 30^\circ, 45^\circ, 60^\circ, 75^\circ$ and 90° , while the initial defect is a rectangular shape with fixed $L=60 \mu\text{m}$ and $W=10 \mu\text{m}$ without the size

effect. Note that the dendrite growth in the grain boundary region is the same for the cases with different defect angles because neither the mechanical strain energy density nor the electrochemical driving forces are determined by the position angles.

When $\theta < 45^\circ$, the crack areas are almost the same, and the total value is high (Region I in Fig. 10a). The crack area decreases substantially as the angle increases when $\theta > 45^\circ$ (Region II). The maximum Mises stress σ_{\max} of Region I (~ 240 MPa) is higher than that of Region II (~ 200 MPa) (Fig. 10b). The fluctuation in the curves comes from the continuing evolution of the phases and structures. Due to the structure evolution induced by crack propagation, there is an obvious drop of σ_{\max} for Region I, and the dropping time of the case with $\theta = 30^\circ$ is the earliest at $\sim t = 120$ s.

We can observe that the area with larger von Mises stresses σ (i.e., the red region) are larger for $\theta = 0^\circ$ and $\theta = 30^\circ$, implying stronger mechanical driving forces to push the crack forward and dendrite growth (Fig. 10d). Besides, σ in the dendrite area is smaller than that of the solid electrolyte area because Young's modulus of lithium is ~ 4.9 GPa, at least one order of magnitude smaller than LLZO's Young's modulus ~ 150 GPa. As the crack propagates, the stress concentration area for $\theta = 30^\circ$ at $t = 115$ s is located within the narrow vicinity (marked in Fig. 10d), and disappears soon at $t = 120$ s. This serves as the responsible reason for the σ_{\max} curve dropping in Fig. 10b.

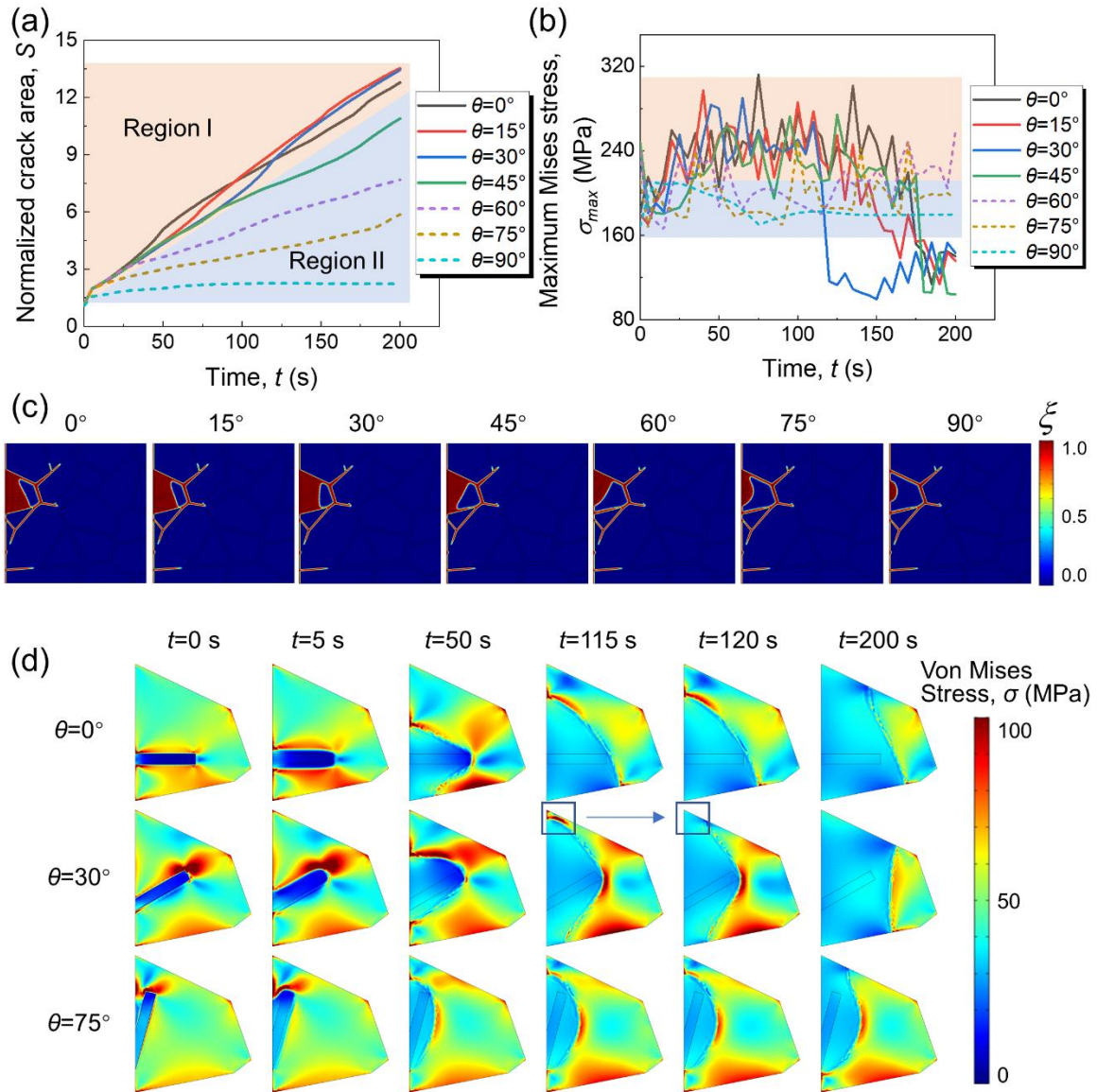


Figure 10 Effect of initial defect angle on dendrite growth and crack propagation behavior: (a) evolution of normalized crack area S ; (b) maximum von Mises stress σ_{\max} in the crack propagation area under different pre-defect angle; (c) Li dendrite ξ growth of different pre-defect angle at 200 s, i.e., 0° , 15° , 30° , 45° , 60° , 75° , and 90° ; (d) von Mises stress σ contour plots for selected pre-defect angles, i.e., 0° , 30° , and 75° .

2.3.1.3 Shape effect

The smoothness of the defect edge varies with the shape, which potentially affects the crack and dendrite growth behavior. As such, four shapes are selected here, i.e., a circle with radius $R=15.96 \mu\text{m}$, an ellipse with semimajor axis $A=25.5 \mu\text{m}$ and semiminor axis

$B=10 \mu\text{m}$, a triangle with base $b=20 \mu\text{m}$ and height $H=40 \mu\text{m}$, and a rectangle with length $L=40 \mu\text{m}$ and width $W=10 \mu\text{m}$. Note that these four types of initial defects share the same area.

The newly developed dendrite area within the grain boundary for all four shapes are almost identical (Fig. 11a), about $6.04 \times 10^{-9} \mu\text{m}^2$ at $t=200 \text{ s}$, showing the independency of the defect shape on the driving forces for dendrite in the grain boundary. However, the total developed dendrite area for circular, elliptical, triangular, and rectangular defects are $6.29 \mu\text{m}^2$, $6.69 \mu\text{m}^2$, $8.66 \mu\text{m}^2$, $10.04 \mu\text{m}^2$, respectively. This clearly demonstrates that the major difference in the dendrite area stems from the cracking situation. The normalized crack area S in Fig. 11b shows the same increasing trend as the curves for WD in Fig. 11a, which again supports the above explanations. The S values for models with circular, elliptical, triangular, and rectangular defects are 1.52, 2.49, 8.06, and 11.47, respectively. The newly cracked area increases little under circular and elliptical defects but rapidly under triangular and rectangular defects because σ_{max} and E_{ave} of the crack region with triangular and rectangular defects are larger than those of circular and elliptical defects (Figs. 11c-d). The fundamental reason should be attributed to the smooth edges of the circle and ellipse alleviate the stress concentration extent significantly.

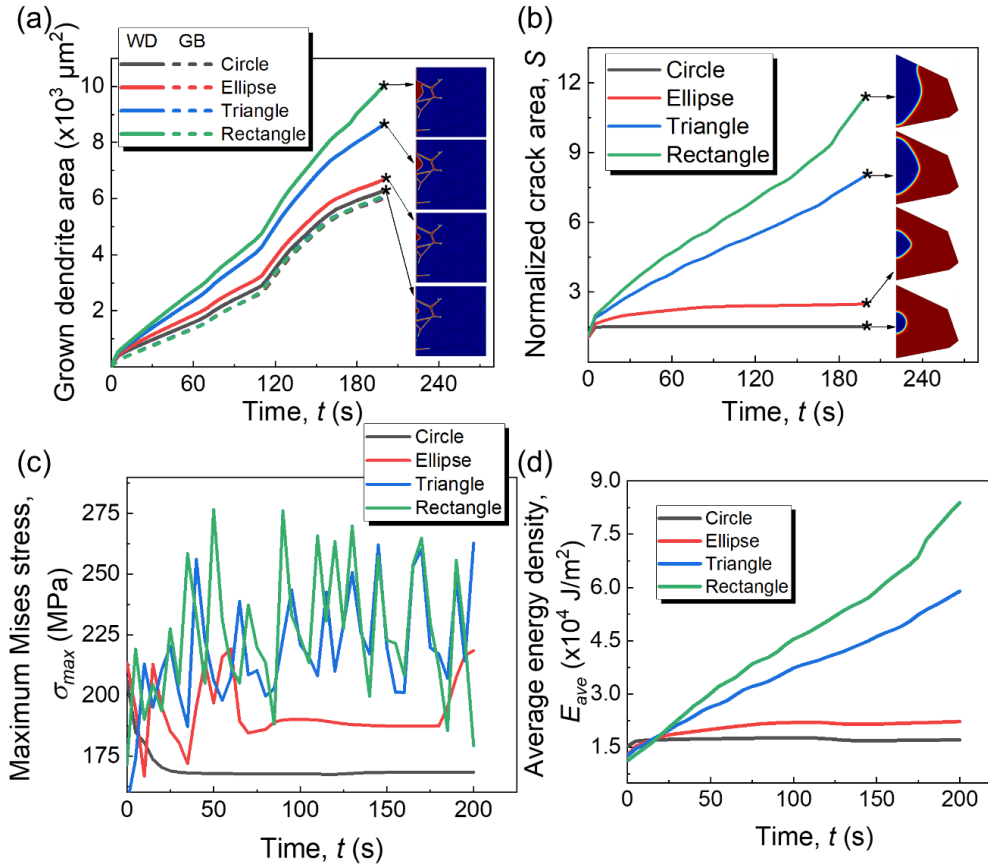


Figure 11 Effect of initial defect shape on dendrite growth and crack propagation behavior: (a) newly grown Li dendrite area in whole domain and in grain boundary; (b) evolution of normalized crack area S ; (c) maximum Mises stress σ_{max} of different pre-defect shape; (d) Average strain energy density E_{ave} of different pre-defect shape.

2.3.2 Stacking pressure effect

Stacking pressure provides a mechanical driving force externally to influence the grain cracks and Li dendrite. To eliminate the effect of the pre-defected pattern when studying the stacking pressure effect, we use the same rectangular defect with length $L=40 \mu\text{m}$, width $W=10 \mu\text{m}$, and angle $\theta=0^\circ$ for all the cases in this section.

During charging, the lithium dendrite grows from the anode side towards the cathode side, and a short circuit is triggered once the dendrite reaches the cathode side. To quantitatively represent the possibility of the short circuit, the distance of the farthest

dendrite tip in the grain boundary from the anode side, X , is analyzed (Fig. 12a). Here, a farther dendrite represents a faster short circuit since the distance between anode and cathode is fixed as 500 μm . Naturally, X increases with time and stacking pressure P ; however, if $P < 10$ MPa, no obvious increase for X can be observed, indicating that smaller stacking pressure will not increase the short circuit risk. The grown dendrite areas in grain boundary S_{GB} is $1.744 \times 10^3 \mu\text{m}^2$ for 0 MPa pressure case where there is only electrochemical driving force $F_{\text{EC}} = -L_{\eta}^{\xi} h'(\xi) \left\{ \exp\left[\frac{(1-\alpha)nF\eta}{RT}\right] - \tilde{c}_{+} \tilde{c}_{e} \exp\left[\frac{(-\alpha)nF\eta}{RT}\right] \right\}$ (the last term from Eq. (6)), is taken as the baseline case. Once the pressure is greater than 0 MPa, an additional mechanical driving force $F_{\text{M}} = -L_{\sigma}^{\xi} \frac{\partial f_{\text{mech}}}{\partial \xi}$ (the second term from Eq. (6)) will be added. At $t=200$ s, compared with the baseline in 100%, S_{GB} are 100.2%, 101.4%, 115.36%, 175.02%, 277.82%, 344.34% and 458.24% for 5, 10, 20, 30, 40, 50 and 60 MPa, respectively (Fig. 12b). In addition, strain-energy induced dendrite growth area accounts for at least 15% if $P > 20$ MPa.

The mechanical driving force F_{M} and electrochemical driving force F_{EC} for dendrite growth as a function of X explicitly demonstrate that a higher mechanical driving force would be for the dendrite if the crack is longer (Figs. 12c and 12d). When the dendrite grows into the crossing region with the grain boundary at about $t=90$ s, substantial drops of F_{M} and F_{EC} can be observed (Figs. 12c and 12d). That is due to the weak interface for the grain boundary. F_{M} increases with P , which further explains the phenomenon that

S_{GB} increases with the stacking pressure. F_M is less than 0.001/s, about two orders of magnitude smaller than F_{EC} when $P < 10$ MPa, demonstrating that mechanical driving force for dendrite induced by such small stacking pressure is trivial. When $P = 60$ MPa, F_M increases to $\sim 0.15/s \sim 0.3/s$. Such value is still small compared to $F_{EC} \sim 0.6/s$; however, it becomes a nontrivial factor. It is not safe to apply a larger stacking press on the ASSBs as it may lead to a severe Li dendrite situation.

The grain boundaries are interconnected in polycrystal material, thus there are quite a few routes for lithium dendrite to grow. The routes for the farthest and shortest dendrites under 60 MPa are R1 and R2, respectively (Fig. 12e). At 200 s, X is 230 μm for R1 while only 101 μm for R2. F_M has a much larger value at dendrite tip (Fig. 12f) to drive dendrite growth. R1 has larger F_M than R2, causing faster dendrite growth in R1. The angle between horizontal line and grain boundary β is larger than 30° in R1 while it is less than 5° for R2 (R2 is almost parallel with the applied pressure direction). The tension and shear-induced strain energy density within the vicinity of R2 is small such that the crack is reluctant to propagate along R2. This implies a new strategy to suppress the dendrite growth by creating more aligned initial defects near the Li/SE interface and voids around the crack tip to release the stress concentration.

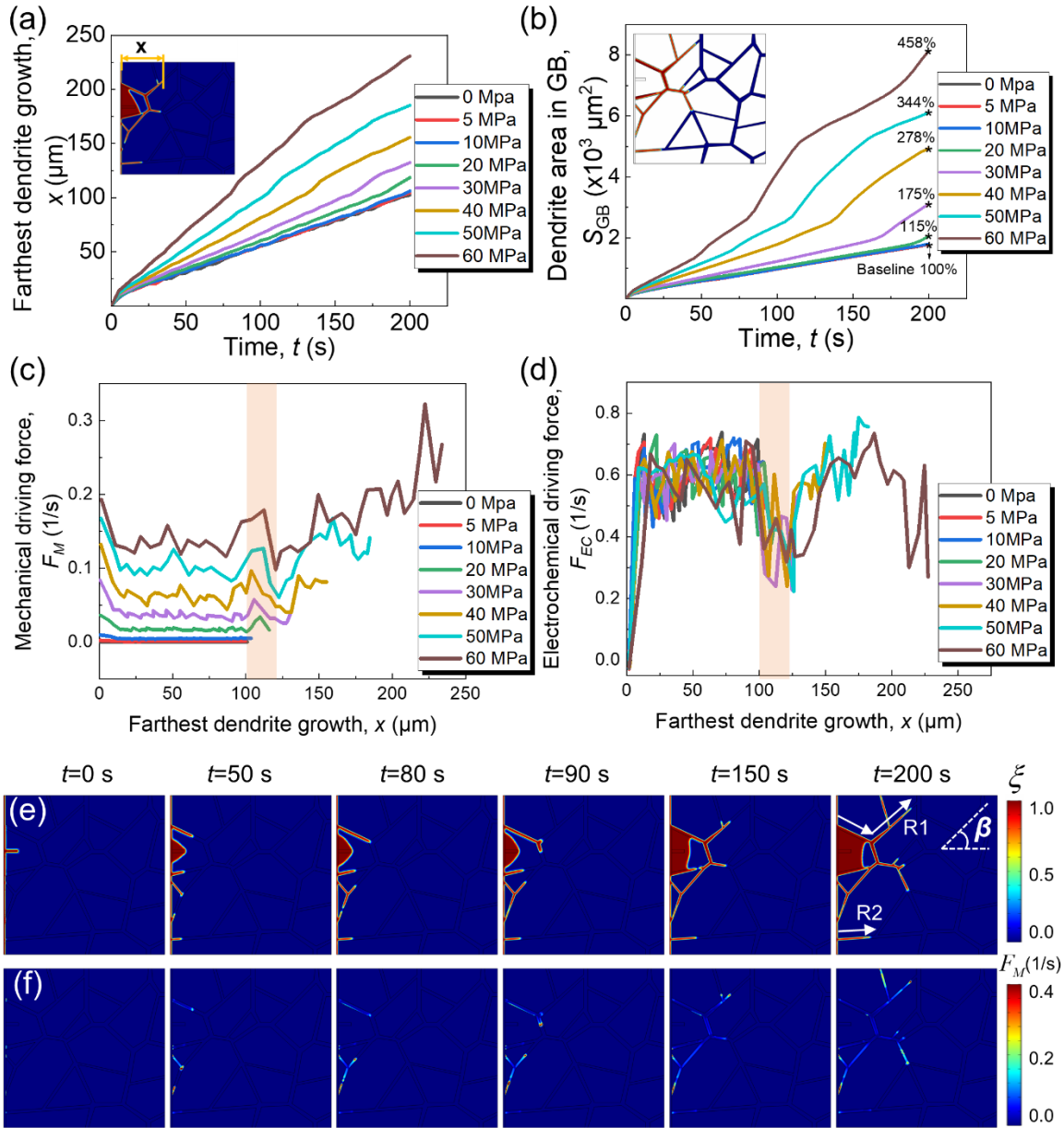


Figure 12 Effect of stacking pressure on dendrite behavior: (a) farthest Li dendrite growth distance X in grain boundary; (b) newly grown dendrite area S_{GB} in grain boundary; (c) mechanical contribution term F_M to the dendrite growth; (d) electrochemical contribution term F_{EC} to the dendrite growth; (e) dendrite growth for 60 MPa pressure; and (f) mechanical contribution term contour plots for 60 MPa pressure.

The other focus in this section is on the crack propagation and corresponding dendrite growth behaviors. The normalized crack area $S=1, 1.002, 1.009, 1.149, 1.832, 2.743, 5.912,$ and $11.426,$ for $P=0, 5, 10, 20, 30, 40, 50,$ and 60 MPa, respectively. Similar to the Li

dendrite, under $P=10$ MPa or less, S are almost the same, which indicates that the driving force for crack propagation is also negligible (Fig. 13a). S increases visibly with pressure from the overall trend, especially when the pressure is above 20 MPa. Intuitively, the crack seldom propagates under $P=0, 5,$ and 10 MPa (Fig. 13b). Crack propagation speeds up with larger pressure when $P>20$ MPa, and particularly, crack nearly occupies the whole grain under 60 MPa, in which case $S=1, 2.854, 5.331, 8.769,$ and 11.426 for $t=0, 50, 100, 150,$ and 200 s, respectively. With a larger newly created open surface (cracked area), more dendrite resides there.

Both the average and maximum von Mises stress and energy density increase with stacking pressure (Figs. 13b and 13c). Both σ_{\max} and E_{\max} curves show fluctuations due to the changing structure, and the dropping of σ_{\max} under 60 MPa at $t=110$ s is also due to the disappearance of the narrow vicinity, similar to Fig. 10d. When $P<20$ MPa, σ_{ave} and E_{ave} curves almost keep the same value all the time due to the little crack propagation and nearly unchanged structure. While σ_{ave} curves show a downward trend when $P>20$ MPa, because the sharp edge between initial defect and grain becomes more smooth; thus the stress concentration area is reduced. Larger stress and energy density together provide a stronger driving force for crack propagation, thus creating more space for dendrite growth. From both views of dendrite growth in the grain boundary and crack propagation, the driving force induced by small stacking pressure blew 10 MPa is small and has a trivial effect in impairing the solid electrolyte. It would be beneficial to apply a stacking pressure

no greater than 10 MPa to improve the electrode/electrolyte interface properties of solid-state batteries without sacrificing safety performance.

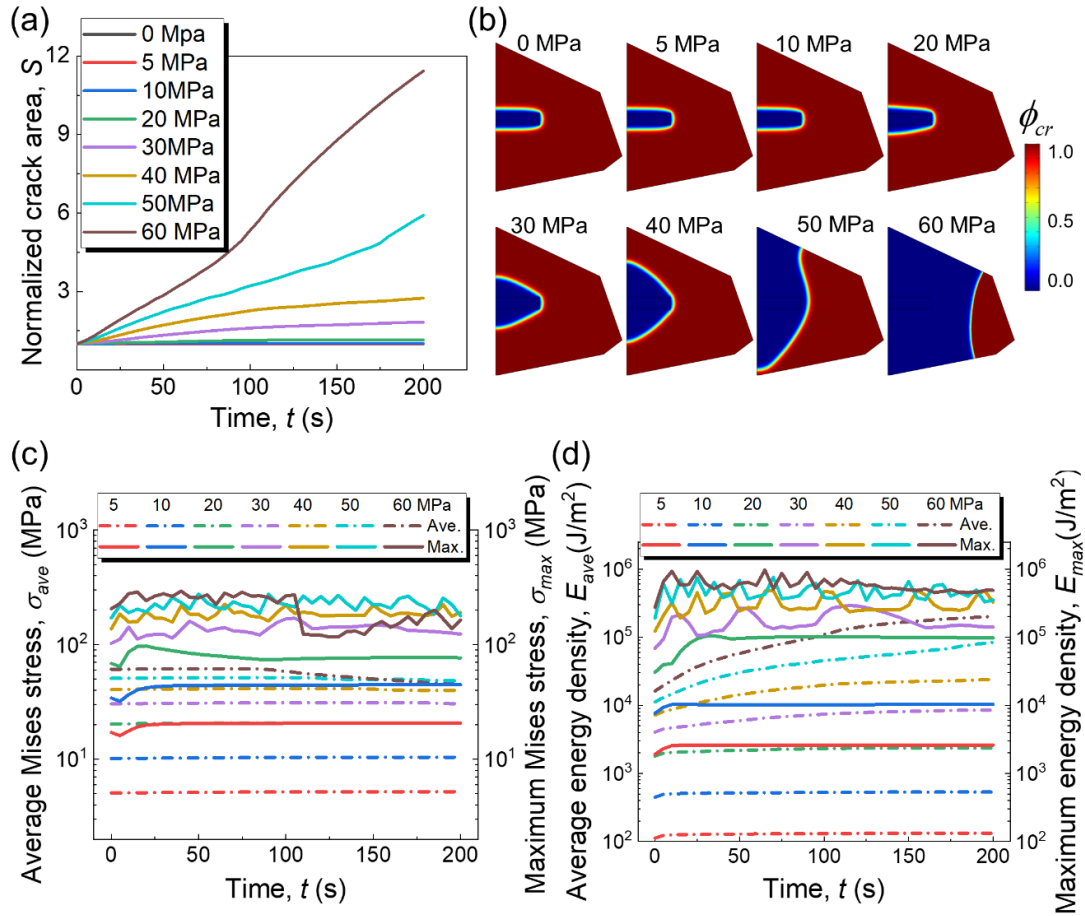


Figure 13 Effect of stacking pressure on crack propagation behavior: (a) normalized crack area S ; (b) contour plots of the crack parameter at 200 s under different pressures; (c) average value σ_{ave} and maximum value σ_{max} of Mises stress in crack propagation area; and (d) average value E_{ave} and maximum value E_{max} of strain energy density in crack propagation area for different stacking pressure.

2.3.3 Fracture threshold strain effect

The mechanical properties, especially the fracture parameters, play an essential role in the crack behavior of solid electrolytes. In this study, the crack propagation is described from the energy conservation perspective, and governed by Eq.(6) where $W_{elastic}$ is the

strain energy density, W_c is LLZO's fracture threshold energy density, i.e., the fracture energy. If W_{elastic} is greater than W_c , crack propagation is favored. Here we only consider the elastic stage of LLZO, then W_c can be expressed as $W_c = E_{\text{SE}}\varepsilon_c^2$ where ε_c is the fracture threshold strain. The fracture threshold strain effect (i.e., the fracture energy effect) is parametrically studied. The baseline ε_{c0} is $6.663\text{e-}6$ calculated from the reference fracture threshold energy density 6.66 J/m^2 ⁷². Different threshold strain values are selected, i.e. $\varepsilon_{c1}=6.663\text{e-}5$, $\varepsilon_{c2}=1.3326\text{e-}4$, $\varepsilon_{c3}=2.6652\text{e-}4$, $\varepsilon_{c4}=3.9978\text{e-}4$, $\varepsilon_{c5}=5.3304\text{e-}4$, $\varepsilon_{c6}=6.663\text{e-}4$, $\varepsilon_{c7}=6.663\text{e-}3$. To eliminate the effect of other factors, the same rectangular defect with length $L=40\ \mu\text{m}$, width $W=10\ \mu\text{m}$, angle $\theta=0^\circ$, and pressure $50\ \text{MPa}$ are used for all the cases in this section.

The crack area increases with decreasing fracture threshold strain ε_c (Figs. 14a and 14c), indicating that the fracture energy can be much more easily exceeded by the strain energy under smaller ε_c , especially when $\varepsilon_c < 4 \times 10^{-4}$. In other words, if ε_c is large enough, the strain energy can hardly reach the fracture energy threshold value, then crack propagation is suppressed. The normalized crack area S values for ε_{ci} ($i=1, 2, \dots, 7$) are 9.66, 9.02, 7.34, 4.18, 2.60, 1.55, 1.44 and 1, respectively (Fig. 14a). The crack maintains its initial area all the time for ε_{c7} , which further validates that large enough ε_c can prevent crack, providing a possible solution to the crack and dendrite problems. The crack propagates fast at the beginning due to the stress concentration caused by the sharp edge of the initial defect (Fig. 14b), then the propagation speed dS/dt gradually decreases to ~ 0

for $\varepsilon_c \geq \varepsilon_{c3}$ because the cracked region edge becomes much smoother and W_{elastic} gradually decreases to have no advantage over W_c . While for $\varepsilon_c < \varepsilon_{c3}$, the speed dS/dt maintains a high level and even increases (Fig. 14b), showing a continuous crack propagation tendency since W_c is much smaller than W_{elastic} under smaller ε_c .

The newly grown dendrite area in the whole domain S_{WD} increases with decreasing ε_c , while in the grain boundary region S_{GB} is almost the same for ε_{ci} ($i=1, 2, \dots, 7$) (Figs. 14d-e), demonstrating that the driving force for dendrite in grain boundary is mainly from the electrochemical aspect and not affected by the crack propagation within grain, and that the S_{WD} difference is caused by the crack behavior. Since the cracked area provides space for dendrite to grow, faster crack propagation speed under smaller ε_c results in larger grown dendrite area, which clarifies larger S_{WD} for $\varepsilon_c < \varepsilon_{c3}$. From the mechanical point of view, increasing ε_c to a large enough value can prevent the crack propagation; however, from the perspective of suppressing dendrite, only dendrite growth related to crack can be prevented by this method, but the dendrite in grain boundary still grows, which indicates that dendrite suppression requires the combination of mechanical and electrochemical methodology.

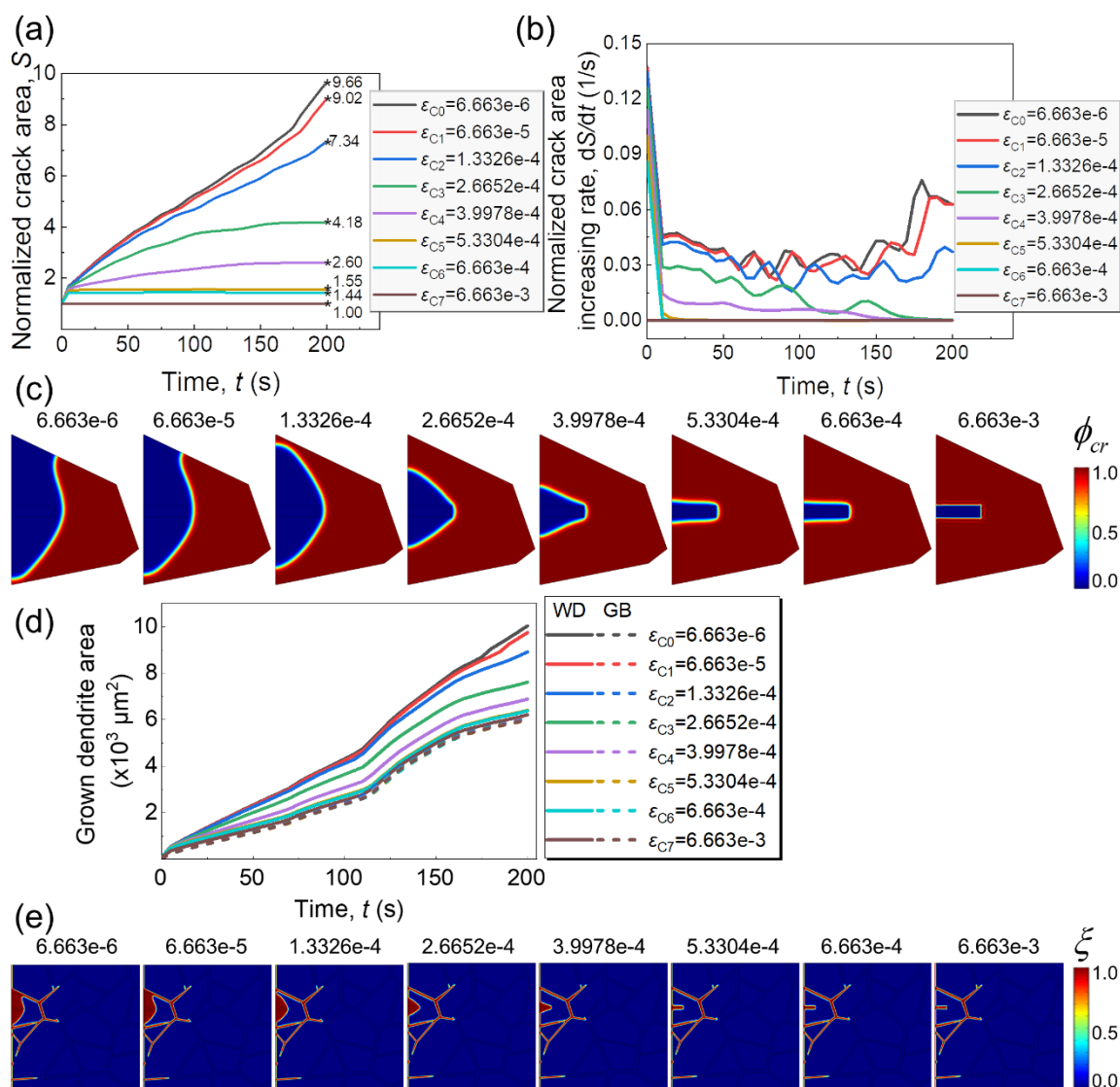


Figure 14 Effect of fracture threshold strain on crack propagation and dendrite growth behavior: (a) evolution of normalized crack area S ; (b) normalized crack area increasing rate dS/dt ; (c) contour plots of the crack parameter at 200 s under different fracture threshold strains; (d) newly grown dendrite area in whole domain and in grain boundary region; and (e) contour plots of dendrite parameter at 200 s under different fracture threshold strains.

2.4 Conclusions

Lithium dendrite and electrode/electrolyte interface defect are two key issues for developing solid-state lithium batteries with the desired cyclability. However, the underlying coupling mechanisms of dendrite growth and interface defect induced crack

propagation under stress remain unknown. In this paper, the coupled electrochemical-mechanical phase-field model is established for the first time to investigate the lithium dendrite growth and crack propagation behavior quantitatively. The lithium anode and the poly-crystalline LLZO solid electrolyte, as well as the pre-defect at Li/LLZO interface, are considered in the model. Based on the developed modeling framework, the effects of pre-defect patterns, including defect length, angle and shape, and stacking pressure, fracture threshold strain, are systematically studied. The dendrite is prone to grow in the grain boundary and cracked regions. Results show that longer defect with a sharp edge and angle $\theta \geq 45^\circ$ causes more severe crack propagation, thus larger dendrite growth area due to larger von Mises stress and strain energy density. The patterns of the initial defects within the grain play an irrelevant role in the dendrite growth within the grain boundary region since the crack in the grain hardly affects the mechanical status in the grain boundary. As for the stacking pressure effect, dendrite grows faster in grain boundary due to larger mechanical driving force induced by larger pressure, while the pressure has little effect on the electrochemical driving force. In the meantime, there is more severe crack propagation in grain, thus larger space for dendrite growth under higher pressure. On the other hand, pressure below 10 MPa has little effect on dendrite growth and crack propagation and can be applied to improve the electrode/electrolyte interface properties of solid-state batteries without sacrificing safety performance. Increasing the fracture threshold strain or fracture energy can suppress the crack and related dendrite growth, and the crack propagation may

be prevented if the fracture threshold strain is large enough. Results lay a strong foundation for the understanding of the electrochemical-mechanical coupled mechanism in the Li dendrite growth and crack propagation in solid electrolytes and provide design guidance for next-generation ASSBs.

CHAPTER 3 COUPLED DENDRITE GROWTH AND CRACK PROPAGATION AT CELL SCALE

In this chapter, by integrating the battery model, mechanical model, phase-field model, and short-circuit model, I establish a physics-based and fully coupled electrochemical-mechanical model, directly bridging the dendrite growth and crack propagation with battery charging/discharging. After validation of the developed model, the effects of electrochemically generated stress, charging rate, electrolyte properties (including conductivity, Young's modulus, and fracture toughness) are thoroughly investigated while considering interfacial defects to provide insights and guidance on the design of ASSBs.

3.1 Methods

3.1.1 Coupling strategy

To describe the crack propagation- and dendrite growth-induced battery short circuit during charging/discharging in ASSBs, we consider four models: 1) the battery model solves the potential and concentration evolution within the electrode and electrolyte during the charging/discharging process; 2) the mechanical model calculates the deformation, stress, and strain fields caused by the overpotential-driven dendrite growth under the constraint of the SE; 3) the phase-field model is used to describe the crack propagation and dendrite growth; and 4) the short-circuit model detects the triggering of the short circuit and calculates the short-circuit resistance.

To couple the four models described above, the following coupling strategy is adopted

modulus, and wide electrochemical stability window⁹⁵ is selected in this study. To generalize the model to accommodate both single-crystal and polycrystalline LLZO and to describe crack propagation/dendrite growth from the cell level, the SE is modeled as a homogenized domain (Fig. 16), which also facilitates the consideration of battery models. Li metal and LiCoO₂(LCO) are used as the anode and cathode, respectively. The left boundary of the electrolyte is considered as the Li anode¹⁰⁹, and the right boundary of the cathode is fixed (Fig. 16). The focus of this study is on the dendrite growth during the charging process without consumption of the Li anode. Then it is assumed that the electrode/electrolyte interfaces have perfect contact and no stacking pressure is applied. The thicknesses of the electrolyte and cathode are L_{cl} and L_{ca} , respectively, and the battery width is W_{bat} . The cell capacity is 1400 $\mu\text{Ah}/\text{cm}^2$. We designate the pre-defect at the Li/SE interface to represent the unavoidable interfacial defects, such as voids, impurities, and cracks (pre-defects in different dimensions cause similar crack propagation behavior (Fig. 17(a))). The absence of interfacial defect can suppress the dendrite initiation/formation, and makes the battery electrochemical performance better (Fig. 17(b)), which indicates that elimination of the interfacial defect is an effective method for suppression of Li dendrite in solid electrolyte. However, currently, the interfacial defects are inevitable, then the focus of this study is on the influence of interfacial defect. Considering the computational efficiency, the pre-existing defect is rectangular with length $L=100 \mu\text{m}$ and width $W=50 \mu\text{m}$. The defect dimension is much smaller (<10%) than the solid electrolyte, and is at the

same magnitude of the crack width reported in the literature⁶⁶.

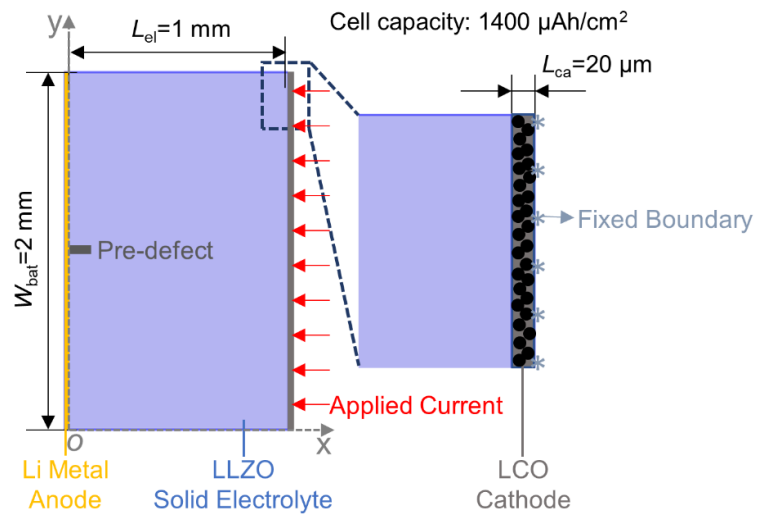


Figure 16 Schematics of the established model including geometry, boundary condition, and defect area.

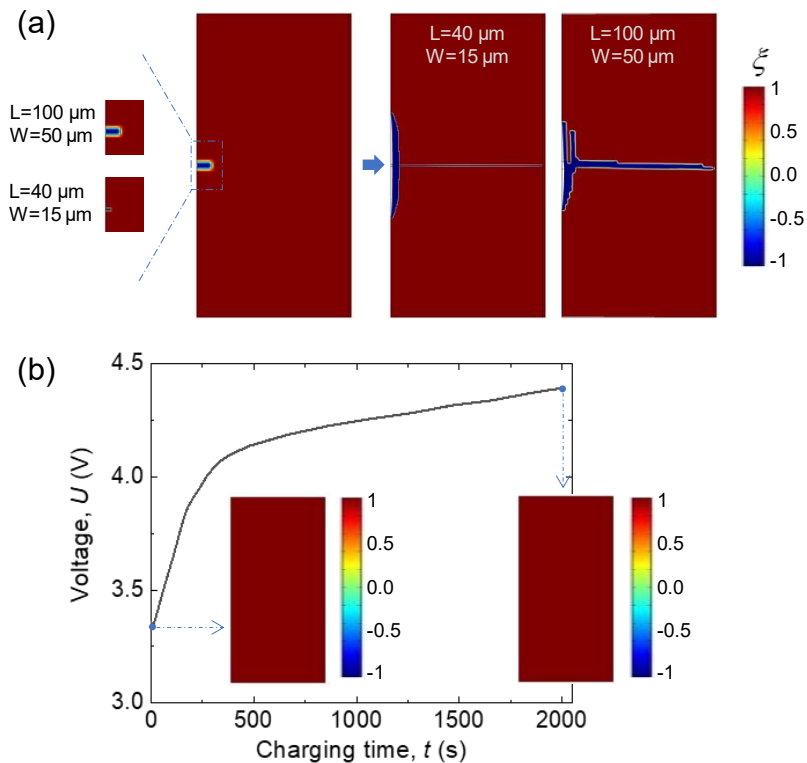


Figure 17 Crack propagation behavior with pre-existing defect of different dimensions. (a) for the large defect, the length $L=100 \mu\text{m}$, width $W=50 \mu\text{m}$; for the small defect, the length $L=40 \mu\text{m}$, width $W=15 \mu\text{m}$; (b) the voltage response for the model without interfacial defect, i.e. the defect size is 0.

3.1.2 Modeling methodology

The battery model calculates the electrochemical status during charging/discharging, including the evolution of the potential and ion concentration. The inorganic solid electrolyte is a single-ion conductor such that only Li ions migrate within the electrolyte to transport charge. Based on the precondition of electroneutrality, the Li-ion concentration is assumed to be uniform in the solid electrolyte.

Since the anode is pure Li metal and no ohmic loss is considered, the anode domain can be neglected. The left boundary of the electrolyte is the Li/LLZO interface, where the charge-transfer kinetics are governed by the Butler-Volmer equation¹⁰⁹:

$$j = j_{0-} \left[\exp\left(\frac{\alpha_a F}{RT} \eta_- \right) - \exp\left(\frac{-\alpha_c F}{RT} \eta_- \right) \right] \quad (15)$$

$$j_{0-} = j_{0-, \text{ref}}(T) \quad (16)$$

where j is the current density; j_{0-} is the exchange current density at the anode/electrolyte interface; α_a and α_c are anodic and cathodic charge-transfer coefficients, respectively; F is Faraday's constant, R is the gas constant, $T=300$ K is the temperature; $j_{0-, \text{ref}}$ is the reference exchange current density. η_- is the overpotential for the electrochemical reaction at the Li/LLZO interface, defined in the following equation:

$$\eta_- = \phi_{s, \text{ext}} - \phi_l \quad (17)$$

where $\phi_{s, \text{ext}}$ is the external electric potential for the Li anode and ϕ_l is the electric potential in the electrolyte phase. Since the anode potential is considered as the ground

potential, then $\phi_{s, \text{ext}} = 0\text{V}$.

Within the LLZO electrolyte, the electric potential is related to the current density, governed by Ohm's law:

$$\mathbf{i}_l = -\sigma_{\text{SE}} \nabla \phi_l \quad (18)$$

where \mathbf{i}_l is the current density in the electrolyte and σ_{SE} is the effective conductivity of the electrolyte. Charge conservation requires:

$$\nabla \cdot \mathbf{i}_l = 0 \quad (19)$$

During charging of the battery, the Li dendrite will grow from anode to cathode, which will affect σ_{SE} :

$$\sigma_{\text{SE}} = h(\xi) \sigma_{\text{LLZO}} + (1 - h(\xi)) \sigma_{\text{Li}} \quad (20)$$

where ξ is the phase-field parameter for crack propagation and σ_{LLZO} and σ_{Li} are the conductivities of LLZO and Li, respectively. The function $h(\xi) = -\frac{1}{4}\xi^3 + \frac{3}{4}\xi + \frac{1}{2}$ is used for the interpolation of material properties of the interface between the LLZO electrolyte and the Li dendrite¹¹⁰, i.e., conductivity, Young's modulus.

At the electrolyte/cathode interface, the electrochemical reaction kinetics are given by the Butler-Volmer equation as well:

$$j = j_{0+} \left[\exp\left(\frac{\alpha_a F}{RT} \eta_+\right) - \exp\left(\frac{-\alpha_c F}{RT} \eta_+\right) \right] \quad (21)$$

$$j_{0+} = j_{0+, \text{ref}} (T) \left(\frac{c_s}{c_{s, \text{ref}}} \right)^{\alpha_c} \left(\frac{c_{s, \text{max}} - c_s}{c_{s, \text{max}} - c_{s, \text{ref}}} \right)^{\alpha_a} \quad (22)$$

where j_{0+} is the exchange current density at the cathode/electrolyte interface; $j_{0+, \text{ref}}$ is

the reference exchange current density; c_s and $c_{s,\text{ref}}$ are the Li-ion concentration and reference Li-ion concentration in the solid phase of the cathode, respectively; and $c_{s,\text{max}}$ is the maximum Li-ion concentration. η_+ is the overpotential for the electrochemical reaction at the LCO/LLZO interface, expressed as:

$$\eta_+ = \phi_s - \phi_l - E_{\text{eq}} \quad (23)$$

where ϕ_s and ϕ_l are the electric potentials in the cathode solid phase and the electrolyte phase, respectively; E_{eq} is the equilibrium potential. ϕ_s is given by Ohm's law:

$$\mathbf{i}_s = -\sigma_s \nabla \phi_s \quad (24)$$

where \mathbf{i}_s is the current density in the solid phase of the cathode and σ_s is the electrical conductivity of the LCO cathode.

Porous electrode theory is adopted to describe the physicochemical phenomena in cathode domain¹¹¹, which sets up current balance for the porous electrode matrix and the pore electrolyte, as well as the mass balance for the pore electrolyte and for Li ions in the electrode particles. Charge conservation requires:

$$\nabla \cdot \mathbf{i}_s = 0 \quad (25)$$

The ion transport in electrolyte within cathode is neglected, and only ion intercalation in cathode particles is considered based on two assumptions: 1) the inorganic solid electrolyte is single-ion conductor in which only Li ions move to transport charge, 2) conservation of charge is maintained within the solid electrolyte, then the ion concentration in electrolyte is considered constant. Therefore, The electron transport is considered in the

whole cathode domain including the electrolyte and particles, governed by the Ohm's law (Eqs. (18) and (24)). The diffusion of Li ions in the active particle of the cathode is governed by Fick's second law:

$$\frac{\partial c_s}{\partial t} = \nabla \cdot (D_s \nabla c_s) \quad (26)$$

where D_s is the Li-ion intercalation diffusivity.

Based on the above governing equations, the following boundary conditions are applied for the battery model.

$$\frac{\partial c_s}{\partial x} = \frac{-j}{FD_s} \quad \text{at } x = L_{\text{el}} \quad (27)$$

$$\frac{\partial c_s}{\partial x} = 0 \quad \text{at } x = L_{\text{el}} + L_{\text{ca}} \quad (28)$$

$$-\mathbf{i}_s \cdot \mathbf{n} = i_{\text{app}} \quad \text{at } x = L_{\text{el}} + L_{\text{ca}} \quad (29)$$

where \mathbf{n} is the unit outward normal vector of the cathode surface and i_{app} is the applied electrode current density at the right boundary of the cathode.

The mechanical model solves the stress and strain fields when the battery suffers electrochemically driven stress. In this study, only small and elastic deformations are considered, as LLZO has a large Young's modulus (i.e., 150 GPa) with a good capability to resist deformation. The governing equation of the mechanical model follows Newton's second law:

$$\rho \frac{\partial^2 \mathbf{u}}{\partial t^2} = \nabla \cdot \mathbf{F}_L (S + S_{\text{ext}}) + F_V \quad (30)$$

where \mathbf{u} is the displacement field, ρ is the material density, \mathbf{F}_L is the deformation gradient, S is the Piola-Kirchhoff stress tensor, S_{ext} is the external stress tensor representing the load contribution from electrochemical overpotential-driven stress, and F_V is the body force. The deformation gradient can be expressed as:

$$\mathbf{F}_L = \mathbf{I} + \nabla \mathbf{u} \quad (31)$$

where \mathbf{I} is the identity matrix and \mathbf{u} is the displacement vector.

The overpotential at the interface of the Li dendrite and the electrolyte η_- drives the dendrite growth under the constraint of the SE, determining the value of hydrostatic stress (i.e., the external stress tensor). For other regions except for the dendrite/electrolyte interface, there is no overpotential influence on the hydrostatic stress. Then, the relationship between S_{ext} and η_- can be expressed as ^{65,80,112}:

$$S_{\text{ext}} = \begin{cases} -\frac{F}{\Omega_{\text{Li}}} \eta_- & \text{at dendrite/electrolyte interface} \\ 0 & \text{for other region} \end{cases} \quad (32)$$

where Ω_{Li} is the partial molar volume of Li metal.

As the crack propagates and the dendrite grows, the Young's modulus of the solid electrolyte E_{SE} evolves as well, represented as:

$$E_{\text{SE}} = h(\xi) E_{\text{LLZO}} + (1 - h(\xi)) E_{\text{Li}} \quad (33)$$

Where E_{LLZO} and E_{Li} are Young's moduli of the LLZO electrolyte and the Li dendrite, respectively.

As for the mechanical boundary conditions, the right boundary of the cathode is fixed:

$$u_x = u_y = 0 \quad \text{at} \quad x = L_{el} + L_{ca} \quad (34)$$

The crack propagation is described by the evolution of the non-conserved phase-field order parameter ξ of the *phase-field model* in this study from the perspective of energy. $\xi = 1$ and $\xi = -1$ represent the intact electrolyte region and the cracked region, respectively. The phase-field method uses a diffuse interface to show the continuous phase-field variable across the interfacial region, and $-1 < \xi < 1$ is the transition interface between the intact and cracked regions. Note that it is assumed that the cracked region is filled with Li dendrite^{49, 68, 113}. The total free energy F_{total} of the system in this study is expressed as follows^{49, 110, 114}:

$$F_{\text{total}} = \int [f_{\text{local}} + f_{\text{grad}} + f_{\text{mech}}] dV \quad (35)$$

where f_{local} is the local energy density, f_{grad} is the gradient energy density, and f_{mech} is the mechanical strain energy density, whose expressions are written as:

$$f_{\text{local}} = \frac{\lambda}{4\varepsilon_{\text{pf}}^2} (1 - \xi)^2 (1 + \xi)^2 \quad (36)$$

$$f_{\text{grad}} = \frac{\lambda}{2} (\nabla \xi)^2 \quad (37)$$

$$f_{\text{mech}} = \frac{1}{2} \sigma_{ij} \varepsilon_{ij} = \frac{1}{2} C_{ijkl}(\xi) \varepsilon_{ij} \varepsilon_{kl} \quad (38)$$

where λ is the mixing energy density, ε_{pf} is the parameter controlling the interface thickness, $C_{ijkl}(\xi)$ is the stiffness (i.e., Young's modulus E_{SE} in Eq. (33)), ε_{ij} and ε_{kl} are strain components. The relationship between λ and ε_{pf} follows¹¹⁴:

$$\lambda = \frac{3E_{\sigma} \varepsilon_{\text{pf}}}{\sqrt{8}} \quad (25 \ 39)$$

where E_σ is the surface energy required to create the new cracked surfaces. We assume that all the mechanical elastic strain energy is used to drive the crack propagation and is transferred to the surface energy without loss. Due to the fact that each newly formed crack has two identical surfaces, the surface energy E_σ is equal to half of the fracture energy G :

$$E_\sigma = \frac{G}{2} \quad (40)$$

$$G = \frac{(1-\nu^2)K_{LLZO}^2}{E_{LLZO}} \quad (41)$$

where K_{LLZO} is the fracture toughness of the LLZO electrolyte and ν is LLZO's Poisson's ratio.

The governing equation for the crack propagation follows the Allen-Cahn equation as 110:

$$\frac{\partial \xi}{\partial t} + \mathbf{u} \cdot \nabla \xi = \nabla \cdot \frac{\gamma \lambda}{\varepsilon_{pf}^2} \nabla \psi \quad (42)$$

where γ is the mobility parameter controlling the crack propagation, written as:

$$\gamma = \chi \varepsilon_{pf}^2 \quad (43)$$

where χ is the mobility tuning parameter reflecting the crack propagation speed. ψ is obtained from the total free energy through the variational method, expressed as:

$$\psi = -\nabla \cdot \varepsilon_{pf}^2 \nabla \xi + (\xi^2 - 1)\xi + \frac{\varepsilon_{pf}^2}{\lambda} \frac{\partial f_{mech}}{\partial \xi} \quad (44)$$

Since the pre-defect is designated at the Li/LLZO interface, the initial value for the pre-defect region is $\xi = -1$; for the remaining intact regions, the initial value is $\xi = 1$.

Once the crack continuously propagates and the dendrite grows to reach the cathode

side, the Li anode and LCO cathode are internally connected by the dendrite, indicating a triggered short circuit.

The short-circuit model is developed to probe whether the dendrite penetrates through the solid electrolyte (i.e., whether $\xi = -1$ at the cathode/electrolyte interface). If the short circuit is detected, the short-circuit resistance R_{short} is calculated by the following equation:

$$R_{\text{short}} = \frac{L_{\text{el}}}{\sigma_{\text{SE_ave}}(\xi) S_{\text{SE}}} \quad (45)$$

where $\sigma_{\text{SE_ave}}(\xi)$ is the average conductivity of the solid electrolyte automatically obtained from the domain probe and S_{SE} is the cross-section area of the electrolyte.

Table 2 Summary of material properties and simulation parameters

| Parameter | Symbol | Value | References |
|---|------------------------|---------------------------------------|------------|
| Anodic charge transfer coefficients | α_a | 0.5 | 103, 109 |
| Cathodic charge transfer coefficients | α_c | 0.5 | 103, 109 |
| Conductivity of LLZO | σ_{LLZO} | 4.43×10^{-2} S/m | 49, 92 |
| Conductivity of Li | σ_{Li} | 1.1×10^7 S/m | 49, 72 |
| Conductivity of LCO cathode | σ_s | 1.13×10^{-1} S/m | 115 |
| Li-ion intercalation diffusivity of cathode | D_s | 5×10^{-13} m ² /s | 116 |
| Faraday's constant | F | 96485 C/mol | 49, 72 |
| Gas constant | R | 8.314 J/mol/K | 49, 72 |
| Temperature | T | 300 K | 72 |

| | | | |
|---|---------------------------|--|------------|
| Density of LLZO | ρ_{LLZO} | 4606 kg/m ³ | 49 |
| Density of Li metal | ρ_{Li} | 534 kg/m ³ | 49 |
| Partial molar volume of Li metal | Ω_{Li} | 1.3×10^{-5} m ³ /mol | 49, 72 |
| Young's modulus of Li metal | E_{Li} | 4.9 GPa | 49, 53 |
| Young's modulus of LLZO | E_{LLZO} | 150 GPa | 49, 53 |
| Poisson's ratio of LLZO | ν | 0.257 | 49, 53 |
| Parameter controlling interface thickness | ε_{pf} | 1×10^{-6} m | estimated |
| Fracture toughness of LLZO | K_{LLZO} | 0.98 MPa $\sqrt{\text{m}}$ | 82 |
| Mobility tuning parameter | χ | 6×10^{-6} (m·s)/kg | estimated |
| Cross-section area of the electrolyte | S_{SE} | 1 m ² | calculated |
| Yield stress of Li metal | $\sigma_{\text{Y, Li}}$ | 0.4 MPa | 47 |

3.2 Results and discussion

3.2.1 Representative results

The charging/discharging voltage versus capacity response of the Li/SE/LCO cell from simulation (Fig. 60 in Appendix A) agrees well with experimental results, and the predicted critical current density is comparable to the reported value, demonstrating the validity of the electrochemical response of the model.

With the pre-existing defect and under a 1C charging rate, the Li dendrite grows around the defect from the beginning of charge until the short circuit. Fig. 18 summarizes the dendrite growth process using the battery model, mechanical model, phase-field model,

and short-circuit model. According to the battery model, the battery voltage increases during the charging process until 423.8 s, at which point the dendrite leads to the short circuit and the voltage drops (Fig. 18(a)).

During the charging process, an uneven overpotential η_- distribution around the pre-existing defect surface affects the interfacial chemical reaction⁶⁵, leading to Li plating around this area (battery model). Since the Li dendrite affects the effective electrolyte conductivity σ_{SE} (Eq. (20)), the electrolyte potential ϕ_l changes accordingly (Eq. (18)) and affects the current density within the SE (Fig. 18(d) and Fig. 19). The high-conductivity dendrite area further facilitates the Li electrodeposition, i.e., dendrite growth, and accelerates the uneven overpotential η_- distribution (phase-field model to battery model).

In addition, the uneven overpotential η_- distribution can change the von Mises stress σ_{Mises} (Fig. 18(c)) and cause crack propagation due to the mechanical strain energy density. The cracks initially become large in random directions, then transverse mainly in the direction from the anode side towards the cathode side (Fig. 18(b)) (battery model to mechanical model). The cracks provide space for Li dendrite growth (mechanical model to phase-field model). In return, the Li dendrite affects the von Mises stress σ_{Mises} and crack propagation (phase-field model to mechanical model). The strong correlation between the mechanical model and the phase-field model leads to a similar von Mises stress and phase-field distribution within the SE, as shown in Fig. 18 (b-c).

However, once the dendrite grows to reach the cathode side, the phase-field variable

$\xi = -1$ is detected at the LCO/LLZO interface at $t=423.8$ s, then the direct electron transportation path is built between the anode and cathode and the current density is mainly concentrated within the dendrite area (Fig. 18(d)), causing the abrupt voltage drop, i.e., the short circuit (short-circuit model).

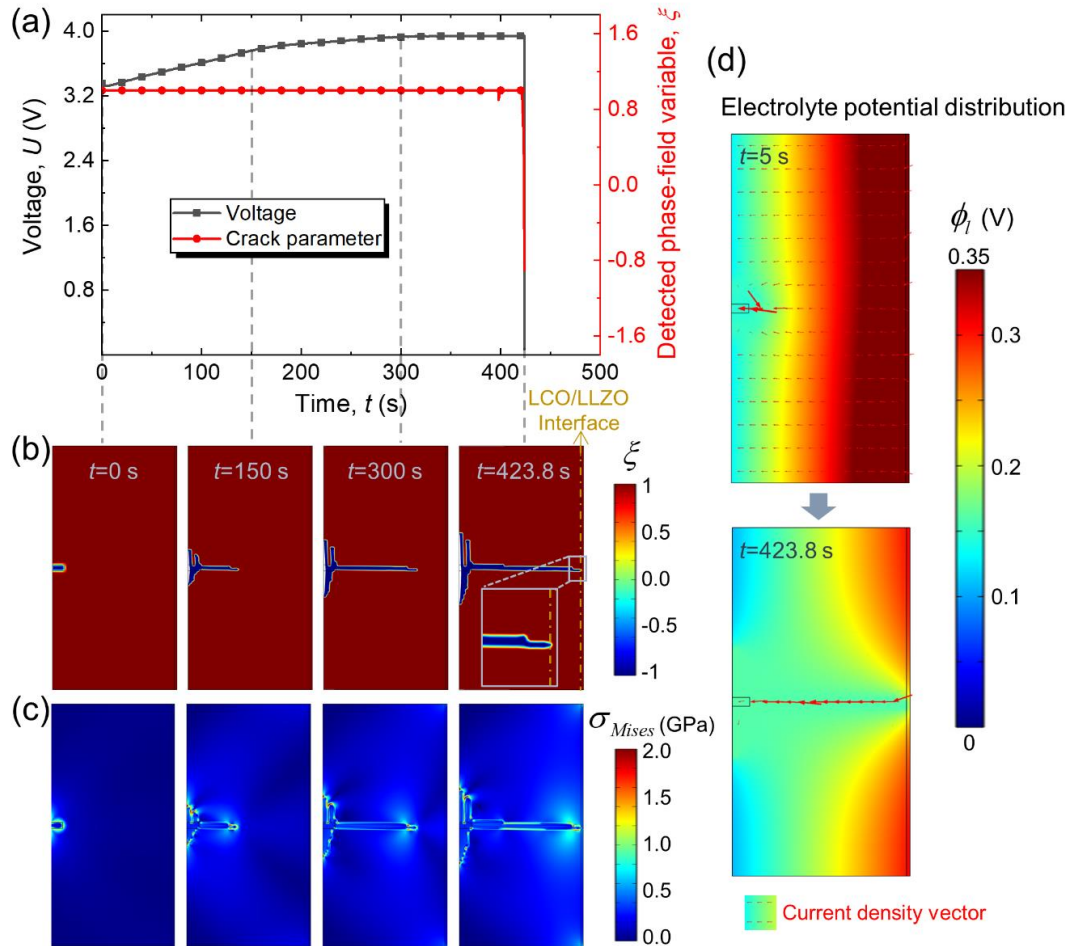


Figure 18 Representative computational results at 1C charging rate. (a) voltage response and detected phase-field variable ξ at the LCO/LLZO interface at 1C charging rate; (b) dendrite growth ξ evolution ($\xi = -1$ for dendrite/crack, $\xi = 1$ for intact solid electrolyte); (c) von Mises stress evolution σ_{Mises} ; (d) electrolyte potential distribution and current density vector (the thicker and longer arrow indicates larger current density) at the beginning and ending time.

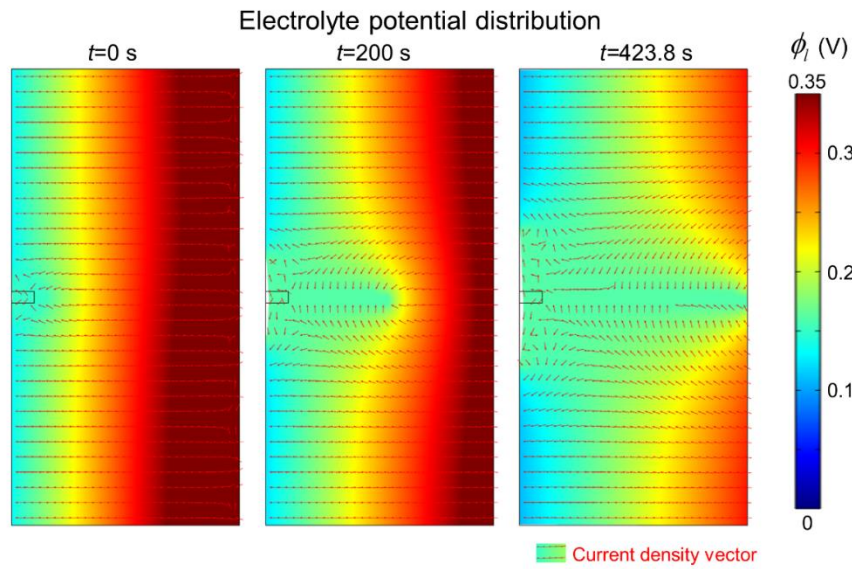


Figure 19 Representative results: electrolyte potential ϕ_l distribution and current density vector (the arrows indicate only the current direction and distribution, not the magnitude).

In the following discussion, representative simulation results are taken as the baseline, and the parametric study is carried out to understand the governing effects of stress, charging rate, Young's modulus σ_{LLZO} , and fracture toughness K_{LLZO} on crack propagation/dendrite growth in the SE and the electrochemical response of the battery.

3.2.2 Governing effect from overpotential-driven stress

During the charging process, there inevitably exists the overpotential η_- at the Li anode/electrolyte interface. The negative η_- will drive Li plating along the SE and the Li interface (Fig. 20(a)). Without the stress effect (i.e., Eq. (32) is disabled), there is no driving force for crack formation/propagation and dendrite growth, and thus no short circuit occurs. The average SE conductivity is kept constant, and the normal voltage profile during the charging process can be seen in Fig. 20(b). When the overpotential-driven stress is

considered, the stress may drive the dendrite growth and crack propagation. As long as the current density exists within the SE, there is a continuous driving force to the newly grown dendrite for further development (Fig. 20(a)).

At the beginning of charge (0~150 s), the battery voltage responses are close to each other, with and without taking stress into consideration, indicating Li plating behavior. After that, the discrepancy in voltages gradually appears and amplifies. The baseline voltage is much lower (Fig. 20(b)), caused by the conductivity change in the SE as a result of dendrite formation. As the dendrite grows, the effective electrolyte conductivity σ_{SE} evolves following the governing law described in Eq. (20). Since the electrical conductivity in the Li dendrite ($\sigma_{Li} = 1.1 \times 10^7$ S/m) is several orders of magnitude higher than the ionic conductivity of the LLZO electrolyte ($\sigma_{LLZO} = 4.43 \times 10^{-2}$ S/m), the dendrite growth significantly increases the effective electrolyte conductivity (Fig. 20(c)). Moreover, σ_{SE} significantly influences the current density distribution within the SE because the current density tends to concentrate at the high σ_{SE} region (Fig. 20(c)), leading to an obvious voltage discrepancy (Fig. 20(b)). At $t=423.8$ s, if the stress effect is enabled, the battery voltage abruptly drops, indicating that the Li dendrite finally reaches the cathode side and the short circuit is triggered (Fig. 21(a)). It is important to note that the voltage response with dendrite growth obviously deviates from normal battery voltage behavior, which inspires us to propose a possible method for the detection of crack and dendrite issues by monitoring the voltage-time curve for real-time battery health management.

The η_- -driven stress mainly distributes close to the dendrite/electrolyte interface, especially at the dendrite tip (Fig. 21(b)). According to Eq. (32), the generated stress is linearly related to the overpotential. Under a 1C charging rate, the stress tensor components σ_{ij} ($i, j = x, y$), and σ_{Mises} all reach the magnitude of GPa (Fig. 20(d)). Such large internal stress causes the strain energy density of 10^8 N/m^2 (Fig. 21(c)), providing a sufficient driving force for crack propagation. The continuous and direct propagation of the crack towards the cathode side (i.e., the transverse direction) is responsible for the internal short circuit. In the meantime, the crack propagates laterally as well, along with the anode/electrolyte interface in the block shape, mainly due to the free mechanical boundary condition for the left boundary and the relatively smaller σ_{xx} (Fig. 21(d)). Note that the Li dendrite soon fills the crack such that no break-apart of the SE is considered here. The stress at the dendrite tip is more concentrated, including σ_{ij} ($i, j = x, y$) and σ_{Mises} (Fig. 20(d)), and the stress component σ_{yy} is larger than σ_{xx} (Fig. 21(d)), which can elucidate the faster crack propagation speed in the transverse direction than in the lateral direction.

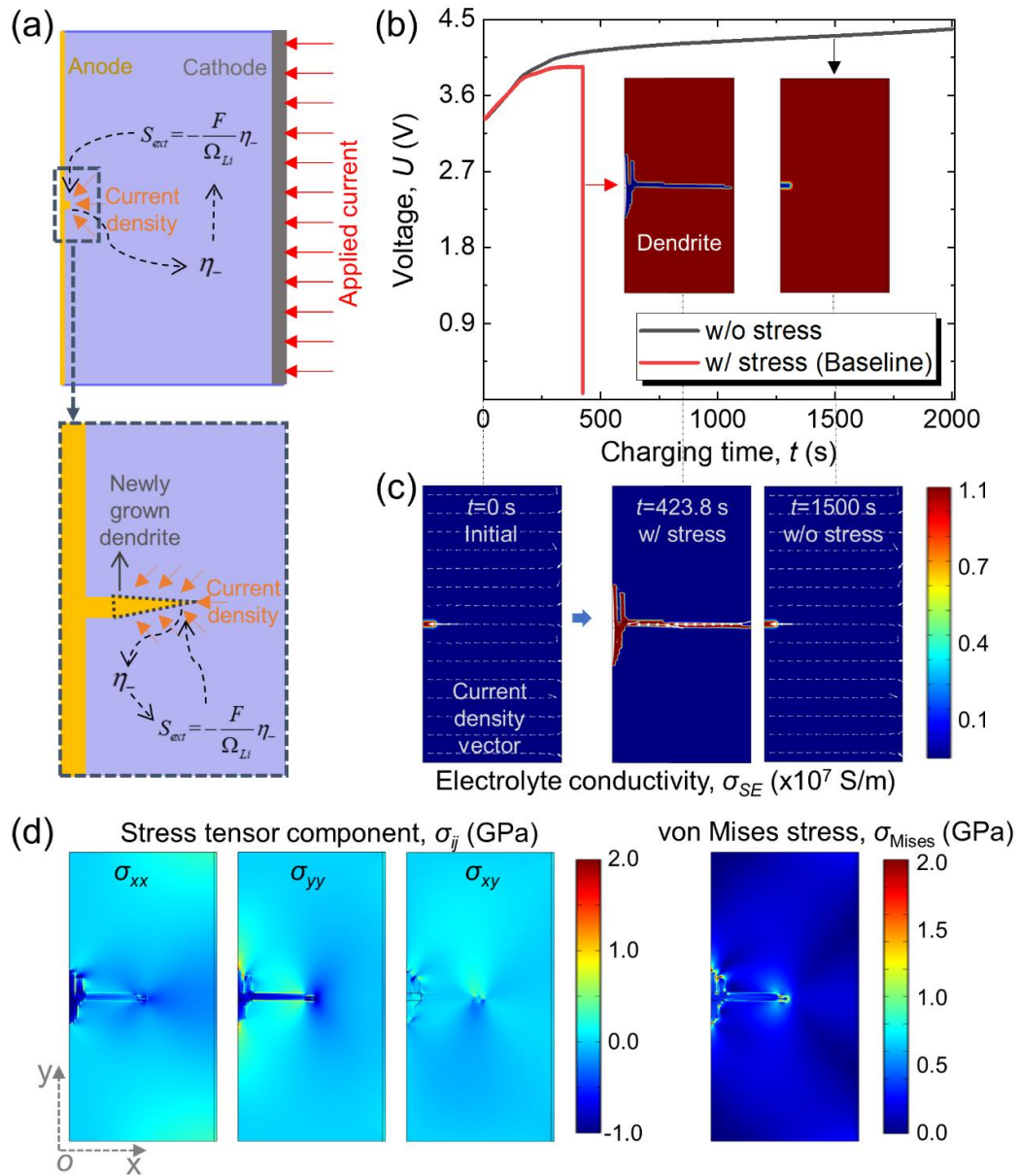


Figure 20 Effect of electrochemically induced stress at 1C charging rate. (a) schematics of the crack propagation/dendrite growth driven by the overpotential-induced stress; (b) voltage vs. time curves for models without and with the stress effect; (c) effective electrolyte conductivity σ_{SE} and current density vector (the thicker and longer arrow indicates larger current density); (d) stress tensor components σ_{xx} , σ_{yy} , σ_{zz} and von Mises stress σ_{Mises} at $t=200$ s.

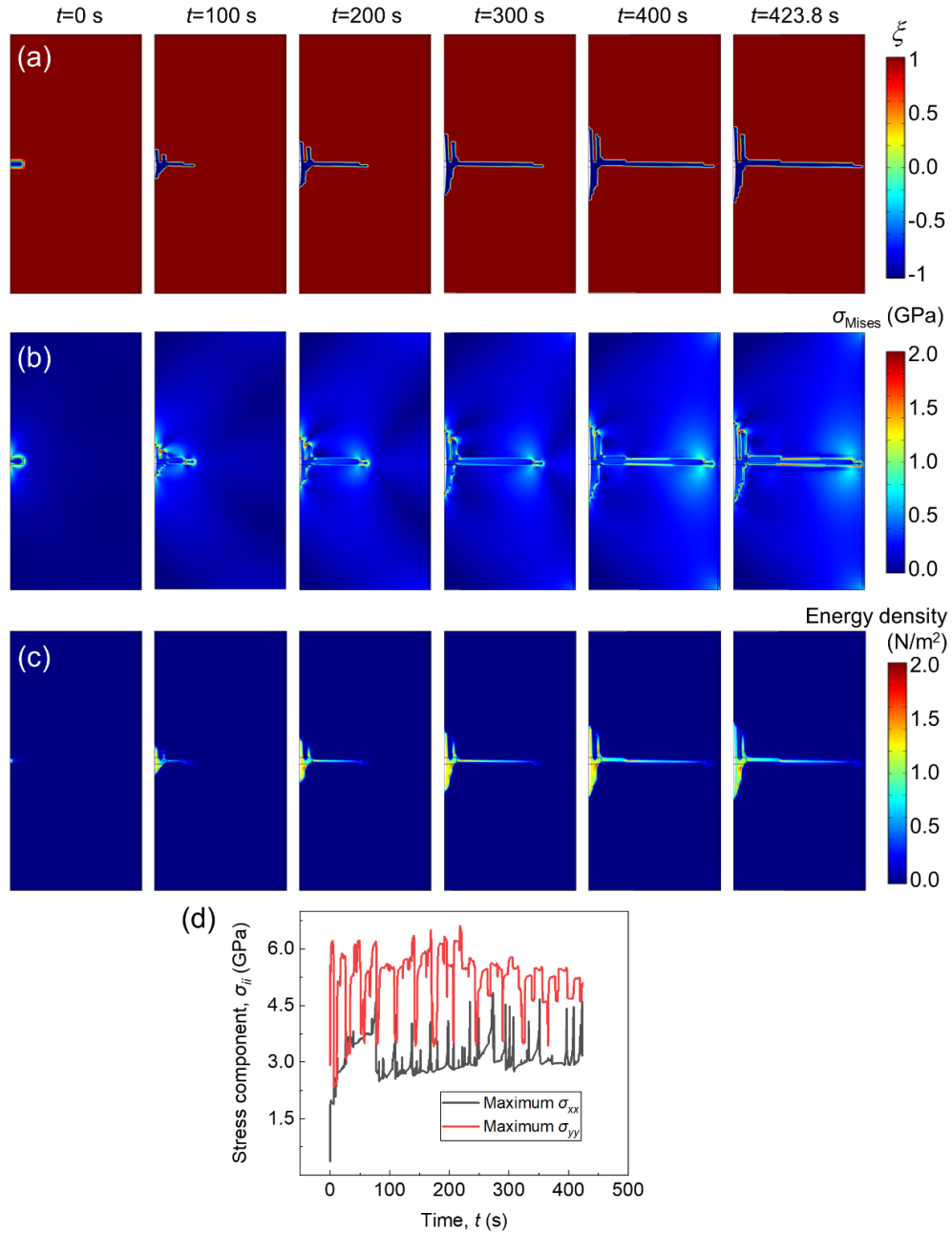


Figure 21 Effect of electrochemically induced stress. (a) dendrite ξ evolution considering the stress effect; (b) von Mises stress evolution σ_{Mises} considering the stress effect; (c) strain energy density considering the stress effect; (d) maximum stress components σ_{xx} and σ_{yy} within the solid electrolyte domain.

3.2.3 Governing effect from the charging rate

Since the current applied to the battery is determined by the charging rate (C-rate) and

the current density within the SE is affected as well to influence the overpotential value, the increased C-rate ultimately results in larger driving stress for faster crack propagation and dendrite growth (Fig. 22(a)). Thus, we investigate the C-rate effect on the crack and the electrochemical behavior considering the values of 0.1C, 0.25C, 0.5C, 1C, 1.5C, and 2C (i.e., current density values of 140, 350, 700, 1400, 2100, 2800 $\mu\text{A}/\text{cm}^2$, respectively).

The battery overpotentials increase with increasing charging rates. For a C-rate no greater than 0.25C, there is no short circuit during the entire charging process. However, once the C-rate exceeds 0.5C, an abrupt voltage drop (i.e., short circuit) is observed (Fig. 22(b)). The higher the charging rate, the less time it takes for a short circuit.

The dendrite growth behavior is also closely related to the C-rate. The Li plating mainly grows along the anode/electrolyte interface (y -axis in Fig. 22(c)) when the C-rate $\leq 0.25\text{C}$ because the left boundary is free, leading to energy-favorable crack growth. For the C-rate $\geq 0.5\text{C}$, the dendrite grows transversely (along the x -axis) to the cathode in a more slender shape (Fig. 22(c)). Moreover, at the short-circuit time, the dendrite grows more in the y -axis at higher C-rates, since the stress tensor components σ_{ij} ($i, j = x, y$) and von Mises stress σ_{Mises} increase with C-rate, and are also large enough under a high C-rate to drive the dendrite propagating in the y -axis (Fig. 23(a)). The fundamental reason for the larger stress is the larger electrochemical overpotential η_- at a higher C-rate; η_- almost remains the same for each C-rate (Fig. 23(b)). The distribution of electrolyte potential ϕ_l for different C-rates at $t=200$ s (Fig. 22(d)) shows that a large C-rate significantly increases

the ϕ_l at the Li/LLZO interface, i.e., from ~ 0.04 V under 0.1C to ~ 0.25 V at 2C, which further validates the large overpotential induced by the high C-rate. Based on η_- and the short-circuit time t_{short} , we establish a safety guidance map for dendrite-induced short circuits (Fig. 22(e)), where the safety region indicates that no short circuit occurs during the whole charging process if the C-rate < 0.25 C and $\eta_- > -0.10$ V.

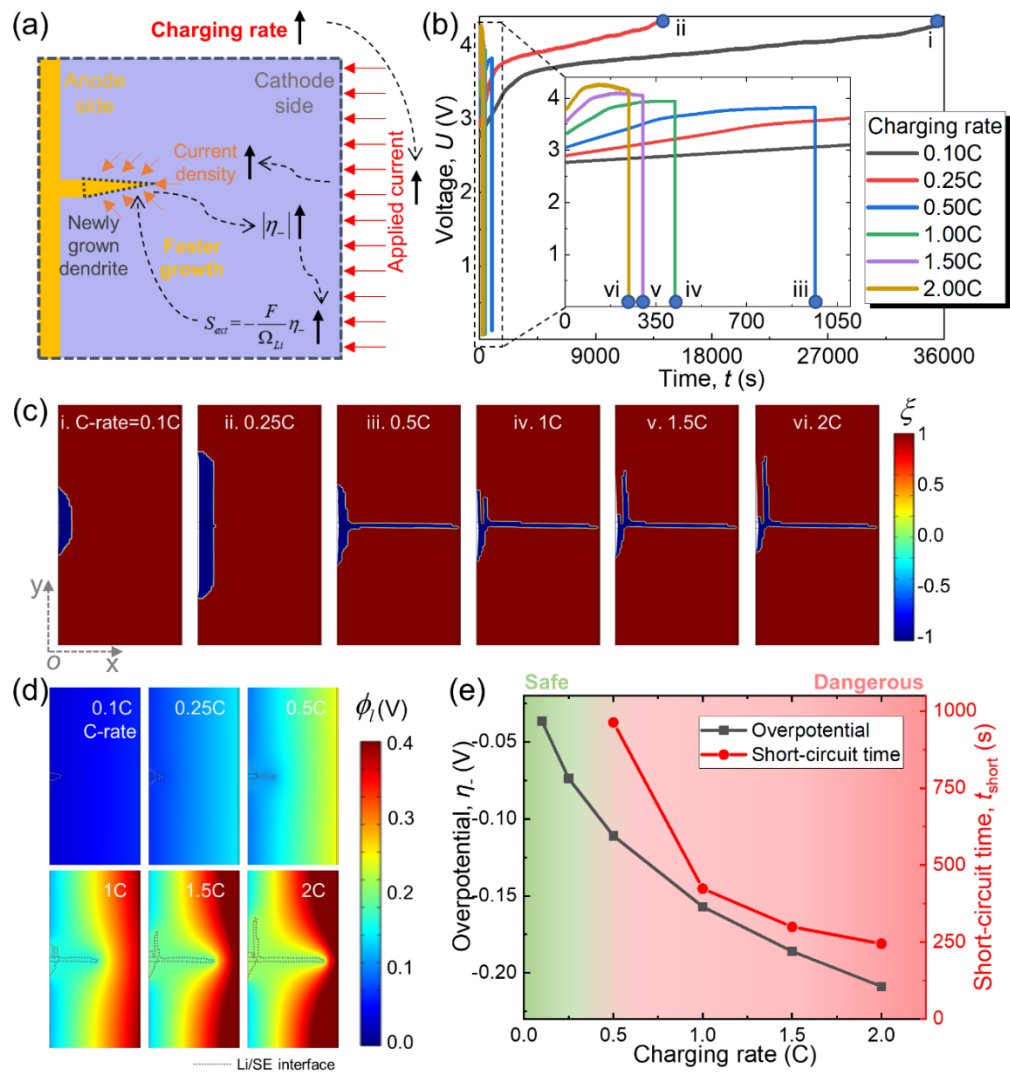


Figure 22 Effect of charging rate. (a) schematics of the charging-rate effect on dendrite growth; (b) voltage vs. time curves; (c) contour plots of phase-field parameter ξ ; (d) electrolyte potential ϕ_l distribution at $t=200$ s; (e) safety guidance map based on overpotential η_- /short-circuit time t_{short} .

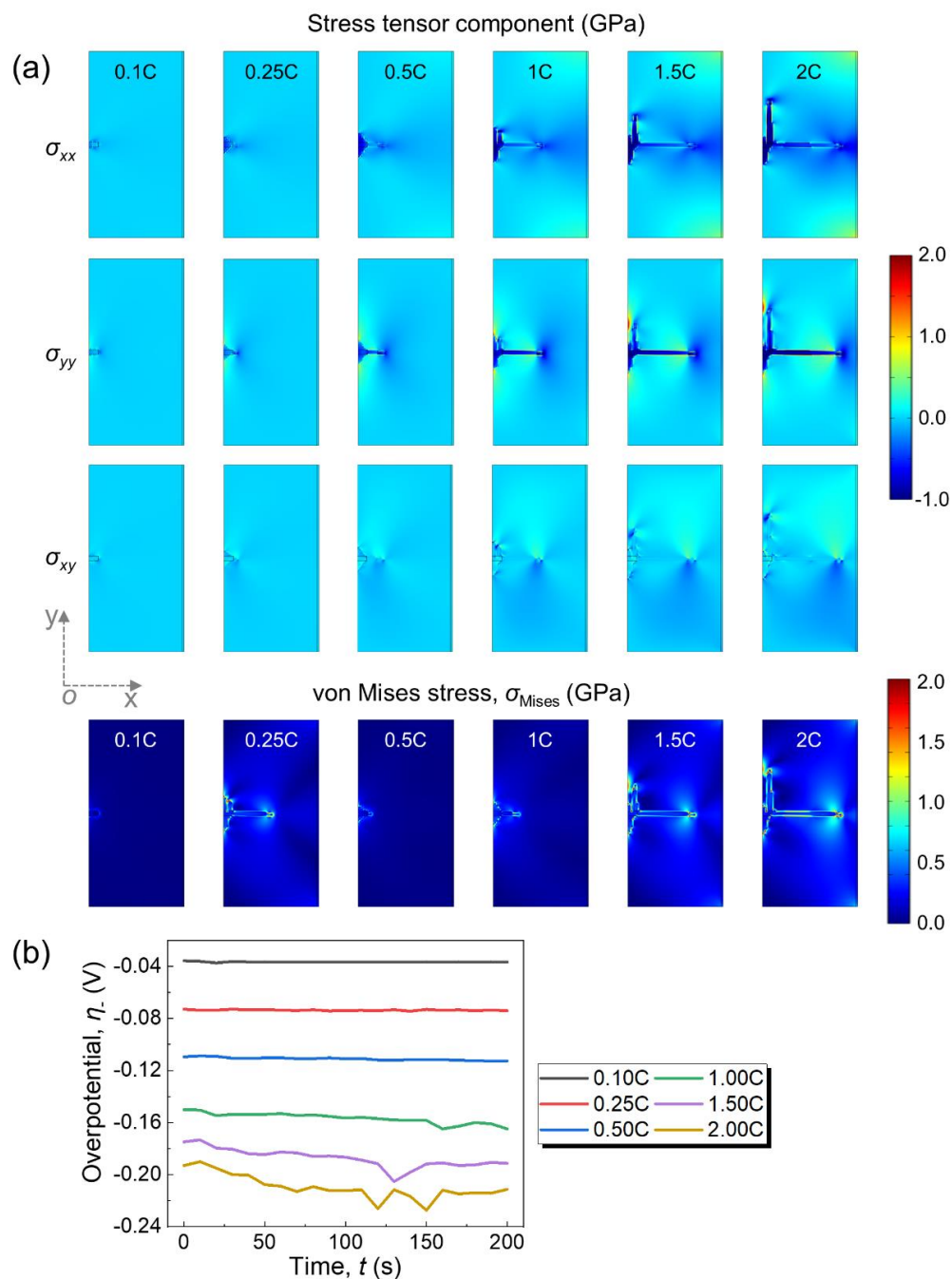


Figure 23 Effect of charging rate. (a) stress tensor components σ_{xx} , σ_{yy} , σ_{zz} , and von Mises stress σ_{Mises} for different C-rates at $t=200$ s; (b) overpotential vs. time curves during 0~200 s.

3.2.4 Governing effect from the electrolyte conductivity

Improving the electrolyte conductivity is one of the major means of improving the

electrochemical behaviors of the ASSB. Here, the LLZO electrolyte conductivity σ_{LLZO} effect on the crack and the electrochemical response is explored. Based on the baseline model, we consider the scenarios of 2.215×10^{-2} S/m, 4.43×10^{-2} S/m, 4.43×10^{-1} S/m, and 4.43 S/m.

Since the electrolyte conductivity directly influences the internal resistance, the electrochemical response of the battery is expected to change. The voltage of the battery during charging is higher under lower σ_{LLZO} (Fig. 24(a)), because a smaller σ_{LLZO} leads to larger battery internal resistance, which indicates that under the same current density (1C is used for all cases here), a higher voltage will be observed. A lower σ_{LLZO} corresponds to an earlier short-circuit time, i.e., $t=374.4$ s, 423.8 s, 553.5 s, and 601 s for $\sigma_{\text{LLZO}} = 2.215 \times 10^{-2}$ S/m, 4.43×10^{-2} S/m, 4.43×10^{-1} S/m, and 4.43 S/m, respectively (Fig. 24(a)). The x -axis crack propagation is dominant, and the crack morphology is similar at different σ_{LLZO} values (Fig. 24(b)). The only slight difference is that there is a slim crack in the y -direction under small σ_{LLZO} (i.e., 2.215×10^{-2} S/m and 4.43×10^{-2} S/m).

σ_{LLZO} mainly influences the electrolyte potential ϕ_l , which directly determines the overpotential η_- . Since the electrolyte with smaller σ_{LLZO} bears higher voltage, the electrolyte potential ϕ_l is larger under the same applied current density, resulting in a higher absolute value of η_- , i.e., at $t=360$ s, $\eta_- = -0.17$ V, -0.162 V, -0.14 V, and -0.135 V for $\sigma_{\text{LLZO}} = 2.215 \times 10^{-2}$ S/m, 4.43×10^{-2} S/m, 4.43×10^{-1} S/m, and 4.43 S/m,

respectively (Fig. 25(a)). The higher η_- drives larger stress; moreover, both the maximum von Mises stress $\sigma_{\text{Mises_max}}$ and the average von Mises stress $\sigma_{\text{Mises_ave}}$ increase with decreasing σ_{LLZO} (Fig. 25(b)), resulting in the correspondingly greater strain energy density. The evolution of the phase-field parameter ξ is driven by the elastic strain energy (Eqs. (42-44)). Thus, the dendrites grow faster under smaller σ_{LLZO} . The above discussion demonstrates that increasing the electrolyte conductivity can not only improve the battery electrochemical performance with a reduced internal resistance, but suppress crack propagation as well.

The dendrite preferentially grows laterally in the y direction under a low C-rate ($<0.5C$) and a high σ_{LLZO} ($>4.43 \times 10^{-1}$ S/m) due to the free left boundary and the smaller driving force; thus, no short circuit occurs (Region 1 in Fig. 24(c-d)). Increasing the C-rate or decreasing σ_{LLZO} both give rise to greater $|\eta_-|$ (absolute value of η_-), which causes a stronger driving force for the crack and dendrite, resulting in an earlier short circuit (Regions 2-3 in Fig. 24(c-d)). An abrupt change of $|\eta_-|$ between Region 2 and Region 3 can be clearly observed in Fig. 24(c). The critical $|\eta_-|$ value at the boundary of Region 2 and Region 3 is about 0.16 V. $|\eta_-|$ is greater than the critical value with C-rate >1 C and $\sigma_{\text{LLZO}} < 4.43 \times 10^{-2}$ S/m, corresponding to the earlier short circuit scenarios. From Fig. 24(d), there exists a specific threshold C-rate (namely, critical current density) value under a certain electrolyte conductivity. At 0.25C or below, there is no short circuit for σ_{LLZO} from 2.215×10^{-2} S/m to 4.43 S/m. Increasing σ_{LLZO} can reduce $|\eta_-|$ and avoid a short

circuit for 0.5C, but if the C-rate > 0.5C, $|\eta_-|$ is still large (>0.1V) and the dendrite growth-induced short circuit is only delayed but not completely prevented. By contrast, the C-rate is in the dominant position in terms of controlling the $|\eta_-|$ and avoiding a short circuit.

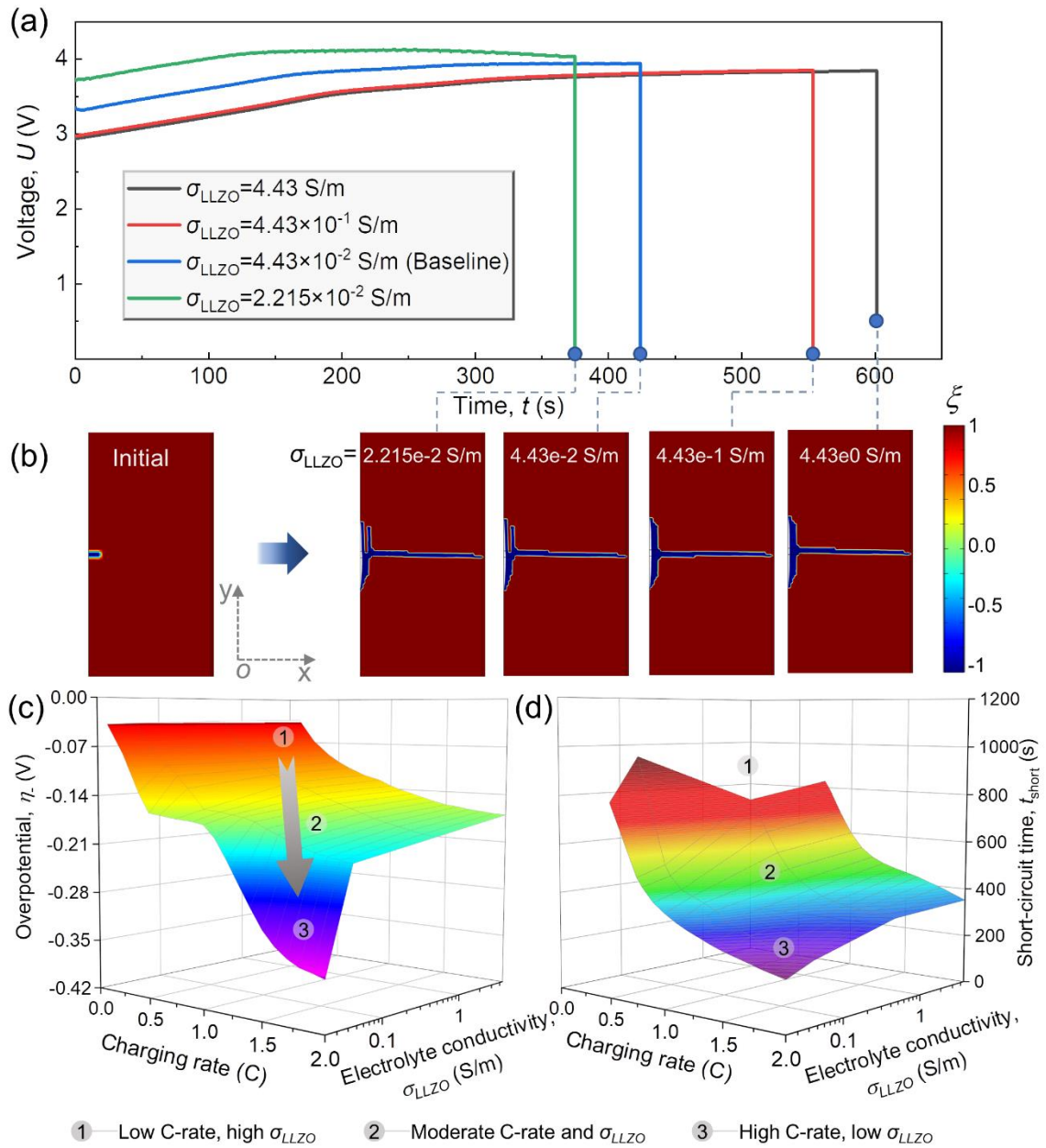


Figure 24 Effect of electrolyte conductivity. (a) voltage vs. time curves; (b) contour plots of crack parameter ξ at short-circuit point; coupled effect of charging rate and electrolyte conductivity σ_{LLZO} on the (c) overpotential η_- and (d) short-circuit time t_{short} .

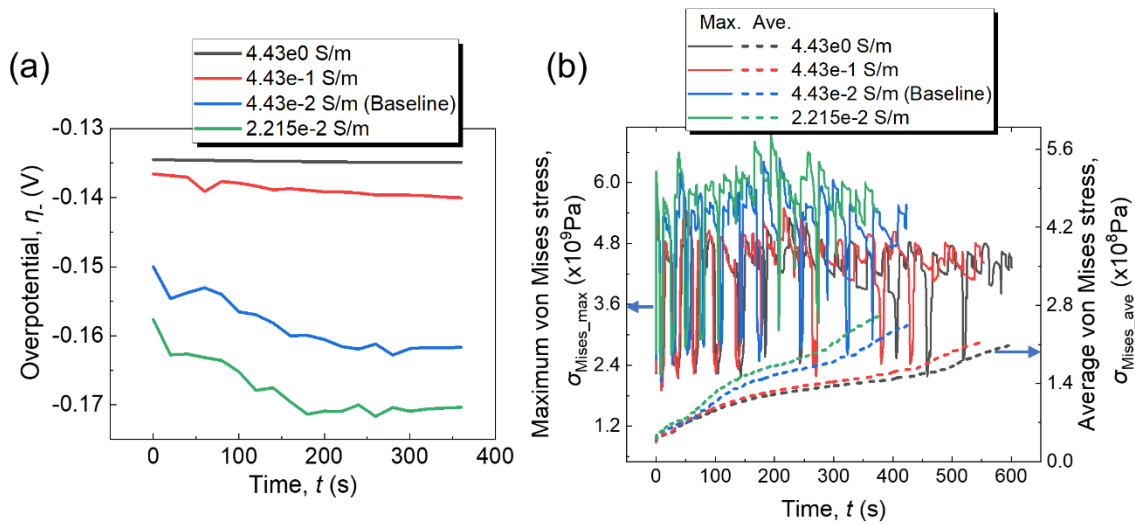


Figure 25 Effect of electrolyte conductivity. (a) overpotential η_- vs. time curves during 0~360 s; (b) maximum von Mises stress $\sigma_{\text{Mises_max}}$ and average von Mises stress $\sigma_{\text{Mises_ave}}$.

3.2.5 Governing effect from Young's modulus

In general, a solid electrolyte with a larger Young's modulus is more resistive to deformation. The inherent nature of how an LLZO electrolyte's Young's modulus E_{LLZO} affects the crack propagation and dendrite growth will be investigated here. Based on the baseline model, we select different E_{LLZO} , i.e., 15 GPa, 50 GPa, 100 GPa, 150 GPa, and 200 GPa.

According to modeling results, the crack grows only along the Li/LLZO interface for a 15 GPa LLZO SE, shown in Fig. 26(a), and no short circuit is observed while the crack growths are along the x axis when $E_{\text{LLZO}}=50$ GPa or above. The short circuits are triggered in all these cases, and the short-circuit triggering time t_{short} decreases with increasing E_{LLZO} if $E_{\text{LLZO}} < 100$ GPa, while t_{short} increases with E_{LLZO} above 100 GPa (Fig. 26(b)); t_{short} is directly related to the transverse dendrite growth. For $E_{\text{LLZO}} \geq 100$ GPa, the farthest dendrite

growth distance x is larger for smaller E_{LLZO} , while the dendrite growth speed for 50 GPa is much lower when approaching the fixed cathode side (Fig. 26(c)), which may explain its longer t_{short} . The low speed at the final stage for 50 GPa is caused by the relatively high fracture energy (Fig. 26(d)).

The crack propagation is described from the energy perspective, and E_{LLZO} will significantly influence both the driving force (the elastic strain energy) as well as the fracture threshold energy (the fracture energy G) in a competing way. Thus, E_{LLZO} will influence the crack propagation and corresponding dendrite growth as well as the short-circuit behavior. The maximum/average von Mises stress increases with E_{LLZO} (Fig. 27), while the average elastic strain energy density E_{ave} increases with $E_{\text{LLZO}} \leq 50$ GPa but decreases with increasing $E_{\text{LLZO}} > 50$ GPa (Fig. 26(d)), which reflects the trends of the driving force. The resistive force G decreases with increasing E_{LLZO} in the whole range (Fig. 26(d)). For $E_{\text{LLZO}} < 40$ GPa, both the maximum and average strain energy density are much smaller (Fig. 27(b)), and the fracture energy is much higher to resist any crack (Fig. 26(d)), demonstrating that $E_{\text{LLZO}} < 40$ GPa produces lower driving force and higher resistance for dendrite growth/crack propagation. As a result, the dendrite induced short circuit is delayed or even prevented at the C-rate of 1 C ($1400 \mu\text{A}/\text{cm}^2$) with $E_{\text{LLZO}} < 40$ GPa, namely the low short-circuit risk, which provides insight for the designing of inorganic solid electrolyte. For $40 \text{ GPa} < E_{\text{LLZO}} < 100$ GPa, E_{ave} maintains at a high level, while G decreases dramatically. Thus, the crack propagates faster, and the short circuit risk

is high as well. For $E_{LLZO} > 100$ GPa, both E_{ave} and G decrease, and the short-circuit time is delayed, which is at a medium risk level (Fig. 26(b)).

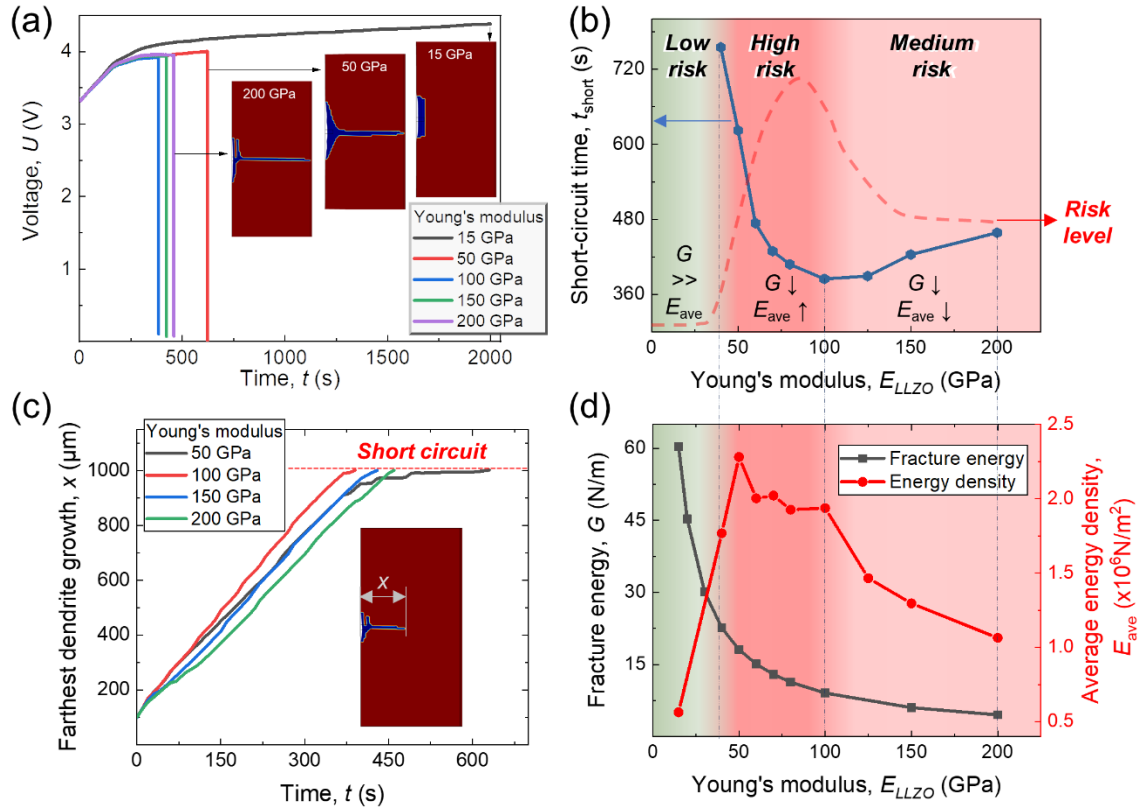


Figure 26 Effect of Young's modulus. (a) voltage vs. time curves for different E_{LLZO} ; (b) short-circuit time for different E_{LLZO} ; (c) farthest dendrite growth x in the transverse direction; (d) fracture energy G and average energy density E_{ave} at $t=250$ s as a function of E_{LLZO} .

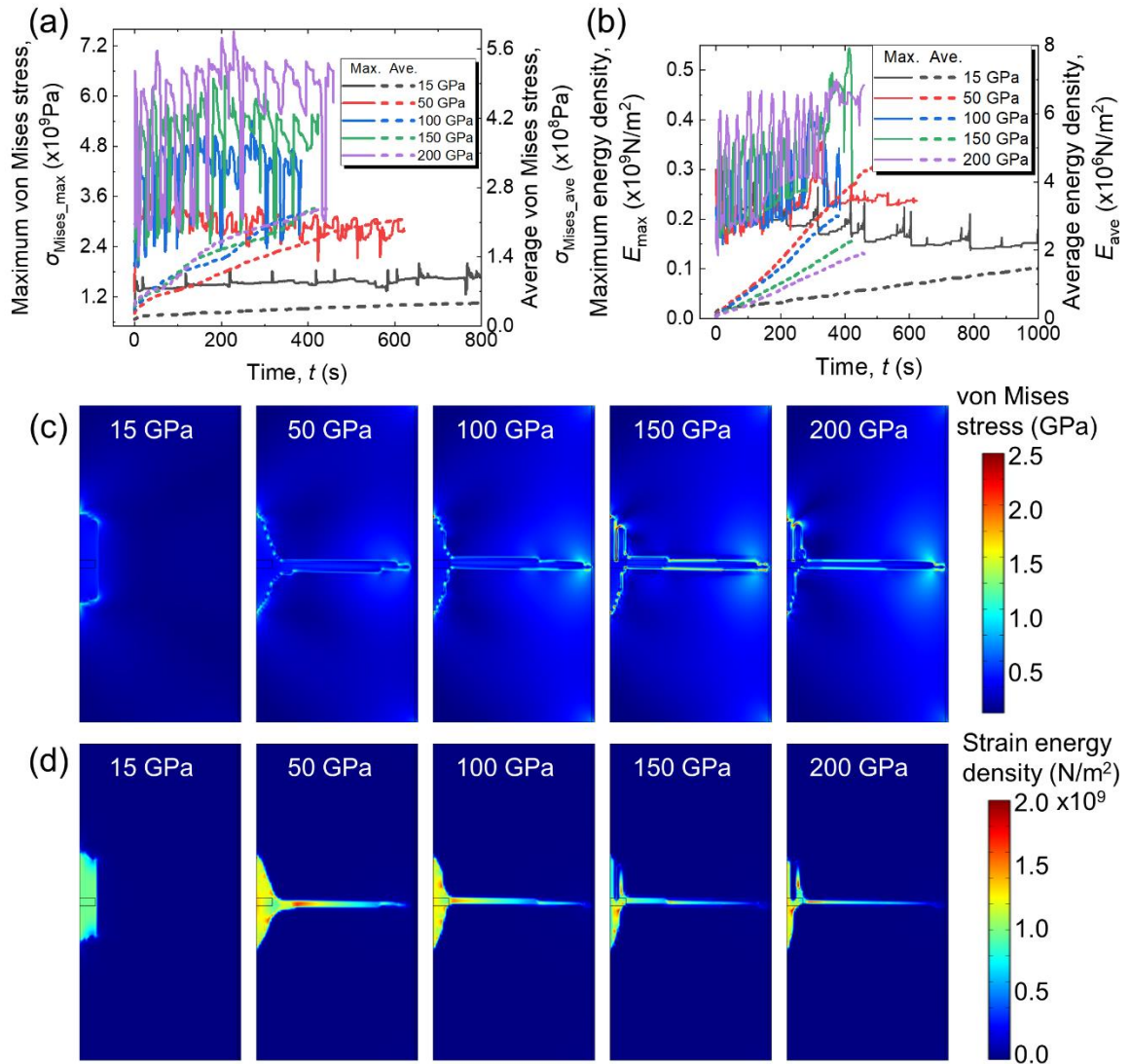


Figure 27 Effect of Young's modulus. (a) maximum von Mises stress $\sigma_{\text{Mises_max}}$ and average von Mises stress $\sigma_{\text{Mises_ave}}$; (b) maximum strain energy density E_{max} and average strain energy density E_{ave} ; (c) von Mises stress σ_{Mises} , and (d) strain energy density E at short-circuit time.

3.2.6 Governing effect from fracture toughness

The fracture toughness of an LLZO electrolyte K_{LLZO} represents LLZO's capability to resist fracture. Based on the baseline model, different K_{LLZO} values are selected to study the fracture toughness effect, i.e., 0.77, 0.98, 1.24, 1.41, and 1.58 $\text{MPa}\sqrt{\text{m}}$. All other

governing factors, i.e., the C-rate (1C), Young's modulus (150 GPa), and pre-defect area, remain the same.

K_{LLZO} only affects the fracture energy. A larger K_{LLZO} represents a higher resistive force to form a crack, resulting in a smaller crack area, which can delay the short-circuit time. For instance, the short-circuit time increases from $t=420.3$ s to $t=621.1$ s when K_{LLZO} increases from $K_{LLZO} = 0.77 \text{ MPa}\sqrt{\text{m}}$ to $1.41 \text{ MPa}\sqrt{\text{m}}$, and may even prevent the short circuit in some extreme cases, e.g., when $K_{LLZO} = 1.58 \text{ MPa}\sqrt{\text{m}}$ (Fig. 28(a-b)). Since the crack propagation speed is faster under smaller K_{LLZO} , the dendrite is more prone to penetrate the electrolyte, resulting in an earlier short circuit. Under smaller K_{LLZO} , the crack will also propagate laterally ($K_{LLZO} = 0.77 \text{ MPa}\sqrt{\text{m}}$ in Fig. 28(b)). Straightforwardly, increasing K_{LLZO} can effectively hinder the crack propagation and delay the short-circuit time; if K_{LLZO} is large enough, the crack can even be prevented.

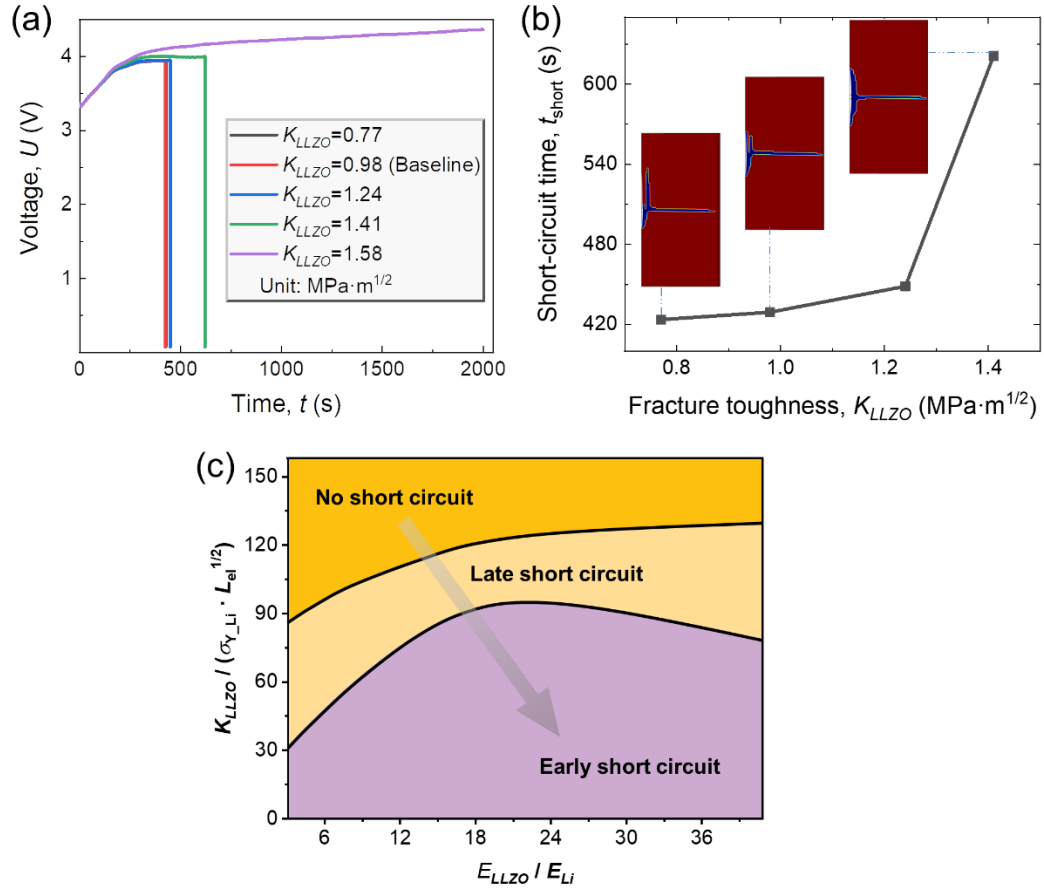


Figure 28 Effect of fracture toughness: (a) voltage vs. time curves; (b) short-circuit time t_{short} as a function of fracture toughness K_{LLZO} ; (c) design map based on the coupled effect of normalized Young's modulus and normalized fracture toughness.

Crack propagation and dendrite growth are responsible for the short circuit. To quantitatively unlock the mechanistic relationship among E_{LLZO} , K_{LLZO} , and t ($t = \infty$ stands for no short circuit), we establish a mechanism map (Fig. 28(c)) with three regions: no short circuit, late short circuit, and early short circuit by using the governing variables of E_{LLZO}/E_{Li} and $K_{LLZO}/\left(\sigma_{Y_Li} \cdot L_{el}^{1/2}\right)$. The early short circuit covers a large part of the domain, leaving a relatively small portion of the design space. That is why we have witnessed the failure of ASSBs during operation. Generally, larger $K_{LLZO}/\left(\sigma_{Y_Li} \cdot L_{el}^{1/2}\right)$

leads to higher safety performance, while E_{LLZO}/E_{Li} needs to avoid a certain domain to obtain a larger design space. This straightforward relationship reveals a much boarder design view for the SE in terms of several key mechanical properties with enhanced and optimized safety and cyclability behaviors by mitigating the short-circuit behavior with the desired Young's modulus and fracture toughness.

3.2.7 Implication on engineering application

Plenty of efforts have been attempted to address the scientific and engineering problem: how to realize the applicable all-solid-state battery with appropriate solid electrolyte and at practical current density. The governing effects of stress, charging rate, electrolyte conductivity σ_{LLZO} , Young's modulus E_{LLZO} , and fracture toughness K_{LLZO} have been comprehensively investigated above, which provide the basic guidance for the development of solid electrolyte and battery management. Based on the findings in this study, we provide insights towards more robust ASSBs in engineering.

The perfect Li/SE interface without any defect has proven to prevent the dendrite initiation and growth (Fig. 17(b)), implying that improvement of Li/SE interfacial property is an effective way to suppress dendrite. However there is inevitable interfacial defect for current inorganic solid electrolyte. One of the main limitations for ASSBs is the critical current density, above which the battery will be short-circuited due to the dendrite growth in solid electrolyte. To make a practical current density for ASSBs, such as 2 mA/cm^2 (i.e., 1.5 C in this study, at which dendrite grows to short circuit the battery (Fig. 22)), both the

electrochemical and mechanical properties of the battery can be considered to reduce the driving force and increase the opposing force for dendrite growth/crack propagation. The driving force mainly stems from the overpotential $|\eta_-|$ related strain energy density (lower $|\eta_-|$ corresponds smaller driving force), and the opposing force comes from the fracture energy.

At the practical current density (1.5 C), increasing σ_{LLZO} from 2.215×10^{-2} S/m to 4.43 S/m can reduce the $|\eta_-|$ from 0.3 V to 0.16 V, while the reduced $|\eta_-| = 0.16$ V is still large enough to cause the dendrite growth- and crack propagation-induced short circuit (Fig. 24(c-d), t_{short} is increased from 263 s to 445 s), which shows that increasing σ_{LLZO} can only delay (but not completely inhibit) the occurrence of short circuit at 1.5 C. In addition to improve electrochemical property, the mechanical properties should also be considered. As indicated in Fig. 26(b), E_{LLZO} below 40 GPa corresponds to the low-risk region with lower strain energy density (driving force) and higher fracture energy (resisting capability), conducive to suppress the dendrite growth. The computational results demonstrate that E_{LLZO} within the low risk region only postpones short circuit at the charging rate of 1.5 C (i.e., t_{short} is delayed from 445 s at 150 GPa to 674 s at 40 GPa). To completely inhibit the dendrite growth induced short circuit, we need to consider the improvement of K_{LLZO} . When K_{LLZO} increases from 0.98 to 1.73 $\text{MPa}\sqrt{\text{m}}$, the dendrite growth is in block shape along y -axis rather than the long strip shape in x -axis (Fig. 29), such that the dendrite induced short circuit is prevented.

Such computation results show a promising direction towards realizing applicable ASSBs with inorganic solid electrolyte after modulation of electrolyte conductivity ($\sim 10^{-1}$ S/m), Young's modulus (< 50 GPa) and fracture toughness ($> 1.7 \text{ MPa}\sqrt{\text{m}}$).

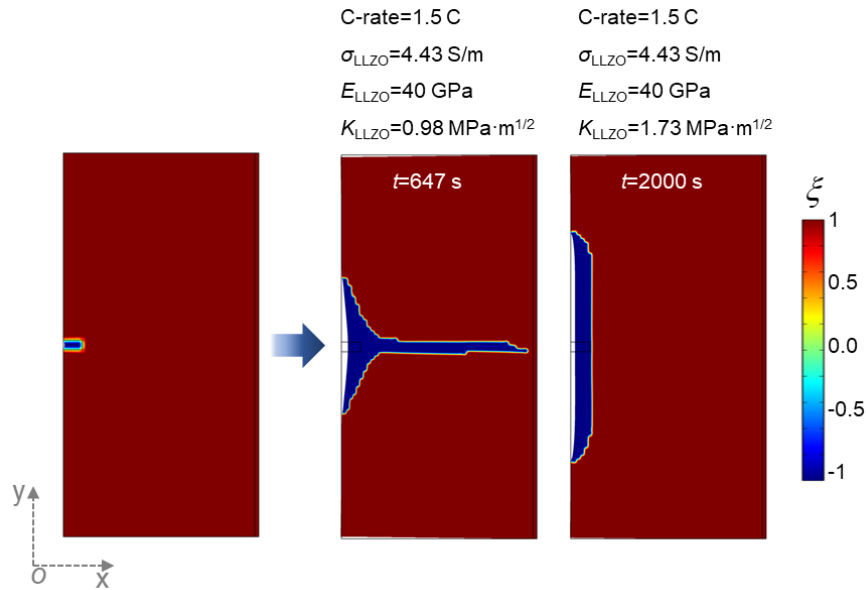


Figure 29 Dendrite ξ evolution at the practical current density $2100 \mu\text{A}/\text{cm}^2$ (i.e., 1.5 C in this study) considering different electrolyte fracture toughness.

3.3 Conclusions

Dendrite growth- and interfacial issues-induced battery failure and poor cyclability are the two main problems hindering the further commercialization of ASSBs. To understand the dendrite growth and crack propagation behavior during battery charging/discharging, considering the interfacial defect, we developed a fully coupled electrochemical-mechanical model, including the battery model, mechanical model, phase-field model, and short-circuit model. After validation, the effects of electrochemically generated stress, charging rate, electrolyte properties (including conductivity, Young's

modulus, and fracture toughness) are comprehensively investigated. When the electrochemically driven stress is considered, there is crack propagation in the SE, and the battery voltage response is different. Eventually, the short circuit is triggered due to dendrite penetration through the SE. We have reached the following conclusions:

- The short circuit occurs earlier with higher C-rate (i.e., C-rate exceeds 0.5C) due to the larger overpotential $|\eta_-|$ -driven crack propagation and dendrite growth.
- The overpotential $|\eta_-|$ increases with decreasing electrolyte conductivity, resulting in an earlier short circuit.
- Increasing σ_{LLZO} can reduce the internal resistance to improve the battery electrochemical performance, as well as lower the crack propagation speed (delaying the internal short-circuit time).
- The Young's modulus E_{LLZO} affects both the competing mechanism serving as a driving force (strain energy density) and the resistance (fracture energy) for the crack. E_{LLZO} within 40~100 GPa accelerates the crack propagation, causing a high short-circuit risk.
- A larger electrolyte fracture toughness K_{LLZO} can suppress or even stop the crack propagation, significantly reducing the internal short circuit risk.

It is reported that the constitutive behavior of the Li metal would be linear elastic first and after it reaches a yield point, the plasticity starts, and the general profile of the plasticity is a plastic flow in general¹¹⁷. The majority of the literature reported the yield

stress magnitude is in the order of 10^1 MPa~ 10^2 MPa with Young's modulus from 2 GPa~20GPa^{79,80}. From our simulation, we may clearly see that when we use $E=4.9$ GPa,

the stress required to drive the crack propagation in our paper can be calculated as

$$\sigma \geq \frac{K_{LLZO}}{\gamma\sqrt{\pi a}} \approx 49 \text{ MPa} \quad ^{65},$$

mainly falls within the linear elastic region. Note that during the contact between Li dendrite and the pristine SE, our linear elastic description of the Li metal model may over predict the crack propagate slightly while during the Li dendrite growing stage, such simplification for Li dendrite has no effects on the results. The domains of lithium dendrite and solid electrolyte are evolving and changing in phase-field methodology, posing great challenges and limitations in defining the complicated mechanical property of the moving area and the interfacial area in the phase field model. In the meantime, the focus of this study is on the interfacial-defect-induced dendrite growth during charging/discharging in cell scale, and the influence of electronic conductivity mainly reflected in micro-scale is not included in the current study. Future work would be considered to solve these limitations. The established physics-based modeling framework unravels the physics-based mechanisms of the crack propagation, dendrite growth, and electrochemical behavior of the ASSBs during charging/discharging. In the meantime, the mechanism map offers critical guidance for the design, evaluation, and improvement of next-generation robust ASSBs.

CHAPTER 4 MITIGATION STRATEGY OF DENDRITE GROWTH

In this chapter, inspired by the nacre-like “brick-and-mortar” structure, I propose the strategy of embedding heterogeneous blocks (HBs) into the solid electrolyte to reduce the short-circuit risk induced by dendrite growth through taking the advantage of mechanical mismatch. To understand the fundamental mechanism, we assume the main body of the electrolyte is LLZO with high conductivity to guarantee low cell resistance, and the HBs are LLZO with enhanced mechanical properties. The governing factors to control the dendrite mitigation effect are comprehensively investigated to provide insights and guidance on the design of dendrite-suppression electrolytes of ASSBs.

4.1 Methodology

The multiphysics model used here is developed to include a) the battery model to describe the electrochemical phenomena; b) mechanical model to calculate the overpotential-induced stress σ fields; c) phase-field model to solve the evolution of dendrite growth and crack propagation (phase-field order parameter $\xi = 1$ for intact SE region, $\xi = -1$ for crack/dendrite region); and d) short-circuit model to detect the triggering of dendrite growth-induced short circuit. These four sub-models are interconnected by transferring relevant physical variables, described by the governing equations (Table 4 in Appendix B). More details of the modeling can be referred to Chapter 3.

The lithium and LiCoO_2 are used as the anode and cathode, respectively (Fig. 30(a))¹¹⁸. The promising LLZO solid electrolyte with high Young’s modulus $E_{\text{LLZO}}=150$ GPa and ionic conductivity $\kappa_{\text{HB}}=0.443$ mS/cm is set as the main body of the electrolyte in this study.

Note that due to the high hydrostatic stress developed within the vicinity of the tip of Li dendrite (Fig. 36), the plasticity of Li material is not considered here. The geometry is simplified as a 2D plane to improve the computational efficiency (Fig. 30(b)). For the dendrite growth simulation (without any heterogeneous blocks) in this study, the model is validated in three ways: 1) the cell voltage response during charging/discharging agrees with the experiment results¹⁴; 2) the predicted critical current density, *i.e.*, threshold value of applied current density to drive dendrite growth is comparable to reported values^{14,60,77}; 3) the simulation morphology of dendrite penetration and its coupled crack propagation is similar to the observations of transverse cracking with minimal branching in the experiment^{40,41,50,66,67}. The current density adopted in this study of 1.918 mA/cm² mimics current densities used in practical ASSBs. Note that the Li dendrite initiation mechanisms, *e.g.*, Li plating and nucleation, are not the focus of this paper. Thus, we pre-define an initial defect with length 4 μm and width 2 μm to initiate dendrite growth. We also confirm that the initial geometry of the defect does not influence the Li dendrite growth (Figure 31). An HB with length L_{HB} and width $W_{HB}=2.5$ μm are selected to demonstrate the representative result. The electrolyte and HBs are assumed to be homogeneous without voids; thus, the effect of the internal void is not considered in this study.

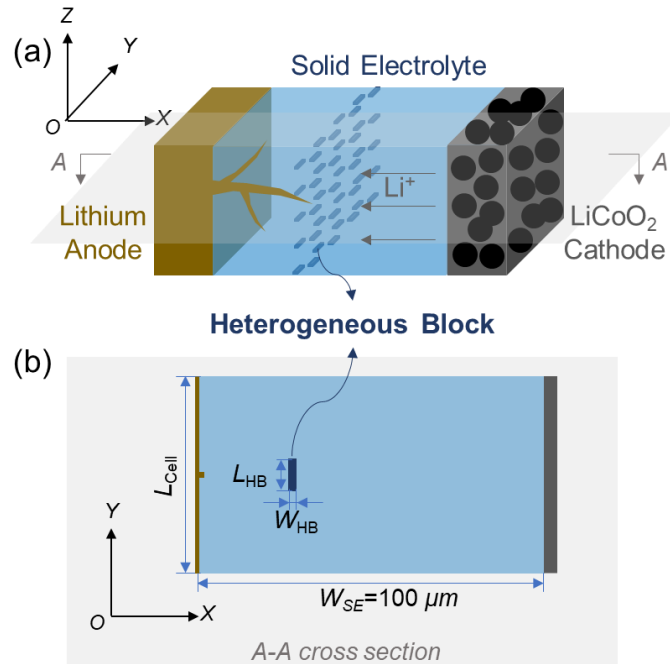


Figure 30 Illustration of the strategy of adding heterogeneous blocks into ASSBs: (a) schematic of 3-D battery structure, (b) simplified 2-D battery model.

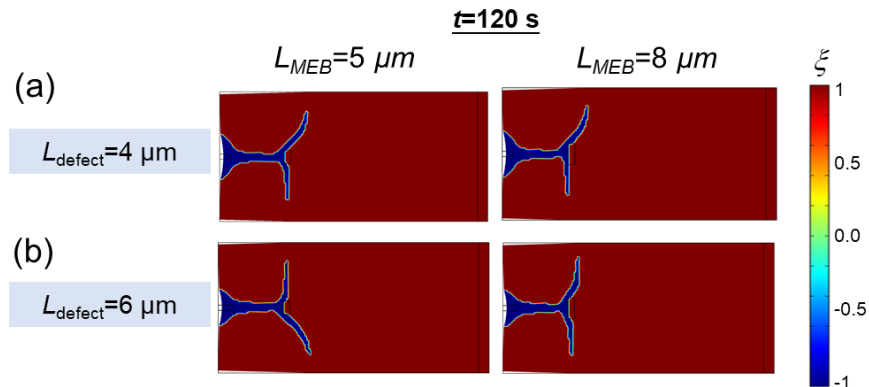


Figure 31 Effect of initial defect length on dendrite mitigation behavior: (a) initial defect length 4 μm ; (b) initial defect length 6 μm .

4.2 Results and discussion

4.2.1 Dendrite propagation

The baseline case is dendrite growth from an interfacial defect at the lithium anode side, that grows along the x -axis. Upon reaching the cathode, the dendrite bridges the SE, and electron transport between the anode and cathode triggers an internal short circuit (ISC)

(Fig. 32). The aim of this study is to investigate possible mitigation mechanisms where this type of dendrite growth-induced short circuit is slowed/stopped by diverting dendrite propagation away from the x -axis direction.

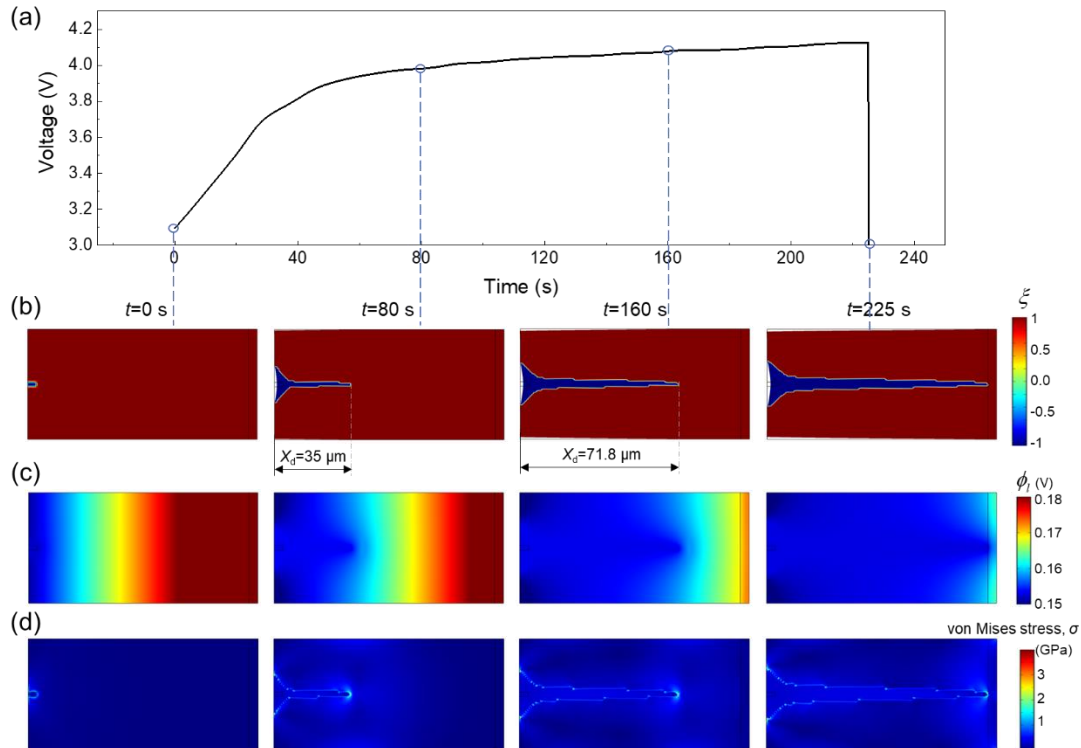


Figure 32 Baseline model: dendrite growth in solid electrolyte without HBs. (a) Voltage response, (b) dendrite growth behavior, (c) electrolyte potential evolution, and (d) von Mises stress distribution.

To determine the dominant properties of HBs that are capable of blocking a dendrite, we conduct parametric studies of Young's modulus E_{HB} , ionic conductivity κ_{HB} , and fracture toughness K_{CHB} . The computational results indicate that adjusting E_{HB} from 100 to 200 GPa or κ_{HB} from 9×10^{-3} to 4.43 mS/cm is incapable of mitigating dendrite growth (Fig. 33(a-b)). However, the dendrite growth behavior (*i.e.*, growing speed, dendrite angle, and length) is highly dependent on K_{CHB} . There are a variety of possible factors that may

promote dendrite penetration within the solid electrolyte, such as cracks, voids, grain boundaries, local electronic structure, and electron segregation at surfaces and interfaces¹¹⁹. The relative contributions of these phenomena are currently not well understood and thus it is difficult to incorporate all of these factors in the model in a meaningful way. Recent experiments provide direct evidence that dendrite growth in some inorganic solid electrolyte can be coupled with the crack propagation^{40,50,66,67}, where dendrite penetration drives crack propagation, and the newly formed crack then provides further space for dendrite growth. The model employed in this study is based on this type of behavior, where internal pressure in the Li-filled filaments drives fracture, and crack extension provides space for further Li metal penetration^{50, 65, 66}. Herein, the lithium filaments are mechanically constrained by the surrounding solid electrolyte, and their continuous growth is then driven by electrochemical deposition that exerts pressure on the neighboring electrolyte. The resulting strain energy in the SE is subsequently relaxed by fracture of the SE which then provides more growth space.

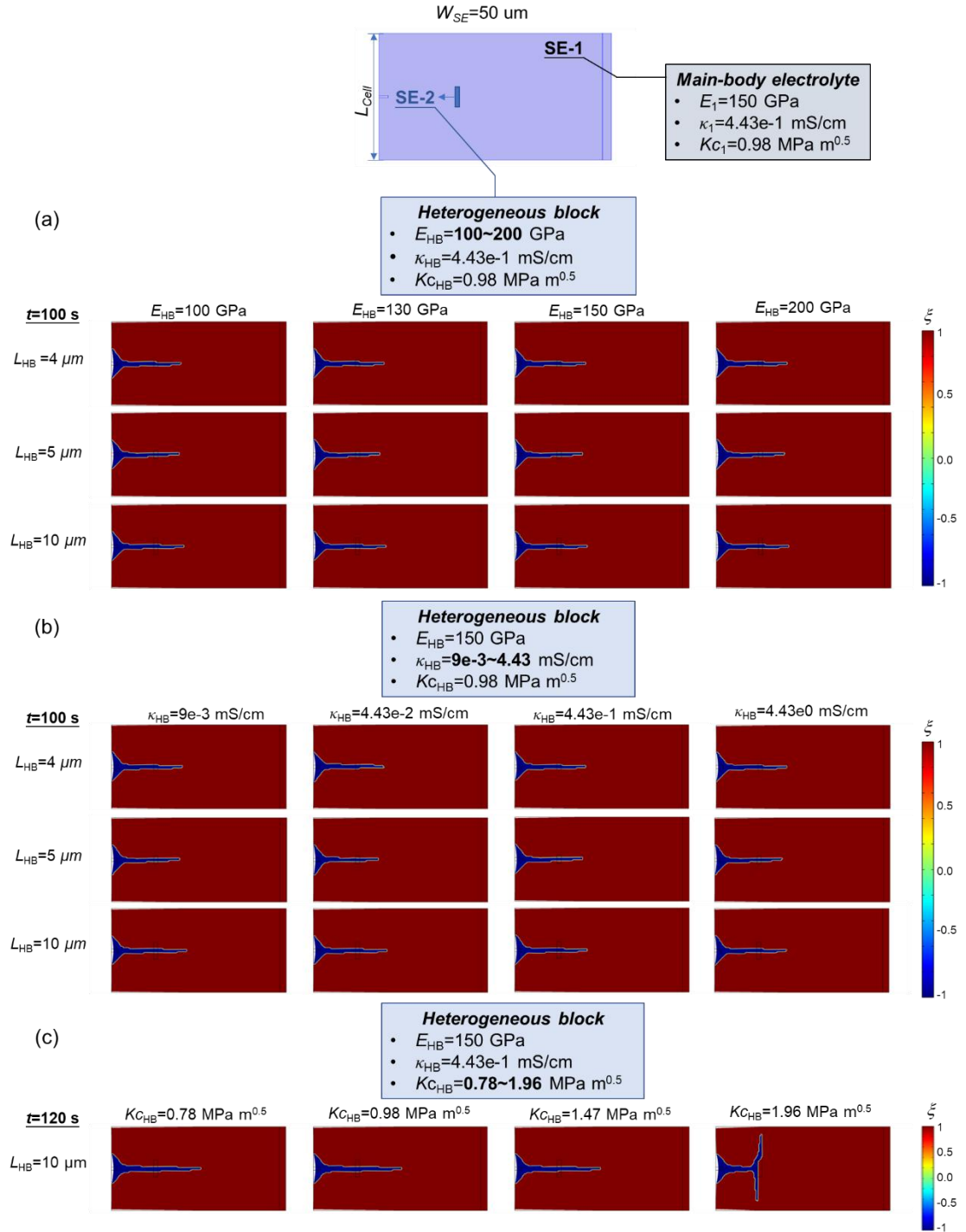


Figure 33 Effects of HBs' properties on dendrite mitigation: (a) Young's modulus effect, (b) ionic conductivity effect, (c) fracture toughness effect.

In the model (governing equations in Table 3), the internal stress $S_{\text{ext}}(x, t)$ is calculated from the overpotential $\eta(x, t)$ in the electrochemical model, and imposed at

the lithium-electrolyte interface, based on $S_{\text{ext}}(x,t) = -F\eta(x,t) / \Omega_{\text{Li}}$ ⁶⁵. This relationship assumes that the Li filaments are highly constrained, such that full pressurization occurs quickly and reaches the maximum hydrostatic stress $S_{\text{ext}}(x,t)$ that is thermodynamically possible for a given electrochemical driving force $\eta(x,t)$ (*i.e.*, the overpotential at the lithium-electrolyte interface). This assumption gives an upper bound on the pressure. Lower stresses are predicted in more detailed models that includes more realistic descriptions of the crack opening displacements and Li plasticity near the base of the crack. However, these effects are neglected here, where the focus is on dendrite growth/crack propagation paths in SE's with heterogeneous mechanical properties over macroscopic time scales. The formulation used here also overestimates the Li flux into the sides of the Li filament, however, this is also a secondary factor since most of the flux enters at or near the dendrite tip. To demonstrate this, additional simulations were conducted with variations in the exchange current density, the applied current density (*i.e.*, faster interface kinetics) and the SE ionic conductivity values. These effects alter the Li-ion flux into the flaw, and in all of these cases the predicted dendrite growth is similar to the baseline case (Fig. 61 in Appendix C). This further justifies the effectiveness of the modeling approach in this study.

The model defines the path for Li dendrite penetration by energy minimization. It is thus consistent with a crack propagation mechanism, where the resistance of the material to crack propagation (*i.e.*, described here by the fracture toughness Kc) reflects its resistance to dendrite penetration. $K_{\text{CHB}}=0.98 \text{ MPa m}^{0.5}$ is used as the baseline value, below

and above which a series of $K_{C_{HB}}$ values (*i.e.*, 0.78, 0.98, 1.47, 1.96) are studied (Fig. 33(c)). The dendrite initially grows along the x -axis through material with small value of Kc (*i.e.*, low dendrite penetration resistance), but the growth direction is diverted to the y -axis by HB with high $K_{C_{HB}}$, *i.e.*, $K_{C_{HB}}=1.96 \text{ MPa m}^{0.5}$. This doubling corresponds to a four fold increase in the fracture resistance, which is sufficient to prevent dendrite growth into the HB (Fig. 33(c)). The crack propagation/dendrite growth here is described by the phase-field method which employs energy conservation, where changes in the strain energy density serve as the driving force. The phase-field model employs continuous property variations across the interface between the two regions, in contrast to the sharp interfaces that are considered in conventional fracture mechanics analyses of crack deflection at bi-material interfaces^{120, 121}. The latter is based on the fracture resistance of the interface, which is not specifically defined in our case. However, the results of these two approaches are generally similar, with deflection induced by a relatively high fracture resistance in the HB layer. Note that when the dendrite deflects along the LLZO-HB interface ($t=70 \text{ s}$, Fig. 34), the stress components σ_{xx} and σ_{xy} correspond to mixed-mode loading (*i.e.*, a combination of Mode-I in-plane tension and Mode-II in-plane shear). In the phase-field method, this overall effect is generally reflected in the strain energy density, *i.e.*, the concentrated energy density at the dendrite tip (*e.g.*, see $t=80 \text{ s}$ in Fig. 34).

Furthermore, the different dendrite growth behavior and mitigation effect are less obvious for the HBs with different E_{HB} and κ_{HB} compared to the fracture toughness $K_{C_{HB}}$

(Fig. 35). To summarize the general trend based on the above trial computational results, K_{CHB} (dendrite penetration resistance) is the primary HB property that alters dendrite propagation, and in general, HBs with higher K_{CHB} can be used to block dendrite growth. Therefore, in the following study, we define HBs with large enough fracture toughness $K_{CHB}=1.96 \text{ MPa m}^{0.5}$ to deflect dendrites (Fig. 33(c)), and the other material properties are set to be the same as those of the main-body LLZO electrolyte.

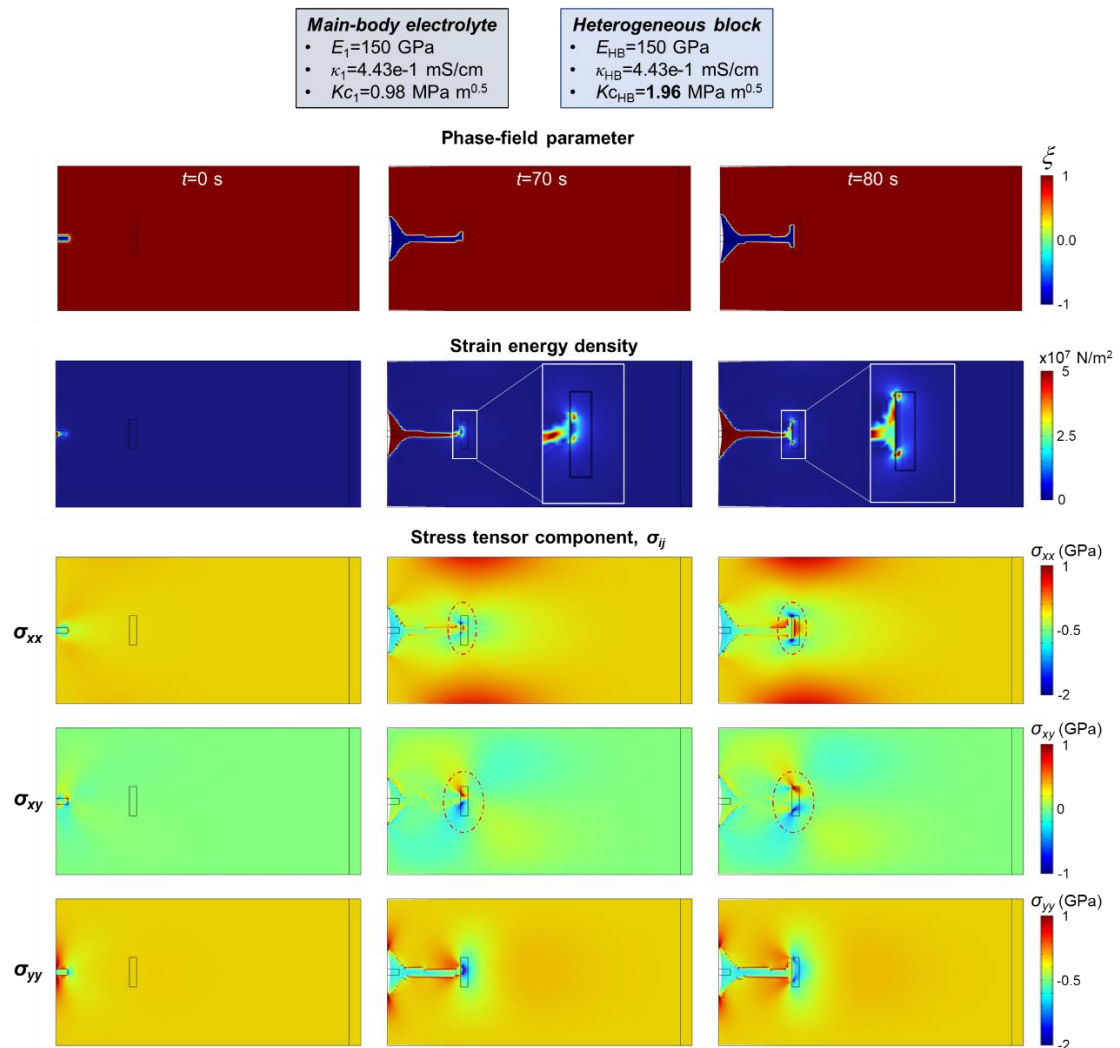


Figure 34 Contour plots of strain energy density and stress tensor components when using high fracture toughness for a heterogeneous block.

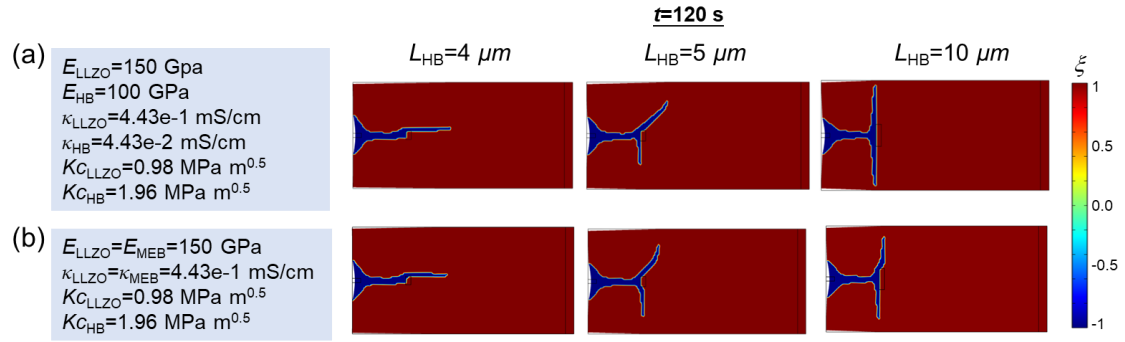


Figure 35 Dendrite mitigation with HBs of different length: (a) HBs with different Young's modulus, ionic conductivity and fracture toughness from main body of LLZO electrolyte; (b) HBs with only different fracture toughness from main body of LLZO electrolyte.

4.2.2 Dendrite mitigation effect with single HB

The risk associated with a dendrite growth-induced short-circuit can be evaluated by calculating the time that it takes for the dendrite to reach the cathode side, *i.e.*, the short-circuit risk is high if dendrite grows to the cathode side within a very short time, while the short-circuit risk is low if it takes a long time for dendrite to reach the cathode, and the risk can be reduced to zero if the dendrite is prevented from reaching the cathode (*i.e.*, the short-circuit time is infinite). To understand the dendrite mitigation effect using HBs, we first embed a single HB and focus on the individual HB's size effect from a structural design perspective. Different cell lengths L_{cell} (*i.e.*, 50 and 100 μm) and normalized HB length $e=L_{\text{HB}}/L_{\text{cell}}$ from 0.05 to 0.2 are considered. Note that adding HB ($\kappa_{\text{HB}}=0.009\text{ mS/cm}$, $K_{\text{C}_{\text{HB}}}=1.96\text{ MPa m}^{0.5}$) into the LLZO electrolyte ($\kappa_{\text{HB}}=0.443\text{ mS/cm}$, $K_{\text{C}_{\text{HB}}}=0.98\text{ MPa m}^{0.5}$) has little influence over the total effective electrolyte conductivity κ_{eff} , (*e.g.*, the κ_{eff} is only reduced 0.49% from 0.443 to 0.4408 mS/cm when adding 10 μm long HB to 50 μm long electrolyte). The ionic conductivity κ_{SE} is defined individually for the main-body of the

electrolyte, the heterogeneous block, and the lithium metal domains. Meanwhile, κ_{eff} will change as the dendrite evolves.¹⁴ The electrolyte conductivity directly determines battery internal resistance which can then influence the electrical potential distribution according to the Ohm's law in the governing equations of Table 4 in Appendix B. Furthermore, the electrolyte potential ϕ_l distribution is similar for the electrolyte with and without HB (Fig. 36(a)), thus demonstrating that the HB has little adverse influence on the overall electrochemical behavior. The potential drop over the heterogeneous block is ~ 0.00109 V (Fig. 36(a)), which is several orders of magnitude smaller than ϕ_l (~ 0.16 V). Thus, the influence of the additional resistance caused by the additional block is negligible. Note that, a significantly lower conductivity in HB compared to the surrounding electrolyte will have a non-trivial impact on the local electrical potential distribution (*i.e.*, by increasing the potential drop within HB domain).

Interestingly, we discover that dendrite growth exhibits different modes when $e=0.05$, 0.1 , and 0.2 (Fig. 36(b)) (where $L_{\text{cell}}=50$ μm , and the corresponding HB length L_{HB} are 2.5 , 5 , 10 μm , respectively). For $e=0.05$ case, the dendrite first grows along the x -axis, then bypasses the HB, and finally approaches the cathode side along the x -axis. This has no effect in preventing the ISC, but it delays the ISC triggering time. For the $e=0.1$ case, after encountering the HB, the dendrite splits into two parts, *i.e.*, the bottom dendrite branch diverges its direction towards the y -axis (no ISC risk anymore). The top branch bypasses the HB and continuously grows along the direction with an angle $\theta \sim 45^\circ$ to the x -axis (Fig.

36(b)), greatly reducing the safety risk by prolonging the dendrite growth path. For $e=0.2$ case, the two dendrite branches both divert their growth direction from the x to y -axis, eliminating short-circuit risk since the dendrite growth along the y -axis will not cause direct contact between anode and cathode. Similar results also apply to the case of $L_{\text{cell}}=100 \mu\text{m}$ with the same e values (Fig. 36(c)).

To illustrate the underlying mechanism, the stress state $\sigma_{ij}(i, j=x, y)$ is extracted at the moment when the dendrite growth first extends beyond the right side of the HB. The stress state here varies with e (Fig. 36(d)): (1) for $e=0.05$, the σ_{yy} (-2.88 GPa) at dendrite tip highlighted in the red dashed circle is larger and more concentrated than σ_{xx} (-1.125 GPa) and σ_{xy} (-1.038 GPa), which drives dendritic growth along the x -axis; (2) for $e=0.1$, the σ_{xx} (-2.6 GPa) and σ_{xy} (-1.16 GPa) are more concentrated at the dendrite tip, with promotes the dendrite branches along the y -axis, and the direction 45° with the x -axis, respectively; (3) for $e=0.2$, the σ_{xx} (-2.6 GPa) at both dendrite tips is larger and more concentrated than σ_{yy} (-1.5 GPa) and σ_{xy} (-1.12 GPa), which explains the dendrite growth preferentially along the y -direction. Both x - and y -axis dendrite growth can eventually damage the cell, *i.e.*, in the x -axis direction it electrically short circuits the cell, and in the y -axis direction it mechanically splits the solid electrolyte (note that here we do not consider the possible growth towards z -direction). However, the SE sample is usually a cylindrical pellet and the thickness of SE (x direction) is at least 1-2 orders of magnitude less than its diameter (y direction)^{18,31}, and experimental characterizations revealed that dendrite prefers to grow

towards the other electrode (*i.e.*, along x direction)^{40,41,122}. As such, the focus of this study is to suppress the x -axis dendrite growth, but attention should also be paid to the y -axis dendrite growth when long-time cycling is included.

To quantitatively evaluate the short-circuit risk R under HB with varied e , the normalized dendrite-growth time t_0/t_x is adopted, based on the dendrite tip reaching the distance $X_d=35\ \mu\text{m}$ (on the right of single HB), where $t_0=80\ \text{s}$ is the baseline time without any HB (Fig. 32), and t_x is the dendrite growth time with the HB. R here is defined to be linear with t_0/t_x , *i.e.*, $R=100\%$ when $t_0/t_x=1$ since the dendrite growth is not delayed nor blocked, and $R=0$ when $t_0/t_x=0$ as the dendrite is completely prevented from growing towards the cathode side. According to the dendrite growth mitigation effect under different e values, three categories are classified based on the short-circuit risk, *i.e.*, small e ($0 < e < 0.1$), medium e ($0.1 < e < 0.18$), and large e ($0.18 < e < 1.0$) (Fig.37). The single HB with small e has little effect in dendrite mitigation and can only elongate the dendrite growth path to delay the ISC time, and the ISC risk is above 80%. The single HB in medium e can partially change the dendrite growth direction to reduce the short-circuit risk below 70%, which may need further modulation in multiple HBs to realize the full mitigation effect. The single HB with large e can change dendrite growth direction from x to y -axis, which is then capable of preventing the dendrite growth-induced ISC completely.

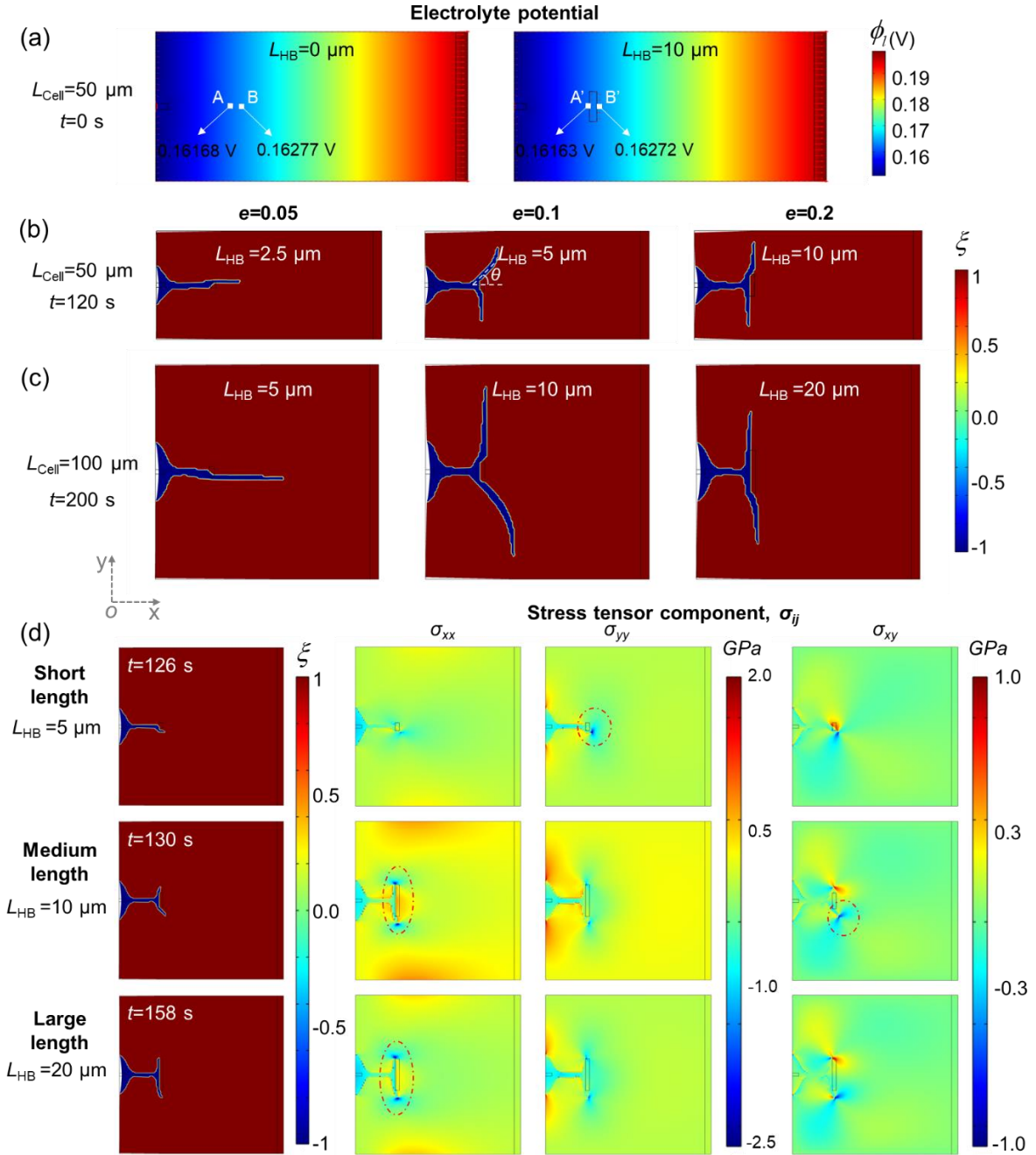


Figure 36 Dendrite growth behavior with a single heterogeneous block: (a) the electrolyte potential ϕ_i distribution without and with adding HB to the electrolyte (Note: the red arrows represent the gradient of the electrolyte potential); dendrite growth under different ratios $e = L_{\text{HB}} / L_{\text{Cell}}$ and cell length L_{Cell} : (b) $L_{\text{Cell}}=50 \mu\text{m}$, (c) $L_{\text{Cell}}=100 \mu\text{m}$; (d) Stress tensor component σ_{ij} ($i, j=x, y$) distribution when the dendrite bypasses the block, with cell length $L_{\text{Cell}}=100 \mu\text{m}$.

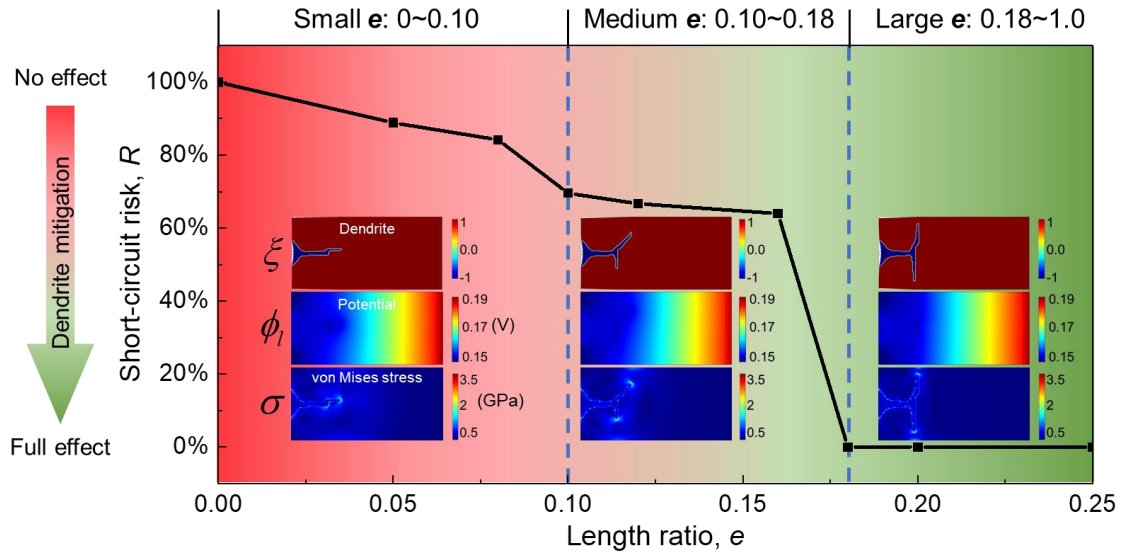


Figure 37 Short-circuit risk and dendrite mitigation effect with a single heterogeneous block under various length ratios $e=L_{HB}/L_{cell}$.

4.2.3 Dendrite mitigation effect with multiple HBs in small e

A single HB with large e can lead to full elimination of the ISC risk (*i.e.*, the dendrite grows along the y -axis), while in cases with small/medium e , the HB cannot fully stop the dendrite growth towards the cathode. As such, we naturally speculate that multiple HBs in small/medium e cases may be able to block dendrite propagation.

Two HB arrangements are considered here, *i.e.*, aligned (A1 type) and staggered (A2 type) (Fig. 38(a)). The two governing geometric parameters are the gap G between adjacent HBs in the same column and the distance D between two neighboring columns. Due to the synergic enhancing effect from neighboring HBs, different dendrite growth mitigation behaviors are observed. As for multiple small- e HBs ($L_{HB}=G=D=4\ \mu\text{m}$, Fig. 38(a)), at $t=70\text{s}$, the dendrite reaches the first-column HBs in both A1 and A2, then it changes growth direction to bypass HB (Fig. 38(b)). In A1, when the dendrite grows to bypass the HB in

the first column, it continues to grow along the x -axis, and the dendrite tip faces the gap in the second column (since the two columns are aligned) ($t=96\text{s}$, Fig. 38(b)). In this case, the second column plays no role in blocking the dendrite growth. In A2, since there is an offset distance between the neighboring columns, the dendrite tip faces the HB in the second column after it crawls across the first column via the gap. In this case, the dendrite growth direction is altered due to the HB in the second column ($t=96\text{s}$, Fig. 38(b)), which elongates the dendrite growth path. Finally, dendrites in both A1 and A2 cases grow to bypass the second column HBs and towards the cathode side. The dendrite in A2 is closer to the cathode than that in A1 case due to the extended dendrite growth path ($t=120\text{s}$, Fig. 38(b)), delaying the ISC time. In short, by properly designing the staggering space, the dendrite growth path can be significantly extended, and the growth angle may also be diverted away from the cathode side. Besides, the total effective electrolyte conductivity κ_{eff} decreases from 0.443 to 0.4343 mS/cm by only 1.96% when A1 or A2 is adopted, and the electrolyte potential is seldomly affected (Fig. 39).

The applied current density i dictates the internal electrochemical reaction kinetics of the cell, which further affects the dendrite growth behavior. Here various current density values are selected to explore its influence, *i.e.*, $i = 0.4795, 0.959, 1.4385, \text{ and } 1.918$ mA/cm². At low current density ($i \leq 0.959$ mA/cm²), dendrite growth occurs along the y -axis without short-circuit risk (Fig. 38(c)). However, when $i \geq 0.959$ mA/cm², the dendrite penetrates the electrolyte and grows towards the cathode. Furthermore, the dendrite reaches

the right edge of the 2nd-column HB earlier with both the A1 and A2 arrangement methods at $i=1.918 \text{ mA/cm}^2$ than it does with the $i=1.4385 \text{ mA/cm}^2$ (Fig. 38(c)), indicating faster dendrite growth at higher current density. Increased current density and simultaneous dendrite suppression are critical requirements for ASSB commercialization, thus $i=1.918 \text{ mA/cm}^2$ is selected in this study to explore dendrite mitigation strategies with practically relevant current densities.

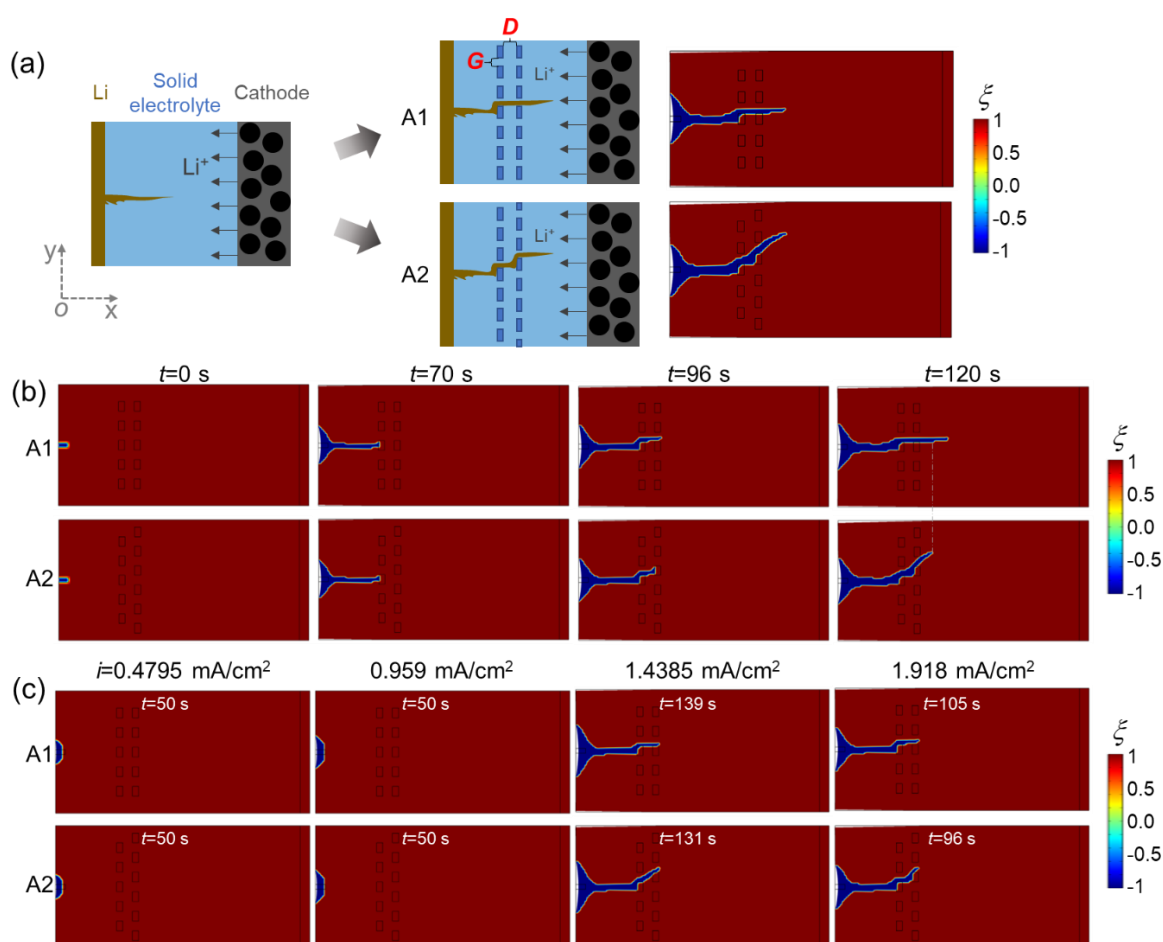


Figure 38 Dendrite mitigation with multiple heterogeneous blocks in small length ratio ϵ : (a) illustration of two representative arrangement methods, (b) the dendrite growth behavior and mitigation effect in the two arrangement methods, (c) dendrite growth behavior at various applied current density.

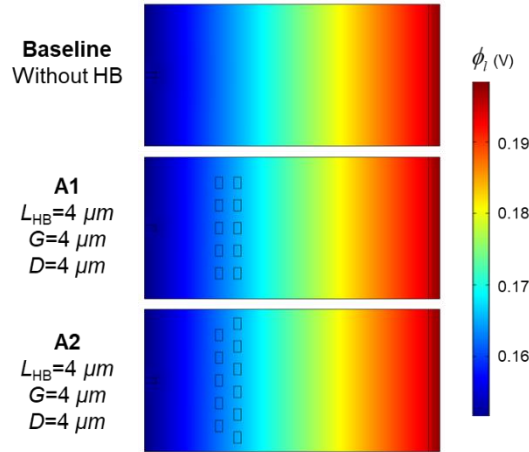


Figure 39 Electrolyte potential distribution with multiple HBs in small e : baseline without any HB, A1 and A2 with multiple HBs ($L_{\text{HB}}=G=D=4 \mu\text{m}$).

4.2.4 Dendrite mitigation effect with multiple HBs in medium e

Again, the HB structures are classified into two categories, the same as in the small- e cases (*i.e.*, A3 and A4 for aligned and staggered lineups, respectively). In the A3 case, after the dendrite grows through the gaps in the first column, it continuously grows along the direction 45° to the x -axis. Once the dendrite meets one of the HBs in the second column, the growth angle further changes along the y -axis for further growth (which turns 90° compared to its original growth path, Fig. 40(a)). In this way, the dendrite growth-induced ISC can be completely prevented. On the other hand, in A4 cases, the dendrite penetrates through the gap in the first column and extends diagonally, then it reaches the gap in the second column, which provides an accessible opportunity for the growth path (Fig. 40(a)). In this case, ISC cannot be entirely avoided, though the dendrite growth path is extended.

As an additional step to obtain comprehensive knowledge about the modulation of the HB arrangement to completely block dendrite growth, a further parametric study is carried out following the effective arrangement method in A3. The dominant geometric parameters

are: (1) the HB length L , (2) the gap G between HBs in the same column, and (3) the distance D between two adjacent columns. To make it more generalized, the normalized gap ratio G/L and distance D/L are used to quantitatively characterize the geometric information. Within the range of medium e , four values are selected, *i.e.*, $e=0.1, 0.12, 0.14, 0.16$. Furthermore, since the large gap and distance provide additional possible space for dendrite growth resulting in poor performance in mitigating dendrite (Fig. 41), the G/L and D/L values are limited within 1.

Similarly, the normalized time t_0/t_x is adopted to evaluate the dendrite growth induced short-circuit risk R . Here t_x is the time when dendrite grows to the right edge of the second-column HBs in each specific arrangement, and t_0 is the corresponding baseline time without any HB. Based on the mitigation effect of HB lineups, we classify the effects into two categories: *Group 0* for completely preventing dendrite from growing towards the cathode (safe region, blue area in Fig. 40(b)), *Group 1* for dendrite still growing to cause a short circuit (dangerous region, non-blue area in Fig. 40(b)). The region of G/L close to 0 is safe, which is much close to the scenario with large e . For $e=0.1$, the dangerous regions in *Group 1* are: Region 1 ($0.1 < G/L < 0.4$), and Region 2 ($0.6 < G/L < 1, 0 < D/L < 0.6$). As e increases to 0.12, the dangerous Regions 1 and 2 are both split into two small regions, one of which further disappears in $e=0.14$. When it comes to $e=0.16$, only a small portion of Region 2 ($0.9 < G/L < 1, 0 < D/L < 0.3$) remains and the high-risk red area (R close to 100%) nearly disappears, indicating a promising dendrite mitigation effect. Thus, for multiple HBs in

medium e , the dendrite can be completely suppressed with specific combination of gap and distance ratios. The overall trend discovered with larger medium e , is the larger safe *Group 0* area and the smaller high-risk red region in dangerous *Group 1*, thus demonstrating better dendrite mitigation.

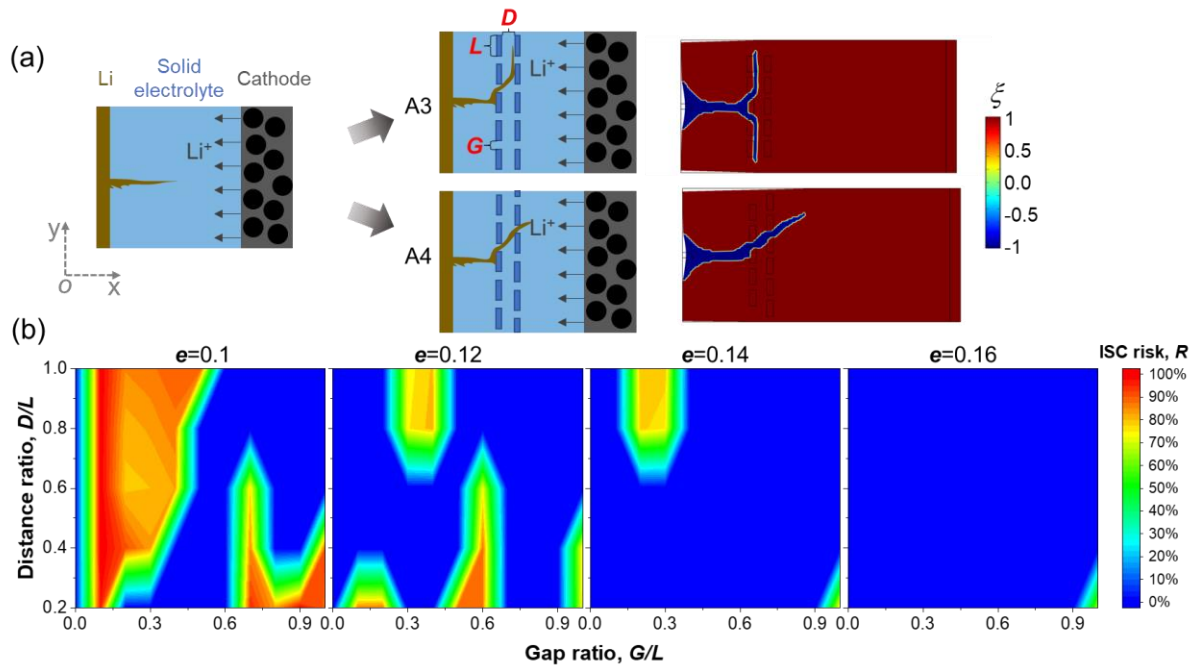


Figure 40 Dendrite mitigation with multiple heterogeneous blocks in medium length ratio e : (a) illustration of two representative arrangement methods, (b) the short-circuit risk as a function of distance ratio D/L , gap ratio G/L , length ratio e .

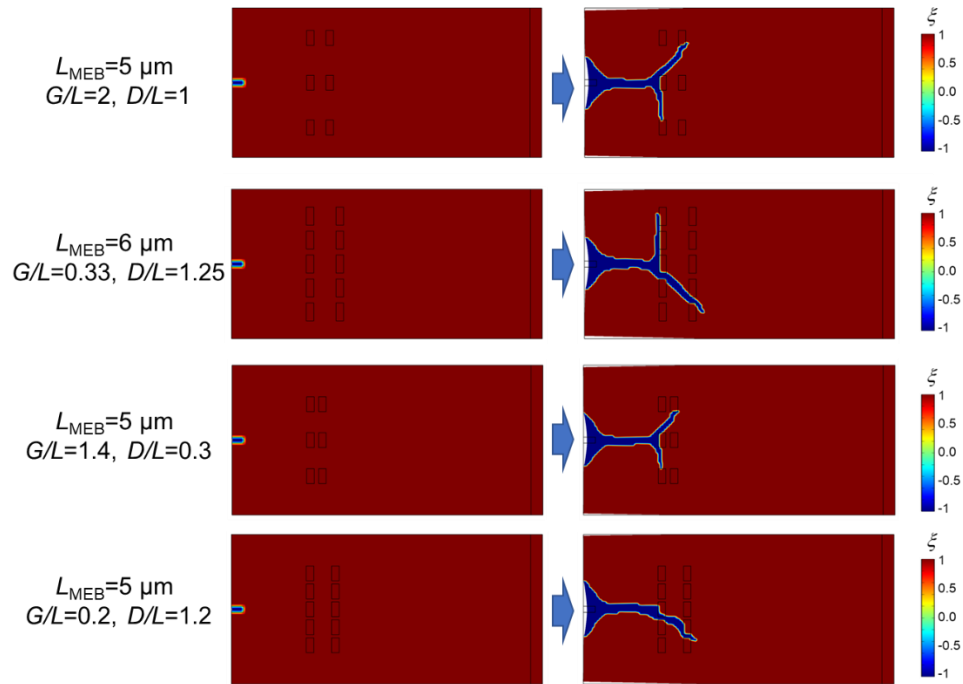


Figure 41 Dendrite mitigation with multiple HBs in medium e .

4.2.5 Multilayer electrolyte design to mitigate dendrite

In extreme cases, HB arrangement with gap $G=0$ becomes a new layer of electrolyte. As such, a multilayer electrolyte structure consisting of a main-body electrolyte and an embedded layer (EL) is formed (Fig. 42), combining the mechanical advantage from HB (high fracture toughness) and electrochemical advantage from baseline electrolyte (high conductivity). To leverage the mechanical stiffness gradient and mismatch, we assign different Young's moduli to the embedded layer and the main body of the electrolyte to improve the overall dendrite mitigation effect of the multilayer electrolyte.

The main-body electrolyte is LLZO with Young's modulus 150 GPa. Here four different Young's modulus E_{EL} (*i.e.*, 50, 100, 150 (baseline), 200 GPa) are considered to investigate the dendrite mitigation effect for the 10 μm thick embedded layer. Note here

that the energy release rate at fracture $G_c = \frac{(1-\nu^2)K_c^2}{E}$ describes the fracture resistance.

To study the effect of Young's modulus, the fracture toughness K_c of the embedded layer is first held constant as $0.98 \text{ MPa m}^{0.5}$ which is same as the main-body electrolyte. As the dendrite grows into the embedded layer, the stress tensor component σ_{yy} at the dendrite tip is -1.436 GPa for $E_{EL}=50 \text{ GPa}$, smaller and less concentrated than the other cases ($\sigma_{yy}=-1.938, -2.39, -2.28 \text{ GPa}$ for $E_{EL}=100, 150, 200 \text{ GPa}$, respectively) (Fig. 42(a)). Accordingly, the short-circuit time is $276, 235, 225, 234 \text{ s}$ for $E_{EL}=50, 100, 150,$ and 200 GPa , respectively, and G_c increases with decreasing E_{EL} , which implies that smaller Young's modulus $E_{EL}=50 \text{ GPa}$ improves dendrite mitigation. As a second case, we set the G_c of the embedded layer to be the same as that of the electrolyte (*i.e.*, $G_c = 3.02 \text{ J/m}^2$) and vary E_{EL} . Similarly, $E_{EL}=50 \text{ GPa}$ leads to better dendrite mitigation and can even keep the dendrite growth within the embedded layer (Fig. 43). Thus, $E_{EL}=50 \text{ GPa}$ is then selected to study the structure effect on dendrite mitigation, and the other properties, including fracture toughness and ionic conductivity, are the same throughout the whole electrolyte.

Three scenarios are then considered to study the multilayer effect on dendrite growth: (1) single embedded layer with thickness $W=10 \text{ }\mu\text{m}$; (2) two embedded layers with both thickness $W/2=5 \text{ }\mu\text{m}$, the gap of $5 \text{ }\mu\text{m}$; and (3) single embedded layer with thickness $W/2=5 \text{ }\mu\text{m}$ (Fig. 42(b-d)). Note that once the HBs become the enhanced layer, the dendrite growth diversion can no longer be achieved without gaps. Thus, we observe a continuous dendrite growth along the initial dendrite direction (Fig. 42(b-d)). The farthest dendrite growth

distance X_d (from the leftmost base to the rightmost tip) is used to intuitively indicate the degree of dendrite mitigation since larger X_d implies earlier short circuit, and smaller X_d represents a better mitigation effect and lower short circuit risk.

For all cases in Fig. 42, the dendrite initiates from the pre-defect area and grows towards the cathode side. At $t=55$ s, the dendrite reaches the left edge of the embedded layer in all the scenarios, then penetrates into the embedded layer and continues to grow along the x -axis. At $t=120$ s, the dendrite reaches the right edge of the embedded layer in *Scenario 1* with $X_d=35$ μm , meanwhile the $X_d=37.3$ μm , 39.2 μm for *Scenarios 2* and *3*, respectively. Later, the dendrite penetrates through all the embedded layers and re-enters the main-body electrolyte as the charging process continues. At $t=160$ s, $X_d=49.8$ μm , 43.8 μm , 57.5 μm for *Scenarios 1, 2, 3*, respectively, while $X_d=71.8$ μm for the baseline case without any embedded layer (Fig. 32). Finally, the dendrite reaches the cathode side, causing short circuits in all the scenarios, and short-circuit time $t_{\text{short}}=276, 290, 262$ s for *Scenarios 1, 2, 3*, respectively. Such results demonstrate the effectiveness of the dendrite growth mitigation for the multilayer. It is also clear that a thicker embedded layer can further slow down the dendrite growth. For the same total thickness, multiple layers with gaps impose more mechanical stiffness gradient transitions on the multilayer electrolyte design, thus leading to better dendrite mitigation. The embedded layer affects dendrite growth mainly by delaying growth speed within EL, thus, the EL thickness is one dominant factor that controls the mitigation effect. EL with different thicknesses (*i.e.*, 10 μm , 5 μm ,

and 0 μm) are considered here. The dendrite grows at the same speed until it reaches the EL region. Then, the dendrite growth speed is reduced by the EL region and the dendrite penetration distance is largest for the baseline case (Fig. 44). The short circuit time is delayed at the thickest EL case (*i.e.*, 10 μm), demonstrating that increasing the EL thickness also helps to mitigate dendrite penetration and reduces short circuit risk.

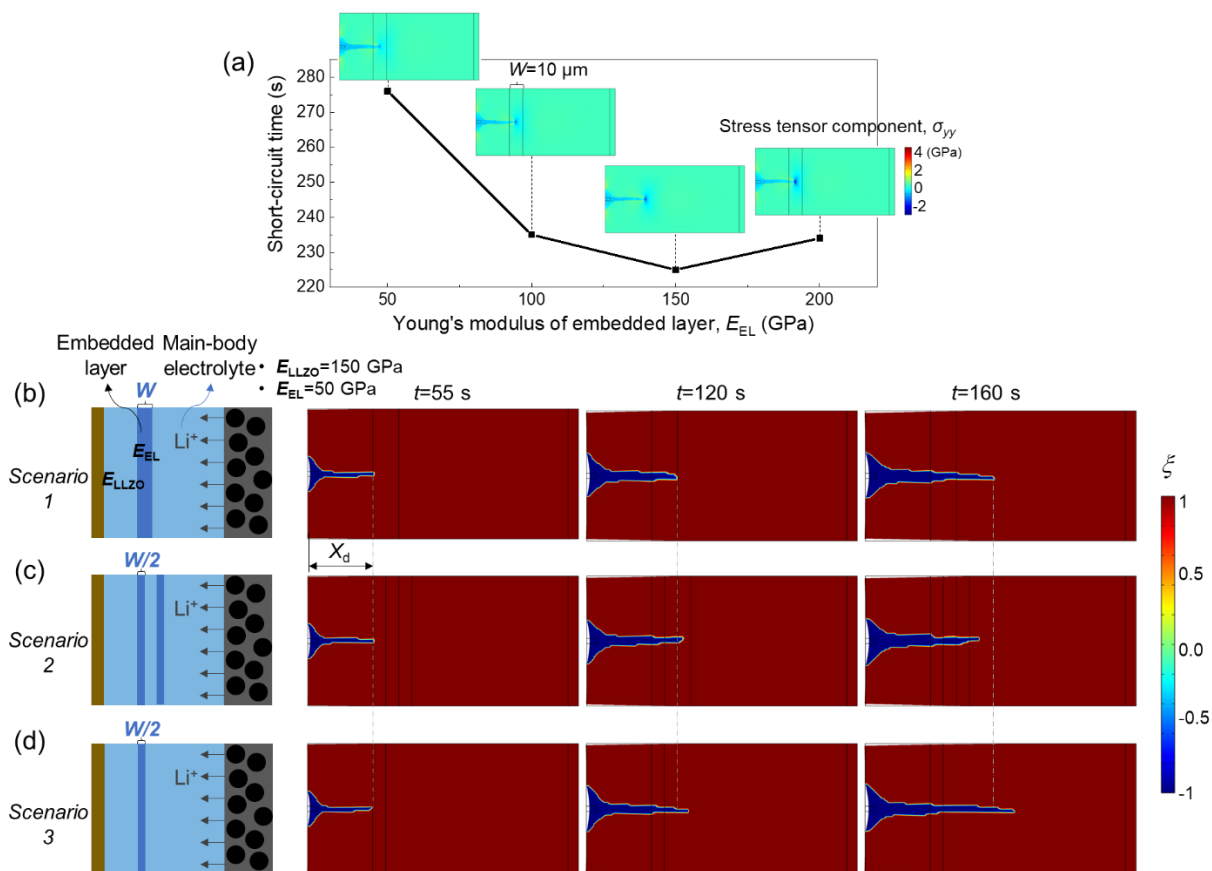


Figure 42 Dendrite mitigation effect with multilayer solid electrolyte design: (a) effect of Young's modulus E_{EL} of the embedded layer, dendrite mitigation behavior of (b) embedded layer with width $W=10 \mu\text{m}$, (c) two embedded layers with both width $W/2=5 \mu\text{m}$, gap $5 \mu\text{m}$, and (d) embedded layer with width $W/2=5 \mu\text{m}$.

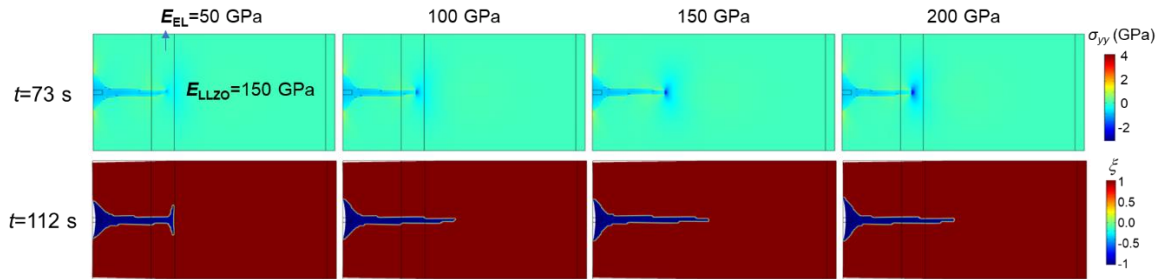


Figure 43 Dendrite mitigation effect by adding the embedded layer (varying Young's modulus E_{EL} , constant fracture resistance G_c): stress tensor component σ_{yy} at 73 s, and dendrite growth at 112 s.

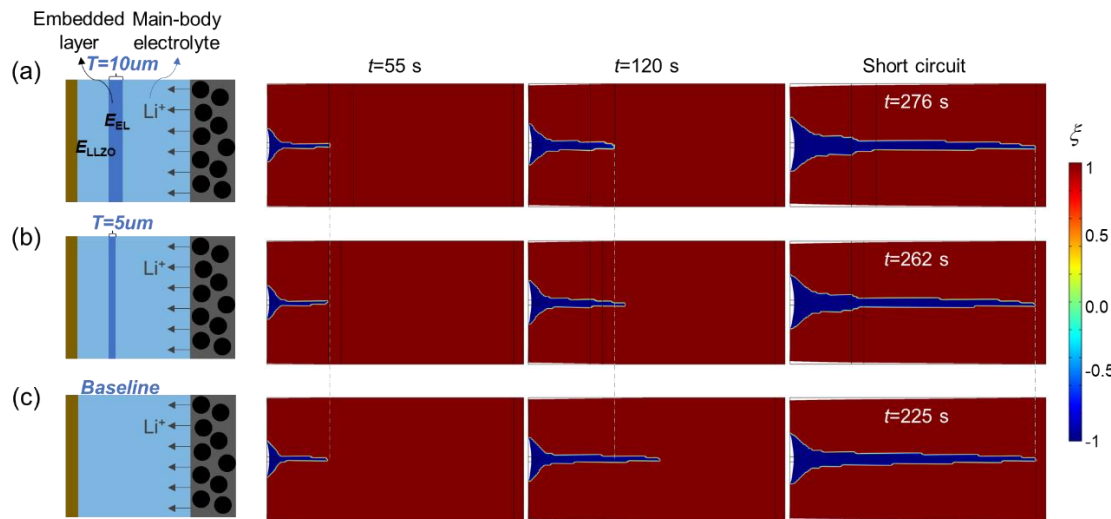


Figure 44 Dendrite mitigation effect with multilayer solid electrolyte design considering different thicknesses of embedded layer: (a) $T=10\ \mu\text{m}$, (b) $T=5\ \mu\text{m}$, (c) baseline $T=0\ \mu\text{m}$.

To provide a clear overview of the dendrite-induced ISC risk, we consider the main governing effects from the length ratio e , along with the quantity and arrangement of HBs, and the Young's modulus of the electrolyte. The resulting map in Fig. 45 for $0 < e < 1$ (regions I and II) shows combined strategies that combine the advantages of HBs' high fracture toughness to suppress dendrite growth and LLZO's high ionic conductivity to maintain electrochemical performance. In Region I (high ISC risk), whether single or multiple HBs are adopted, the dendrite-induced short circuit is not prevented but only delayed by the

elongated growth path, for both small e ($0 < e < 0.1$) area and medium e ($0.1 < e < 0.18$) area using the A4 arrangement method. Nevertheless, multiple HBs in medium e through the specific A3 arrangement are capable of completely suppressing dendrite growth towards the cathode (Fig. 40), and single/multiple HBs in large e can prevent the dendrite-induced short circuit as well, both of which are included in Region II (zero ISC risk). At $e=1$ (Region III), the strategy becomes a multilayer electrolyte structure consisting of main-body electrolyte and embedded layer to mitigate dendrite growth through stiffness gradient design. In this case, the electrolytes have different Young's moduli E_{EL} compared to the main-body electrolyte, and their other properties are the same. Although the dendrite-induced ISC is not completely prevented in Region III, electrolytes with smaller E_{EL} in more and thicker layers show promising dendrite mitigation effects to delay the short-circuit time significantly.

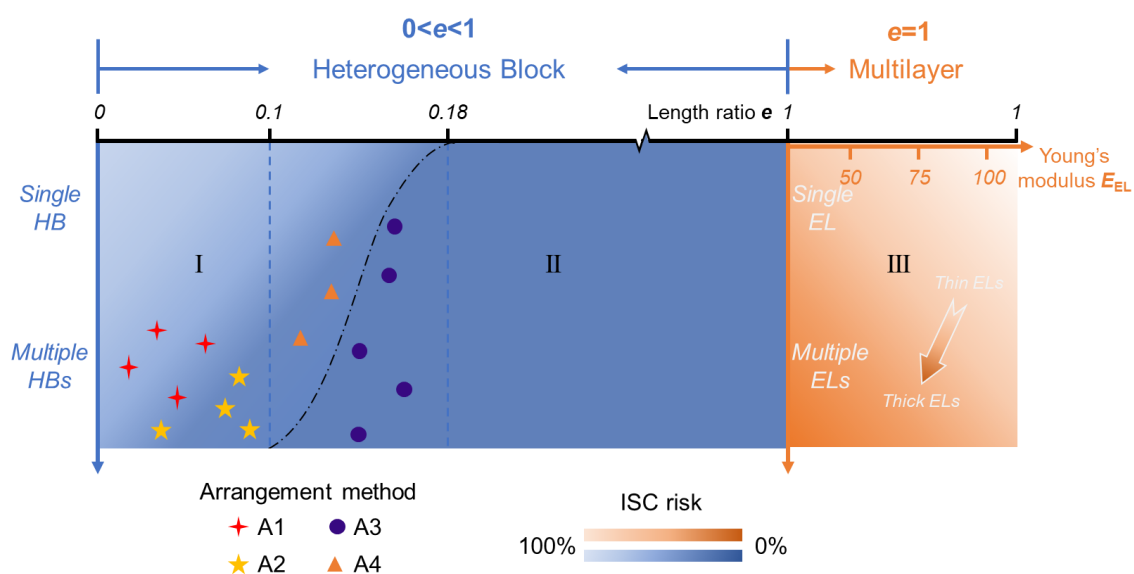


Figure 45 Overview of the ISC risk as a function of length ratio e , quantity and arrangement of HB, and quantity and Young's modulus of the embedded layer.

4.4 Conclusions

The dendritic growth-induced ISC safety issue is one of the main problems to be solved for the successful implementation of ASSBs. Inspired by “brick-and-mortar” toughening mechanisms, we propose the strategy of adding heterogeneous blocks into SEs. Dendrite growth mitigation is then evaluated with an established multiphysics modeling framework under practical current density. The effect of adding HBs within the electrolyte on dendrite mitigation is then comprehensively investigated by considering the HB length, arrangement method, and multilayer design. Our major findings are:

- The nominal length e of the HB dominates the dendrite mitigation effect with a single HB. Specifically, large e ($0.18 < e < 1$) may completely change dendrite growth direction and prevent short circuit, while medium e ($0.1 < e < 0.18$) can partially block dendrite growth, and small e ($0 < e < 0.1$) can only mitigate dendrite growth to a limited extent.
- Multiple HBs with medium e , modulated by a specific arrangement method, can fully mitigate dendrite penetration, while multiple HBs with small e only elongate the dendrite growth path and delay the short-circuit time.
- The multilayer SE structure shows promise for mitigating dendrites and delaying short circuits, especially when thicker and multiple embedded layers with smaller Young’s modulus are adopted.

These results reveal that adding HBs with high fracture resistance is a promising

approach to mitigate dendrites and reduce short-circuit risk. To implement these findings, additional consideration of actual microstructural effects is needed. Current LLZO electrolyte have a $G_c \approx 3 \text{ J/m}^2$ with Young's modulus 150 GPa, fracture toughness $0.985 \text{ MPa m}^{0.5}$, and Poisson's ratio 0.257. In polycrystalline ceramics varying the grain size can have some effect on G_c , however, in most cases these effects are well below the 4:1 ratio used in the model. Differences this large can be created by varying porosity¹²³, but this might limit overall performance of the SE in other ways. In some ceramics, large increases in G_c are obtained with elongated whisker-like grain structures (e.g., Si_3N_4), and our results indicate that focused efforts to create these structures in SEs are potentially worthwhile. Ultimately, nanocomposites that employ second phases may provide a wider array of options for engineering HBs with large G_c differences¹²⁴. The mesoscale model with a homogenized electrolyte domain in this study focuses on the mitigation of dendrite-induced short circuit risk. In future work, this can be further improved with a multiscale approach by including the intricate polycrystalline electrolyte structure to predict the transgranular or intergranular dendrite penetration.

CHAPTER 5 ELECTROCHEMICAL-MECHANICAL COUPLING FAILURE

MECHANISM OF COMPOSITE CATHODE

In this chapter, I develop the three-dimensional fully coupled electrochemical-mechanical model to obtain an in-depth understanding of the mechanical instability issues inside the composite cathode of ASSBs. The model considers the complicated heterogeneous particle structure as well as battery electrochemical kinetics, Li diffusion process, mechanical deformation, and interfacial debonding. The quantitative results from the established model give out insights into the mechanisms of interfacial debonding and particle bulk damage, which further result in the degradation of the cell performance. The governing effects from charging rates (C-rates), heterogeneous properties, interfacial strength, and particle position are then comprehensively investigated to provide possible solutions to improve the robustness of composite cathode in ASSBs.

5.1 Methodology

To investigate the coupled electrochemical-mechanical behavior inside composite cathode of ASSBs, the 3D representative region including composite cathode, LLZO electrolyte and lithium anode surface is selected as the target domain in this study (Fig. 46). The composite cathode is further composed of the $\text{LiNi}_{1/3}\text{Co}_{1/3}\text{Mn}_{1/3}\text{O}_2$ (NCM111) secondary particle, electrolyte-carbon black domain (ECBD). The secondary particle consisting of 53 primary particles ranging in size from 0.1 to 3 μm with random shapes and orientations is stochastically generated through Voronoi tessellation via a Python script.

The radius of the secondary particle is 5 μm . Since the focus of this study is on the failure mechanism of composite cathode, especially on the particle-related phenomena, the ECBD and electrolyte domain (ED) are simplified as homogenized regions with effective properties in the model. The cross section of the representative region is a 15 μm \times 15 μm square, and the length of the ECBD and electrolyte domain (ED) are 25 μm and 15 μm , respectively. The right boundary of ED is the lithium anode surface. The left boundary is the cathode current collector where the external charging/discharging current is applied.

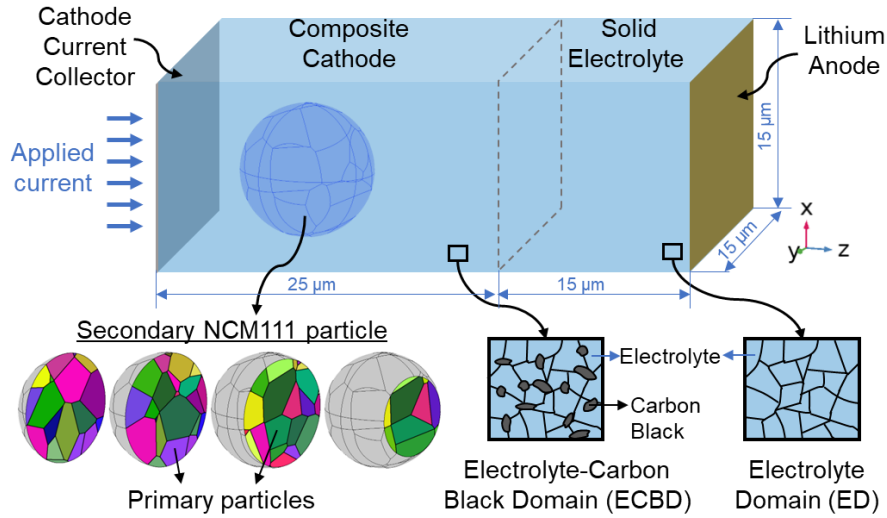


Figure 46 Illustration of the established 3D model consisting of composite cathode (NCM111 secondary particle, electrolyte-carbon black domain (ECBD)), LLZO solid electrolyte domain (ED), and lithium anode.

Electrochemical reaction kinetics. The electrochemical reaction kinetics at the electrolyte-particle interface is described by the Butler-Volmer relationship:

$$I_{\text{BV}^+} = I_{0^+} \left[\exp\left(\frac{\alpha_a F \eta_+}{RT}\right) - \exp\left(\frac{-\alpha_c F \eta_+}{RT}\right) \right] \quad (46)$$

where I_{BV^+} is the local charge transfer current density, I_{0^+} is the exchange current density, F is the Faraday's constant, R is the gas constant, T is temperature, α_a and α_c are the

anodic and cathodic charge transfer coefficients, respectively; η_+ is the overpotential expressed as:

$$\eta_+ = \phi_s - \phi_l - E_{\text{eq}} - \frac{\Omega \sigma_h}{F} - \Delta \eta_{\text{int}} \quad (47)$$

where ϕ_s and ϕ_l represent the electrical potential in the solid phase and the electrolyte phase, respectively; E_{eq} is the equilibrium potential, Ω is the partial molar volume of lithium in the active material, $\sigma_h = (\sigma_{11} + \sigma_{22} + \sigma_{33})/3$ is the hydrostatic stress, $\Delta \eta_{\text{int}} = R_{\text{int}} \cdot I_{\text{BV}}$ is the overpotential drop induced by the increase interfacial resistance R_{int} as a result of particle-ECBD interface debonding. The term $-\Omega \sigma_h / F$ considers the stress effect on overpotential (namely, the interfacial reaction kinetics).

Within the ECBD and ED areas, the electric current density obeys Ohm's law, governed by the following equations:

$$\mathbf{i}_l = -\kappa_l^{\text{eff}} \nabla \phi_l \quad (48)$$

$$\mathbf{i}_s = -\kappa_s^{\text{eff}} \nabla \phi_s \quad (49)$$

where the i_l and i_s are the current density in the electrolyte domain and the remaining electrically conductive domain, respectively; $\kappa_l^{\text{eff}} = \varepsilon_l^{1.5} \kappa_l$ and κ_s^{eff} are the effective electrolyte conductivity and effective electrical conductivity, respectively; ε_l is the electrolyte volume fraction, κ_l is the solid electrolyte conductivity. Furthermore, the charge conservation requires:

$$\nabla \cdot \mathbf{i}_l = 0 \quad (50)$$

$$\nabla \cdot \mathbf{i}_s = 0 \quad (51)$$

At the electrolyte-lithium interface, the charge transfer reaction kinetics is governed by Butler-Volmer equation as well:

$$I_{\text{BV.}} = I_{0-} \left[\exp\left(\frac{\alpha_a F \eta_-}{RT}\right) - \exp\left(\frac{-\alpha_c F \eta_-}{RT}\right) \right] \quad (52)$$

$$\eta_- = \phi_s - \phi_l - E_{\text{eq}} \quad (53)$$

The following boundary conditions are applied for the electrochemical process: $-\mathbf{i}_s \cdot \mathbf{n}_c = i_{\text{app}}$ at left boundary $z=0$, $\phi_s = 0$ V at right boundary $z=40$ μm , where \mathbf{n}_c is the unit outward normal vector of the cathode surface, and i_{app} is the applied current density at the cathode current collector.

Diffusion process. The diffusion of Li ions into the NCM secondary particle is affected by both the concentration gradient and stress effect, described by the Fick's second law of diffusion:

$$\frac{\partial c}{\partial t} + \nabla \cdot \mathbf{J}_s = 0 \quad (54)$$

$$\mathbf{J}_s = -D_s \left(\nabla c - \frac{\Omega c}{RT} \nabla \sigma_h \right) \quad (55)$$

where c is the bulk Li concentration in the particle, \mathbf{J}_s is the Li flux,

$$D_s = \begin{bmatrix} 1 \times 10^{-14} & 0 & 0 \\ 0 & 1 \times 10^{-14} & 0 \\ 0 & 0 & 1 \times 10^{-20} \end{bmatrix} \text{ m}^2/\text{s} \text{ is the diffusion coefficient which is anisotropic,}$$

i.e., $D_{s11}=1 \times 10^{-14}$, $D_{s22}=1 \times 10^{-14}$, $D_{s33}=1 \times 10^{-20}$ m^2/s along [100], [010], [001]

crystallographic orientations of the NCM primary particle, respectively.^{125, 126} Note that the

crystallographic orientations of the primary particles are randomly created, and the

adjacent primary particles hold different directions. The Li flux for the particle is from the interfacial current density of the charge transfer reaction:

$$\mathbf{J}_s \cdot \mathbf{n}_l = -\frac{I_{\text{BV}^+}}{F} \quad (56)$$

where the \mathbf{n}_l is the unit normal vector from the electrolyte to the particle surface.

Mechanical deformation. The equilibrium equation of solid mechanics follows

$$\nabla \cdot \boldsymbol{\sigma} + \mathbf{f}_V = 0 \quad (57)$$

where the stress tensor $\boldsymbol{\sigma}$ is given by Hooke's law for linear elasticity as $\boldsymbol{\sigma} = \mathbf{C}:\boldsymbol{\varepsilon}_{\text{el}}$, \mathbf{f}_V is the body force per unit volume which equal zero here, \mathbf{C} and $\boldsymbol{\varepsilon}_{\text{el}}$ are the constitutive tensor and elastic strain tensor, respectively. Furthermore, the total strain $\boldsymbol{\varepsilon}$ is related to the displacement field \mathbf{u} :

$$\boldsymbol{\varepsilon} = \frac{1}{2} \left((\nabla \mathbf{u})^T + \nabla \mathbf{u} \right) \quad (58)$$

In this study, the total strain $\boldsymbol{\varepsilon}$ also follows:

$$\boldsymbol{\varepsilon} = \boldsymbol{\varepsilon}_{\text{el}} + \boldsymbol{\varepsilon}_{\text{Li}} \quad (59)$$

where $\boldsymbol{\varepsilon}_{\text{Li}}$ is lithiation/delithiation-induced strain. It's assumed that $\boldsymbol{\varepsilon}_{\text{Li}}$ is proportional to the normalized Li concentration c_n in the particle, $c_n = c/c_{\text{max}}$, where c_{max} is the maximum Li concentration at the fully lithiated state, written as:

$$\boldsymbol{\varepsilon}_{\text{Li}} = \boldsymbol{\beta}_c c_n \quad (60)$$

where $\boldsymbol{\beta}_c$ is the lithiation expansion coefficient which is anisotropic, expressed as:

$$\boldsymbol{\beta}_c = \boldsymbol{\theta}_\beta \beta_{c_0}(c) / 3 \quad (61)$$

where $\boldsymbol{\theta}_\beta = \begin{bmatrix} 1 & 0 & 0 \\ 0 & 1 & 0 \\ 0 & 0 & -1 \end{bmatrix}$ is the coefficient matrix, $\beta_{c0}(c)$ is the intercalation-induced

volumetric strain in NCM particle as a function of Li concentration defined by the curve in Fig. 47,⁷ and the volumetric strain is converted to linear strain in each single direction through multiplying by one-third. Furthermore, the lithiation-induced volume change in [001] orientation of the NCM particle is opposite to that of the other two orientations,¹²⁵ thus $\theta_{\beta11}=1$, $\theta_{\beta22}=1$, $\theta_{\beta33}=-1$ for [100], [010], [001] orientations, respectively. According to the reference,¹²⁵ the absolute values of $\theta_{\beta ij}$ ($i, j=1, 2, 3$) are close, which are assumed to be the same in this study. The symmetric mechanical boundary conditions are applied to the side surfaces of the cell.

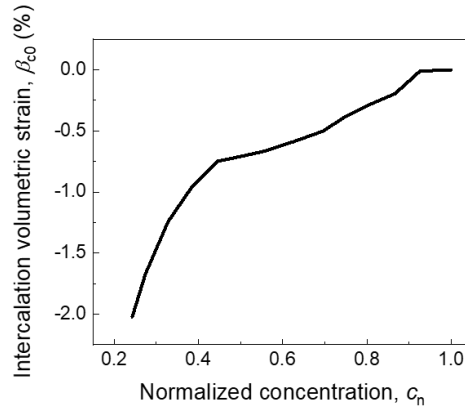


Figure 47 Intercalation-induced volumetric strain β_{c0} of NCM111 particle as a function of normalized concentration c_n .⁷

Interfacial debonding. The cohesive zone model is adopted to describe the debonding/separation behavior of the particle-ECBD interface. The quadratic failure criterion is used to predict the onset of separation:^{127, 128}

$$\left(\frac{\langle \tau_I \rangle}{\sigma_{cI}}\right)^2 + \left(\frac{\tau_{II}}{\sigma_{cII}}\right)^2 + \left(\frac{\tau_{III}}{\sigma_{cIII}}\right)^2 = 1 \quad (62)$$

where τ is the element traction and σ_c is critical stress (i.e., interfacial strength) in single mode with the subscripts I, II, III denoting separation Mode I (tensile mode), Mode II (shear mode), Mode III (tear mode), respectively. The Macaulay bracket $\langle \cdot \rangle$ is defined as

$$\langle x \rangle = \begin{cases} 0, & x < 0 \\ x, & x \geq 0 \end{cases}, \text{ which further implies that normal compressive stress is not assumed to}$$

initiate the separation.

The mixed-mode relative displacement u_m quantitatively characterizes the displacement in the adhesive layer, defined as:

$$u_m = \sqrt{\langle u_I \rangle^2 + u_{II}^2} \quad (63)$$

where u_I and u_{II} are the displacements in normal direction and tangential direction, respectively.

The power-law mixed-mode failure criterion is selected to describe the propagation of the debonding process, expressed as:¹²⁸

$$\left(\frac{G_I}{G_{Ic}} \right)^\alpha + \left(\frac{G_{II}}{G_{IIc}} \right)^\alpha = 1 \quad (64)$$

where G_{Ic} and G_{IIc} are the critical tensile and shear energy release rates (i.e., fracture toughness), respectively, α is the mode mixity exponent. In this study, the interfacial strength σ_c and fracture toughness G_c are assumed to be the same for tensile in the normal direction and shear in the tangential direction.

The actual debonding gap λ between the particle surface and ECBD region is automatically detected by the model, which will influence the particle-ECBD interfacial resistance R_{int} by:^{129,130}

$$R_{\text{int}} = R_{\text{int}}^{\text{ref}} \left(e^{\lambda/\lambda_{\text{ref}}} - 1 \right) \quad (65)$$

where the $R_{\text{int}}^{\text{ref}}$ is the reference interfacial resistance, λ_{ref} is the reference gap. The interfacial resistance R_{int} further affects the overpotential and the corresponding charge transfer reaction kinetics at the interface.

The material properties and parameters are summarized in Table 3. The one-dimensional (1D) battery model is established with NCM111 cathode, LLZO solid electrolyte and lithium anode (Fig. 48). The predicted charging/discharging potential (NCM111 vs. Li/Li^+) vs. specific capacity curves by the 1D model agree well with the experiment results,¹³¹ which verifies the electrochemical parameters adopted in the 3D model in Fig. 46. Based on the validated modeling framework, further investigation into the electrochemical-mechanical coupling failure mechanism is carried out.

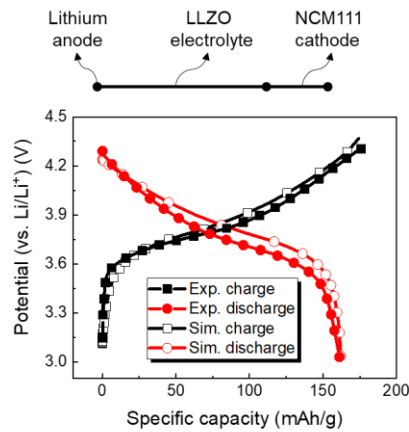


Figure 48 Comparison of the charge/discharge voltage vs specific capacity curves between experiment and simulation.

Table 3 Summary of material properties and simulation parameters

| Parameter | Symbol | Value | References |
|--------------------------------------|-------------------------------|---|------------|
| Anodic charge transfer coefficient | α_a | 0.5 | 14 |
| Cathodic charge transfer coefficient | α_c | 0.5 | 14 |
| Partial molar volume of Li metal | Ω | $9 \times 10^{-6} \text{ m}^3/\text{mol}$ | 7 |
| Faraday's constant | F | 96485 C/mol | -- |
| Gas constant | R | 8.314 J/mol/K | -- |
| Temperature | T | 293.15 K | -- |
| Electrolyte volume fraction in ECBD | ε_l | 0.9 | Estimated |
| Solid electrolyte conductivity | κ_l | 0.08 S/m | 131 |
| Electrical conductivity in ECBD | κ_s^{eff} | 1 S/m | 132 |
| Li diffusivity in particle | D_s | $D_{s11}=D_{s22}=1 \times 10^{-14} \text{ m}^2/\text{s};$ $D_{s33}=1 \times 10^{-20} \text{ m}^2/\text{s}$ | 125, 126 |
| Interfacial strength | σ_c | 100 MPa | 130 |
| Fracture toughness | G_c | 1 J/m ² | Estimated |
| Young's modulus of solid electrolyte | E_{SE} | 150 GPa | 49 |
| Young's modulus of NCM particle | E_{NCM} | 78 GPa | 133 |
| Mode mixity exponent | a | 1 | Estimated |
| Reference interfacial resistance | $R_{\text{int}}^{\text{ref}}$ | $2 \times 10^{-3} \text{ } \Omega/\text{m}^2$ | 130 |
| Reference gap | λ_{ref} | 10 nm | 130 |

5.2 Results

To obtain a basic understanding about the typical failure phenomena in composite cathode, the focus is firstly on the scenario of the cell including one NCM111 secondary particle in cathode domain (Fig. 46) at 1C constant-current (CC) charging and CC discharging scenario. The lower and upper cut-off voltages are 3 V and 4.3 V, respectively. The total charging and discharging times are 3103 s and 3008 s, respectively (Fig. 49(a)), with a Columbic efficiency (CE) of 96.94%, indicating the capacity loss caused by the internal impedance going on inside the cell. The focus of this study is mainly on the failure mechanism of composite cathode from two aspects: (a) the interfacial failure between cathode particle and its surrounding ECBD, and (b) the bulk damage inside cathode particle.

As for the interfacial failure between particle and ECBD, the concern is mainly with the interface debonding issue. Upon charging, delithiation occurs within NCM111 particle, whose overall volumetric strain is negative,⁷ i.e., the volume of NCM111 particle shrinks during delithiation (Fig. 50(a)). Meanwhile, the LLZO solid electrolyte owns the Young's modulus of 150 GPa, representing a strong stiffness to resist deformation. As a result, the interface between the particle and its surrounding ECBD begins to separate (Fig. 49(b)) once the onset criterion of the interfacial debonding is fulfilled (Eq. (52) in the Methodology part). Here the average interfacial debonding gap D_{G_ave} and maximum gap D_{G_max} are adopted to quantitatively characterize the progressive failure process at the particle-ECBD interface (Fig. 49(b)), the former representing the overall debonding

situation and the latter indicating the worst-case scenario. D_{G_ave} and D_{G_max} both gradually increase until $t=2200$ s to $D_{G_ave}=0.3$ nm and $D_{G_max}=6.8$ nm, then they rapidly increase to their maximum values $D_{G_ave}=14.3$ nm and $D_{G_max}=55$ nm at charging end ($t=3103$ s), which significantly raises the interfacial impedance, and the interfacial electrical resistance R_{int} considered in the model is exponentially related to the debonding gap (Fig. 50(b)). The increased R_{int} will cause higher charging voltage to reach the upper cut-off voltage earlier, resulting in smaller charging capacity acceptance of the cell. Meanwhile, higher R_{int} reduces the overpotential at particle-ECBD interface (Eq. (47)), thus, the electrochemical reaction kinetics is retarded. Around the charging end and discharging beginning ($t=3100\sim 3350$ s), D_{G_ave} and D_{G_max} remain at a high-value plateau, because the maximum volumetric strain (Fig. 49(c)) and the volume change of the whole particle (Fig. 50(a)) reach a plateau which directly determines the corresponding debonding gap. After $t=3350$ s, the lithiation induces the particle volume expansion, then the debonding gap decreases and the interfacial contact gradually recovers (Fig. 49(b)). The interfacial resistance exists and acts continuously during the CC discharging, possibly causing the capacity loss and the above mentioned 96.94% CE. Furthermore, at the discharging end, the debonding gap is not completely recovered ($D_{G_ave}=0.255$ nm and $D_{G_max}=0.889$ nm), which may further accumulate in long-time cycling to contribute to the performance degradation.

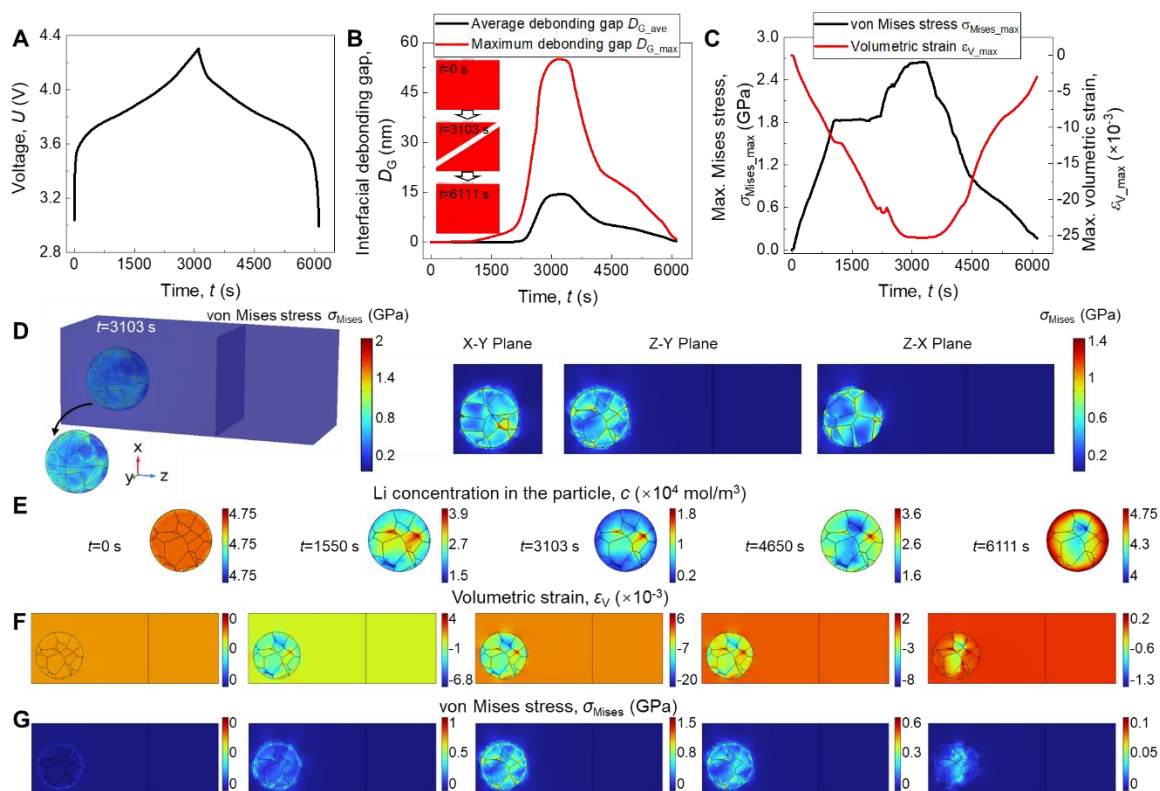


Figure 49 Electrochemical-mechanical coupled behavior of the composite cathode. (a) Cell charging/discharging voltage curve. (b) The average and maximum debonding gap at the particle-electrolyte interface, D_{G_ave} and D_{G_max} . (c) The maximum von Mises stress σ_{Mises_max} and maximum volumetric strain ε_{V_max} (negative value due to volume shrinkage) of the particle during charging/discharging. (d) The von Mises stress σ_{Mises} of the 3D cell and its cross sections at X-Y, Z-Y, Z-X planes. The contour plots of various variables at different times, including $t=0$ s (charging beginning), 1550 s (charging midpoint), 3103 s (charging end), 4650 s (discharging midpoint), and 6111 s (discharging end): (e) Li concentration in the particle c , (f) volumetric strain ε_V , and (g) von Mises stress σ_{Mises} .

The failure inside the NCM secondary particle comes down to the cracking or pulverization issues. The maximum von Mises stress σ_{Mises_max} within the particle domain increases during the CC charging process from initial stress-free status to $\sigma_{Mises_max}=2.64$ GPa at $t=3103$ s (Fig. 49(c)), which basically is the result of the lithiation/delithiation-induced deformation as well as the constraint from the surrounding ECBD. Such a large

stress is most probably to cause the cracking failure of the particle. At the charging end ($t=3103$ s), the stress is mainly concentrated around and inside the particle domain, and the region away from the particle remains at a low stress status, as can be seen from the 3D profiles of von Mises stress σ_{Mises} of the whole cell (Fig. 49(d)). To take a further look at the phenomena occurring inside the secondary particle, three 2D cross sections are cut from the 3D geometry, i.e., X-Y, Z-Y, and Z-X planes. Surprisingly, σ_{Mises} distributes nonuniformly in all the cross sections, especially at the boundaries of the primary particles (Fig. 49(d)). The Z-Y profiles of the dominant variables (namely, Li concentration c , volumetric strain ε_V , and von Mises stress σ_{Mises}) at specific times are collected to give out an understanding of the overall evolution process during battery operation, including the charging/discharging start, middle, and end times (i.e., $t=0, 1550, 3103, 4650, 6111$ s). At the beginning, the particle is at a free-stress/strain state with uniform initial concentration distribution ($t=0$ s, Figs. 49(e-g)). During the charging process (along with delithiation of NCM particle), c decreases throughout the particle, simultaneously showing the overall trend of smaller c closer to the particle surface ($t=1550$ s, Fig. 49(e)), due to the fact that charge transfer reaction occurs at the particle-ECBD interface. However, c evolves in a nonuniform way, which is caused by the randomly distributed primary particles with different crystallographic orientations. Since both the diffusivity and expansion coefficient are different along [100], [010], [001] directions of the primary particles, the overall Li diffusion and volume change show markedly anisotropic behaviors for the secondary

particle, eventually resulting in the significant nonuniformity of c and ε_v ($t=1550$ s, Figs. 49(e-f)). Though the overall volumetric strain is negative for NCM secondary particle during charging (i.e., secondary particle volume shrinks), the delithiation-induced strains are negative along [100] and [010] directions (volume contraction) while positive along [001] direction (volume expansion). Such mismatch of volume change further aggravates the nonuniformity of the strain (Fig. 49(f)). giving rise to the nonuniform stress profiles (Fig. 49(g)). As the charging process continues, the maximum stress and strain increase, and the stress/strain fields become more inhomogeneous, especially at the boundaries of the small primary particles ($t=3103$ s, Figs. 49(f-g)), eventually leading to the experimentally observed cracks inside NCM secondary particles^{125, 134, 135} because of weaker grain boundary connections between primary particles compared to particle bulk domains. During the discharging process, the lithiation leads to larger c closer to secondary particle surface ($t=4650$ s and 6111 s, Fig. 49(e)). The nonuniform c and the inhomogeneous volume change of the primary particles (expansion along [100], [010] directions, contraction along [001] direction) cause the nonuniformity of strain and stress distribution ($t=4650$ s and 6111 s, Figs. 49(e-f)). Interestingly, at discharging end, the Li concentration is not recovered to its initial state, and there are residual stress and strain within the particles, which may partially contribute to the above mentioned 96.94% CE and may also accumulate during the cycling to further degrade the cell performance.

In short, both interface debonding failure at the particle-ECBD interface and the cracking failure inside the particle are the results from electrochemistry-mechanics interactions, mainly from three aspects: (1) lithiation-induced volume contraction under the constraint by the surrounding stiff ECBD; (2) structural inhomogeneity caused by the randomly distributed crystallographic orientations of the primary particles with anisotropic Li diffusion; (3) nonuniform Li concentration and volume variation mismatch-caused concentrated stress around the boundaries of primary particles. The failure mechanism of composite cathode in ASSBs is basically understood, based on which the effects from various governing factors are investigated, including the charging rate, heterogeneity, interfacial strength, and particle position, to further dig out the dominant variables and provide possible improvement guidance on improvement of composite cathode.

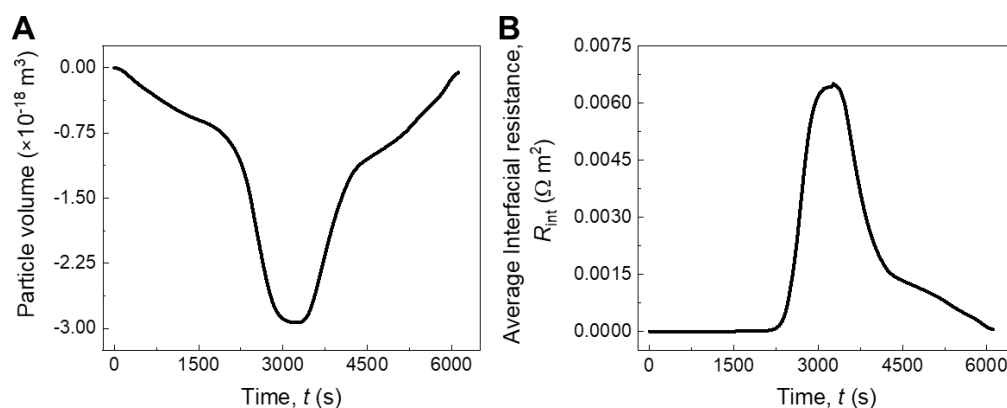


Figure 50 (a) The total volume change of the NCM111 secondary particle during the charging/discharging at 1C. (b) The average interfacial resistance R_{int} calculated from the average debonding gap.

5.3 Discussion

5.3.1 Charging rate effect

Achieving high charging rates (C-rates) is one of the main limiting factors for the commercialization of the current ASSBs, due to the severe mechanical instability and dendritic issues at large applied current densities. A series of C-rates are selected herein, i.e., 0.1C, 0.5C, 1C, 2C, to investigate the C-rate effect on the failure behavior inside composite cathode of ASSBs. To fairly compare the results at different time scales from various C-rates, the actual time t is normalized by the nominal charging time τ at each C-rate, namely $\tau=36000$ s, 7200 s, 3600 s, 1800 s for 0.1C, 0.5C, 1C, 2C, respectively. The CC charging-CC discharging scenario is discussed here, and the scenario with constant-voltage (CV) charging is included in the supplementary materials.

The cell at a higher C-rate shows a smaller charging/discharging capacity (Fig. 51(a)), which is usually attributed to the larger interfacial polarization and larger voltage drop caused by internal resistance, but the root cause is that the Li stored in the NCM secondary particle is less exchanged to anode at higher C-rates (Fig. 51(b)). With the help of the established model, the total amount of Li M_{Li} is calculated by integral of the Li concentration c within the secondary particle domain, and M_{Li} decreases during charging due to the delithiation and vice versa for discharging (Fig. 51(b)). For the secondary particle, the initial $M_{Li}=24.659\times 10^{-12}$ mol at $t=0$ s decreases to $M_{Li}=1.666\times 10^{-12}$, 2.362×10^{-12} , 3.203×10^{-12} , 4.615×10^{-12} mol at the charging end for 0.1C, 0.5C, 1C, 2C, respectively,

which serves as the direct evidence that more Li remains within the NCM particle without participating the charge transfer reaction at a higher C-rate, thus the charging capacity is reduced. The concentration c that directly indicates the delithiation state determines the volumetric strain ε_V (Fig. 51(c)) and the corresponding deformation (namely, particle volume change, Fig. 52) where particle is in a volume shrinkage process during charging, resulting in increased stress σ_{Mises} inside the particle (Fig. 51(d)). Note that the peak values of maximum ε_V and σ_{Mises} are very close for all the C-rates, i.e., $\varepsilon_{V_max}=-0.0253$ and $\sigma_{\text{Mises_max}}=2.64$ GPa, since they all reach the plateau stage. Nevertheless, the particle at high C-rates owns a less contracted volume (Fig. 52) due to more Li remained in the particle, especially at 2C case, thus the peak values of the maximum and average debonding gaps of particle-ECBD interface are smaller at 2C at charging end, i.e., $D_{G_ave}=13.5$ nm and $D_{G_max}=52.5$ nm, compared to $D_{G_ave}=14.3$ nm and $D_{G_max}=55$ nm at 1C (Figs. 51(e-f)).

The higher C-rate appears to contribute less to the interfacial failure and bulk damage during charging process, evaluated by D_G and σ_{Mises} , respectively, whereas, the situation is completely reversed once the discharging process is included. During the discharging (lithiation of NCM particle), the Li amount M_{Li} in the particle increases, and correspondingly, the other main state variables (i.e., ε_V , σ_{Mises} , D_{G_ave} and D_{G_max}) gradually recover. However, these variables are incapable to completely recover at discharging end to their initial state at charging beginning (Fig. 51(b-f)). The total Li amount $M_{\text{Li}}=24.518 \times 10^{-12}$, 24.058×10^{-12} , 23.647×10^{-12} , 22.772×10^{-12} mol at the discharging end

for 0.1C, 0.5C, 1C, 2C, respectively, are lower than the initial $M_{Li}=24.659\times 10^{-12}$ mol at $t=0$ s, which also indicates that M_{Li} at a higher C-rate shows a larger residual discrepancy to the fully recovered state (Fig. 51(b)). Consequently, at the discharging end, the maximum volumetric strain and von Mises stress have larger residual values at higher C-rates, i.e., $\varepsilon_{V_max}=-0.0398\times 10^{-3}$, -0.835×10^{-3} , -3.032×10^{-3} , -5.891×10^{-3} , and $\sigma_{Mises_max}=0.003$, 0.048, 0.166, 0.327 GPa for 0.1C, 0.5C, 1C and 2C, respectively (Fig. 51(c-d)). Possible damage to the bulk particle could be caused by the residual ε_V and σ_{Mises} , especially at high C-rates with larger residual stress/strain, which may also be further accumulated after a long-term cycling and the progressive damage finally leads to the crack or pulverization of the particle. Furthermore, the particle volume at discharging end cannot be restored to its original state of good interfacial contact with the surrounding ECBD (Fig. 52), and the unrecovered interface debonding gap after the CC discharging is larger at higher C-rates, i.e., $D_{G_ave}=0.01$, 0.052, 0.255, 0.762 nm and $D_{G_max}=0.036$, 0.181, 0.889, 2.688nm for 0.1C, 0.5C, 1C and 2C, respectively (Fig. 51(e-f)), indicating larger interfacial impedance at higher C-rates, which could partially contribute to the deteriorated performance at higher C-rates. The cell at higher C-rates shows a worse interfacial contact and larger residual stress/strain within bulk particle after CC charging and discharging, which may be alleviated by adding the CV charging step but still cannot be completely recovered (Fig. 53).

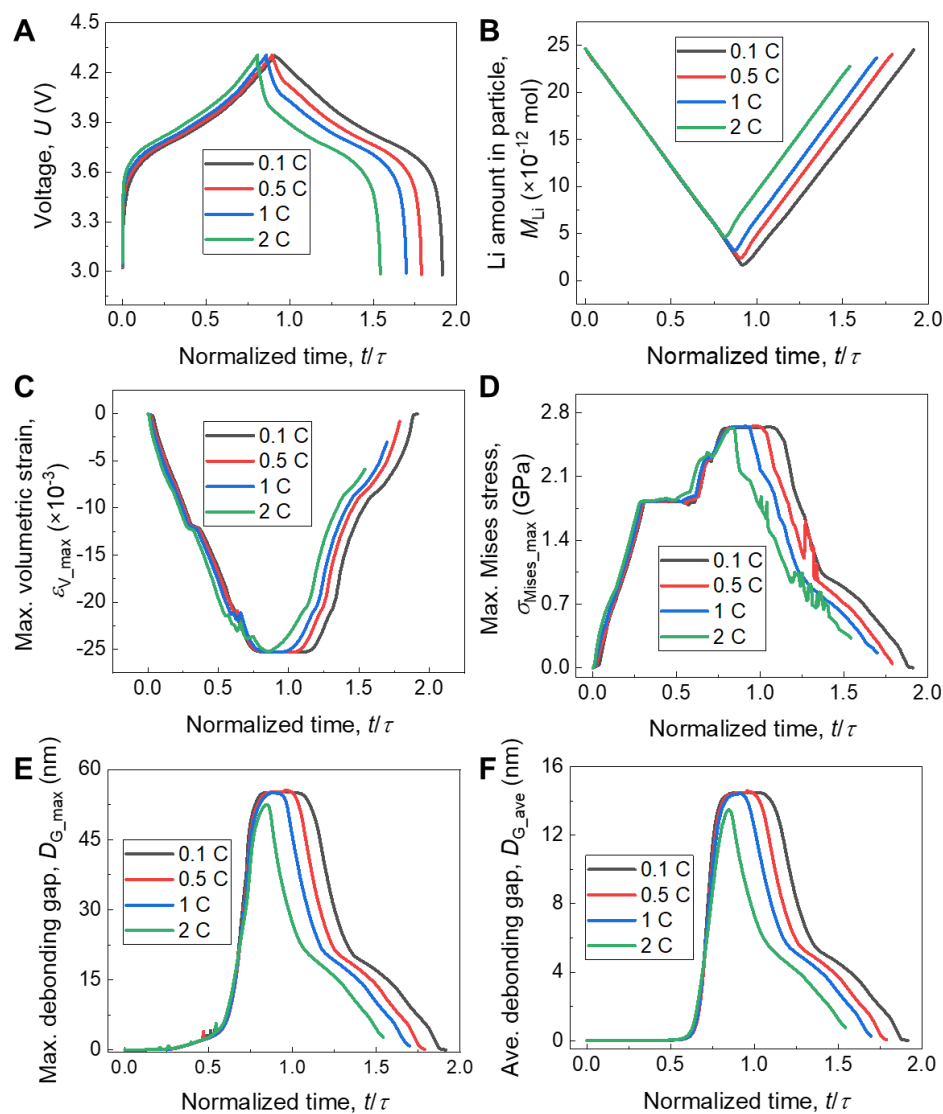


Figure 51 Effect of charging rate on the electrochemical-mechanical behavior of composite cathode in ASSBs. (a) Cell charging/discharging voltage curves of different charging rates, i.e., C-rate=0.1C, 0.5C, 1C, and 2C. (b) Li amount M_{Li} in the secondary NMC-111 particle. (c) Maximum volumetric strain of the particle ε_{V_max} . (d) Maximum von Mises stress for the particle σ_{Mises_max} . (e) Maximum interfacial debonding gap D_{G_max} . (f) Average interfacial debonding gap D_{G_ave} . Note that the time t is normalized by the nominal charging time τ ($\tau=36000s, 7200s, 3600s, \text{ and } 1800s$ for 0.1C, 0.5C, 1C and 2C, respectively).

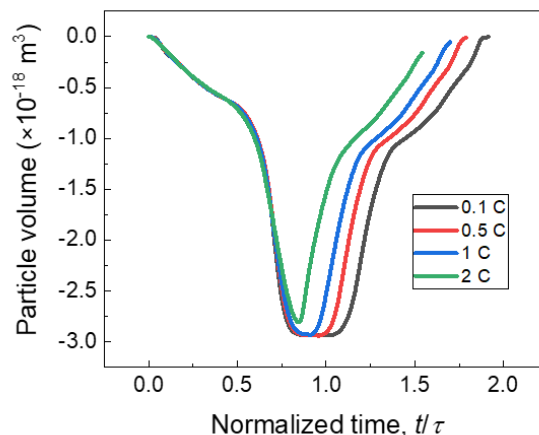


Figure 52 The total volume change of the particle during the charging/discharging at various C-rates.

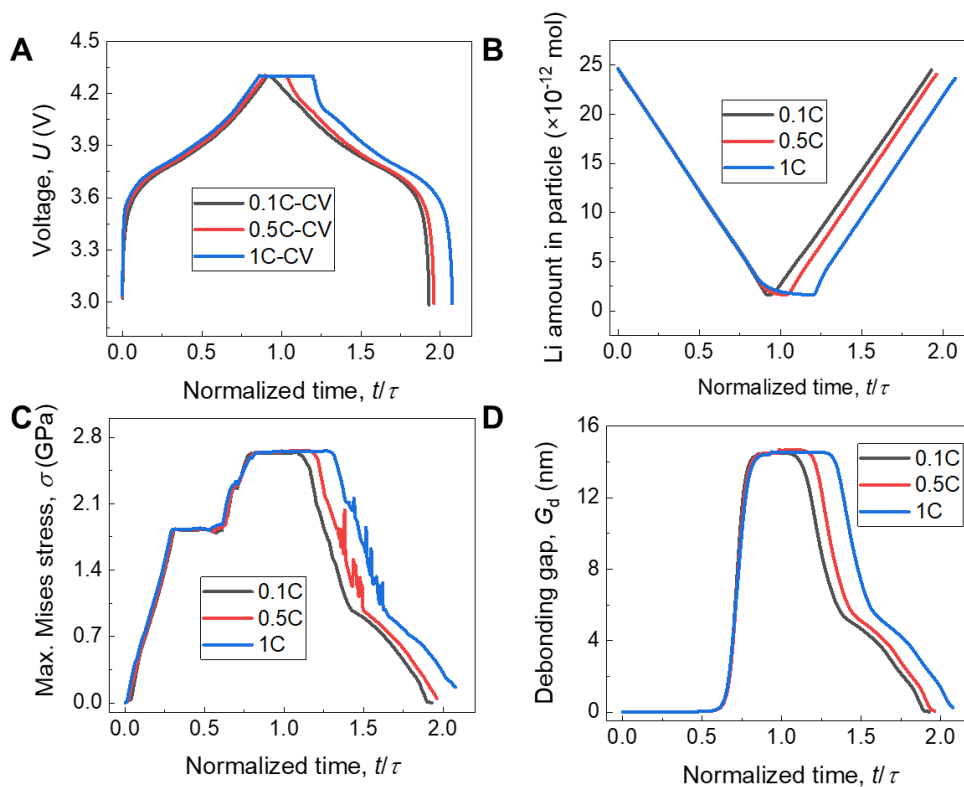


Figure 53 Effect of charging rate on the electrochemical-mechanical behavior of composite cathode in ASSBs with constant-voltage (CV) charging stage taken into account. (a) Cell charging/discharging voltage curves of different charging rates, i.e., C-rate=0.1C, 0.5C, 1C. (b) Li amount M_{Li} in the secondary NMC-111 particle. (c) Maximum von Mises stress for the particle σ_{Mises_max} . (d) Average interfacial debonding gap D_{G_ave} .

5.3.2 Heterogeneity effect

The NCM secondary particle is the heterogeneous mixture composed of many randomly distributed primary particles with various size and different crystallographic orientations. The orientation-determined Li diffusivity and expansion coefficient of primary particles lead to significant heterogeneous distribution of the Li concentration, stress, strain within the secondary particle (Figs. 49(e-f)). In the baseline model, the anisotropic diffusivity D_s (Eq. (55)) and anisotropic expansion coefficient matrix θ_β (Eq. (61)) are employed, i.e., $D_{s11}=1 \times 10^{-14}$, $D_{s22}=1 \times 10^{-14}$, $D_{s33}=1 \times 10^{-20}$ m²/s, and $\theta_{\beta11}=1$, $\theta_{\beta22}=1$, $\theta_{\beta33}=-1$ along [100], [010], [001] directions of each primary particle, respectively, which serves as the baseline scenario (*Case 1*). To further look into the heterogeneity effect, various cases with different D_s and M_β are considered (Fig. 54)--*Case 1*: baseline scenario; *Case 2*: isotropic D_s ($D_{sii}=1 \times 10^{-14}$ m²/s ($i=1, 2, 3$)), and θ_β ($\theta_{\beta11}=\theta_{\beta22}=1$, $\theta_{\beta33}=-1$); *Case 3*: isotropic D_s , and θ_β ($\theta_{\beta11}=\theta_{\beta22}=1$, $\theta_{\beta33}=-0.5$); *Case 4*: isotropic D_s , and θ_β ($\theta_{\beta11}=\theta_{\beta22}=1$, $\theta_{\beta33}=0$). Specifically, *Case 1* and *2* are to explore the heterogeneity effect from diffusivity, and *Case 2*, *3* and *4* are to study the heterogeneity effect from expansion. Note that 1C C-rate is selected for all the following discussions.

Switching Li diffusivity D_s from the anisotropic *Case 1* to isotropic *Case 2*, the cell charging/discharging time are both elongated from 3103 s/3008 s to 3185 s/3155 s (Fig. 54(a)), due to the facts that the particle is more delithiated during charging and less Li remains at the charging end in *Case 2*, and more Li remains at the discharging end in *Case*

1 (Fig. 54(b)). The corresponding Columbic efficiency is increased from 96.94% (*Case 1*) to 99.06% (*Case 2*), indicating that increasing D_s and reducing the diffusive anisotropy are beneficial for battery performance improvement. Since the maximum volumetric strain and particle volume change during charging are close for *Case 1* and 2 (Figs. 55(a-b)), the peak values of debonding gap D_{G_ave} and stress σ_{Mises_max} are also close (Figs. 54(c-d)). However, the Li concentration shows a much greater nonuniformity in *Case 1* (Fig. 54(e)). Moreover, at the discharging end, the residual Li amount in the particle ($\Delta M_{Li} = M_{Li, \text{charging beginning}} - M_{Li, \text{discharging end}}$) in anisotropic *Case 1* $\Delta M_{Li} = 1.012 \times 10^{-12}$ mol is larger than that of isotropic *Case 2* $\Delta M_{Li} = 0.744 \times 10^{-12}$ mol, which is caused by the slow diffusivity $D_{s33} = 1 \times 10^{-20}$ m²/s in *Case 1*. Larger ΔM_{Li} results in larger residual debonding gap and stress at the discharging end, namely, $D_{G_ave} = 0.255$ nm and $\sigma_{Mises_max} = 0.166$ GPa in *Case 1*, both larger than $D_{G_ave} = 0.092$ nm and $\sigma_{Mises_max} = 0.069$ GPa in *Case 2*. It implies that, smaller and anisotropic D_s could also impose more mechanical damage to the particle and debonding issue in addition to the capacity reduction.

The lithiation/delithiation-induced deformation along [001] direction of the NCM primary particle is opposite to other directions, as can be reflected by $\theta_{\beta11} = 1$, $\theta_{\beta22} = 1$, $\theta_{\beta33} = -1$ along [100], [010], [001] directions, respectively, which causes the deformation mismatch of adjacent primary particles (Fig. 49(f)) since their orientations are randomly generated and distributed. Such deformation mismatch further induces greater stress heterogeneity inside the secondary particle, and the stress mainly concentrates along the

boundaries of primary particles (*Case 1-2*, Fig. 54(f)). *Case 3* and *4* take $\theta_{\beta 33}=-0.5$ and $\theta_{\beta 33}=0$, respectively, which means less opposite deformation to other two directions ($\theta_{\beta 11}=\theta_{\beta 22}=1$) compared to *Case 2* ($\theta_{\beta 33}=-1$). The deformation mismatch (i.e., volumetric strain heterogeneity) in *Case 4* is significantly alleviated than *Case 3*, which is also much better than *Case 2* (Fig. 55(d)). Subsequently, the peak values of the von Mises stress and the stress distribution nonuniformity both follow *Case 4*<*Case 3*<*Case 2* (Figs. 54(d) and (f)). Furthermore, due to the more uniform stress profile and thus less stress effect on Li diffusion (Eq. (55)), the Li concentration profile is more uniform in *Case 4* than *Case 3* and *Case 2* (Fig. 54(e)). Since the deformation along [001] direction is less expanded and more contracted for *Case 3-4* than *Case 2* during the charging process, the particle volume at the charging end *Case 4*<*Case 3*<*Case 2* (Fig. 55(b)) causes the interface debonding gap *Case 4*>*Case 3*>*Case 2* (Fig. 54(c)). The larger interfacial resistance caused by the larger debonding gap results in higher voltage drop across the interface (Fig. 55(c)) and thus shorter charging period of *Case 4* (Fig. 54(a)). To briefly summarize, the less opposite and less anisotropic expansion coefficient will cause more uniform concentration, strain, and stress profiles, thus less adverse effect from heterogeneous structure, which shows a promising improvement direction to control the crystallographic orientations of primary particles.

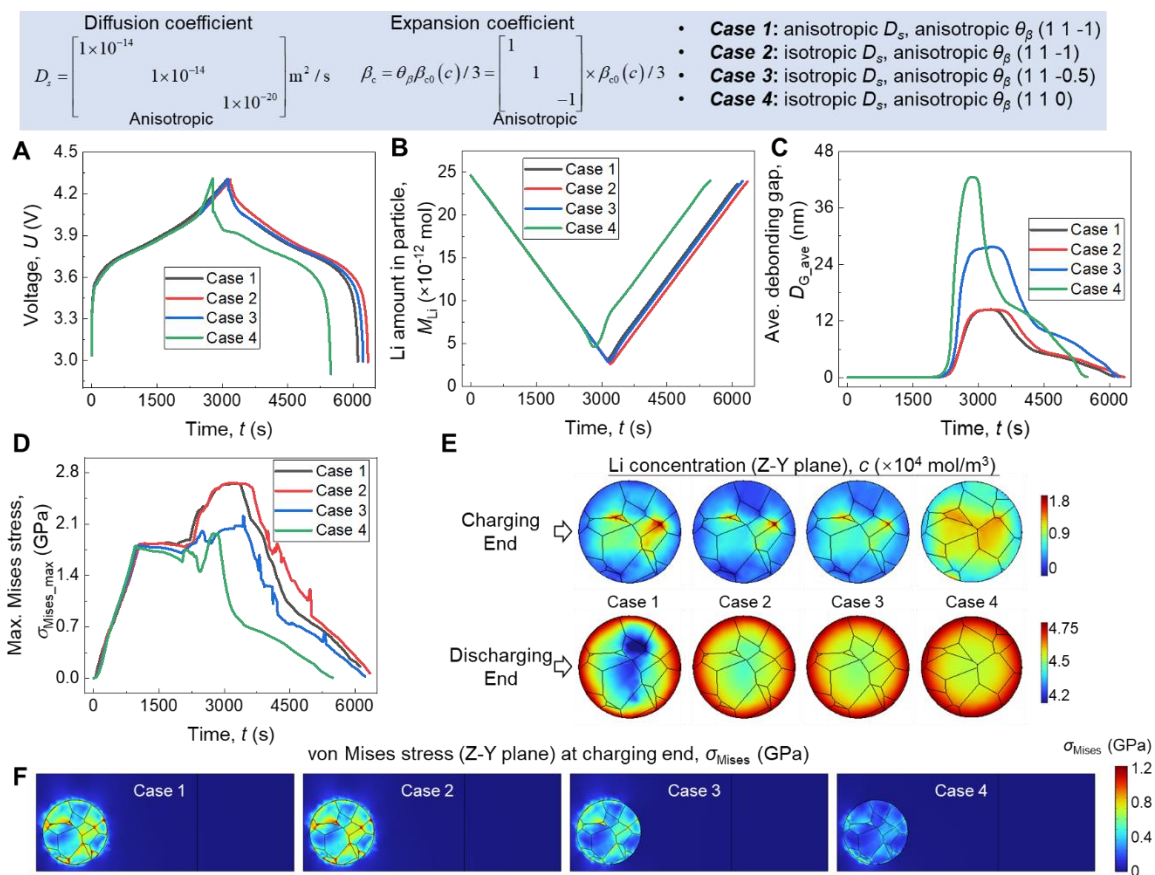


Figure 54 Effect of heterogeneity from diffusivity and expansion coefficient on the electrochemical-mechanical behavior of composite cathode in ASSBs. (a) Cell charging/discharging voltage curves at different diffusion and expansion cases. (b) Li amount M_{Li} in the NCM111 secondary particle. (c) Average interfacial debonding gap $D_{G,ave}$. (d) Maximum von Mises stress for the particle $\sigma_{Mises,max}$. (e) Li concentration c profiles of the Z - Y plane in the NCM111 secondary particle, at charging end and discharging end. (f) von Mises stress σ_{Mises} profiles of the Z - Y plane at charging end.

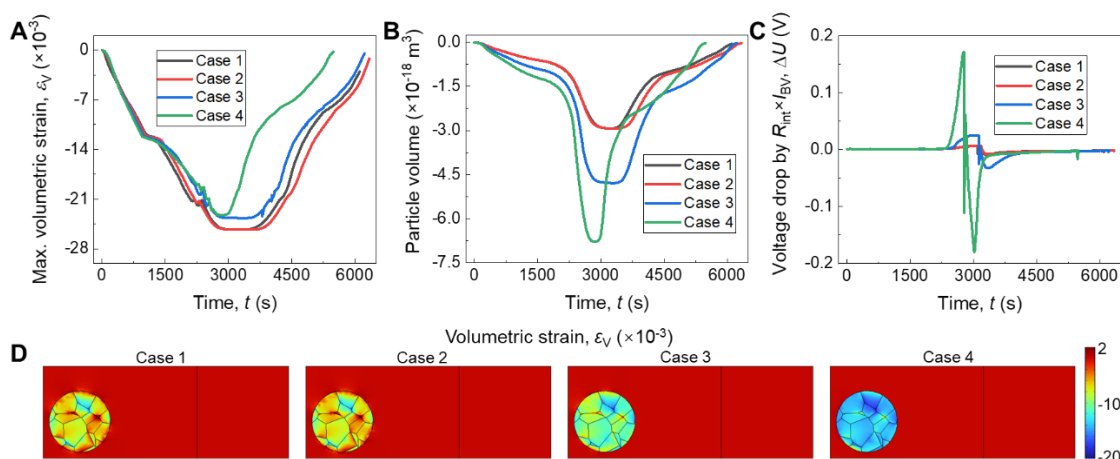


Figure 55 Effect of heterogeneity from diffusivity and expansion coefficient on the electrochemical-mechanical behavior of composite cathode in ASSBs. (a) Maximum volumetric strain of the particle ε_{V_max} . (b) Total volume change of the particle during the charging/discharging. (c) The average value of the voltage drop caused by the interfacial resistance induced by interface debonding gap. (d) The Z-Y plane contour plots of volumetric strain at charging end.

5.3.3 Interfacial strength effect

Interfacial modification or increasing the interfacial strength is a commonly adopted method to improve the interface contact between particle and surrounding electrolyte for better long-term cyclability performance. However, one question still remains to be answered: is stronger interfacial strength always beneficial for the composite cathode? Herein various interfacial strength σ_c are selected as *Case 1-4*, namely, $\sigma_c=50, 100$ (baseline), 200, 500 MPa, and based on the reference distance of 10 nm, the corresponding fracture toughness G_c also varies ($G_c=0.5, 1, 2, 5 \text{ J/m}^2$, for *Case 1-4*, respectively). Note that the strength is assumed the same in normal and shear directions.

The cell voltage shows little difference at different interfacial strength in *Case 1-4* (Fig. 56(a)), which can be explained by their close Li amount in the particle (Fig. 57(a)). The interfacial strength serves as the mechanical constraint boundary condition for the deformation of the particle. Since stronger interfacial strength imposes a higher threshold value for the onset of interfacial separation/debonding, the interfacial debonding gap D_{G_ave} decreases with increasing σ_c (Fig. 56(b)) and the D_{G_ave} peak values are 19.9, 14.3, 1.1, 0.027 nm for $\sigma_c=50, 100, 200, 500$ MPa, respectively. The similar trend also exists for D_{G_max} (Fig. 57(b)). The debonding gap is nearly 0 at *Case 4* with high $\sigma_c=500$ MPa, indicating that increasing the interfacial strength to a certain value can address the interface debonding issue. The average value of voltage drop across the interface caused by the interfacial resistance is larger at lower σ_c , but the maximum value is still small below 0.015V (Fig. 57(a)), which can also explain the close voltage responses at *Case 1-4*. Since the higher σ_c constrains the volume shrinkage of the particle more strictly during charging, the volumetric strain ε_{V_max} gets larger to adapt to the particle contraction under the stronger constraint (Fig. 56(c), resulting in larger stress σ_{Mises_max} (Fig. 56(d)). Both ε_{V_max} and σ_{Mises_max} peak values increase with σ_c , i.e., $\varepsilon_{V_max}=-26\times 10^{-3}$, -25.3×10^{-3} , -33.7×10^{-3} , -46.2×10^{-3} , and $\sigma_{Mises_max}=2.1, 2.64, 3.86, 9.7$ GPa for $\sigma_c=50, 100, 200, 500$ MPa, respectively. σ_{Mises} on the particle surface at certain points significantly increases with σ_c , as shown by the red region in Fig. 56(e), and σ_{Mises} inside the particle also shows an increasing trend (Fig. 56(f)). The peak stress σ_{Mises_max} reaches above 9GPa at $\sigma_c=500$ MPa,

which is most probably to cause mechanical damage to the particle, such as crack or pulverization. Based on the above discussion, it's discovered that, increasing the interfacial strength inside composite cathode has competing contributions to the cell performance: suppressing the interface debonding to reduce interfacial impedance, and inducing high stress to cause possible mechanical damage to the particle. Thus, controlling the particle volume variation and adopting appropriate interfacial strength may be a proper way to both ensure interfacial contact and avoid particle damage.

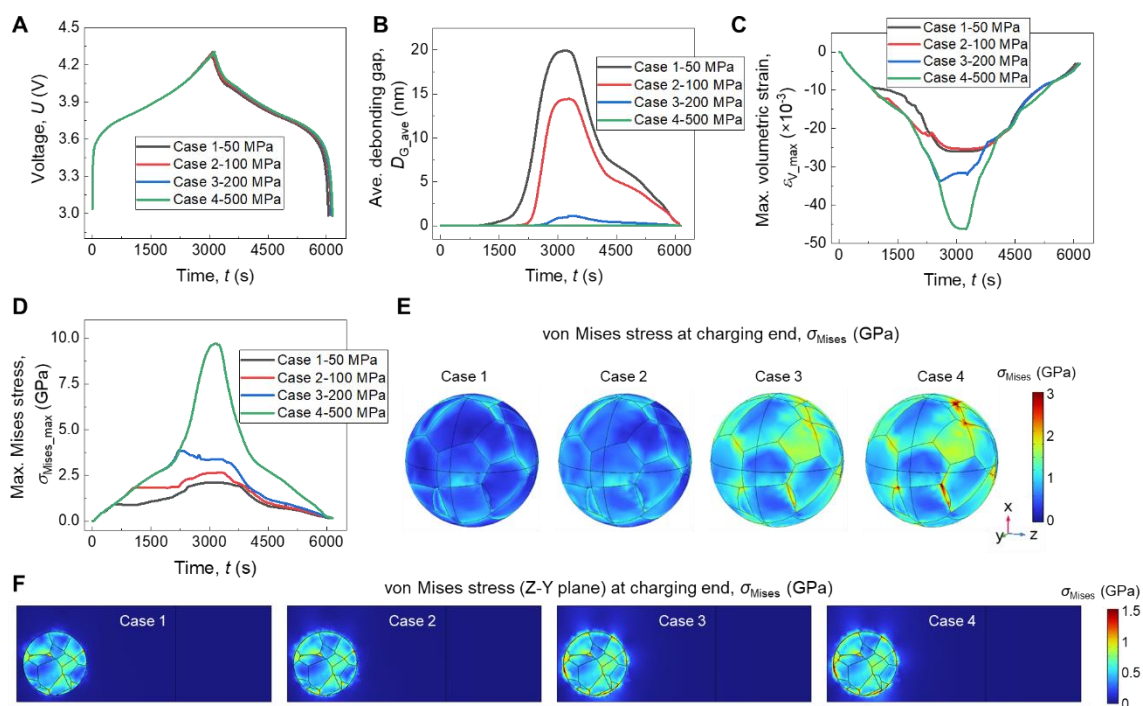


Figure 56 Effect of interfacial debonding strength on the electrochemical-mechanical behavior of composite cathode in ASSBs. (a) Cell charging/discharging voltage curves at different interface debonding strength, i.e., 50 MPa, 100 MPa, 200MPa, and 500MPa. (b) Average interfacial debonding gap D_{G_ave} . (c) Maximum volumetric strain of the particle ε_{V_max} . (d) Maximum von Mises stress for the particle σ_{Mises_max} . (e) Von Mises stress σ_{Mises} profiles of the particle at charging end. (f) Von Mises stress σ_{Mises} profiles of the Z-Y plane at charging end.

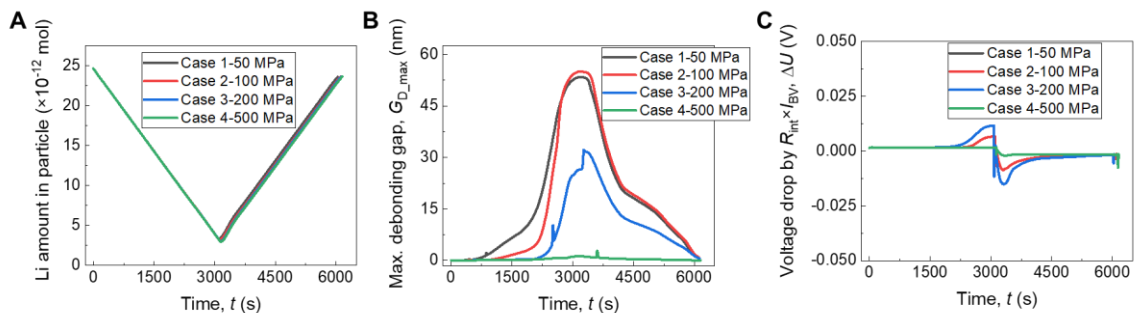


Figure 57 Effect of interfacial debonding strength on the electrochemical-mechanical behavior of composite cathode in ASSBs. (a) Li amount M_{Li} in the NCM secondary particle at different interfacial strength, i.e., 50 MPa, 100 MPa, 200MPa, and 500MPa. (b) Maximum debonding gap at the electrolyte-particle interface D_{G_max} . (c) The average value of the voltage drop caused by the interfacial resistance induced by interface debonding gap.

5.3.4 Particle position effect

The composite cathode in ASSBs contains numerous NCM secondary particles, whose positions are randomly distributed in x , y , z directions. Usually the active materials in the x - y plane are considered uniform at a fixed z value. Here the effect from particle position along the z direction on the electrochemical-mechanical behavior of composite cathode in ASSBs is investigated. Two particles are included, i.e., P1 and P2 (Fig. 58(a)). P1 is closer to the anode side and P2 is closer to cathode current collector, and the z -axis distance between P1 and P2 is 12 μm . The stress mainly concentrates around or within the particle domain (Fig. 58(a)).

During charging, the movement direction of Li ions is from cathode particle to the anode side, and the NCM particle closer to anode side will be firstly delithiated, which can be evidenced by the lower Li amount in P1 at charging beginning (Fig. 59). Similarly, during discharging, the particle closer to anode side is more lithiated, and P1 has a larger

Li amount at discharging end than P2. The peak value of the maximum interfacial debonding gap D_{G_max} of P1 is 26.93 nm larger than 26.66 nm of P2 (Fig. 58(b)), indicating that the particle closer to anode side suffers worse interface debonding issue, which implies that gradient design for the interfacial strength may be in need to make the particle interfacial durability the same through the thickness. Moreover, during the middle stage of the charging process ($t=1200\sim 2200$ s), the maximum volumetric strain ε_{V_max} of P1 is about 2×10^{-3} larger than that of P2 (Fig. 58(c)), which demonstrates more serious deformation in P1. Correspondingly, the maximum von Mises stress σ_{Mises_max} within P1 is also larger during this period (Fig. 58(d)), indicating larger mechanical damage occurring in P1. The above results indicate the particle closer to anode side suffers more severe interfacial debonding and bulk damage, which should be treated with enhanced properties during fabrication.

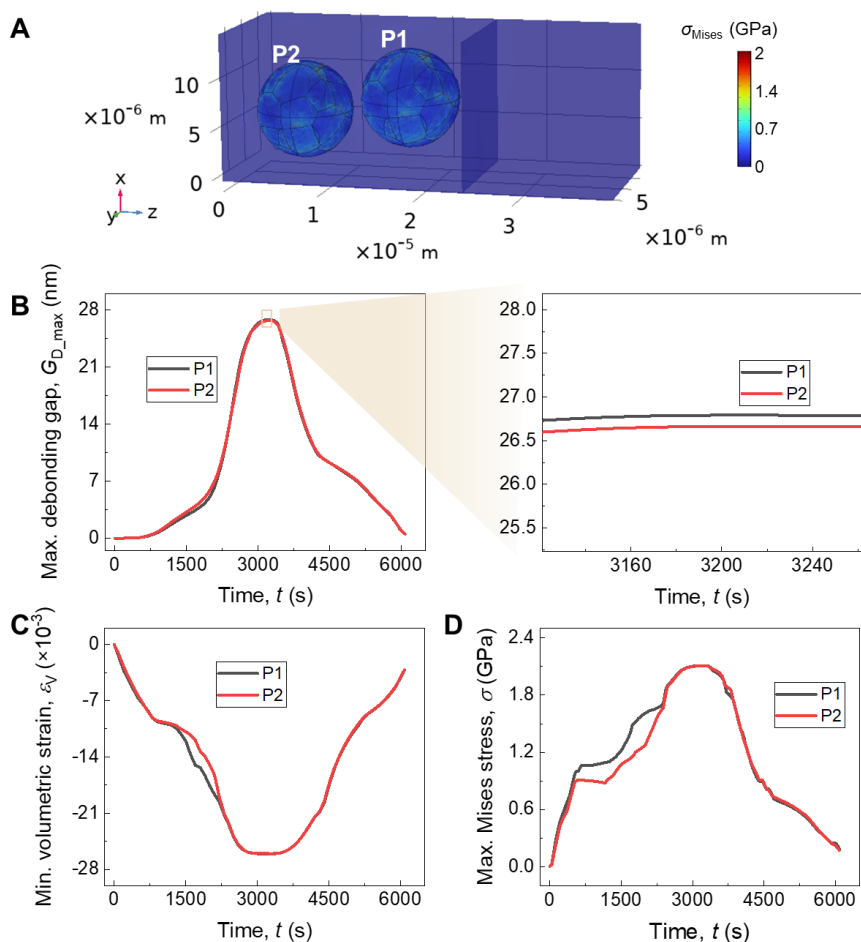


Figure 58 Effect of particle position on the electrochemical-mechanical behavior of composite cathode in ASSBs. (a) Von Mises stress σ_{Mises} profiles of the cell at charging end. (b) Maximum interfacial debonding gap D_{G_max} . (c) Maximum volumetric strain of the particle ε_{V_max} . (d) Maximum von Mises stress for the particle σ_{Mises_max} .

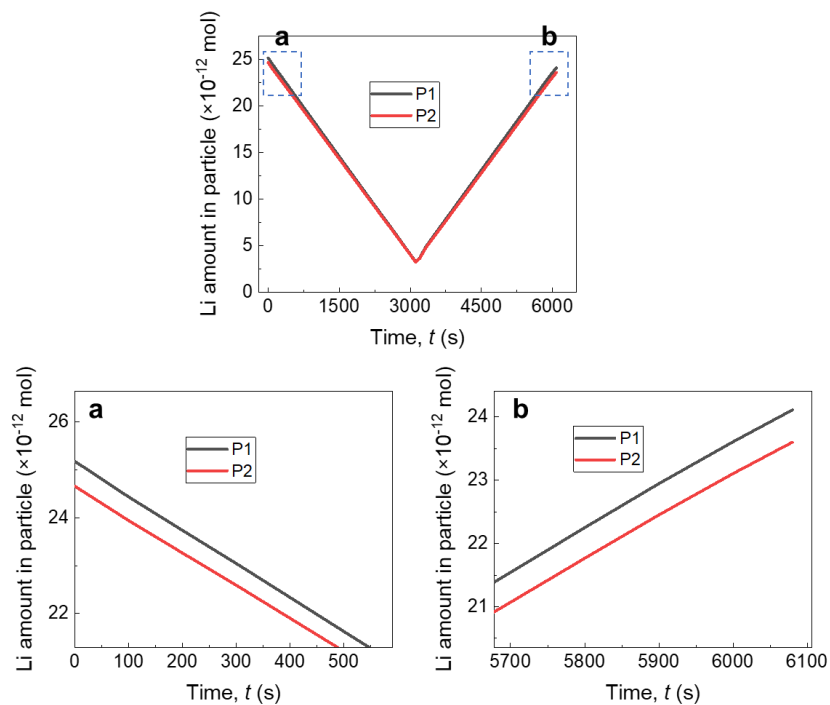


Figure 59 Li amount in the NCM secondary particles (P1 and P2), with zoomed-in views at charging beginning and discharging end.

5.4 Conclusion

The failure issues occurring inside the composite cathode of ASSBs are complicated multiphysics phenomena involving electrochemistry and mechanics, mainly manifested as particle damage and the interfacial failure. Considering the electrochemical reaction kinetics, Li diffusion process, mechanical deformation and interface debonding, the 3D electrochemical-mechanical coupled model is developed in this study to unravel the underlying failure mechanism. The randomly distributed NCM111 primary particles inside the secondary particle result in the anisotropic Li diffusion and volume variation, which lead to significant nonuniformity of the Li concentration, strain, and stress profiles

especially along the boundaries of primary particles, finally causing the internal cracks or pulverization of the secondary particle. The NCM particle volume shrinks during charging while under the constraint of the surrounding stiff ECBD domain, gradually inducing the interface debonding and increasing the interfacial impedance to degrade cell capacity. Cell at larger C-rates show a smaller charging capacity and larger residual stress/strain/debonding gap at discharging end, thus more likely to deteriorate the performance, which may be partially improved by adding CV charging step. Furthermore, more homogeneous Li diffusivity and less anisotropic expansion coefficient will cause more uniform concentration, strain and stress profiles, thus reducing adverse effect from heterogeneous structure. Increasing the interfacial strength between particle and ECBD can suppress the interface debonding but also induce high stress to cause possible mechanical damage to the particle, so simultaneously controlling the particle volume variation and adopting appropriate interfacial strength may be a proper way to both ensure interfacial contact and avoid particle damage. Lastly, particle closer to anode side suffers more severe interfacial debonding and bulk damage, which may be improved with enhanced properties during fabrication. Results in this study provide comprehensive understanding of the electrochemical-mechanical coupling failure mechanism inside composite cathode, shedding light on the further improvement of more robust composite cathode for ASSBs.

CHAPTER 6 CONCLUDING REMARKS

In this work, we developed a systematic study of the multiphysics behavior for dendrite growth and mechanical instability of composite cathode in ASSBs. First, the fully coupled electrochemical-mechanical phase-field model at the electrolyte scale was developed to study the coupled dendrite growth and crack propagation behaviors in polycrystalline solid electrolyte. It was revealed that the newly formed crack provides further space for dendrite to grow and the grain boundary is the preferential path for dendrite growth. We found that applying stacking pressure to ASSBs can improve interfacial contact but also provide mechanical driving force for dendrite and crack. Then, the multiphysics modeling framework integrating the battery model, mechanical model, phase-field model and short-circuit model was established to investigate the entire process from battery charging to dendrite growth and to the final short circuit. The overpotential-induced interfacial stress between dendrite and SE was found to drive the dendrite penetration through SE to short circuit the ASSB cell at high C-rates, and the stress status at the dendrite tip determines the dendrite growth direction. The governing effects from C-rates, electrolyte conductivity, Young's modulus, and fracture toughness were comprehensively discussed. Furthermore, inspired by the "brick-and-mortar" structure, the dendrite mitigation strategy was proposed by inserting heterogeneous blocks into solid electrolyte to reduce the lithium penetration-induced short circuit risk, and the overall mechanism map for mitigation strategy was provided. Last, the three-dimensional fully

coupled electrochemical-mechanical model was developed to investigate the mechanical instability issues inside composite cathode of ASSBs, considering the electrochemical reaction kinetics, Li diffusion within particle, mechanical deformation, and interfacial debonding. It was discovered that the NCM particle volume shrinkage under the constraint of the surrounding electrolyte causes the interfacial debonding with increased interfacial resistance to degrade the cell capacity. The randomly distributed NCM primary particles further result in the anisotropic Li diffusion and volume variation inside the secondary particle, resulting in significant nonuniformity of the Li concentration, strain, and stress distributions. Such inhomogeneities ultimately cause the internal cracks or particle pulverization.

This work explores the dendritic issue and mechanical instability problem inside ASSBs from particle scale to cell scale through the multiphysics modeling approaches. The established electrochemical-mechanical models reflect the real physical processes from battery operation to dendrite growth inside solid electrolyte and particle-electrolyte interfacial failure, and quantitatively reveal the evolution of dominant variables including dendrite order parameter, concentration, potential, deformation, stress, and interfacial debonding gap. The results provide directions for the cell operating conditions (*i.e.*, stacking pressure, C-rate), material selection (*i.e.*, electrolyte with high fracture toughness and high conductivity, and active particle with minimum volume variation and heterogeneity), electrolyte structure design, and interfacial modification (*i.e.*, appropriate

interfacial strength), to improve the dendritic issue and mechanical damage of the active particles in ASSBs. This work gives out an in-depth understanding of the complicated electrochemical-mechanical coupling mechanism as well as provides insightful mechanistic design guidance maps for robust and safe ASSB cells.

REFERENCES

- [1] Y. Jia, J. Li, C. Yuan, X. Gao, W. Yao, M. Lee and J. Xu, Data-Driven Safety Risk Prediction of Lithium-Ion Battery, *Adv. Energy Mater.* 11 (2021) 2003868.
- [2] J. Deng, C. Bae, A. Denlinger and T. Miller, Electric Vehicles Batteries: Requirements and Challenges, *Joule* 4 (2020) 511-515.
- [3] C. Yuan, X. Gao, H. K. Wong, B. Feng and J. Xu, A Multiphysics Computational Framework for Cylindrical Battery Behavior upon Mechanical Loading Based on LS-DYNA, *J. Electrochem. Soc.* 166 (2019) A1160-A1169.
- [4] B. Liu, Y. Jia, C. Yuan, L. Wang, X. Gao, S. Yin and J. Xu, Safety issues and mechanisms of lithium-ion battery cell upon mechanical abusive loading: A review, *Energy Storage Mater.* 24 (2020) 85-112.
- [5] C. Yuan, L. Wang, S. Yin and J. Xu, Generalized separator failure criteria for internal short circuit of lithium-ion battery, *J. Power Sources* 467 (2020)
- [6] B. Liu, Y. Jia, J. Li, S. Yin, C. Yuan, Z. Hu, L. Wang, Y. Li and J. Xu, Safety issues caused by internal short circuits in lithium-ion batteries, *J. Mater. Chem. A* 6 (2018) 21475-21484.
- [7] R. Koerver, W. Zhang, L. De Biasi, S. Schweidler, A. O. Kondrakov, S. Kolling, T. Brezesinski, P. Hartmann, W. G. Zeier and J. Janek, Chemo-mechanical expansion of lithium electrode materials – on the route to mechanically optimized all-solid-state batteries, *Energy Environ. Sci.* 11 (2018) 2142-2158.
- [8] J. Schnell, T. Günther, T. Knoche, C. Vieider, L. Köhler, A. Just, M. Keller, S. Passerini and G. Reinhart, All-solid-state lithium-ion and lithium metal batteries – paving the way to large-scale production, *J. Power Sources* 382 (2018) 160-175.
- [9] H.-D. Lim, J.-H. Park, H.-J. Shin, J. Jeong, J. T. Kim, K.-W. Nam, H.-G. Jung and K. Y. Chung, A review of challenges and issues concerning interfaces for all-solid-state batteries, *Energy Storage Mater.* 25 (2020) 224-250.
- [10] Z. Yu, X. Zhang, C. Fu, H. Wang, M. Chen, G. Yin, H. Huo and J. Wang, Dendrites in Solid-State Batteries: Ion Transport Behavior, Advanced Characterization, and Interface Regulation, *Adv. Energy Mater.* 11 (2021) 2003250.
- [11] D. Lin, Y. Liu and Y. Cui, Reviving the lithium metal anode for high-energy batteries, *Nat Nanotechnol* 12 (2017) 194-206.
- [12] D. Cao, X. Sun, Q. Li, A. Natan, P. Xiang and H. Zhu, Lithium Dendrite in All-Solid-State Batteries: Growth Mechanisms, Suppression Strategies, and Characterizations, *Matter* 3 (2020) 57-94.
- [13] Y. Zhao, P. Stein, Y. Bai, M. Al-Siraj, Y. Y. W. Yang and B. X. Xu, A review on modeling of electrochemo-mechanics in lithium-ion batteries, *J. Power Sources* 413 (2019) 259-283.
- [14] C. Yuan, W. Lu and J. Xu, Unlocking the Electrochemical–Mechanical Coupling Behaviors of Dendrite Growth and Crack Propagation in All-Solid-State Batteries, *Adv. Energy Mater.* 11 (2021) 2101807.
- [15] J. Zhu, X. Li, C. Wu, J. Gao, H. Xu, Y. Li, X. Guo, H. Li and W. Zhou, A Multilayer Ceramic Electrolyte for All-Solid-State Li Batteries, *Angew Chem Int Ed Engl* 60 (2021) 3781-3790.
- [16] K. H. Kim, Y. Iriyama, K. Yamamoto, S. Kumazaki, T. Asaka, K. Tanabe, C. A. J. Fisher, T. Hirayama, R. Murugan and Z. Ogumi, Characterization of the interface between LiCoO₂ and Li₇La₃Zr₂O₁₂ in an all-solid-state rechargeable lithium battery, *J. Power Sources* 196 (2011) 764-767.
- [17] S. Ohta, T. Kobayashi, J. Seki and T. Asaoka, Electrochemical performance of an all-solid-state lithium

- ion battery with garnet-type oxide electrolyte, *J. Power Sources* 202 (2012) 332-335.
- [18] J. Wei, H. Kim, D.-C. Lee, R. Hu, F. Wu, H. Zhao, F. M. Alamgir and G. Yushin, Influence of annealing on ionic transfer and storage stability of Li₂S–P₂S₅ solid electrolyte, *J. Power Sources* 294 (2015) 494-500.
- [19] D. Wang, C. Zhu, Y. Fu, X. Sun and Y. Yang, Interfaces in Garnet -Based All -Solid-State Lithium Batteries, *Adv. Energy Mater.* 10 (2020) 2001318.
- [20] Z. Tong, S. B. Wang, Y. K. Liao, S. F. Hu and R. S. Liu, Interface Between Solid-State Electrolytes and Li-Metal Anodes: Issues, Materials, and Processing Routes, *ACS Appl. Mater. Inter.* 12 (2020) 47181-47196.
- [21] Y. Xiao, Y. Wang, S.-H. Bo, J. C. Kim, L. J. Miara and G. Ceder, Understanding interface stability in solid-state batteries, *Nat. Rev. Mater.* 5 (2019) 105-126.
- [22] T. Shi, Y.-Q. Zhang, Q. Tu, Y. Wang, M. C. Scott and G. Ceder, Characterization of mechanical degradation in an all-solid-state battery cathode, *J. Mater. Chem. A* 8 (2020) 17399-17404.
- [23] D. Bistri, A. Afshar and C. V. Di Leo, Modeling the chemo-mechanical behavior of all-solid-state batteries: a review, *Meccanica* (2020)
- [24] D. Grazioli, O. Verners, V. Zadin, D. Brandell and A. Simone, Electrochemical-mechanical modeling of solid polymer electrolytes: Impact of mechanical stresses on Li-ion battery performance, *Electrochim. Acta* 296 (2019) 1122-1141.
- [25] G. Bucci, T. Swamy, Y.-M. Chiang and W. C. Carter, Modeling of internal mechanical failure of all-solid-state batteries during electrochemical cycling, and implications for battery design, *J. Mater. Chem. A* 5 (2017) 19422-19430.
- [26] A. Kim, S. Woo, M. Kang, H. Park and B. Kang, Research Progresses of Garnet-Type Solid Electrolytes for Developing All-Solid-State Li Batteries, *Front Chem* 8 (2020) 468.
- [27] W. Zhao, J. Yi, P. He and H. Zhou, Solid-State Electrolytes for Lithium-Ion Batteries: Fundamentals, Challenges and Perspectives, *Electrochem. Energ. Rev.* 2 (2019) 574-605.
- [28] F. Zheng, M. Kotobuki, S. Song, M. O. Lai and L. Lu, Review on solid electrolytes for all-solid-state lithium-ion batteries, *J. Power Sources* 389 (2018) 198-213.
- [29] M. Dirican, C. Yan, P. Zhu and X. Zhang, Composite solid electrolytes for all-solid-state lithium batteries, *Materials Science and Engineering: R: Reports* 136 (2019) 27-46.
- [30] X. Yu and A. Manthiram, A Long Cycle Life, All-Solid-State Lithium Battery with a Ceramic–Polymer Composite Electrolyte, *ACS Appl. Energy Mater.* 3 (2020) 2916-2924.
- [31] Y. Yin, C.-S. Jiang, H. Guthrey, C. Xiao, N. Seitzman, C. Ban and M. Al-Jassim, Improved Stability and Cyclability of Ceramic Solid Electrolyte by Coating Polymer, *J. Electrochem. Soc.* 167 (2020)
- [32] Y. Kim, H. Jo, J. L. Allen, H. Choe, J. Wolfenstine, J. Sakamoto and G. Pharr, The Effect of Relative Density on the Mechanical Properties of Hot-Pressed Cubic Li₇La₃Zr₂O₁₂, *J. Am. Ceram. Soc.* 99 (2016) 1367-1374.
- [33] X. B. Cheng, R. Zhang, C. Z. Zhao and Q. Zhang, Toward Safe Lithium Metal Anode in Rechargeable Batteries: A Review, *Chem Rev* 117 (2017) 10403-10473.
- [34] C. Monroe and J. Newman, The Impact of Elastic Deformation on Deposition Kinetics at Lithium/Polymer Interfaces, *J. Electrochem. Soc.* 152 (2005)
- [35] F. Liang, Y. Sun, Y. Yuan, J. Huang, M. Hou and J. Lu, Designing inorganic electrolytes for solid-state

- Li-ion batteries: A perspective of LGPS and garnet, *Materials Today* (2021)
- [36] T. Famprakis, P. Canepa, J. A. Dawson, M. S. Islam and C. Masquelier, Fundamentals of inorganic solid-state electrolytes for batteries, *Nat Mater* 18 (2019) 1278-1291.
- [37] J. Li, C. Ma, M. Chi, C. Liang and N. J. Dudney, Solid Electrolyte: the Key for High-Voltage Lithium Batteries, *Adv. Energy Mater.* 5 (2015)
- [38] X. Gao, Y.-N. Zhou, D. Han, J. Zhou, D. Zhou, W. Tang and J. B. Goodenough, Thermodynamic Understanding of Li-Dendrite Formation, *Joule* 4 (2020) 1864-1879.
- [39] H. Sun, Q. Liu, J. Chen, Y. Li, H. Ye, J. Zhao, L. Geng, Q. Dai, T. Yang, H. Li, Z. Wang, L. Zhang, Y. Tang and J. Huang, In Situ Visualization of Lithium Penetration through Solid Electrolyte and Dead Lithium Dynamics in Solid-State Lithium Metal Batteries, *ACS Nano* 15 (2021) 19070–19079.
- [40] S. Heo, D. Lee, K. Kim, Y. Kim, D.-J. Yun, S. Park, J. Lee, S. Kim, J.-S. Kim and S. Park, Short-circuit mechanism induced by crack propagation spurred by inhomogeneous electric field in garnet-based solid electrolyte, *J. Power Sources* 510 (2021)
- [41] E. Kazyak, R. Garcia-Mendez, W. S. LePage, A. Sharafi, A. L. Davis, A. J. Sanchez, K.-H. Chen, C. Haslam, J. Sakamoto and N. P. Dasgupta, Li Penetration in Ceramic Solid Electrolytes: Operando Microscopy Analysis of Morphology, Propagation, and Reversibility, *Matter* 2 (2020) 1025-1048.
- [42] M. Golozar, A. Paoletta, H. Demers, S. Savoie, G. Girard, N. Delaporte, R. Gauvin, A. Guerfi, H. Lorrmann and K. Zaghib, Direct observation of lithium metal dendrites with ceramic solid electrolyte, *Sci Rep* 10 (2020) 18410.
- [43] T. Krauskopf, R. Dippel, H. Hartmann, K. Pepller, B. Mogwitz, F. H. Richter, W. G. Zeier and J. Janek, Lithium-Metal Growth Kinetics on LLZO Garnet-Type Solid Electrolytes, *Joule* 3 (2019) 2030-2049.
- [44] F. Han, A. S. Westover, J. Yue, X. Fan, F. Wang, M. Chi, D. N. Leonard, N. J. Dudney, H. Wang and C. Wang, High electronic conductivity as the origin of lithium dendrite formation within solid electrolytes, *Nat. Energy* 4 (2019) 187-196.
- [45] X. Wang, W. Zeng, L. Hong, W. Xu, H. Yang, F. Wang, H. Duan, M. Tang and H. Jiang, Stress-driven lithium dendrite growth mechanism and dendrite mitigation by electroplating on soft substrates, *Nat. Energy* 3 (2018) 227-235.
- [46] M. Yang, Y. Liu, A. M. Nolan and Y. Mo, Interfacial Atomistic Mechanisms of Lithium Metal Stripping and Plating in Solid-State Batteries, *Adv Mater* 33 (2021) e2008081.
- [47] A. Verma, H. Kawakami, H. Wada, A. Hirowatari, N. Ikeda, Y. Mizuno, T. Kotaka, K. Aotani, Y. Tabuchi and P. P. Mukherjee, Microstructure and Pressure-Driven Electrodeposition Stability in Solid-State Batteries, *Cell Rep. Phys. Sci.* 2 (2021)
- [48] K. Tantratian, H. Yan, K. Ellwood, E. T. Harrison and L. Chen, Unraveling the Li Penetration Mechanism in Polycrystalline Solid Electrolytes, *Adv. Energy Mater.* 11 (2021)
- [49] C. Yuan, X. Gao, Y. Jia, W. Zhang, Q. Wu and J. Xu, Coupled crack propagation and dendrite growth in solid electrolyte of all-solid-state battery, *Nano Energy* 86 (2021)
- [50] Z. Ning, D. S. Jolly, G. Li, R. De Meyere, S. D. Pu, Y. Chen, J. Kasemchainan, J. Ihli, C. Gong, B. Liu, D. L. R. Melvin, A. Bonnin, O. Magdysyuk, P. Adamson, G. O. Hartley, C. W. Monroe, T. J. Marrow and P. G. Bruce, Visualizing plating-induced cracking in lithium-anode solid-electrolyte cells, *Nat. Mater.* 20 (2021) 1121–1129.
- [51] J. A. Lewis, F. J. Q. Cortes, Y. Liu, J. C. Miers, A. Verma, B. S. Vishnugopi, J. Tippens, D. Prakash, T.

- S. Marchese, S. Y. Han, C. Lee, P. P. Shetty, H. W. Lee, P. Shevchenko, F. De Carlo, C. Saldana, P. P. Mukherjee and M. T. McDowell, Linking void and interphase evolution to electrochemistry in solid-state batteries using operando X-ray tomography, *Nat Mater* 20 (2021) 503-510.
- [52] X. Liu, R. Garcia-Mendez, A. R. Lupini, Y. Cheng, Z. D. Hood, F. Han, A. Sharafi, J. C. Idrobo, N. J. Dudney, C. Wang, C. Ma, J. Sakamoto and M. Chi, Local electronic structure variation resulting in Li 'filament' formation within solid electrolytes, *Nat Mater* 20 (2021) 1485-1490.
- [53] H.-K. Tian, Z. Liu, Y. Ji, L.-Q. Chen and Y. Qi, Interfacial Electronic Properties Dictate Li Dendrite Growth in Solid Electrolytes, *Chem. Mater.* 31 (2019) 7351-7359.
- [54] E. J. Cheng, A. Sharafi and J. Sakamoto, Intergranular Li metal propagation through polycrystalline $\text{Li}_{6.25}\text{Al}_{10.25}\text{La}_3\text{Zr}_{20}\text{O}_{12}$ ceramic electrolyte, *Electrochim. Acta* 223 (2017) 85-91.
- [55] Y. Tian, F. Ding, H. Zhong, C. Liu, Y.-B. He, J. Liu, X. Liu and Q. Xu, $\text{Li}_{6.75}\text{La}_3\text{Zr}_{1.75}\text{Ta}_{0.25}\text{O}_{12}$ @amorphous Li_3OCl composite electrolyte for solid state lithium-metal batteries, *Energy Storage Mater.* 14 (2018) 49-57.
- [56] Z. Ahmad and V. Viswanathan, Stability of Electrodeposition at Solid-Solid Interfaces and Implications for Metal Anodes, *Phys Rev Lett* 119 (2017) 056003.
- [57] K. J. Harry, D. T. Hallinan, D. Y. Parkinson, A. A. MacDowell and N. P. Balsara, Detection of subsurface structures underneath dendrites formed on cycled lithium metal electrodes, *Nat Mater* 13 (2014) 69-73.
- [58] R. Raj and J. Wolfenstine, Current limit diagrams for dendrite formation in solid-state electrolytes for Li-ion batteries, *J. Power Sources* 343 (2017) 119-126.
- [59] N. Imanishi, M. Matsui, Y. Takeda and O. Yamamoto, Lithium Ion Conducting Solid Electrolytes for Aqueous Lithium-air Batteries, *Electrochemistry* 82 (2014) 938-945.
- [60] F. Flatscher, M. Philipp, S. Ganschow, H. M. R. Wilkening and D. Rettenwander, The natural critical current density limit for $\text{Li}_7\text{La}_3\text{Zr}_{20}\text{O}_{12}$ garnets, *J. Mater. Chem. A* 8 (2020) 15782-15788.
- [61] F. Shen, M. B. Dixit, X. Xiao and K. B. Hatzell, Effect of Pore Connectivity on Li Dendrite Propagation within LLZO Electrolytes Observed with Synchrotron X-ray Tomography, *Acs Energy Lett.* 3 (2018) 1056-1061.
- [62] Y. Ren, Y. Shen, Y. Lin and C.-W. Nan, Direct observation of lithium dendrites inside garnet-type lithium-ion solid electrolyte, *Electrochemistry Communications* 57 (2015) 27-30.
- [63] S. Yu and D. J. Siegel, Grain Boundary Contributions to Li-Ion Transport in the Solid Electrolyte $\text{Li}_7\text{La}_3\text{Zr}_{20}\text{O}_{12}$ (LLZO), *Chem. Mater.* 29 (2017) 9639-9647.
- [64] Y. Li, Z. Wang, C. Li, Y. Cao and X. Guo, Densification and ionic-conduction improvement of lithium garnet solid electrolytes by flowing oxygen sintering, *J. Power Sources* 248 (2014) 642-646.
- [65] L. Porz, T. Swamy, B. W. Sheldon, D. Rettenwander, T. Frömling, H. L. Thaman, S. Berendts, R. Uecker, W. C. Carter and Y.-M. Chiang, Mechanism of Lithium Metal Penetration through Inorganic Solid Electrolytes, *Adv. Energy Mater.* 7 (2017)
- [66] S. Hao, S. R. Daemi, T. M. M. Heenan, W. Du, C. Tan, M. Storm, C. Rau, D. J. L. Brett and P. R. Shearing, Tracking lithium penetration in solid electrolytes in 3D by in-situ synchrotron X-ray computed tomography, *Nano Energy* 82 (2021)
- [67] J. Tippens, J. C. Miers, A. Afshar, J. A. Lewis, F. J. Q. Cortes, H. Qiao, T. S. Marchese, C. V. Di Leo, C. Saldana and M. T. McDowell, Visualizing Chemomechanical Degradation of a Solid-State Battery Electrolyte, *Acs Energy Lett.* 4 (2019) 1475-1483.

- [68] S. S. Shishvan, N. A. Fleck, R. M. McMeeking and V. S. Deshpande, Dendrites as climbing dislocations in ceramic electrolytes: Initiation of growth, *J. Power Sources* 456 (2020)
- [69] S. S. Shishvan, N. A. Fleck, R. M. McMeeking and V. S. Deshpande, Growth rate of lithium filaments in ceramic electrolytes, *Acta Mater.* 196 (2020) 444-455.
- [70] X. Song, Y. Lu, F. Wang, X. Zhao and H. Chen, A coupled electro-chemo-mechanical model for all-solid-state thin film Li-ion batteries: The effects of bending on battery performances, *J. Power Sources* 452 (2020)
- [71] G. Liu and W. Lu, A Model of Concurrent Lithium Dendrite Growth, SEI Growth, SEI Penetration and Regrowth, *J. Electrochem. Soc.* 164 (2017) A1826-A1833.
- [72] P. Barai, K. Higa, A. T. Ngo, L. A. Curtiss and V. Srinivasan, Mechanical Stress Induced Current Focusing and Fracture in Grain Boundaries, *J. Electrochem. Soc.* 166 (2019) A1752-A1762.
- [73] Q. Tu, L. Barroso-Luque, T. Shi and G. Ceder, Electrodeposition and Mechanical Stability at Lithium-Solid Electrolyte Interface during Plating in Solid-State Batteries, *Cell Rep. Phys. Sci.* 1 (2020)
- [74] M. Yang and Y. Mo, Interfacial Defect of Lithium Metal in Solid-State Batteries, *Angew Chem Int Ed Engl* (2021)
- [75] E. G. Herbert, S. A. Hackney, V. Thole, N. J. Dudney and P. S. Phani, Nanoindentation of high-purity vapor deposited lithium films: A mechanistic rationalization of diffusion-mediated flow, *Journal of Materials Research* 33 (2018) 1347-1360.
- [76] C. D. Fincher, D. Ojeda, Y. Zhang, G. M. Pharr and M. Pharr, Mechanical properties of metallic lithium: from nano to bulk scales, *Acta Mater.* 186 (2020) 215-222.
- [77] Y. Tang, L. Zhang, J. Chen, H. Sun, T. Yang, Q. Liu, Q. Huang, T. Zhu and J. Huang, Electro-chemo-mechanics of lithium in solid state lithium metal batteries, *Energy Environ. Sci.* (2021)
- [78] M. Jackle and A. Gross, Microscopic properties of lithium, sodium, and magnesium battery anode materials related to possible dendrite growth, *J Chem Phys* 141 (2014) 174710.
- [79] C. Xu, Z. Ahmad, A. Aryanfar, V. Viswanathan and J. R. Greer, Enhanced strength and temperature dependence of mechanical properties of Li at small scales and its implications for Li metal anodes, *Proc. Natl. Acad. Sci.* 114 (2017) 57-61.
- [80] L. Zhang, T. Yang, C. Du, Q. Liu, Y. Tang, J. Zhao, B. Wang, T. Chen, Y. Sun, P. Jia, H. Li, L. Geng, J. Chen, H. Ye, Z. Wang, Y. Li, H. Sun, X. Li, Q. Dai, Y. Tang, Q. Peng, T. Shen, S. Zhang, T. Zhu and J. Huang, Lithium whisker growth and stress generation in an in situ atomic force microscope-environmental transmission electron microscope set-up, *Nat Nanotechnol* 15 (2020) 94-98.
- [81] A. Masias, N. Felten, R. Garcia-Mendez, J. Wolfenstine and J. Sakamoto, Elastic, plastic, and creep mechanical properties of lithium metal, *J. Mater. Sci.* 54 (2018) 2585-2600.
- [82] F. Zhang, Q.-A. Huang, Z. Tang, A. Li, Q. Shao, L. Zhang, X. Li and J. Zhang, A review of mechanics-related material damages in all-solid-state batteries: Mechanisms, performance impacts and mitigation strategies, *Nano Energy* 70 (2020)
- [83] R. Koerver, I. Aygün, T. Leichtweiß, C. Dietrich, W. Zhang, J. O. Binder, P. Hartmann, W. G. Zeier and J. Janek, Capacity Fade in Solid-State Batteries: Interphase Formation and Chemomechanical Processes in Nickel-Rich Layered Oxide Cathodes and Lithium Thiophosphate Solid Electrolytes, *Chem. Mater.* 29 (2017) 5574-5582.
- [84] J. Park, D. Kim, W. A. Appiah, J. Song, K. T. Bae, K. T. Lee, J. Oh, J. Y. Kim, Y.-G. Lee, M.-H. Ryu

- and Y. M. Lee, Electrode design methodology for all-solid-state batteries: 3D structural analysis and performance prediction, *Energy Storage Mater.* 19 (2019) 124-129.
- [85] Y. Chen, Z. Wang, X. Li, X. Yao, C. Wang, Y. Li, W. Xue, D. Yu, S. Y. Kim, F. Yang, A. Kushima, G. Zhang, H. Huang, N. Wu, Y. W. Mai, J. B. Goodenough and J. Li, Li metal deposition and stripping in a solid-state battery via Coble creep, *Nature* 578 (2020) 251-255.
- [86] S. Shinzo, E. Higuchi, M. Chiku, A. Hayashi and H. Inoue, Control of Dendritic Growth of the Lithium Metal in All-Solid-State Lithium Metal Batteries: Effect of the Current Collector with Microsized Pores, *ACS Appl. Mater. Inter.* 12 (2020) 22798-22803.
- [87] C. L. Tsai, V. Roddatis, C. V. Chandran, Q. Ma, S. Uhlenbruck, M. Bram, P. Heitjans and O. Guillon, Li₇La₃Zr₂O₁₂ Interface Modification for Li Dendrite Prevention, *ACS Appl. Mater. Inter.* 8 (2016) 10617-26.
- [88] K. K. Fu, Y. Gong, B. Liu, Y. Zhu, S. Xu, Y. Yao, W. Luo, C. Wang, S. D. Lacey, J. Dai, Y. Chen, Y. Mo, E. Wachsman and L. Hu, Toward garnet electrolyte-based Li metal batteries: An ultrathin, highly effective, artificial solid-state electrolyte/metallic Li interface, *Sci. Adv.* 3 (2017)
- [89] Z. Lu, Z. Yang, C. Li, K. Wang, J. Han, P. Tong, G. Li, B. S. Vishnugopi, P. P. Mukherjee, C. Yang and W. Li, Modulating Nanoinhomogeneity at Electrode-Solid Electrolyte Interfaces for Dendrite-Proof Solid-State Batteries and Long-Life Memristors, *Adv. Energy Mater.* 11 (2021)
- [90] A. Kato, H. Kowada, M. Deguchi, C. Hotehama, A. Hayashi and M. Tatsumisago, XPS and SEM analysis between Li/Li₃PS₄ interface with Au thin film for all-solid-state lithium batteries, *Solid State Ionics* 322 (2018) 1-4.
- [91] R. Hongahally Basappa, T. Ito, T. Morimura, R. Bekarevich, K. Mitsuishi and H. Yamada, Grain boundary modification to suppress lithium penetration through garnet-type solid electrolyte, *J. Power Sources* 363 (2017) 145-152.
- [92] H.-Y. Li, B. Huang, Z. Huang and C.-A. Wang, Enhanced mechanical strength and ionic conductivity of LLZO solid electrolytes by oscillatory pressure sintering, *Ceram. Int.* 45 (2019) 18115-18118.
- [93] L. Ye and X. Li, A dynamic stability design strategy for lithium metal solid state batteries, *Nature* 593 (2021) 218-222.
- [94] K. Kataoka, H. Nagata and J. Akimoto, Lithium-ion conducting oxide single crystal as solid electrolyte for advanced lithium battery application, *Sci Rep* 8 (2018) 9965.
- [95] L. Buannic, B. Orayech, J.-M. López Del Amo, J. Carrasco, N. A. Katcho, F. Aguesse, W. Manalastas, W. Zhang, J. Kilner and A. Llordés, Dual Substitution Strategy to Enhance Li⁺ Ionic Conductivity in Li₇La₃Zr₂O₁₂ Solid Electrolyte, *Chem. Mater.* 29 (2017) 1769-1778.
- [96] L. Zhang, K. Yang, J. Mi, L. Lu, L. Zhao, L. Wang, Y. Li and H. Zeng, Na₃PSe₄: A Novel Chalcogenide Solid Electrolyte with High Ionic Conductivity, *Adv. Energy Mater.* 5 (2015)
- [97] J. M. Doux, H. Nguyen, D. H. S. Tan, A. Banerjee, X. Wang, E. A. Wu, C. Jo, H. Yang and Y. S. Meng, Stack Pressure Considerations for Room-Temperature All-Solid-State Lithium Metal Batteries, *Adv. Energy Mater.* 10 (2019)
- [98] M. J. Wang, R. Choudhury and J. Sakamoto, Characterizing the Li-Solid-Electrolyte Interface Dynamics as a Function of Stack Pressure and Current Density, *Joule* 3 (2019) 2165-2178.
- [99] C. Lee, S. Y. Han, J. A. Lewis, P. P. Shetty, D. Yeh, Y. Liu, E. Klein, H.-W. Lee and M. T. McDowell, Stack Pressure Measurements to Probe the Evolution of the Lithium-Solid-State Electrolyte Interface,

- Acs Energy Lett. (2021) 3261-3269.
- [100] S. Y. Han, C. Lee, J. A. Lewis, D. Yeh, Y. Liu, H.-W. Lee and M. T. McDowell, Stress evolution during cycling of alloy-anode solid-state batteries, *Joule* (2021)
- [101] Y. Qi, C. Ban and S. J. Harris, A New General Paradigm for Understanding and Preventing Li Metal Penetration through Solid Electrolytes, *Joule* 4 (2020) 2599-2608.
- [102] P. Zuo and Y. P. Zhao, A phase field model coupling lithium diffusion and stress evolution with crack propagation and application in lithium ion batteries, *Phys Chem Chem Phys* 17 (2015) 287-97.
- [103] L. Chen, H. W. Zhang, L. Y. Liang, Z. Liu, Y. Qi, P. Lu, J. Chen and L.-Q. Chen, Modulation of dendritic patterns during electrodeposition: A nonlinear phase-field model, *J. Power Sources* 300 (2015) 376-385.
- [104] L.-Q. Chen, Phase-Field Models for Microstructure Evolution, *Annu. Rev. Mater. Res.* 32 (2002) 113-140.
- [105] X. Shen, R. Zhang, P. Shi, X. Chen and Q. Zhang, How Does External Pressure Shape Li Dendrites in Li Metal Batteries?, *Adv. Energy Mater.* 11 (2021)
- [106] L. Liang and L.-Q. Chen, Nonlinear phase field model for electrodeposition in electrochemical systems, *Appl. Phys. Lett.* 105 (2014)
- [107] P. J. Kumar, K. Nishimura, M. Senna, A. Düvel, P. Heitjans, T. Kawaguchi, N. Sakamoto, N. Wakiya and H. Suzuki, A novel low-temperature solid-state route for nanostructured cubic garnet $\text{Li}_7\text{La}_3\text{Zr}_2\text{O}_{12}$ and its application to Li-ion battery, *Rsc Adv.* 6 (2016) 62656-62667.
- [108] R. D. Armstrong, T. Dickinson and J. Turner, The breakdown of β -alumina ceramic electrolyte, *Electrochim. Acta* 19 (1974) 187-192.
- [109] S. D. Fabre, D. Guy-Bouyssou, P. Bouillon, F. Le Cras and C. Delacourt, Charge/Discharge Simulation of an All-Solid-State Thin-Film Battery Using a One-Dimensional Model, *J. Electrochem. Soc.* 159 (2011) A104-A115.
- [110] B. Liu and J. Xu, Cracks of Silicon Nanoparticles in Anodes: Mechanics–Electrochemical-Coupled Modeling Framework Based on the Phase-Field Method, *ACS Appl. Energy Mater.* 3 (2020) 10931-10939.
- [111] Marc Doyle, Thomas F. Fuller and J. Newman, Modeling of Galvanostatic Charge and Discharge of the Lithium/Polymer/Insertion Cell, *J. Electrochem. Soc.* 140 (1993) 1526-1533.
- [112] A. Mistry and P. P. Mukherjee, Molar Volume Mismatch: A Malefactor for Irregular Metallic Electrodeposition with Solid Electrolytes, *J. Electrochem. Soc.* 167 (2020)
- [113] M. Klinsmann, F. E. Hildebrand, M. Ganser and R. M. McMeeking, Dendritic cracking in solid electrolytes driven by lithium insertion, *J. Power Sources* 442 (2019)
- [114] Y. Hou, P. Yue, Q. Xin, T. Pauli, W. Sun and L. Wang, Fracture failure of asphalt binder in mixed mode (Modes I and II) by using phase-field model, *Road Mater. Pavement Des.* 15 (2013) 167-181.
- [115] M. Tang, P. Albertus and J. Newman, Two-Dimensional Modeling of Lithium Deposition during Cell Charging, *J. Electrochem. Soc.* 156 (2009)
- [116] D. E. Stephenson, E. M. Hartman, J. N. Harb and D. R. Wheeler, Modeling of Particle-Particle Interactions in Porous Cathodes for Lithium-Ion Batteries, *J. Electrochem. Soc.* 154 (2007) A1146-A1155.
- [117] W. S. LePage, Y. Chen, E. Kazyak, K.-H. Chen, A. J. Sanchez, A. Poli, E. M. Arruda, M. D. Thouless and N. P. Dasgupta, Lithium Mechanics: Roles of Strain Rate and Temperature and Implications for

- Lithium Metal Batteries, *J. Electrochem. Soc.* 166 (2019) A89-A97.
- [118] C. Yuan, B. W. Sheldon and J. Xu, Heterogeneous Reinforcements to Mitigate Li Penetration through Solid Electrolytes in All-Solid-State Batteries, *Adv. Energy Mater.* (2022)
- [119] Q. Lv, Y. Jiang, B. Wang, Y. Chen, F. Jin, B. Wu, H. Ren, N. Zhang, R. Xu, Y. Li, T. Zhang, Y. Zhou, D. Wang, H. Liu and S. Dou, Suppressing lithium dendrites within inorganic solid-state electrolytes, *Cell Rep. Phys. Sci.* 3 (2022)
- [120] H. Ming-Yuan and J. W. Hutchinson, Crack deflection at an interface between dissimilar elastic materials, *International Journal of Solids and Structures* 25 (1989) 1053-1067.
- [121] J. Parmigiani and M. Thouless, The roles of toughness and cohesive strength on crack deflection at interfaces, *J. Mech, Phys. Solids* 54 (2006) 266-287.
- [122] W. Guo, F. Shen, J. Liu, Q. Zhang, H. Guo, Y. Yin, J. Gao, Z. Sun, X. Han and Y. Hu, In-situ optical observation of Li growth in garnet-type solid state electrolyte, *Energy Storage Mater.* 41 (2021) 791-797.
- [123] M. J. O'Brien and B. W. Sheldon, Porous Alumina Coating with Tailored Fracture Resistance for Alumina Composites, *J. Am. Ceram. Soc.* 82 (1999) 3567-3574.
- [124] C. E. Athanasiou, M. Y. Jin, C. Ramirez, N. P. Padture and B. W. Sheldon, High-Toughness Inorganic Solid Electrolytes via the Use of Reduced Graphene Oxide, *Matter* 3 (2020) 212-229.
- [125] S. Lou, Q. Liu, F. Zhang, Q. Liu, Z. Yu, T. Mu, Y. Zhao, J. Borovilas, Y. Chen, M. Ge, X. Xiao, W. K. Lee, G. Yin, Y. Yang, X. Sun and J. Wang, Insights into interfacial effect and local lithium-ion transport in polycrystalline cathodes of solid-state batteries, *Nat Commun* 11 (2020) 5700.
- [126] J. Y. Ko, M. Varini, M. Klett, H. Ekström and G. Lindbergh, Porous Electrode Model with Particle Stress Effects for $\text{Li}(\text{Ni}_{1/3}\text{Co}_{1/3}\text{Mn}_{1/3})\text{O}_2$ Electrode, *J. Electrochem. Soc.* 166 (2019) A2939-A2949.
- [127] C. W.C., W. M.R. and J. M., A comparison of failure criteria to predict delamination of unidirectional glass/epoxy specimens waisted through the thickness, *Composites* 23 (1992) 158-166.
- [128] L. De Lorenzis, D. Fernando and J.-G. Teng, Coupled mixed-mode cohesive zone modeling of interfacial debonding in simply supported plated beams, *International Journal of Solids and Structures* 50 (2013) 2477-2494.
- [129] X. Gao and J. Xu, Multiscale Modeling of Electro-Chemo-Mechanical Degradation in Si/C Core-Shell Anode for the Lithium-Ion Battery of High Energy Density, *J. Electrochem. Energy Convers. Storage* 18 (2021)
- [130] R. Xu, Y. Yang, F. Yin, P. Liu, P. Cloetens, Y. Liu, F. Lin and K. Zhao, Heterogeneous damage in Li-ion batteries: Experimental analysis and theoretical modeling, *J. Mech, Phys. Solids* 129 (2019) 160-183.
- [131] C. Roitzheim, Y.J. Sohn, L.-Y. Kuo, G. Häuschen, M. Mann, D. Sebold, M. Finsterbusch, P. Kaghazchi, O. Guillon and D. Fattakhova-Rohlfing, All-Solid-State Li Batteries with NCM-Garnet-Based Composite Cathodes: The Impact of NCM Composition on Material Compatibility, *ACS Appl. Energy Mater.* (2022)
- [132] A. Schmidt, E. Ramani, T. Carraro, J. Joos, A. Weber, M. Kamlah and E. Ivers-Tiffée, Understanding Deviations between Spatially Resolved and Homogenized Cathode Models of Lithium-Ion Batteries, *Energy Technology* 9 (2021)
- [133] E. J. Cheng, K. Hong, N. J. Taylor, H. Choe, J. Wolfenstine and J. Sakamoto, Mechanical and physical

- properties of $\text{LiNi}_{0.33}\text{Mn}_{0.33}\text{Co}_{0.33}\text{O}_2$ (NMC), *Journal of the European Ceramic Society* 37 (2017) 3213-3217.
- [134] H.-H. Ryu, K.-J. Park, C. S. Yoon and Y.-K. Sun, Capacity Fading of Ni-Rich $\text{Li}[\text{Ni}_x\text{Co}_y\text{Mn}_{1-x-y}]\text{O}_2$ ($0.6 \leq x \leq 0.95$) Cathodes for High-Energy-Density Lithium-Ion Batteries: Bulk or Surface Degradation?, *Chem. Mater.* 30 (2018) 1155-1163.
- [135] S. H. Jung, U. H. Kim, J. H. Kim, S. Jun, C. S. Yoon, Y. S. Jung and Y. K. Sun, Ni-Rich Layered Cathode Materials with Electrochemo-Mechanically Compliant Microstructures for All-Solid-State Li Batteries, *Adv. Energy Mater.* 10 (2019)

APPENDIX A: Validation of the Established Modeling Framework

The charging/discharging process is adopted to calibrate and validate the established model to assure the validity of the battery model and the phase-field model. The thicknesses for the LLZO electrolyte and the LiCoO₂ (LCO) cathode, $L_{el}=2$ mm and $L_{ca}=0.5$ μm , are from Ref.¹⁷ To conform to the reference's experimental setup, there is no pre-defect area at the Li/LLZO interface and the stress effect is excluded (i.e., Eq. (32) is disabled). Then the galvanostatic charging/discharging is performed under a 0.1C charging rate ($3.5 \mu\text{A}/\text{cm}^2$) in the range of 2.5–4.2V. The charging/discharging voltage vs. capacity response from the simulation agrees well with experimental results (Fig. 60), demonstrating the validity of the electrochemical response of the model.

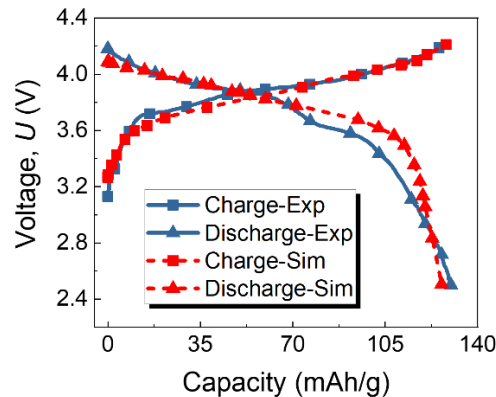


Figure 60 Model validation: comparison of charge/discharge curves between experiment and simulation.

Based on the validated parameters, a parametric study is carried out. Considering the computational efficiency, 20 μm is adopted as the cathode thickness. From the results of the governing effect from the charging rate, it can be roughly deduced that 0.25C is the critical C-rate and the corresponding current density is about $350 \mu\text{A}/\text{cm}^2$, which is within

the range of critical current density for the LLZO electrolyte reported in the literature,⁶⁰ which also demonstrates the validity of the developed model.

APPENDIX B: List of Governing Equations

Table 4 Main governing equations in the modeling framework

| Sub-model | Function | Equation |
|---------------------|---|---|
| Battery model | Butler-Volmer equation at cathode/anode-electrolyte interface | $j = j_{0+} \left[\exp\left(\frac{\alpha_a F}{RT} \eta_+\right) - \exp\left(\frac{-\alpha_c F}{RT} \eta_+\right) \right]$ $j = j_{0-} \left[\exp\left(\frac{\alpha_a F}{RT} \eta_-\right) - \exp\left(\frac{-\alpha_c F}{RT} \eta_-\right) \right]$ |
| | Overpotential for the electrochemical reaction at cathode/anode-electrolyte interface | $\eta_+ = \phi_s - \phi_l - E_{\text{eq}}; \eta_- = \phi_{s, \text{ext}} - \phi_l$ |
| | Ohm's law and Charge conservation in electrode and electrolyte phases | $\mathbf{i}_s = -\kappa_s \nabla \phi_s; \mathbf{i}_l = -\kappa_{\text{SE}} \nabla \phi_l; \nabla \cdot \mathbf{i}_s = 0; \nabla \cdot \mathbf{i}_l = 0$ |
| | Diffusion of Li ions in the active particle of the cathode | $\frac{\partial c_s}{\partial t} = \nabla \cdot (D_s \nabla c_s)$ |
| Mechanical model | Mechanical governing equation following Newton's second law | $\rho \frac{\partial^2 \mathbf{u}}{\partial t^2} = \nabla \cdot \mathbf{F}_L (S + S_{\text{ext}}) + F_V$ |
| | Overpotential-induced stress at the interface between dendrite and electrolyte | $S_{\text{ext}} = -\frac{F}{\Omega_{\text{Li}}} \eta_-$ |
| Phase-field model | Total free energy of the system | $F_{\text{total}} = \int [f_{\text{local}} + f_{\text{grad}} + f_{\text{mech}}] dV$ |
| | Dendrite/crack growth governing equation following the Allen-Cahn equation | $\frac{\partial \xi}{\partial t} + \mathbf{u} \cdot \nabla \xi = \nabla \cdot \frac{\gamma \lambda}{\varepsilon_{\text{pf}}^2} \nabla \psi$ |
| Short-circuit model | Calculation of short-circuit resistance | $R_{\text{short}} = \frac{L_{\text{el}}}{\sigma_{\text{SE_ave}}(\xi) S_{\text{SE}}}$ |

APPENDIX C: Clarification of the Phase-field Modeling Approach

Since battery is charged by constant current, so the current density is almost unchanged as a response to the outside constant current charging, which means the interface kinetics will be forced to be constant. By increasing the exchange current density j_0 and decreasing the ionic conductivity (case 2, Fig. 61(a)), electrolyte potential φ_l is larger for smaller j_0 , then the overpotential is more negative and the stress is thus larger to drive the crack. To make faster interface kinetics, the external applied current density i_{appl} is increased (case 3, Fig. 61(a)) and in this case, the dendrite grows faster also in a similar way, which can justify our approach. The crack length and width vs. time show the detailed information about the evolution process (Fig. 61(b)). Note that we didn't set any value for W_2 . We only set the initial defect ($L=4$ μm , $W=2$ μm) at the left boundary, and the dendrite then grows automatically upon charging. We found that the W_2 is also related to the mesh size, i.e., W_2 is smaller when smaller mesh is used, but their growth patterns are similar. Along with this, we select a suitable mesh size (0.725 μm) in this study to consider the balance of accuracy and computational efficiency. Moreover, the Li-ion flux is added not only to the tip. Actually, the Li is added around the dendrite, but the dendrite tip has a more negative overpotential so it grows faster; meanwhile, the stress status makes the dendrite further grow along the x axis since the dendrite is slim and long along x axis (just like crack propagation). The phase-field model is developed from the perspective of energy conservation, and it preferentially chooses the path which has a larger energy release rate.

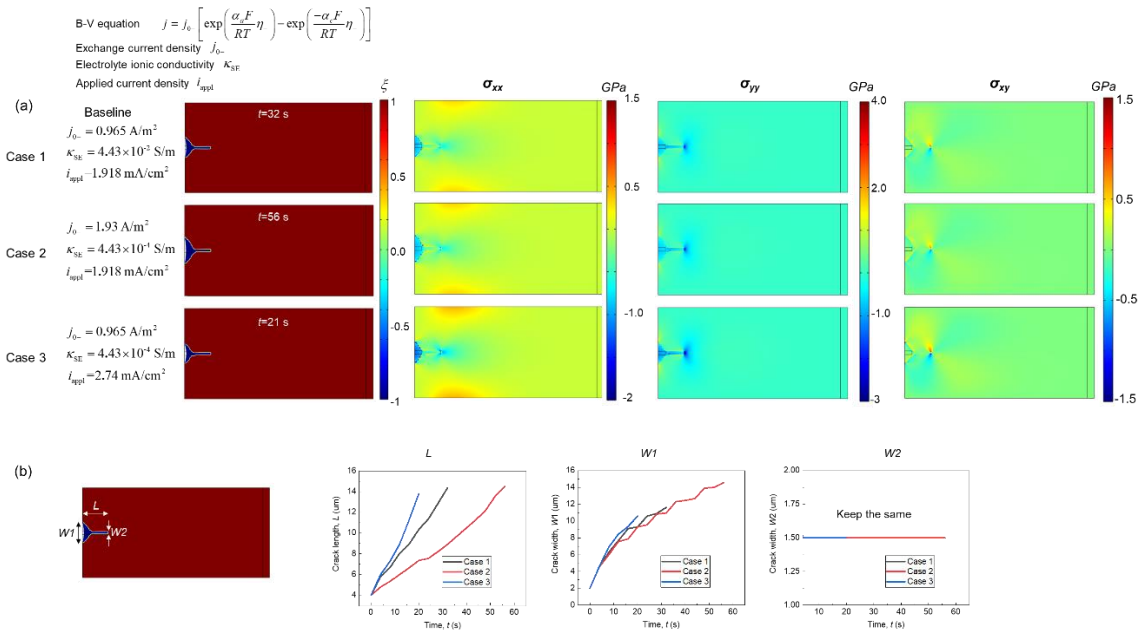


Figure 61 (a) Comparison of the dendrite growth between two cases with different exchange current density, electrolyte ionic conductivity, and applied current density. The results show that, these cases have similar dendrite growth pattern. (b) The crack length and width vs. time.

APPENDIX D: PERMISSION LETTERS

Here are the licenses for reusing the contents from my previous publications.

ELSEVIER LICENSE TERMS AND CONDITIONS

Sep 14, 2022

This Agreement between Mr. Chunhao Yuan ("You") and Elsevier ("Elsevier") consists of your license details and the terms and conditions provided by Elsevier and Copyright Clearance Center.

| | |
|--|---|
| License Number | 5387630726215 |
| License date | Sep 14, 2022 |
| Licensed Content Publisher | Elsevier |
| Licensed Content Publication | Nano Energy |
| Licensed Content Title | Coupled crack propagation and dendrite growth in solid electrolyte of all-solid-state battery |
| Licensed Content Author | Chunhao Yuan,Xiang Gao,Yikai Jia,Wen Zhang,Qingliu Wu,Jun Xu |
| Licensed Content Date | Aug 1, 2021 |
| Licensed Content Volume | 86 |
| Licensed Content Issue | n/a |
| Licensed Content Pages | 1 |
| Start Page | 106057 |
| End Page | |
| Type of Use | post on a website |
| Requestor type | academic/educational institute |
| Portion | full article |
| Format | electronic |
| Are you the author of this Elsevier article? | Yes |
| Will you be translating? | No |
| Home page URL | https://about.proquest.com/en/dissertations/ |
| Client / Sponsor | ProQuest |
| Expected posting date | Nov 2022 |
| Requestor Location | Mr. Chunhao Yuan 9810 Campus Walk Ln Apt L Charlotte, NC 28262 United States Attn: Mr. Chunhao Yuan |
| Publisher Tax ID | 98-0397804 |
| Billing Type | Invoice |
| Billing Address | Mr. Chunhao Yuan 9810 Campus Walk Ln Apt L Charlotte, NC 28262 United States Attn: Chunhao Yuan |
| Total | 0.00 USD |
| Terms and Conditions | |

INTRODUCTION

1. The publisher for this copyrighted material is Elsevier. By clicking "accept" in connection with completing this licensing transaction, you agree that the following terms and conditions apply to this transaction (along with the Billing and Payment terms and conditions established by Copyright Clearance Center, Inc. ("CCC"), at the time that you opened your Rightslink account and that are available at any time at <http://myaccount.copyright.com>).

GENERAL TERMS

2. Elsevier hereby grants you permission to reproduce the aforementioned material subject to the terms and conditions indicated.
3. Acknowledgement: If any part of the material to be used (for example, figures) has appeared in our publication with credit or acknowledgement to another source, permission must also be sought from that source. If such permission is not obtained then that material may not be included in your publication/copies. Suitable acknowledgement to the source must be made, either as a footnote or in a reference list at the end of your publication, as follows:
"Reprinted from Publication title, Vol /edition number, Author(s), Title of article / title of chapter, Pages No., Copyright (Year), with permission from Elsevier [OR APPLICABLE SOCIETY COPYRIGHT OWNER]." Also Lancet special credit - "Reprinted from The Lancet, Vol. number, Author(s), Title of article, Pages No., Copyright (Year), with permission from Elsevier."
4. Reproduction of this material is confined to the purpose and/or media for which permission is hereby given.
5. Altering/Modifying Material: Not Permitted. However figures and illustrations may be altered/adapted minimally to serve your work. Any other abbreviations, additions, deletions and/or any other alterations shall be made only with prior written authorization of Elsevier Ltd. (Please contact Elsevier's permissions helpdesk [here](#)). No modifications can be made to any Lancet figures/tables and they must be reproduced in full.
6. If the permission fee for the requested use of our material is waived in this instance, please be advised that your future requests for Elsevier materials may attract a fee.
7. Reservation of Rights: Publisher reserves all rights not specifically granted in the combination of (i) the license details provided by you and accepted in the course of this licensing transaction, (ii) these terms and conditions and (iii) CCC's Billing and Payment terms and conditions.
8. License Contingent Upon Payment: While you may exercise the rights licensed immediately upon issuance of the license at the end of the licensing process for the transaction, provided that you have disclosed complete and accurate details of your proposed use, no license is finally effective unless and until full payment is received from you (either by publisher or by CCC) as provided in CCC's Billing and Payment terms and conditions. If full payment is not received on a timely basis, then any license preliminarily granted shall be deemed automatically revoked and shall be void as if never granted. Further, in the event that you breach any of these terms and conditions or any of CCC's Billing and Payment terms and conditions, the license is automatically revoked and shall be void as if never granted. Use of materials as described in a revoked license, as well as any use of the materials beyond the scope of an unrevoked license, may constitute copyright infringement and publisher reserves the right to take any and all action to protect its copyright in the materials.
9. Warranties: Publisher makes no representations or warranties with respect to the licensed material.
10. Indemnity: You hereby indemnify and agree to hold harmless publisher and CCC, and their respective officers, directors, employees and agents, from and against any and all claims arising out of your use of the licensed material other than as specifically authorized pursuant to this license.
11. No Transfer of License: This license is personal to you and may not be sublicensed, assigned, or transferred by you to any other person without publisher's written permission.
12. No Amendment Except in Writing: This license may not be amended except in a writing signed by both parties (or, in the case of publisher, by CCC on publisher's behalf).
13. Objection to Contrary Terms: Publisher hereby objects to any terms contained in any purchase order, acknowledgment, check endorsement or other writing prepared by you, which terms are inconsistent with these terms and conditions or CCC's Billing and Payment terms and conditions. These terms and conditions, together with CCC's Billing and Payment terms and conditions (which are incorporated herein), comprise the entire agreement between you and publisher (and CCC) concerning this licensing transaction. In the event of any conflict between your obligations established by these terms and conditions and those established by CCC's Billing and Payment terms and conditions, these terms and conditions shall control.
14. Revocation: Elsevier or Copyright Clearance Center may deny the permissions described in this License at their sole discretion, for any reason or no reason, with a full refund payable to you. Notice of such denial will be made using the contact information provided by you. Failure to receive such notice will not alter or invalidate the denial. In no event will Elsevier or Copyright Clearance Center be responsible or liable for any costs, expenses or damage incurred by you as a result of a denial of your permission request, other than a refund of the amount(s) paid by you to Elsevier and/or Copyright Clearance Center for denied permissions.

LIMITED LICENSE

The following terms and conditions apply only to specific license types:

15. **Translation:** This permission is granted for non-exclusive world **English** rights only unless your license was granted for translation rights. If you licensed translation rights you may only translate this content into the languages you requested. A professional translator must perform all translations and reproduce the content word for word preserving the integrity of the article.
16. **Posting licensed content on any Website:** The following terms and conditions apply as follows: Licensing material from an Elsevier journal: All content posted to the web site must maintain the copyright information line on the bottom of each image; A hyper-text must be included to the Homepage of the journal from which you are licensing at <http://www.sciencedirect.com/science/journal/xxxx> or the Elsevier homepage for books at <http://www.elsevier.com>; Central Storage: This license does not include permission for a scanned version of the material to be stored in a central repository such as that provided by Heron/XanEdu. Licensing material from an Elsevier book: A hyper-text link must be included to the Elsevier homepage at <http://www.elsevier.com>. All content posted to the web site must maintain the copyright information line on the bottom of each image.

Posting licensed content on Electronic reserve: In addition to the above the following clauses are applicable: The web site must be password-protected and made available only to bona fide students registered on a relevant course. This permission is granted for 1 year only. You may obtain a new license for future website posting.

17. For journal authors: the following clauses are applicable in addition to the above:

Preprints:

A preprint is an author's own write-up of research results and analysis, it has not been peer-reviewed, nor has it had any other value added to it by a publisher (such as formatting, copyright, technical enhancement etc.).

Authors can share their preprints anywhere at any time. Preprints should not be added to or enhanced in any way in order to appear more like, or to substitute for, the final versions of articles however authors can update their preprints on arXiv or RePEc with their Accepted Author Manuscript (see below).

If accepted for publication, we encourage authors to link from the preprint to their formal publication via its DOI. Millions of researchers have access to the formal publications on ScienceDirect, and so links will help users to find, access, cite and use the best available version. Please note that Cell Press, The Lancet and some society-owned have different preprint policies. Information on these policies is available on the journal homepage.

Accepted Author Manuscripts: An accepted author manuscript is the manuscript of an article that has been accepted for publication and which typically includes author-incorporated changes suggested during submission, peer review and editor-author communications. Authors can share their accepted author manuscript:

- immediately
 - via their non-commercial person homepage or blog
 - by updating a preprint in arXiv or RePEc with the accepted manuscript
 - via their research institute or institutional repository for internal institutional uses or as part of an invitation-only research collaboration work-group
 - directly by providing copies to their students or to research collaborators for their personal use
 - for private scholarly sharing as part of an invitation-only work group on commercial sites with which Elsevier has an agreement
- After the embargo period
 - via non-commercial hosting platforms such as their institutional repository
 - via commercial sites with which Elsevier has an agreement

In all cases accepted manuscripts should:

- link to the formal publication via its DOI
- bear a CC-BY-NC-ND license - this is easy to do
- if aggregated with other manuscripts, for example in a repository or other site, be shared in alignment with our hosting policy not be added to or enhanced in any way to appear more like, or to substitute for, the published journal article.

Published journal article (JPA): A published journal article (PJA) is the definitive final record of published research that appears or will appear in the journal and embodies all value-adding publishing activities including peer review co-ordination, copy-editing, formatting, (if relevant) pagination and online enrichment.

Policies for sharing publishing journal articles differ for subscription and gold open access articles:

Subscription Articles: If you are an author, please share a link to your article rather than the full-text. Millions of researchers have access to the formal publications on ScienceDirect, and so links will help your users to find, access, cite, and use the best available version.

Theses and dissertations which contain embedded PJAs as part of the formal submission can be posted publicly by the awarding institution with DOI links back to the formal publications on ScienceDirect.

If you are affiliated with a library that subscribes to ScienceDirect you have additional private sharing rights for others' research accessed under that agreement. This includes use for classroom teaching and internal training at the institution (including use in course packs and courseware programs), and inclusion of the article for grant funding purposes.

Gold Open Access Articles: May be shared according to the author-selected end-user license and should contain a [CrossMark logo](#), the end user license, and a DOI link to the formal publication on ScienceDirect.

Please refer to Elsevier's [posting policy](#) for further information.

18. For book authors the following clauses are applicable in addition to the above: Authors are permitted to place a brief summary of their work online only. You are not allowed to download and post the published electronic version of your chapter, nor may you scan the printed edition to create an electronic version. **Posting to a repository:** Authors are permitted to post a summary of their chapter only in their institution's repository.

19. Thesis/Dissertation: If your license is for use in a thesis/dissertation your thesis may be submitted to your institution in either print or electronic form. Should your thesis be published commercially, please reapply for permission. These requirements include permission for the Library and Archives of Canada to supply single copies, on demand, of the complete thesis and include permission for Proquest/UMI to supply single copies, on demand, of the complete thesis. Should your thesis be published commercially, please reapply for permission. Theses and dissertations which contain embedded PJAs as part of the formal submission can be posted publicly by the awarding institution with DOI links back to the formal publications on ScienceDirect.



This is a License Agreement between Chunhao Yuan ("User") and Copyright Clearance Center, Inc. ("CCC") on behalf of the Rightsholder identified in the order details below. The license consists of the order details, the Marketplace Order General Terms and Conditions below, and any Rightsholder Terms and Conditions which are included below.

All payments must be made in full to CCC in accordance with the Marketplace Order General Terms and Conditions below.

| | | | |
|-------------------------|-------------|--------------------|------------------------------------|
| Order Date | 08-Sep-2022 | Type of Use | Republish in a thesis/dissertation |
| Order License ID | 1266602-1 | Publisher | Wiley - VCH Verlag GmbH & Co. KGaA |
| ISSN | 1614-6840 | Portion | Chapter/article |

LICENSED CONTENT

| | | | |
|--------------------------|---|-------------------------|---------------------------|
| Publication Title | Advanced Energy Materials | Rightsholder | John Wiley & Sons - Books |
| Article Title | Unlocking the Electrochemical-Mechanical Coupling Behaviors of Dendrite Growth and Crack Propagation in All-Solid-State Batteries | Publication Type | e-Journal |
| Author/Editor | Wiley-VCH. | Start Page | 2101807 |
| Date | 01/01/2011 | Issue | 36 |
| Language | English | Volume | 11 |
| Country | Germany | | |

REQUEST DETAILS

| | | | |
|--|---|------------------------------------|----------------------------------|
| Portion Type | Chapter/article | Rights Requested | Main product |
| Page range(s) | 1-14 | Distribution | United States |
| Total number of pages | 14 | Translation | Original language of publication |
| Format (select all that apply) | Electronic | Copies for the disabled? | No |
| Who will republish the content? | Publisher, for profit | Minor editing privileges? | No |
| Duration of Use | Life of current and all future editions | Incidental promotional use? | No |
| Lifetime Unit Quantity | Up to 499 | Currency | USD |

NEW WORK DETAILS

| | | | |
|------------------------|---|-----------------------------------|---------------|
| Title | MECHANICAL INSTABILITY OF THE INTERFACES IN SOLID-STATE BATTERIES | Institution name | UNC Charlotte |
| Instructor name | Chunhao Yuan | Expected presentation date | 2022-11-01 |

ADDITIONAL DETAILS

The requesting person / organization to appear on the license Chunhao Yuan

REUSE CONTENT DETAILS

| | | | |
|---|---|--|---|
| Title, description or numeric reference of the portion(s) | MECHANICAL INSTABILITY OF THE INTERFACES IN SOLID-STATE BATTERIES | Title of the article/chapter the portion is from | Unlocking the Electrochemical-Mechanical Coupling Behaviors of Dendrite Growth and Crack Propagation in All-Solid-State Batteries |
| Editor of portion(s) | Yuan, Chunhao; Lu, Wenquan; Xu, Jun | Author of portion(s) | Yuan, Chunhao; Lu, Wenquan; Xu, Jun |
| Volume of serial or monograph | 11 | Publication date of portion | 2021-09-23 |
| Page or page range of portion | 2101807 | | |



This is a License Agreement between Chunhao Yuan ("User") and Copyright Clearance Center, Inc. ("CCC") on behalf of the Rightsholder identified in the order details below. The license consists of the order details, the Marketplace Order General Terms and Conditions below, and any Rightsholder Terms and Conditions which are included below.

All payments must be made in full to CCC in accordance with the Marketplace Order General Terms and Conditions below.

| | | | |
|------------------|-------------|-------------|------------------------------------|
| Order Date | 08-Sep-2022 | Type of Use | Republish in a thesis/dissertation |
| Order License ID | 1266601-1 | Publisher | Wiley - VCH Verlag GmbH & Co. KGaA |
| ISSN | 1614-6840 | Portion | Chapter/article |

LICENSED CONTENT

| | | | |
|-------------------|---|------------------|---------------------------|
| Publication Title | Advanced Energy Materials | Country | Germany |
| Article Title | Heterogeneous Reinforcements to Mitigate Li Penetration through Solid Electrolytes in All-Solid-State Batteries | Rightsholder | John Wiley & Sons - Books |
| Author/Editor | Wiley-VCH. | Publication Type | e-Journal |
| Date | 01/01/2011 | Start Page | 2201804 |
| Language | English | | |

REQUEST DETAILS

| | | | |
|---------------------------------|---|-----------------------------|----------------------------------|
| Portion Type | Chapter/article | Rights Requested | Main product |
| Page range(s) | 1-11 | Distribution | United States |
| Total number of pages | 11 | Translation | Original language of publication |
| Format (select all that apply) | Electronic | Copies for the disabled? | No |
| Who will republish the content? | Publisher, for profit | Minor editing privileges? | No |
| Duration of Use | Life of current and all future editions | Incidental promotional use? | No |
| Lifetime Unit Quantity | Up to 499 | Currency | USD |

NEW WORK DETAILS

| | | | |
|-----------------|---|----------------------------|---------------|
| Title | MECHANICAL INSTABILITY OF THE INTERFACES IN SOLID-STATE BATTERIES | Institution name | UNC Charlotte |
| Instructor name | Chunhao Yuan | Expected presentation date | 2022-11-01 |

ADDITIONAL DETAILS

<https://marketplace.copyright.com/rs-ui-web/mp/license/bfac495f-ede7-43f8-9273-0bce7d98d291/2dae0c45-ee84-4f55-bab2-d8c0b5305dac>

8/22, 8:29 AM <https://marketplace.copyright.com/rs-ui-web/mp/license/bfac495f-ede7-43f8-9273-0bce7d98d291/2dae0c45-ee84-4f55-bab2-d8c0b5305dac>

The requesting person / organization to appear on the license Chunhao Yuan

REUSE CONTENT DETAILS

| | | | |
|--|---|---|---|
| Title, description or numeric reference of the portion(s) | MECHANICAL INSTABILITY OF THE INTERFACES IN SOLID-STATE BATTERIES | Title of the article/chapter the portion is from | Heterogeneous Reinforcements to Mitigate Li Penetration through Solid Electrolytes in All-Solid-State Batteries |
| Editor of portion(s) | Yuan, Chunhao; Sheldon, Brian W.; Xu, Jun | Author of portion(s) | Yuan, Chunhao; Sheldon, Brian W.; Xu, Jun |
| Volume of serial or monograph | N/A | Publication date of portion | 2022-08-23 |
| Page or page range of portion | 2201804 | | |

RIGHTSHOLDER TERMS AND CONDITIONS

No right, license or interest to any trademark, trade name, service mark or other branding ("Marks") of WILEY or its licensors is granted hereunder, and you agree that you shall not assert any such right, license or interest with respect thereto. You may not alter, remove or suppress in any manner any copyright, trademark or other notices displayed by the Wiley material. This Agreement will be void if the Type of Use, Format, Circulation, or Requestor Type was misrepresented during the licensing process. In no instance may the total amount of Wiley Materials used in any Main Product, Compilation or Collective work comprise more than 5% (if figures/tables) or 15% (if full articles/chapters) of the (entirety of the) Main Product, Compilation or Collective Work. Some titles may be available under an Open Access license. It is the Licensors' responsibility to identify the type of Open Access license on which the requested material was published, and comply fully with the terms of that license for the type of use specified. Further details can be found on Wiley Online Library <http://olabout.wiley.com/WileyCDA/Section/id-410895.html>.

Marketplace Order General Terms and Conditions

The following terms and conditions ("General Terms"), together with any applicable Publisher Terms and Conditions, govern User's use of Works pursuant to the Licenses granted by Copyright Clearance Center, Inc. ("CCC") on behalf of the applicable Rightsholders of such Works through CCC's applicable Marketplace transactional licensing services (each, a "Service").

1) **Definitions.** For purposes of these General Terms, the following definitions apply:

"License" is the licensed use the User obtains via the Marketplace platform in a particular licensing transaction, as set forth in the Order Confirmation.

"Order Confirmation" is the confirmation CCC provides to the User at the conclusion of each Marketplace transaction. "Order Confirmation Terms" are additional terms set forth on specific Order Confirmations not set forth in the General Terms that can include terms applicable to a particular CCC transactional licensing service and/or any Rightsholder-specific terms.

"Rightsholder(s)" are the holders of copyright rights in the Works for which a User obtains licenses via the Marketplace platform, which are displayed on specific Order Confirmations.

"Terms" means the terms and conditions set forth in these General Terms and any additional Order Confirmation Terms collectively.

"User" or "you" is the person or entity making the use granted under the relevant License. Where the person accepting the Terms on behalf of a User is a freelancer or other third party who the User authorized to accept the General Terms on the User's behalf, such person shall be deemed jointly a User for purposes of such Terms.

"Work(s)" are the copyright protected works described in relevant Order Confirmations.

2) **Description of Service.** CCC's Marketplace enables Users to obtain Licenses to use one or more Works in accordance with all relevant Terms. CCC grants Licenses as an agent on behalf of the copyright rightsholder identified in the relevant Order Confirmation.

3) **Applicability of Terms.** The Terms govern User's use of Works in connection with the relevant License. In the event of any conflict between General Terms and Order Confirmation Terms, the latter shall govern. User acknowledges that Rightsholders have complete discretion whether to grant any permission, and whether to place any limitations on any grant, and that CCC has no right to supersede or to modify any such discretionary act by a Rightsholder.

4) **Representations; Acceptance.** By using the Service, User represents and warrants that User has been duly authorized by the User to accept, and hereby does accept, all Terms.

5) **Scope of License; Limitations and Obligations.** All Works and all rights therein, including copyright rights, remain the sole and exclusive property of the Rightsholder. The License provides only those rights expressly set forth in the terms and conveys no other rights in any Works

6) **General Payment Terms.** User may pay at time of checkout by credit card or choose to be invoiced. If the User chooses to be invoiced, the User shall: (i) remit payments in the manner identified on specific invoices, (ii) unless otherwise specifically stated in an Order Confirmation or separate written agreement, Users shall remit payments upon receipt of the relevant invoice from CCC, either by delivery or notification of availability of the invoice via the Marketplace platform, and (iii) if the User does not pay the invoice within 30 days of receipt, the User may incur a service charge of 1.5% per month or the maximum rate allowed by applicable law, whichever is less. While User may exercise the rights in the License immediately upon receiving the Order Confirmation, the License is automatically revoked and is null and void, as if it had never been issued, if CCC does not receive complete payment on a timely basis.

7) **General Limits on Use.** Unless otherwise provided in the Order Confirmation, any grant of rights to User (i) involves only the rights set forth in the Terms and does not include subsequent or additional uses, (ii) is non-exclusive and non-transferable, and (iii) is subject to any and all limitations and restrictions (such as, but not limited to, limitations on duration of use or circulation) included in the Terms. Upon completion of the licensed use as set forth in the Order Confirmation, User shall either secure a new permission for further use of the Work(s) or immediately cease any new use of the Work(s) and shall render inaccessible (such as by deleting or by removing or severing links or other locators) any further copies of the Work. User may only make alterations to the Work if and as expressly set forth in the Order Confirmation. No Work may be used in any way that is defamatory, violates the rights of third parties (including such third parties' rights of copyright, privacy, publicity, or other tangible or intangible property), or is otherwise illegal, sexually explicit, or obscene. In addition, User may not conjoin a Work with any other material that may result in damage to the reputation of the Rightsholder. User agrees to inform CCC if it becomes aware of any infringement of any rights in a Work and to cooperate with any reasonable request of CCC or the Rightsholder in connection therewith.

8) **Third Party Materials.** In the event that the material for which a License is sought includes third party materials (such as photographs, illustrations, graphs, inserts and similar materials) that are identified in such material as having been used by permission (or a similar indicator), User is responsible for identifying, and seeking separate licenses (under this Service, if available, or otherwise) for any of such third party materials; without a separate license, User may not use such third party materials via the License.

9) **Copyright Notice.** Use of proper copyright notice for a Work is required as a condition of any License granted under the Service. Unless otherwise provided in the Order Confirmation, a proper copyright notice will read substantially as follows: "Used with permission of [Rightsholder's name], from [Work's title, author, volume, edition number and year of copyright]; permission conveyed through Copyright Clearance Center, Inc." Such notice must be provided in a reasonably legible font size and must be placed either on a cover page or in another location that any person, upon gaining access to the material which is the subject of a permission, shall see, or in the case of republication Licenses, immediately adjacent to the Work as used (for example, as part of a by-line or footnote) or in the place where substantially all other credits or notices for the new work containing the republished Work are located. Failure to include the required notice results in loss to the Rightsholder and CCC, and the User shall be liable to pay liquidated damages for each such failure equal to twice the use fee specified in the Order Confirmation, in addition to the use fee itself and any other fees and charges specified.

10) **Indemnity.** User hereby indemnifies and agrees to defend the Rightsholder and CCC, and their respective employees and directors, against all claims, liability, damages, costs, and expenses, including legal fees and expenses, arising out of any use of a Work beyond the scope of the rights granted herein and in the Order Confirmation, or any use of a Work which has been altered in any unauthorized way by User, including claims of defamation or infringement of rights of copyright, publicity, privacy, or other tangible or intangible property.

11) **Limitation of Liability.** UNDER NO CIRCUMSTANCES WILL CCC OR THE RIGHTSHOLDER BE LIABLE FOR ANY DIRECT, INDIRECT, CONSEQUENTIAL, OR INCIDENTAL DAMAGES (INCLUDING WITHOUT LIMITATION DAMAGES FOR LOSS OF BUSINESS PROFITS OR INFORMATION, OR FOR BUSINESS INTERRUPTION) ARISING OUT OF THE USE OR INABILITY TO USE A WORK, EVEN IF ONE OR BOTH OF THEM HAS BEEN ADVISED OF THE POSSIBILITY OF SUCH DAMAGES. In any event, the total liability of the Rightsholder and CCC (including their respective employees and directors) shall not exceed the total amount actually paid by User for the relevant License. User assumes full liability for the actions and omissions of its principals, employees, agents, affiliates, successors, and assigns.

12) **Limited Warranties.** THE WORK(S) AND RIGHT(S) ARE PROVIDED "AS IS." CCC HAS THE RIGHT TO GRANT TO USER THE RIGHTS GRANTED IN THE ORDER CONFIRMATION DOCUMENT. CCC AND THE RIGHTSHOLDER DISCLAIM ALL OTHER WARRANTIES RELATING TO THE WORK(S) AND RIGHT(S), EITHER EXPRESS OR IMPLIED, INCLUDING WITHOUT LIMITATION IMPLIED WARRANTIES OF MERCHANTABILITY OR FITNESS FOR A PARTICULAR PURPOSE. ADDITIONAL RIGHTS MAY BE REQUIRED TO USE ILLUSTRATIONS, GRAPHS, PHOTOGRAPHS, ABSTRACTS, INSERTS, OR OTHER PORTIONS OF THE WORK (AS OPPOSED TO THE ENTIRE WORK) IN A MANNER CONTEMPLATED BY USER; USER UNDERSTANDS AND AGREES THAT NEITHER CCC NOR THE RIGHTSHOLDER MAY HAVE SUCH ADDITIONAL RIGHTS TO GRANT.

13) **Effect of Breach.** Any failure by User to pay any amount when due, or any use by User of a Work beyond the scope of the License set forth in the Order Confirmation and/or the Terms, shall be a material breach of such License. Any breach not cured within 10 days of written notice thereof shall result in immediate termination of such License without further notice. Any unauthorized (but licensable) use of a Work that is terminated immediately upon notice thereof may be liquidated by payment of the Rightsholder's ordinary license price therefore; any unauthorized (and unlicensable) use that is not terminated immediately for any reason (including, for example, because materials containing the Work cannot reasonably be recalled) will be subject to all remedies available at law or in equity, but in no event to a payment of less than three times the Rightsholder's ordinary license price for the most closely analogous licensable use plus Rightsholder's and/or CCC's costs and expenses incurred in collecting such payment.

14) **Additional Terms for Specific Products and Services.** If a User is making one of the uses described in this Section 14, the additional terms and conditions apply:

a) **Print Uses of Academic Course Content and Materials (photocopies for academic coursepacks or classroom handouts).** For photocopies for academic coursepacks or classroom handouts the following additional terms apply:

i) The copies and anthologies created under this License may be made and assembled by faculty members individually or at their request by on-campus bookstores or copy centers, or by off-campus copy shops and other similar entities.

ii) No License granted shall in any way: (i) include any right by User to create a substantively non-identical copy of the Work or to edit or in any other way modify the Work (except by means of deleting material immediately preceding or following the entire portion of the Work copied) (ii) permit "publishing ventures" where any particular anthology would be systematically marketed at multiple institutions.

iii) Subject to any Publisher Terms (and notwithstanding any apparent contradiction in the Order Confirmation arising from data provided by User), any use authorized under the academic pay-per-use service is limited as follows:

A) any License granted shall apply to only one class (bearing a unique identifier as assigned by the institution, and thereby including all sections or other subparts of the class) at one institution;

B) use is limited to not more than 25% of the text of a book or of the items in a published collection of essays, poems or articles;

C) use is limited to no more than the greater of (a) 25% of the text of an issue of a journal or other periodical or (b) two articles from such an issue;

D) no User may sell or distribute any particular anthology, whether photocopied or electronic, at more than one institution of learning;

E) in the case of a photocopy permission, no materials may be entered into electronic memory by User except in order to produce an identical copy of a Work before or during the academic term (or analogous period) as to which any particular permission is granted. In the event that User shall choose to retain materials that are the subject of a photocopy permission in electronic memory for purposes of producing identical copies more than one day after such retention (but still within the scope of any permission granted), User must notify CCC of such fact in the applicable permission request and such retention shall constitute one copy actually sold for purposes of calculating permission fees due; and

F) any permission granted shall expire at the end of the class. No permission granted shall in any way include any right by User to create a substantively non-identical copy of the Work or to edit or in any other way modify the Work (except by means of deleting material immediately preceding or following the entire portion of the Work copied).

iv) **Books and Records; Right to Audit.** As to each permission granted under the academic pay-per-use Service, User shall maintain for at least four full calendar years books and records sufficient for CCC to determine the numbers of copies made by User under such permission. CCC and any representatives it may designate shall have the right to audit such books and records at any time during User's ordinary business hours, upon two days' prior notice. If any such audit shall determine that User shall have underpaid for, or underreported, any photocopies sold or by three percent (3%) or more, then User shall bear all the costs of any such audit; otherwise, CCC shall bear the costs of any such audit. Any amount determined by such audit to have been underpaid by User shall immediately be paid to CCC by User, together with interest thereon at the rate of 10% per annum from the date such amount was originally due. The provisions of this paragraph shall survive the termination of this License for any reason.

b) **Digital Pay-Per-Uses of Academic Course Content and Materials (e-coursepacks, electronic reserves, learning management systems, academic institution intranets).** For uses in e-coursepacks, posts in electronic reserves, posts in learning management systems, or posts on academic institution intranets, the following additional terms apply:

i) The pay-per-uses subject to this Section 14(b) include:

A) **Posting e-reserves, course management systems, e-coursepacks for text-based content**, which grants authorizations to import requested material in electronic format, and allows electronic access to this material to members of a designated college or university class, under the direction of an instructor designated by the college or university, accessible only under appropriate electronic controls (e.g., password);

B) **Posting e-reserves, course management systems, e-coursepacks for material consisting of photographs or other still images not embedded in text**, which grants not only the authorizations described in Section 14(b)(i)(A) above, but also the following authorization: to include the requested material in course materials for use consistent with Section 14(b)(i)(A) above, including any necessary resizing, reformatting or modification of the resolution of such requested material (provided that such modification does not alter the underlying editorial content or meaning of the requested material, and provided that the resulting modified content is used solely within the scope of, and in a manner consistent with, the particular authorization described in the Order Confirmation and the Terms), but not including any other form of manipulation, alteration or editing of the requested material;

C) **Posting e-reserves, course management systems, e-coursepacks or other academic distribution for audiovisual content**, which grants not only the authorizations described in Section 14(b)(i)(A) above, but also the following authorizations: (i) to include the requested material in course materials for use consistent with Section 14(b)(i)(A) above; (ii) to display and perform the requested material to such members of such class in the physical classroom or remotely by means of streaming media or other video formats; and (iii) to "clip" or reformat the requested material for purposes of time or content management or ease of delivery, provided that such "clipping" or reformatting does not alter the underlying editorial content or meaning of the requested material and that the resulting material is used solely within the scope of, and in a manner consistent with, the particular authorization described in the Order Confirmation and the Terms. Unless expressly set forth in the relevant Order Confirmation, the License does not authorize any other form of manipulation, alteration or editing of the requested material.

ii) Unless expressly set forth in the relevant Order Confirmation, no License granted shall in any way: (i) include any right by User to create a substantively non-identical copy of the Work or to edit or in any other way modify the Work (except by means of deleting material immediately preceding or following the entire portion of the Work copied or, in the case of Works subject to Sections 14(b)(1)(B) or (C) above, as described in such Sections) (ii) permit "publishing ventures" where any particular course materials would be systematically marketed at multiple institutions.

iii) Subject to any further limitations determined in the Rightsholder Terms (and notwithstanding any apparent contradiction in the Order Confirmation arising from data provided by User), any use authorized under the electronic course content pay-per-use service is limited as follows:

A) any License granted shall apply to only one class (bearing a unique identifier as assigned by the institution, and thereby including all sections or other subparts of the class) at one institution;

B) use is limited to not more than 25% of the text of a book or of the items in a published collection of essays, poems or articles;

C) use is limited to not more than the greater of (a) 25% of the text of an issue of a journal or other periodical or (b) two articles from such an issue;

D) no User may sell or distribute any particular materials, whether photocopied or electronic, at more than one institution of learning;

E) electronic access to material which is the subject of an electronic-use permission must be limited by means of electronic password, student identification or other control permitting access solely to students and instructors in the class;

F) User must ensure (through use of an electronic cover page or other appropriate means) that any person, upon gaining electronic access to the material, which is the subject of a permission, shall see:

- o a proper copyright notice, identifying the Rightsholder in whose name CCC has granted permission,
- o a statement to the effect that such copy was made pursuant to permission,
- o a statement identifying the class to which the material applies and notifying the reader that the material has been made available electronically solely for use in the class, and
- o a statement to the effect that the material may not be further distributed to any person outside the class, whether by copying or by transmission and whether electronically or in paper form, and User must also ensure that such cover page or other means will print out in the event that the person accessing the material chooses to print out the material or any part thereof.

G) any permission granted shall expire at the end of the class and, absent some other form of authorization, User is thereupon required to delete the applicable material from any electronic storage or to block electronic access to the applicable material.

iv) Uses of separate portions of a Work, even if they are to be included in the same course material or the same university or college class, require separate permissions under the electronic course content pay-per-use Service. Unless otherwise provided in the Order Confirmation, any grant of rights to User is limited to use completed no later than the end of the academic term (or analogous period) as to which any particular permission is granted.

v) **Books and Records; Right to Audit.** As to each permission granted under the electronic course content Service, User shall maintain for at least four full calendar years books and records sufficient for CCC to determine the numbers of copies made by User under such permission. CCC and any representatives it may designate shall have the right to audit such books and records at any time during User's ordinary business hours, upon two days' prior notice. If any such audit shall determine that User shall have underpaid for, or underreported, any electronic copies used by three percent (3%) or more, then User shall bear all the costs of any such audit; otherwise, CCC shall bear the costs of any such audit. Any amount determined by such audit to have been underpaid by User shall immediately be paid to CCC by User, together with interest thereon at the rate of 10% per annum from the date such amount was originally due. The provisions of this paragraph shall survive the termination of this license for any reason.

c) **Pay-Per-Use Permissions for Certain Reproductions (Academic photocopies for library reserves and interlibrary loan reporting) (Non-academic internal/external business uses and commercial document delivery).** The License expressly excludes the uses listed in Section (c)(i)-(v) below (which must be subject to separate license from the applicable Rightsholder) for: academic photocopies for library reserves and interlibrary loan reporting; and non-academic internal/external business uses and commercial document delivery.

- i) electronic storage of any reproduction (whether in plain-text, PDF, or any other format) other than on a transitory basis;
- ii) the input of Works or reproductions thereof into any computerized database;
- iii) reproduction of an entire Work (cover-to-cover copying) except where the Work is a single article;
- iv) reproduction for resale to anyone other than a specific customer of User;
- v) republication in any different form. Please obtain authorizations for these uses through other CCC services or directly from the rightsholder.

Any license granted is further limited as set forth in any restrictions included in the Order Confirmation and/or in these Terms.

d) **Electronic Reproductions in Online Environments (Non-Academic-email, intranet, internet and extranet).** For "electronic reproductions", which generally includes e-mail use (including instant messaging or other electronic transmission to a defined group of recipients) or posting on an intranet, extranet or Intranet site (including any display or performance incidental thereto), the following additional terms apply:

- i) Unless otherwise set forth in the Order Confirmation, the License is limited to use completed within 30 days for any use on the Internet, 60 days for any use on an intranet or extranet and one year for any other use, all as measured from the "republication date" as identified in the Order Confirmation, if any, and otherwise from the date of the Order Confirmation.
- ii) User may not make or permit any alterations to the Work, unless expressly set forth in the Order Confirmation (after request by User and approval by Rightsholder); provided, however, that a Work consisting of photographs or other still images not embedded in text may, if necessary, be resized, reformatted or have its resolution modified without additional express permission, and a Work consisting of audiovisual content may, if necessary, be "clipped" or reformatted for purposes of time or content management or ease of delivery (provided that any such resizing, reformatting, resolution modification or "clipping" does not alter the underlying editorial content or meaning of the Work used, and that the resulting material is used solely within the scope of, and in a manner consistent with, the particular License described in the Order Confirmation and the Terms.

15) **Miscellaneous.**

- a) User acknowledges that CCC may, from time to time, make changes or additions to the Service or to the Terms, and that Rightsholder may make changes or additions to the Rightsholder Terms. Such updated Terms will replace the prior terms and conditions in the order workflow and shall be effective as to any subsequent Licenses but shall not apply to Licenses already granted and paid for under a prior set of terms.
- b) Use of User-related information collected through the Service is governed by CCC's privacy policy, available online at www.copyright.com/about/privacy-policy/.
- c) The License is personal to User. Therefore, User may not assign or transfer to any other person (whether a natural person or an organization of any kind) the License or any rights granted thereunder; provided, however, that, where applicable, User may assign such License in its entirety on written notice to CCC in the event of a transfer of all or substantially all of User's rights in any new material which includes the Work(s) licensed under this Service.
- d) No amendment or waiver of any Terms is binding unless set forth in writing and signed by the appropriate parties, including, where applicable, the Rightsholder. The Rightsholder and CCC hereby object to any terms contained in any writing prepared by or on behalf of the User or its principals, employees, agents or affiliates and purporting to govern or otherwise relate to the License described in the Order Confirmation, which terms are in any way inconsistent with any Terms set forth in the Order Confirmation, and/or in CCC's standard operating procedures, whether such writing is prepared prior to, simultaneously with or subsequent to the Order Confirmation, and whether such writing appears on a copy of the Order Confirmation or in a separate instrument.
- e) The License described in the Order Confirmation shall be governed by and construed under the law of the State of New York, USA, without regard to the principles thereof of conflicts of law. Any case, controversy, suit, action, or proceeding arising out of, in connection with, or related to such License shall be brought, at CCC's sole discretion, in any federal or state court located in the County of New York, State of New York, USA, or in any federal or state court whose geographical jurisdiction covers the location of the Rightsholder set forth in the Order Confirmation. The parties expressly submit to the personal jurisdiction and venue of each such federal or state court.